A 250 GHz Photonic Band Gap Gyrotron Amplifier

by

Emilio A. Nanni

M.S. (EECS), Massachusetts Institute of Technology (2010)
B.S. (EE), University of Missouri - Rolla (2007)
B.S. (Physics), University of Missouri - Rolla (2007)

Submitted to the
Department of Electrical Engineering and Computer Science
in partial fulfillment of the requirements for the degree of

Doctor of Philosophy

at the

MASSACHUSETTS INSTITUTE OF TECHNOLOGY

June 2013

Author .....
Department of Electrical Engineering and Computer Science
March 26, 2013

Certified by .....
Richard J. Temkin
Senior Research Scientist, Department of Physics
Thesis Supervisor

Accepted by .....
Professor Leslie A. Kolodziejski
Chairman, Committee on Graduate Students
Department of Electrical Engineering and Computer Science

A 250 GHz Photonic Band Gap Gyrotron Amplifier

by

Emilio A. Nanni

Submitted to the Department of Electrical Engineering and Computer Science
on March 26, 2013, in partial fulfillment of the
requirements for the degree of
Doctor of Philosophy

Abstract

This thesis reports the theoretical and experimental investigation of a novel gyrotron traveling-wave-tube (TWT) amplifier at 250 GHz. The gyrotron amplifier designed and tested in this thesis has achieved a peak small signal gain of 38 dB at 247.7 GHz, with a 32 kV, 0.35 A electron beam and a 8.9 T magnetic field. The instantaneous -3 dB bandwidth of the amplifier at peak gain is 0.4 GHz. A peak output power of 45 W has been measured. The output power is not saturated but is limited by the 7.5 mW of available input power. The amplifier can be tuned for operation from 245-256 GHz. With a gain of 24 dB and centered at 253.25 GHz the widest instantaneous -3 dB bandwidth of 4.5 GHz was observed for a 19 kV, 0.305 A electron beam. To achieve stable operation at these high frequencies, the amplifier uses a novel photonic band gap (PBG) interaction circuit. The PBG interaction circuit confines the TE_{03}-like mode which couples strongly to the electron beam. The PBG circuit provides stability from oscillations by supporting the propagation of TE modes in a narrow range of frequencies, allowing for the confinement of the operating TE_{03}-like mode while rejecting the excitation of oscillations at lower frequencies. Experimental results taken over a wide range of parameters, 15-30 kV and 0.25-0.5 A, show good agreement with a theoretical model. The theoretical model incorporates cold test measurements for the transmission line, input coupler, PBG waveguide and mode converter. This experiment achieved the highest frequency of operation (250 GHz) for a gyrotron amplifier. At present, there are no other amplifiers in this frequency range that are capable of producing either high gain or high-output power. With 38 dB of gain and 45 W this is also the highest gain observed above 94 GHz and the highest output power achieved above 140 GHz by any conventional-voltage vacuum electron device based amplifier. The output power, output beam pattern, instantaneous bandwidth, spectral purity and shot-to-shot stability of the amplified pulse meet the basic requirements for the implementation of this device on a pulsed dynamic nuclear polarization (DNP) nuclear magnetic resonance (NMR) spectrometer.

Thesis Supervisor: Richard J. Temkin

Title: Senior Research Scientist, Department of Physics

Acknowledgments

If I learned one thing in graduate school its that research is a process which benefits tremendously from the efforts, contributions and thoughts of the many collaborators involved. First in this regard is my adviser, Richard Temkin, to whom I owe a huge debt of gratitude. I would like to thank Michael Shapiro for answering every question I asked and Ivan Mastovsky, whose help in the lab was of utmost importance.

My fellow graduate students made my time here so enjoyable and interesting. I thank Brian Munroe for breaks at the gym; David Tax for coffee, granola bars and the Bruins; Sasha Soane for enriching all of our lives; Jason Hummelt for reminding me to take a deep breath and enjoy life; and Elizabeth Kowalski for being an awesome and patient office mate. I thank Samantha Lewis, the most exceptional UROP, for her help in the lab. I also thank my Waves and Beams co-workers and friends Colin Joye, Antonio Torrezan, Roark Marsh, JieXi Zhang, Sam Schaub, Sergey Arsenyev, Xueying Liu, Sudheer Jawla, Alan Cook, Hae Jin Kim and Paul Woskov for many chats and lots of help.

A special thank you to Sam Schaub, Sasha Soane and Elizabeth Kowalski for their comments and edits on my thesis.

I can't forget my friends from the FBML: Prof. Robert Griffin, Alexander Barnes, Vladimir Michaelis and the other graduate students and postdocs. Keep up the good work. For always being ready and willing to lend a hand, I thank Ron DeRocher, Ajay Thakkar, Michael Mullins and Jeff Bryant.

Finally and most importantly, I need to thank my loving family for all their support. My mother and father who gave me the best childhood, filled with so many unique experiences and opportunities. My sister who is the most caring person I know and my brother for reminding me I'm lucky because I get to do something I love. My wonderful wife Sarah, you were there every step of the way. I can't imagine going through this experience without you. I am so blessed to have met you.

Contents

List of Figures

List of Tables

Abbreviations and Acronyms

AC	Alternating current
BWO	Backward-wave oscillator
CE	Cross effect
CPI	Communication and Power Industries, Inc.
CVD	Capacitive voltage divider
CW	Continuous wave
DAQ	Data acquisition
DC	Direct current
DNP	Dynamic nuclear polarization
EIO	Extended interaction oscillator
ECRH	Electron cyclotron resonance heating
EPR	Electron paramagnetic resonance
HFSS	High Frequency Structure Simulator
IAP	Institute of Applied Physics
IF	Intermediate frequency
LO	Local oscillator
MAGY	Maryland Gyrotron self-consistent code
MAS	Magic angle spinning
MIG	Magnetron injection gun
MIT	Massachusetts Institute of Technology
NMR	Nuclear magnetic resonance

NRL	U.S. Naval Research Laboratory
NTHU	National Tsing Hua University
PBG	Photonic band gap
RF	Radio frequency
SE	Solid effect
TE	Transverse electric
TM	Transverse magnetic
TWT	Traveling-wave tube
VDI	Virginia Diodes, Inc.
VNA	Vector network analyzer

Chapter 1

Introduction

1.1 Motivation

High-power sources in the millimeter wave, sub-millimeter wave and THz regime of the electromagnetic spectrum are of great interest due to their potential applications in spectroscopy, communications and radar. Many of these applications require the source to provide phase stability and control. However, there are currently no commercially available devices that can meet this requirement while providing output powers $\geq$ 100 W. Among the most exciting applications for high power THz sources is pulsed dynamic nuclear polarization (DNP) nuclear magnetic resonance (NMR) spectroscopy. Microwave-driven DNP experiments are now recognized as a powerful method of enhancing signals in solid state and solution NMR and imaging. DNP improves the sensitivity of NMR spectra by about a factor of 100 [17]. DNP has been demonstrated successfully up to 16.4 T (^{1}H/e$^-$ frequencies of 700 MHz / 460 GHz) using a gyrotron oscillator [18]. However, modern NMR spectroscopy is moving to higher magnetic fields, where much better spectral resolution is achieved. This increase in magnetic field results in a decrease in the achievable enhancement as ω_0^{-1} for the cross effect and ω_0^{-2} for the solid effect [71], where ω_0 is the frequency of operation. Circumventing these reductions in DNP enhancements requires the use of time domain-DNP (pulsed-DNP) experiments. The extension of pulsed-DNP to higher magnetic fields requires the development of THz sources at the relevant fre-

quencies with phase control and the ability to generate the required pulse sequences. Gyrotron amplifiers are the most promising technology available because they offer the possibility of achieving high gain and broad bandwidth even as the frequency of operation moves into the THz band.

1.2 Gyrotron Oscillators and Amplifiers

The generation of millimeter and sub-millimeter wavelength radiation at high power has proved to be a significant challenge. Solid state devices cannot be considered as a possibility for high power generation at such high frequencies (hundreds of GHz) due to scalability and efficiency issues. Classical microwave tubes, e.g. klystrons and traveling wave tubes, can produce high power (kW) electromagnetic radiation up to 100 GHz [73], but these slow wave devices require physical structures in the interaction cavity that are smaller than the wavelength of operation. This small element size produces difficulties with thermal damage and manufacturing of the interaction cavity. Gyrotrons are a form of electron cyclotron resonance maser capable of producing kilowatts to megawatts of output power in the microwave, millimeter wave and terahertz bands [63, 42, 70, 122, 159]. Gyrotrons were initially proposed due to the cyclotron resonance instability that was discovered independently in the late 1950s by R. Twiss [166], J. Schneider [144] and A. Gaponov [66]. This led to the invention of the gyrotron in a similar configuration to the one described in Section 2.2 by Gaponov et al. [67] with 190 W continuous wave (CW) power at 12 mm wavelength. This was followed by the design of gyrotrons in the 1970s that could produce several kW of power at frequencies up to 300 GHz by Zaytsev et al. [181]. To minimize the thermal load, the production of pulse gyrotron oscillators with several hundred kW of power and high frequencies was completed in the 1980s [157]. In the past two decades the focus has shifted from simply achieving higher frequency devices to providing useful millimeter and sub-millimeter wave sources for Electron Cyclotron Resonance Heating (ECRH) of plasmas [156], DNP NMR and Electron Paramagnetic Resonance (EPR) experiments [17]. This shift changed the focus to

providing reliability, efficient power conversion and delivery, larger bandwidth and signal stability.

Gyrotrons operate by the resonant interaction between the eigenmodes of an interaction cavity, typically cylindrical, and a mildly relativistic electron beam that is gyrating in a constant axial magnetic field. The most basic configuration of a gyrotron consists of a magnetron injection gun (MIG) that launches an annular electron beam into the hollow bore of a solenoidal, often superconducting, magnet. The orientation of the DC electric field that extracts the electron beam from the cathode produces a beam that has both a perpendicular and parallel velocity component to the axial field produced by the solenoidal magnet. As the electron beam travels into the central bore, it undergoes adiabatic compression that increases its orbital momentum. The beam enters a metallic cavity that has an eigenmode resonance that is close to a harmonic of the frequency at which the electron gyrates around the magnetic field line. The electron beam surrenders some of its kinetic energy to the electromagnetic mode through stimulated emission. The electrons exit the cavity and are deposited on a metallic collector. In its simplest configuration, the collector can also hold an axial dielectric window that couples the electromagnetic radiation out of the device. However, it is often convenient to convert the wave into a Gaussian beam that can be efficiently extracted in a transverse direction using mirrors.

Table 1.1 shows some leading CW and pulse gyrotron experiments in terms of frequency of operation, power output, and bandwidth. In Figure 1-1, the achieved single device power output for solid state and vacuum electron devices is plotted. The THz gap is clearly visible with conventional gyrotrons having a clear supremacy for the 100-500 GHz range.

A new class of device called the gyrotron traveling-wave-tube (TWT) amplifier (gyrotron amplifier, gyro-TWT, gyro-amplifier) also emerged from the discovery of the cyclotron resonance instability [44], described in Section 2.3 of this paper. In recent years, gyrotron amplifiers have demonstrated high-output power levels with significant gain bandwidths [43, 36, 25]. A gyrotron amplifier works on the same

Table 1.1: Illustrative THz Gyrotron Oscillator Experiments

Source	Year	Frequency (GHz)	Cyclotron Harmonic	Mode (TE_{mnp})	V (kV)	I (A)	P (W)
MIT[19]	2012	250	1	$TE_{5,2,1}$	12	0.18	35
MIT[165]	2011	330	2	$TE_{4,3,1}$	10.1	0.19	18
CPI[141]	2010	263	1	$TE_{0,3,1}$	13	0.05	80
Fukui[85]	2010	395	2	$TE_{0,6,1}$	12	0.300	40
MIT[163]	2010	460	2	$TE_{11,2,1}$	13	0.1	16
IAP[179]	2009	260	2	$TE_{0,6,1}$	13	0.4	100
MIT[81]	2004	460	2	$TE_{0,6,1}$	12.4	0.13	8
MIT[97]	2000	250	1	$TE_{0,3,1}$	12	0.05	25
IAP[181]	1973	326	2	$TE_{2,3,1}$	27.9	0.9	1500
Fukui[86]	1998	301	1	$TE_{0,3,1}$	14	0.08	17

fundamental principles as a gyrotron oscillator for the extraction of energy from an electron beam. However, the amplifier is operated under conditions that suppress self-start oscillations, including backward wave oscillations (BWOs) that could disrupt the operation of the device. Amplification is achieved in a gyrotron amplifier by a convective instability that results from the interaction of a mildly relativistic, annular, gyrating electron beam and a transverse electric (TE) mode in a waveguide immersed in a strong static axial magnetic field (B_0), described in Section 2.1. The grazing intersection between the dispersion relation lines of the cyclotron resonance and a TE waveguide mode near the waveguide cutoff results in high gain and moderate bandwidth. The Doppler shifted electron beam resonance condition is given by

$$\omega - s\Omega/\gamma - k_z v_z = 0 \tag{1.1}$$

and the waveguide mode dispersion relation is

$$\omega^2 - k_z^2 c^2 - k_\perp^2 c^2 = 0, \tag{1.2}$$

where ω is the frequency of the wave; $\Omega = eB_0/m_e$ is the non-relativistic cyclotron frequency of the gyrating electrons; e and m_e are, respectively, the charge and the rest mass of the electron; γ is the relativistic mass factor; $s = 1$ is the cyclotron har-

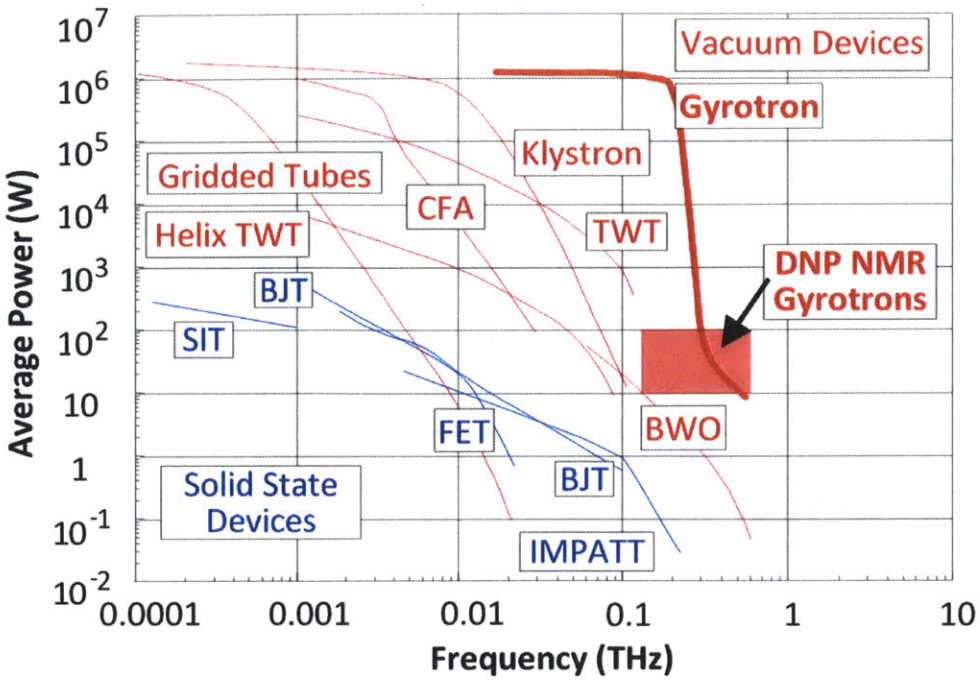

Figure 1-1: Power output for vacuum electron and solid state devices [111].

monic number; k_z and $k_\perp$ are the longitudinal and transverse propagation constants, respectively, of the waveguide mode; v_z is the axial velocity of the electrons and c is the speed of light. This requires the design of an interaction circuit that supports the propagation of a mode at the correct frequency while appearing lossy to frequencies and modes outside the region of interest. This is usually performed by inserting lossy ceramics, severs and selecting geometries with favorable dispersion relations [91]. Further complications arise when considering the design of an amplifier above 100 GHz because the operational mode of the amplifier cannot be a fundamental mode due to compression restrictions of the electron beam. When the transverse dimension of the electron beam is on the order of the operational wavelength a higher order mode interaction circuit is required. In a gyrotron amplifier, the signal of interest must be efficiently coupled into the cavity at the beginning of the interaction region. The wave propagates along the amplifier circuit while extracting energy from the electron beam until it is removed from the device with an output coupler in a similar fashion to the oscillator.

Additional types of amplifiers, alternative to the gyrotron TWT amplifier, include

the gyro-klystron and the gyro-twystron. The gyro-klystron consists of a series of isolated cavities with electromagnetic coupling for the first cavity and the final cavity [180, 52, 29, 30]. The bunching mechanism is driven by the input signal in the first cavity. The gyro-klystron can achieve significant efficiencies and it is insensitive to velocity spread similar to the gyrotron oscillator. However, the bandwidth of the gyro-klystron is limited and it requires precise tuning of the cavities. The gyro-twystron is a hybrid between the gyrotron TWT amplifier and a gyro-klystron. The gyro-twystron consists of an initial bunching cavity followed by a traveling wave section for the output [28, 27]. This configuration limits the sensitivity of the amplifier to the frequency of the initial cavity, but it decreases the gain with respect to a gyro-klystron and the bandwidth is still limited when compared to a gyrotron TWT amplifier.

1.3 Background of Gyrotron Amplifiers

Gyrotron TWT amplifiers were first studied in the early 1970s, mainly at the Naval Research Laboratory (NRL), with devices in the X and Ku bands that operated in the fundamental waveguide mode [20, 132]. These early studies showed how the promise of high gain and high-output power in gyrotron amplifiers was limited by the strong forward and backward wave gyrotron oscillations near the waveguide cutoff and interaction at higher harmonics.

More recently, a scheme of distributed loading was proposed by the research group at the National Tsing Hua University (NTHU) in Taiwan to suppress the gyrotron backward wave oscillations (gyro-BWO) and forward wave gyrotron oscillations near the waveguide cutoff. A proof-of-principle device demonstrated over 70 dB of gain at 35 GHz [43]. This device operated in the fundamental TE_{11} waveguide mode. Subsequently, a TE_{01} high average power device based on this concept was demonstrated at NRL [121] and a TE_{01} device was demonstrated at 94 GHz by Communication and Power Industries, Inc. (CPI) [26]. A comparison of recent gyrotron amplifier experiments is shown in Table 1.2.

Table 1.2: Recent Gyrotron Amplifier Experiments

	Frequency (GHz)	Gain (dB)	P_{out} (kW)	Voltage (kV)	Current (A)
UESTC (2010) [169]	34	40	160	70	10
MIT (2008) [91]	140	34	0.8	37	2.7
CPI (2005) [26]	95	43	1.5	30	1.8
NRL (2004) [134]	35	60	78	70	6
MIT (2003) [148]	140	29	30	65	7
NTHU (1998) [43]	35	70	93	100	3.5

Operation at fundamental modes is not feasible at high frequencies such as 250 GHz where the radius of the interaction structure would be on the order of a fraction of a millimeter. This results in high ohmic losses and presents a significant challenge in transporting an electron beam over long distances (~300 mm) without causing beam interception on the waveguide walls. In prior research at MIT, gyrotron amplifiers with high power (30 kW) and low power (0.8 kW) have been successfully demonstrated at 140 GHz [150, 91]. These experiments used a novel quasioptical, overmoded interaction structure which allows for single mode operation in a higher order mode. The interaction circuit consists of a confocal waveguide with severs for additional suppression of oscillations. Such a mode-selective open waveguide imparts high diffractive losses to the lower order modes which tend to interact with the beam more strongly. This selective loading of the lower order modes allows for stable operation in a higher order mode. Though mode selective, the confocal waveguide has an azimuthally asymmetric field profile which reduces its interaction efficiency with the annular beam produced by the MIG that is typically used in gyrotrons.

Instantaneous gain bandwidth often plays a role in determining the successful implementation of an amplifier. One important application of millimeter waves is in spectroscopy, where coherent pulses are needed for optical pumping of molecular states. The pulses must be shorter than the relaxation time, typically requiring sub-nanosecond (or picosecond scale) pulse lengths [23]. Sub-nanosecond microwave pulses have been demonstrated in a vacuum electron device by super-radiance [69], but such pulses cannot be used for spectroscopy. Sub-nanosecond pulses must con-

tain a spectral bandwidth exceeding the transform limit of $f_{BW} \approx 1$ GHz. In the conventional microwave bands at frequencies of one to several GHz, the required gain bandwidth to amplify such picosecond pulses is generally not available, since f_{BW} is a large fraction of the carrier frequency. In recent years, high power, wideband amplifiers in the millimeter wave band have been developed that are suitable for amplifying picosecond pulses. For example, a form of klystron called an extended interaction klystron has been developed at 95 GHz with a gain bandwidth of about 1 GHz. This amplifier has been used to successfully amplify 1 kW output pulses as short as 800 ps [32]. A gyrotron amplifier at 95 GHz has been demonstrated with a gain bandwidth of 6.5 GHz at an output power level of 2 kW [25]. This gyrotron amplifier could in principle be used to amplify a 150 ps pulse. Amplification of picosecond pulses was tested with the MIT 140 GHz wideband gyrotron amplifier [93]. Detailed studies were needed of the amplification process in gyrotron amplifiers because of the possibility of distortion in amplification of picosecond pulses. Pulses as short as 400 ps were amplified with minor distortion and 1 ns pulses were amplified with almost no distortion. The broadening of the pulses from waveguide dispersion and limited gain bandwidth was characterized and these were shown to be the contributing factors to the pulse distortion.

1.4 Photonic Band Gap Structures

As mentioned in Section 1.2, the gyrotron amplifier requires a circuit able to suppress the interaction between the electron beam and modes that are not of interest. At long wavelengths, when the operational mode is close to the fundamental mode of the waveguide, this circuit can be achieved with the use of dielectric loading which is placed such that it suppresses the undesired mode while having limited impact on the operational mode. However, at shorter wavelengths, where a highly overmoded circuit is required, dielectric loading becomes difficult to fabricate because of the decrease in size. Additionally, the design of the dielectric loading such that it suppresses all dangerous modes becomes difficult because of the increasing number of modes that must

be taken into account. Photonic band gap (PBG) structures offer the promise of a frequency selective circuit where the boundary condition at the waveguide "wall" can prevent undesired oscillations. A PBG is defined as a periodic structure in one, two or three dimensions that is composed of metal and/or dielectric components where certain frequencies are not allowed to propagate through the lattice. PBG structures have been demonstrated successfully as optical waveguides [98] and accelerator structures [152]. A common example of a PBG is a Bragg reflector composed of alternating layers of dielectric. Bragg reflectors are often used in optics because of their frequency selective properties. Figure 1-2 is an example of a Bragg reflector made from AlAs and AlGaAs layering on a GaAs substrate. The reflected power for 25 paired layers is shown in Figure 1-3. Primarily metallic PBG structures are of interest for gyrotron oscillators [149] and amplifiers due to their inherent compatibility with the presence of the electron beam (negating concern of charge buildup on dielectric surfaces). The global band gap of a 2D triangular lattice of metallic rods and its implementation as a waveguide is described in Section 3.3.

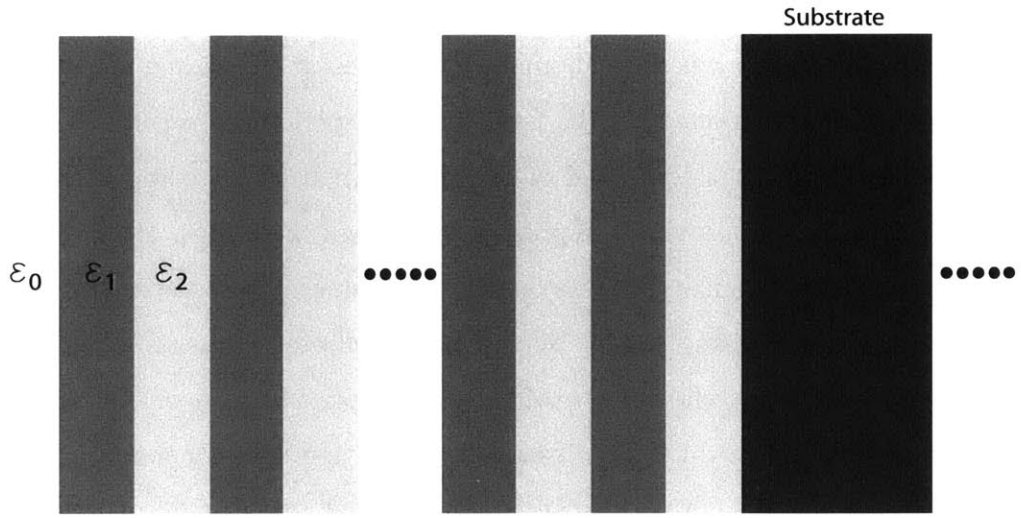

Figure 1-2: Schematic of an optical Bragg reflector.

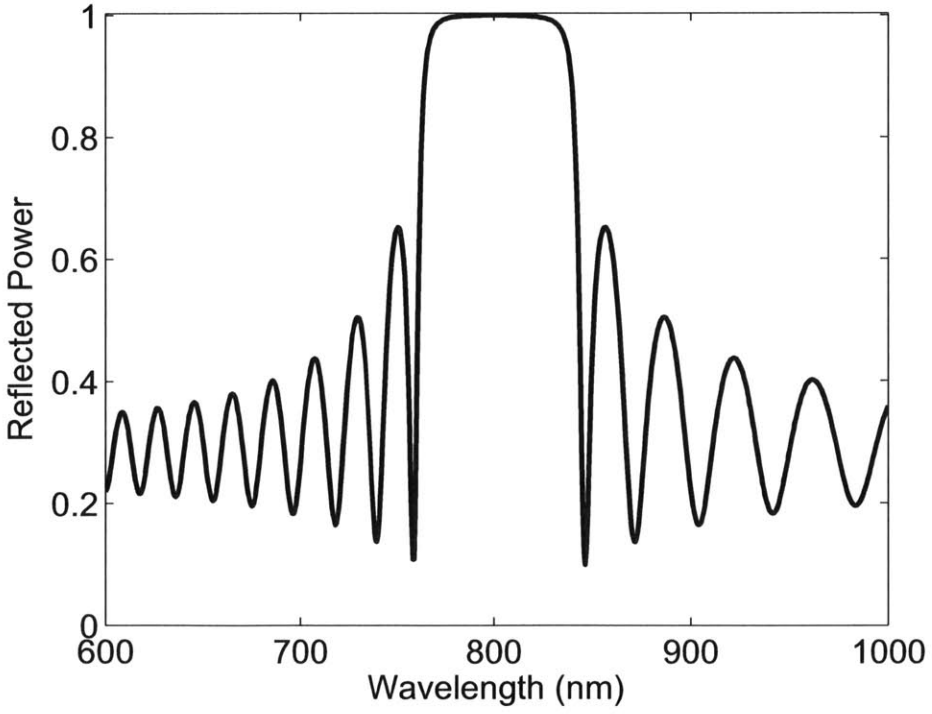

Figure 1-3: Bragg reflector optimized for operation at 800 nm.

1.5 THz Dynamic Nuclear Polarization NMR

NMR is the preferred spectroscopic approach for the solution of problems in many areas of science, including physics, chemistry, biology, materials science, and medicine. The excellent resolution of NMR is a consequence of long nuclear relaxation times that are due to the small magnetic moments of the nuclear spins that couple weakly to the surrounding lattice. The small size of these magnetic moments, however, leads to reduced sensitivity in NMR experiments.

DNP increases the sensitivity of NMR by transferring the large spin polarization from stable paramagnetic centers to the nuclear spin reservoir [1]. In 1953 Overhauser [131] proposed that it was possible to transfer polarization to nuclei from electrons in metals by saturating the electron transition. This technique was experimentally verified by Carver and Slichter [38]. The DNP approach to NMR was extended to solid dielectrics by Abragam and Proctor [2] who first characterized the solid effect (SE). In the 1980's, Wind, Yannoni, Schaefer and colleagues [3, 147, 171] performed DNP in conjunction with magic-angle-spinning (MAS) NMR.

Microwave-driven DNP experiments are now recognized as a powerful method of enhancing signals in solid state and solution NMR and imaging. DNP improves the sensitivity of NMR spectra by approximately a factor of 100, thus reducing the acquisition time in multidimensional NMR experiments by roughly 10^4 [17]. This enhancement permits studies of larger molecules, reaction dynamics or high-throughput screening [74]. The theoretical maximum enhancement in the case of ^{1}H spins is given by the relationship $\gamma_S/\gamma_I \approx 660$ [131] where γ_S and γ_I are the electron and nuclear gyromagnetic ratios, indicating further developments to DNP methods and instrumentation should result in still higher enhancements. The power level desired from the THz source in DNP is highly dependent on several experimental factors including the mechanism of polarization, sample temperature, sample volume, polarizing agent and coupling efficiency of the source. Fundamentally, the power level needed is related to the electron relaxation rate which must be overcome in order to transfer polarization to the nucleus [172, 173]. Experimentally, the theoretical maximum

enhancement from DNP is not achieved and is often limited by the available THz power.

These early, successful efforts in microwave-driven DNP NMR could be extended to magnetic fields of up to about 3.4 T using commercially available sources, such as solid state multipliers, klystrons, etc., at a frequency of up to 94 GHz [10]. However, modern NMR spectroscopy has pushed to much higher magnetic fields, where much better spectral resolution is achieved. The extension of DNP NMR to high magnetic fields had to wait for the development of THz sources of radiation at the relevant frequencies. Fortunately, the development of the THz gyrotron enabled this extension of DNP NMR into the high magnetic field regime.

The first DNP NMR experiments using a gyrotron were conducted by Becerra et al. in 1993 at the MIT Francis Bitter Magnet Laboratory at a magnetic field of 5 T, corresponding to 211 MHz NMR frequency and 140 GHz microwave frequency [22]. This successful advance was followed at MIT by extension of the technique to 9 T with the development of a 250 GHz gyrotron for use in a 380 MHz spectrometer [15] and later to 16 T with the development of a 460 GHz gyrotron for a 700 MHz spectrometer [80, 18]. Research on the gyrotron also led to the discovery of broadband tuning of the gyrotron source, which could be useful in partially covering the electron spin resonance spectrum in DNP NMR experiments [80, 164].

As described by Griffin and Prisner in a recent article, DNP NMR is truly enjoying a "renaissance" at the present time [74]. Some examples of recently developed THz DNP NMR systems include a 260 GHz / 400 MHz spectrometer in operation in Frankfurt, Germany [56, 8] and a 395 GHz / 600 MHz spectrometer operating at the Osaka Institute in Japan [105]. Instrumentation for a 263 GHz / 400 MHz DNP NMR system has been developed by industry and used in DNP NMR research [8, 141, 168].

1.5.1 Mechanisms of DNP

The structure and function of biomolecules are strongly correlated. Determining three-dimensional structural detail of proteins at an atomic resolution is crucial to understanding how they work as machines, how they catalyze chemical reactions,

how they bind to each other, as well as how they interact with drugs and signaling molecules. By far, the most powerful technique available for structure determination is X-ray diffraction. However, there are certain drawbacks to X-ray crystallography; namely, the highly ordered crystalline environment required to record diffraction patterns does not accurately represent a biological environment. *In vivo*, proteins are present in solution, bound to or embedded inside the cellular membrane, intrinsically disordered, or arrange themselves into amyloid fibrillar strands. For such molecules in a biologically realistic environment, X-ray diffraction is not applicable, and the magnetic resonance of nuclear and electron spins can be leveraged to determine structural detail. In particular, the site-specific signals of nuclear spins can reveal sub-angstrom level structural detail of proteins and molecules. Due to the excellent resolution of NMR spectra, NMR has evolved as the preferred spectroscopic approach for the solution of problems in many areas of science, including physics, chemistry, biology, materials science, and more recently, medicine. Nevertheless, the sensitivity of NMR experiments is low when compared to other spectroscopic approaches. Furthermore, since both high resolution solid and solution state NMR are utilized with increasing frequency in structural studies of macromolecular biological systems (proteins, nucleic acids, etc.), sensitivity continues to be an issue of paramount importance in the successful application of the technique.

DNP has successfully improved the sensitivity in NMR experiments by factors of 20-400 (corresponding to 400-160,000 in acquisition time) [104, 90], depending on the experimental conditions such as temperature, solvent composition, deuteration levels, radical type and concentration, etc. The increased signal intensity shortens the acquisition time, reduces the amount of sample required and allows the acquisition of multidimensional spectra with high signal to noise. The following subsections illustrate the mechanism of polarization transfer for efficient DNP at high fields and show that large DNP polarization enhancements are consistently obtained at high field. These results demonstrate applications to structural studies of biologically significant systems which would not be feasible without DNP.

DNP was first proposed and performed in the 50's [131, 38], and in the 80's DNP

experiments were incorporated into MAS experiments with a goal of increasing signal intensities in the spectra [147, 171]. MAS of samples in solid-state NMR (SSNMR) spectroscopy reduces line broadening in spectra by spinning at the magic angle of 54.7^o with respect to the magnetic field, B_0. These initial MAS DNP experiments used 40 GHz microwaves (1.5 T) and the solid effect (SE); signal enhancements of 25 were observed at ~300 K [3, 4, 5, 7, 6]. Subsequently, DNP experiments were initiated at MIT at 140 and 250 GHz (5 and 9 T fields) [22, 15, 68, 142, 140, 16, 103] using gyrotrons.

The two mechanisms that are most important for CW DNP processes in MAS experiments are the solid effect (SE) and the cross effect (CE). Which of the two mechanisms dominate (SE or CE) depends on the size of the inhomogeneous breadth, Δ, and the homogeneous breadth, δ, of the electron paramagnetic resonance (EPR) spectrum, compared to the nuclear Larmor frequency, ω_{0I}.

The SE is a two spin process (Figure 1-4(a) left) that governs the polarization process when $\omega_{0I} > \Delta, \delta$ and thus requires a radical with a narrow line such as trityl (Figure 1-4(b), (d) left). The frequency dependence of the enhancement profile for trityl is illustrated in Figure 1-4(c) (left) and shows minima and maxima when the irradiation frequency is $\omega_{0S} \pm \omega_{0I}$, where forbidden electron-nuclear flip-flops are excited leading to a negative or positive enhancement. Since the SE utilizes forbidden transitions the enhancements scale as ω_0^{-2} and are therefore attenuated at higher fields [71].

The CE, a three spin effect (Figure 1-4(a), right), is a DNP mechanism that has been shown to yield more efficient transfers at high-field. It relies on the fact that the resonance frequencies of two electrons in the EPR spectrum, ω_{0S1} and ω_{0S2}, satisfy the condition $\omega_{0S1} - \omega_{0S2} = \omega_{0I}$ (Figure 1-4(b),(c) right) and, as such, the enhancements scale as ω_0^{-1}. Furthermore, the CE works well with a large set of radicals such as nitroxides (TEMPO and its relatives), in which $\Delta > \omega_{0I} > \delta$ at high field. Assuming dipole-dipole couplings exist amongst the two electrons and the nucleus, THz irradiation near either ω_{0S1} or ω_{0S2} flips one of the electrons up, and a subsequent three spin cross relaxation process occurs with the energy difference

between the two electron spins going into polarizing the nuclear spin.

The efficiency of CE depends on two spatial factors: (1) the distance between the electron spins, which determines the electron-electron dipolar coupling and (2) the relative orientation of the two radicals, which determines, via the g-anisotropy tensors, the frequency separation $\omega_{0S1} - \omega_{0S2}$. For the case of biradical polarizing agents, both of these factors can be optimized by design of the molecular linkage tethering two nitroxide groups such as that found in 1-(TEMPO-4-oxy)-3-(TEMPO-4-amino)propan-2-ol (TOTAPOL) [83] (Figure 1-4(d), right) and bis-TEMPO-bis-ketal (bTbK) [104]. The magnitude of the maximum enhancement obtained with the water-soluble TOTAPOL radical is ~175 at 212 MHz with 6 W of THz power [83], an improvement by a factor of ~4 from monomeric nitroxides like TEMPO. Since the tether connecting the two TEMPO groups is relatively flexible, their relative orientation is not tightly constrained and many biradicals do not have the correct geometry corresponding to the desired separation frequency. Therefore, with a more rigid tether that can lock the two TEMPOs at a desired relative orientation, it is possible to further improve the performance of a polarizing agent. Enhancements of 250 with 4 W of THz power are achieved using bTbK, a new biradical connecting two TEMPOs with a rigid bis-ketal tether [104]. Thus, significant gains in enhancements have been realized by optimization of polarizing agents for high-field DNP.

An important point illustrated in Figure 1-4(c) is that magnetic field (B_0) has to be swept to the appropriate point in the EPR spectrum in order to optimize the DNP enhancement. In present day DNP spectrometers, this is accomplished with a superconducting sweep coil that was installed on the magnet at the time it was manufactured. In NMR magnets that lack a sweep coil, a tunable source of THz radiation would be useful.

Other spectroscopic techniques are enabled by double resonance (NMR and microwave) methods. The Overhauser effect (OE) [131] is important for conducting solids (metals, etc.) and solution samples. Thermal mixing involves a homogeneously broadened EPR spectrum [12] that is present at low magnetic field and, as such, is

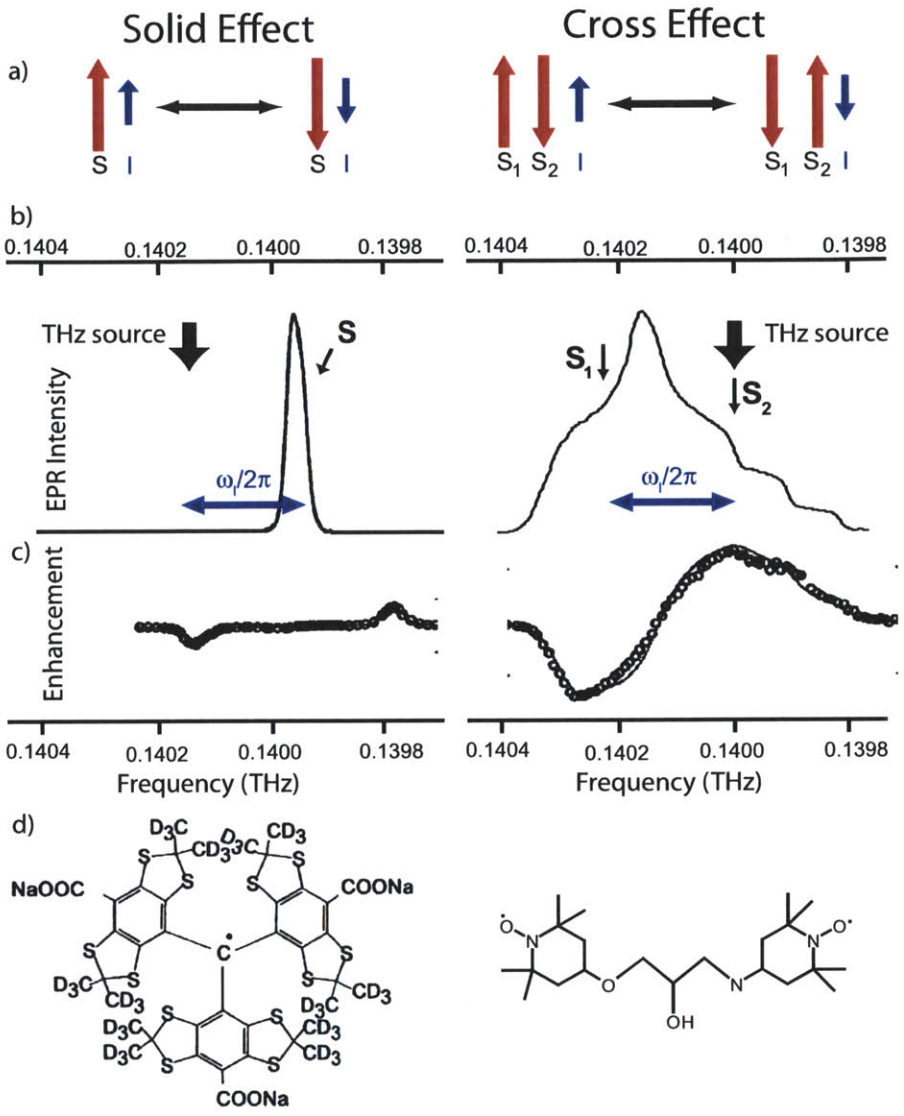

Figure 1-4: Common DNP polarization transfer mechanisms in solid dielectrics. (a) In the SE, one electron and one nuclear spin flip simultaneously with excitation from THz radiation, whereas the CE involves two electron spins and one nuclear spin. (b) EPR spectra of the radicals that are the polarization source in THz DNP experiments. (left) The SE utilizes narrow line radicals such as trityl. (right) EPR spectra of nitroxide radicals such as TEMPO or TOTAPOL are much broader and used for the CE. (c) Field/frequency dependent profiles of the two mechanisms. In the SE (left) the THz source is set to ω_{0I} away from the center of the EPR line. (right) For the CE, the THz radiation is on resonance with one of the two electrons involved. (d) Chemical structures of typical radicals used for the SE; trityl (left) has a mostly isotropic environment around the unpaired electron density which results in a similar resonance frequency (narrow line) across the powder average of the crystallites. TOTAPOL (right) for the CE, more anisotropic chemical environments around the electron density yield broader lines such that two electrons are separated by ω_{0I} and fulfill the matching condition. (Adapted from [82])

not applicable for THz DNP.

1.5.2 Time Domain DNP

The cross effect enhancements described in Section 1.5.1 were acquired at 211 MHz, and as one moves to higher magnetic fields these will scale as ω_0^{-1}. The CE relies on satisfying the matching conditions $\omega_{0S1} - \omega_{0S2} = \omega_{0I}$, which becomes less likely as the EPR spectrum is broadened at higher fields, leading to the ω_0^{-1} dependence. At 800 MHz, where much biological NMR is currently performed, enhancements will be reduced to ~60. When the next generation NMR spectrometers at 1.2 GHz become available this number will drop to ~40. For the solid effect (SE), the enhancement scales as ω_0^{-2}, since the mechanism involves mixing of states. So, if one observes a SE enhancement of 100 at 200 MHz, then at 800 MHz the SE enhancement will be reduced to < 10. The SE relies on mixing of electron and nuclear states, which is reduced as the Zeeman frequencies are increased, leading to the ω_0^{-2} dependence of the transition moment. Time domain DNP experiments can be used to circumvent these reductions in DNP enhancements. These experiments are typically performed in the electronic rotating frame, and the electron Zeeman term is removed from any matching conditions and transition moments. Thus, these mechanisms do not scale with B_0. Also, optimization of conditions accelerates the transfer, improving the rate of DNP.

With the availability of a high power THz source capable of providing phase control and specific pulse sequences, one can explore approaches to pulsed DNP including: the integrated solid effect (ISE), nuclear rotating frame DNP (NRF-DNP), the dressed-state solid effect (DSSE) and nuclear-spin orientation via electron-spin locking (NOVEL).

1.6 Current Effort

This thesis presents the design, fabrication and testing of a PBG gyrotron TWT amplifier. The circuit is based on a PBG structure made of a two dimensional triangular

lattice of metal rods. This novel interaction structure for gyrotron amplifiers is highly mode selective and has strong coupling with the electron beam resulting in a high interaction efficiency. The dimensions of the lattice are tuned so that it acts as a reflector in a narrow band of frequencies around the operating mode. A defect is created in the lattice by removing some rods, allowing a higher order mode to be confined with high a quality factor (Q). Other higher or lower frequency modes that can exist in the defect suffer significant losses because of the partially transparent lattice. This amplifier will ultimately be applied to coherent molecular spectroscopy. Therefore, the bandwidth has been an important consideration to ensure the amplification of very short pulses without distortion, since it is important to the application.

This thesis is organized as follows: Chapter 2 presents the theory of operation for gyrotron oscillators and amplifiers; Chapter 3 describes the development of low-loss THz waveguides needed to test and implement the amplifier; Chapter 4 explains the design of the PBG gyrotron amplifier; Chapter 5 details the experimental setup used to test the amplifier; Chapter 6 describes the testing methodology and experimental results of the amplifier; Chapter 7 contains concluding remarks.

Chapter 2

Theory of Gyrotron Oscillators and Amplifiers

2.1 Axial and Azimuthal Bunching of Electrons

An electron beam propagating along a magnetic field line is subject to a variety of instabilities. Of particular importance are the axial and azimuthal bunching mechanisms of the electromagnetic electron cyclotron instability. The electron cyclotron maser instability is driven by the azimuthal bunching mechanism and requires a relativistic treatment. The Weibel-type instability is driven by axial bunching and does not require relativistic treatment. Both mechanisms exist and compete against each other when an external magnetic field is present [45].

Assume an infinite homogeneous magnetic field, $B_0\hat{z}$, with the electron distribution given by

$$f_0 = \delta(p_\perp - p_{\perp 0})\delta(p_z)/2\pi p_\perp \tag{2.1}$$

where $p_\perp$ is the transverse momentum, p_z is the axial momentum and $p_{\perp 0}$ is a constant. This distribution represents streaming electrons in the moving frame. This monoenergetic beam would be the ideal case for an experiment designed to extract energy from the electrons, and it approximates the electron beam produced by high quality electron guns.

If we perturb the electron beam with an electromagnetic wave, the system will require the linearized relativistic Vlasov equation,

$$\frac{\partial}{\partial t}f_1 + \mathbf{v}\cdot\frac{\partial}{\partial \mathbf{x}}f_1 - \frac{e}{c}\mathbf{v}\times\mathbf{B}_0\cdot\frac{\partial}{\partial \mathbf{p}}f_1 = e\left(\mathbf{E}_1 + \frac{1}{c}\mathbf{v}\times\mathbf{B}_1\right)\cdot\frac{\partial}{\partial \mathbf{p}}f_0 \tag{2.2}$$

and the combined Maxwell's equations,

$$\nabla\times\nabla\times\mathbf{E}_1 = -\frac{1}{c^2}\frac{\partial^2}{\partial t^2}\mathbf{E}_1 - \frac{4\pi}{c^2}\frac{\partial}{\partial t}J_1 \tag{2.3}$$

to fully describe the physics of the interaction. A subscript 0 or 1 represents the initial or perturbed quantity, respectively. The electron distribution is f, E is the electric field, B is the magnetic field, and the current J is defined as

$$\mathbf{J}_1 = -e\int f_1\mathbf{v}d^3p. \tag{2.4}$$

Simplifying the above equations and performing perturbative analysis for a wave that propagates as $e^{ik_z z - i\omega t}$, we obtain the relativistic dispersion relation [45]:

$$\omega^2 - k_z^2c^2 = -\pi\omega_p^2\int_0^\infty p_\perp dp_\perp\int_{-\infty}^\infty dp_z$$
$$\times\left[\left(\omega - \frac{k_z p_z}{\gamma m}\right)p_\perp\frac{\partial f_0}{\partial p_\perp} + \frac{k_z}{\gamma m}p_\perp^2\frac{\partial f_0}{\partial p_z}\right](\gamma\omega - k_z p_z/m - \Omega)^{-1}$$

where $\omega_p^2 = 4\pi ne^2/m$, $\Omega = eB_0/mc$, and $\gamma = (1+p_\perp^2/m^2c^2+p_z^2/m^2c^2)^{1/2}$. This expression is for any generic distribution of the electrons. However, we can simplify further by considering the monoenergetic case from Equation (2.1) that is most relevant to practical devices. This reduces the dispersion relation to

$$\omega^2 - k_z^2c^2 = \frac{\omega_p^2}{\gamma_0}\left(\frac{\omega}{\omega - \Omega/\gamma_0} - \frac{\beta_{\perp 0}^2(\omega^2 - k_z^2c^2)}{2(\omega - \Omega/\gamma_0)^2}\right) \tag{2.5}$$

where $\gamma_0 = (1 + p_{\perp 0}^2/m^2c^2)^{1/2}$ and $\beta_{\perp 0} = p_{\perp 0}/\gamma_0 mc$. To extract some physical interpretation from Equation (2.5) one should make note that the last term on the right hand side is where the axial and azimuthal bunching mechanisms reside. The

azimuthal and axial bunching are represented by the ω^2 and $c^2k_z^2$ terms respectively. Furthermore, the denominator $(\omega - \Omega/\gamma_0)$ imposes a requirement that the frequency of oscillation for the wave must meet the condition $\omega \approx \Omega/\gamma_0$ in order to produce a large instability. This can be understood as a requirement for synchronous behavior between the electrons and the electromagnetic wave. Additionally, if the phase velocity of the wave is equal to the speed of light there is no instability present, defining an inflection point between an instability dominated by axial and azimuthal bunching. If

$$\omega^2/k_z^2 > c^2, \tag{2.6}$$

the phase velocity of the wave is greater than the speed of light and azimuthal bunching dominates. If

$$\omega^2/k_z^2 < c^2, \tag{2.7}$$

the phase velocity of the wave is less than the speed of light and axial bunching dominates. In Figure 2-1 the solution to Equation (2.5) is plotted for $\Omega/\gamma_0\omega_p = 10$ and $\gamma_0 = 1.02$. We note that the instability is only present when the frequency of the fast and slow wave meets the condition $\omega/\omega_p = 10$ as required for synchronous behavior. The instability for the fast and slow wave is only present when Equations (2.6) and (2.7) are satisfied.

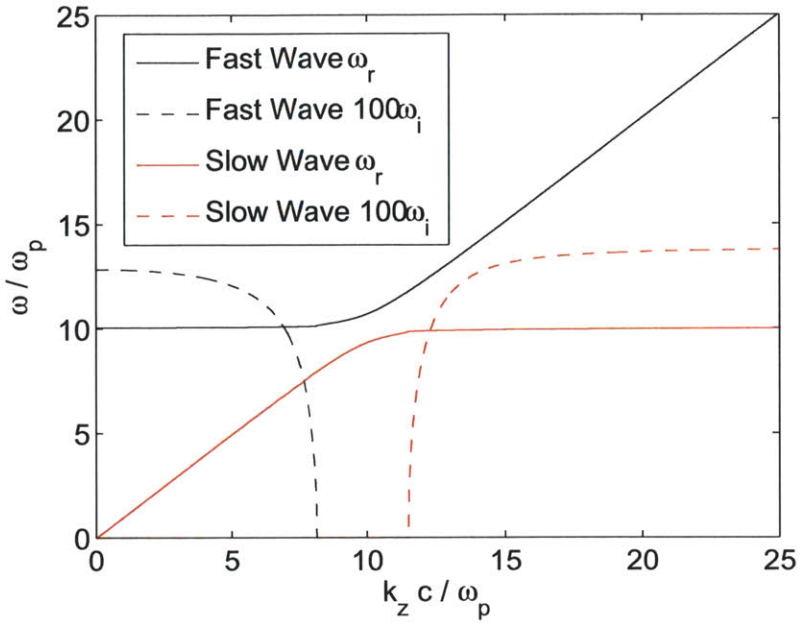

Figure 2-1: The solution to Equation (2.5) for $\Omega/\gamma_0\omega_p = 10$ and $\gamma_0 = 1.02$. The real and imaginary part of ω are labeled as ω_r and ω_i, respectively.

Gyrotrons oscillators and amplifiers are both fast wave devices that rely on the electron cyclotron maser instability, driven by the azimuthal bunching mechanism. Due to this bunching mechanism, a relativistic treatment is required to explain these devices properly.

2.2 Fundamentals of Gyrotron Oscillators

As mentioned in Section 1.2, electron cyclotron resonance masers (gyrotrons) are fast wave devices, i.e. the phase velocity of the wave is greater than the speed of light. They are capable of producing high average power in the microwave, millimeter wave and sub-millimeter wave range. The most basic configuration of a gyrotron can be seen in Figure 2-2. The magnetron injection gun that launches an annular electron beam would be located to the left of Figure 2-2(a). The axial magnetic field is produced by a solenoidal magnet than can either be a pulsed magnet or a DC superconducting magnet. As the electron beam travels through the central bore, it enters a metallic cavity that has an eigenmode resonance that is close in frequency to a harmonic of the

frequency at which the electron gyrates around the magnetic field line. The electron beam surrenders some of its kinetic energy to the electromagnetic mode through stimulated emission.

In order for the electron to interact with the electromagnetic mode in the cavity, the relativistic electron frequency must be close to the frequency of oscillation for the cavity mode [44]. The relativistic cyclotron frequency is

$$\Omega_c = \frac{eB_0}{\gamma m_e}, \tag{2.8}$$

where B_0 is the DC axial magnetic field, γ is the relativistic mass factor, m_e is the electron mass, e is the charge of the electron. In a cylindrical cavity the dispersion relation for TE modes is

$$k^2 - k_t^2 - k_z^2 = 0, \tag{2.9}$$

where $k = w\sqrt{\mu_0 \epsilon_0}$ is the wave vector in free space, $k_t = \nu_{mp}/r_w$ is the transverse propagation constant, ν_{mp} is the p^{th} root of the m^{th} order Bessel function and k_z is the axial propagation constant. It can be shown [21] that the Doppler shifted resonance for the electron becomes

$$\omega - k_z v_z - s\Omega_c = 0, \tag{2.10}$$

and when the frequency of the mode and the resonance intersect, as seen in Figure 2-3, oscillation and stimulated emission can occur. The blue and red line in Figure 2-3 are the electron beam dispersion relations for $s = 1$ and $s = 2$, respectively. The blue dot is a fundamental forward wave oscillation, the red dot is a second harmonic forward wave oscillation and the green dot is a fundamental backward wave oscillation.

2.2.1 Nonlinear Theory of Gyrotron Oscillators

To understand the operation of a gyrotron oscillator, we must describe the interaction between an energetic electron and the electromagnetic mode confined in the resonator or interaction cavity. Like all vacuum electron devices, gyrotrons extract kinetic

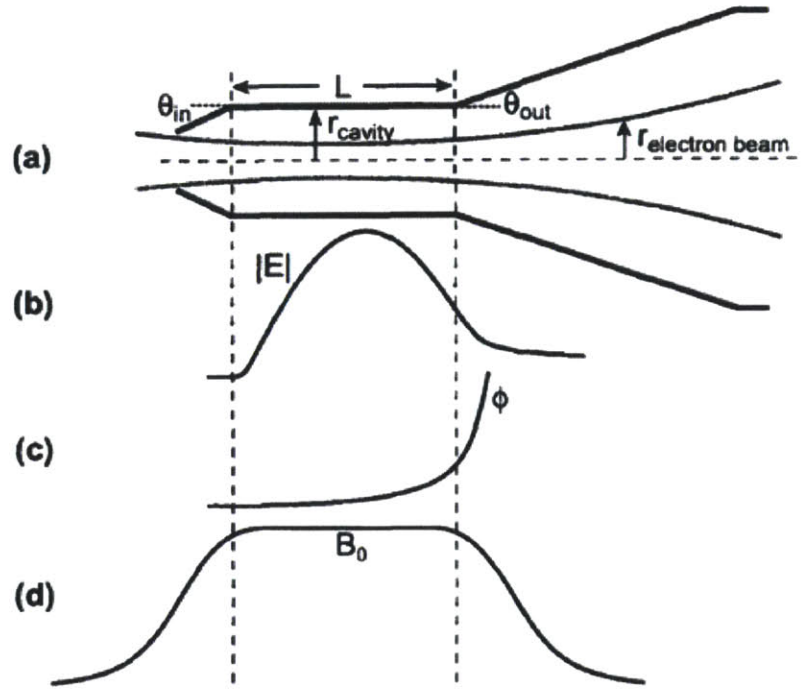

Figure 2-2: Cross section of the interaction region along the axis of the DC magnetic field with (a) a view of the electron beam passing through the physical structure, (b) the amplitude (c) and phase of the RF electric field and (d) the DC magnetic field [79].

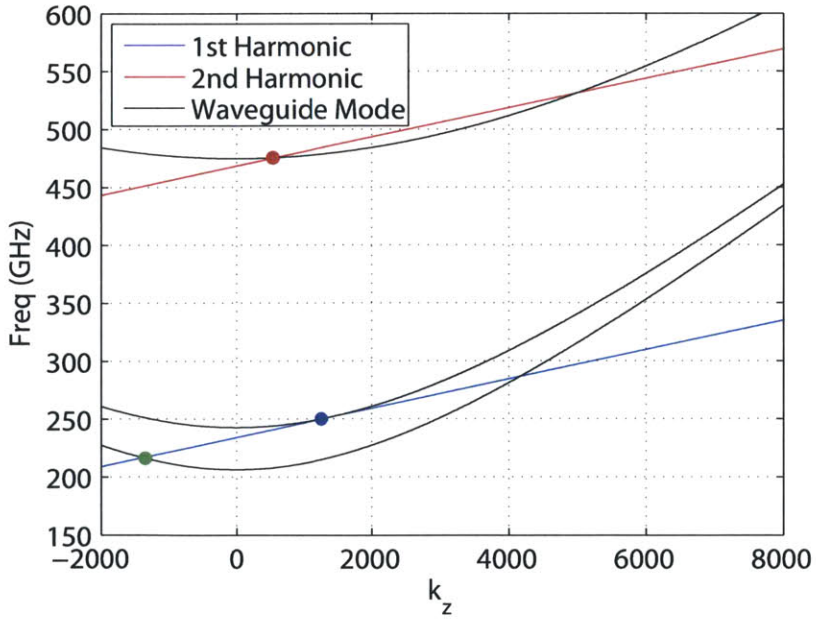

Figure 2-3: Dispersion diagram for cyclotron resonance and cylindrical waveguide modes.

energy from the electron beam as it passes through the interaction cavity. However, a gyrotron does not extract any energy from the axial component of the velocity, only from the transverse direction.

This energy extraction is made possible because an electron traveling in a circular path around a DC magnetic field will feel an accelerating or decelerating force from the oscillating electric field that can deposit or extract energy from the electron. The initial change in energy that results from the applied force causes more energetic electrons to rotate slower and less energetic electrons to rotate faster because of the change in γ and Ω_c. The different rotational frequencies can produce phase bunched electrons that act coherently to deposit energy into the electromagnetic mode of the cavity. This process can be described by the pendulum equations that relate the change in energy and momentum for the electron to the electric and magnetic fields that are present. These equations of motion are

$$\frac{\partial \mathcal{E}}{\partial t} = -e\mathbf{v} \cdot \mathbf{E}, \tag{2.11}$$

$$\frac{\partial \mathbf{p}}{\partial t} = -e\mathbf{E} - \frac{e}{c}\mathbf{v} \times \mathbf{B}, \tag{2.12}$$

where the electron energy is $\mathcal{E}$, the momentum is $\mathbf{p}$, the RF electric field is $\mathbf{E}$, the DC magnetic field is $\mathbf{B}$ and the velocity of the electron is $\mathbf{v}$. We are able to ignore the effect of the oscillating magnetic field on the electron because the gyration of the electron is dominated by the axial magnetic field $\mathbf{B} = B_0\mathbf{z}$. The instantaneous kinetic energy and momentum of a relativistic electron are $\mathcal{E} = \gamma m_e c^2$ and $|\mathbf{p}| = \gamma\beta m_e c$ respectively, where $\gamma = (1 - \beta_\perp^2 - \beta_\parallel^2)^{-\frac{1}{2}}$ and $\beta = v/c$. The $\perp$ symbolizes the component that is transverse to the beam and the $\parallel$ represents the axial or z component. It will be useful to convert these equations into normalized variables and to solve the standard and practical case of a cylindrical resonator. The normalized variables will relate to relevant design constraints to be discussed later. To begin this process, we convert to a relative energy for the electron $w = 1 - \gamma/\gamma_0$, which relates to the energy differential through $\frac{\partial w}{\partial t} = \frac{\partial}{\partial t}(1 - \gamma/\gamma_0) = (-1/\gamma_0 m_e c^2)\frac{\partial \mathcal{E}}{\partial t}$. It is also convenient to convert to a normalized axial position $Z = \omega z/\beta_{\parallel 0} c$, which relates to the spatial

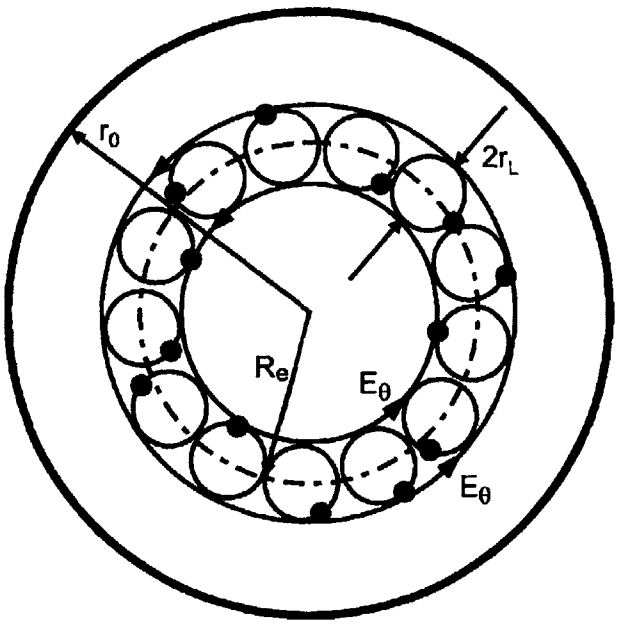

Figure 2-4: Cross section of the interaction region with black dots representing electrons on their gyration orbit [79]. The waveguide radius is r_0, the Larmor radius is r_L, the guiding center radius is R_e and E_θ denotes the $\hat{\theta}$ component of the electric field.

differential through $\frac{\partial z}{\partial t} = \beta_\parallel$ and $\frac{\partial}{\partial t} = \omega\beta_\parallel/\beta_{\parallel 0}\frac{\partial}{\partial Z}$. The values of $\beta_{\parallel 0}$ and γ_0 are defined at the beginning of the interaction region, and ω is the angular frequency of the electromagnetic wave. Applying these conditions to Equation (2.11) yields

$$\frac{\partial w}{\partial Z} = \frac{e}{(m_e c)^2 \omega}\frac{\beta_{\parallel 0}}{\gamma\gamma_0\beta_\parallel}\mathbf{p}\cdot\mathbf{E}. \tag{2.13}$$

In order to distinguish the magnitude and phase of the transverse momentum of the electron and electric field, we can write these quantities in complex notation, $\mathbf{p} = p_x + ip_y = p_+ = |p_+|e^{i\alpha}$ and $\mathbf{E} = E_x + iE_y = E_+ = |E_+|e^{i(\omega t+\psi)}$. The angular term α for the electron's momentum is defined at the center of gyration for the electron which is at a radius R_e as seen in Figure 2-4. Now we can express the energy in terms of the real part of our complex variables

$$\frac{\partial w}{\partial Z} = \frac{e}{(m_e c)^2 \omega}\frac{\beta_{\parallel 0}}{\gamma\gamma_0\beta_\parallel}\mathrm{Re}(p_+^* E_+). \tag{2.14}$$

By taking equation (2.12) and considering the complex transverse momentum $|p_+|e^{i\alpha}$ we find that $\frac{\partial \mathbf{p}}{\partial t} = e^{i\alpha}\left(\frac{\partial |p_+|}{\partial t} + |p_+| i\frac{\partial \alpha}{\partial t}\right)$. Dividing by $e^{i\alpha}$ and solving for the imaginary part provides an equation that describes the change in phase with position for the momentum of the electron

$$\frac{\partial \alpha}{\partial Z} = \frac{\beta_{\parallel 0}\omega_c}{\beta_\parallel \omega} - \frac{e\beta_{\parallel 0}}{\omega \beta_\parallel |p_+|}\mathrm{Im}(p_+^* E_+), \tag{2.15}$$

where $\omega_c = eB_0/m_e c\gamma$ is the cyclotron resonant frequency. The traditional configuration for a gyrotron consists of a cylindrical interaction region with a down-taper leading towards the electron gun and an up-taper facing the electron beam collector and the output window for the microwave signal. With this resonant configuration, the dominant contribution to the Q-factor will be the diffractive Q = Q_{diff}. This diffractive Q is large enough that we can write a fixed expression for the field distribution $f(z) = e^{-(k_\parallel z)^2}$ which is a valid assumption for our configuration. The electric field in the transverse direction is identical to the TE_{mp} modes for a cylindrical waveguide along with a variation in the amplitude in the z direction. The fields are

$$\mathbf{E} = (E_R \hat{R} + E_{\phi_0}\hat{\phi}_0)e^{i(\omega t + \psi)},$$

$$E_R = i(m/k_\perp R)E_0 f(z) J_m(k_\perp R)e^{-im\phi_0},$$

$$E_{\phi_0} = E_0 f(z) J'_m(k_\perp R)e^{-im\phi_0},$$

where $k_\perp = \nu_{mp}/r_0$ and $w \approx sw_c$. These field expressions are written in the coordinate frame (R, ϕ_0) which is centered in the middle of the solenoid. As stated previously, the complex expression for momentum considers the phase of the electron as it rotates about its center of gyration. Therefore, we also need our field expression to be centered around the same point. Haldar and Beck were able to convert from a reference frame in the center of the cavity to the center of the orbit for the electron using Graf's formula for Bessel functions [75]. This produces a series solution, but only one term will interact in a coherent fashion with the s^{th} order resonance. This allows us to

express the fields as

$$\mathbf{E} = (E_{rs}\hat{r} + E_{\phi s}\hat{\phi})e^{i(\omega t+\psi)},$$

$$E_{rs} = i(s/k_\perp r)E_0 f(z)J_{m\pm s}(k_\perp R_e)J_s(k_\perp r)e^{-im\phi_0}e^{-is(\phi-\phi_0)},$$

$$E_{\phi s} = E_0 f(z)J_{m\pm s}(k_\perp R_e)J'_s(k_\perp r)e^{-im\phi_0}e^{-is(\phi-\phi_0)}.$$

In order to evaluate Equations (2.14) and (2.15) we need the complex expression $E_+ = E_x + iE_y = Re(E_{rs}e^{i(\omega t+\psi)})e^{i\phi} + Re(E_{\phi s}e^{i(\omega t+\psi)})ie^{i\phi}$, which gives

$$E_+ = -E_r \sin[\omega t - s\phi + \psi - (m-s)\phi_0]e^{i\phi} + E_\phi \cos[\omega t - s\phi + \psi - (m-s)\phi_0]ie^{i\phi},$$

where $E_r = |E_{rs}|$ and $E_\phi = |E_{\phi s}|$. If we set $\theta = \omega t - s\phi$, the complex expression becomes

$$E_+ = -E_r \sin[\theta + \psi - (m-s)\phi_0]e^{i\phi} + E_\phi \cos[\theta + \psi - (m-s)\phi_0]ie^{i\phi},$$

since ϕ is the angular position of the electron from its gyrocenter, it is related to the angular phase of its momentum by $\alpha = \phi + \pi/2$ because the position vector is orthogonal to the velocity vector for the electron. This changes the field expression to

$$E_+ = E_r \sin[\theta + \psi - (m-s)\phi_0]ie^{i\alpha} + E_\phi \cos[\theta + \psi - (m-s)\phi_0]e^{i\alpha},$$

and allows us to evaluate Equations (2.14) and (2.15) quite simply

$$\frac{\partial w}{\partial Z} = \frac{e}{\gamma_0 m_e c w}p'_\perp E_\phi \cos[\theta + \psi - (m-s)\phi_0], \tag{2.16}$$

$$\frac{\partial \theta}{\partial Z} = \delta_0 - w - \frac{se}{\gamma_0 m_e c w}\frac{(1-w)}{p'_\perp}E_r \sin[\theta + \psi - (m-s)\phi_0], \tag{2.17}$$

where $\delta_0 = 1 - \omega_{c0}/\omega$, $\omega_{c0} = eB/m_e c\gamma_0$ and $p'_\perp = (|p_+|/\gamma_0 m_e c) = (\beta^2_{\perp 0} - 2w + w^2)^{1/2}$. The value of δ_0 is equivalent to the detuning of the magnetic field as it relates to the ratio of the initial cyclotron resonance frequency and the frequency of the electromagnetic wave. Conveniently, we can set $\psi - (m-s)\phi_0 = \pi/2$ because there

is no axial bunching and the electrons at the input have a random phase about their gyrocenter, which further reduces our equations to

$$\frac{\partial w}{\partial Z} = \frac{E_\phi}{sB_0} p'_\perp \sin\theta, \tag{2.18}$$

$$\frac{\partial \theta}{\partial Z} = \delta_0 - w - \frac{E_r}{B_0}\frac{(1-w)}{p'_\perp}\cos\theta. \tag{2.19}$$

It is interesting to note that the radial electric field changes the energy of the electron and the azimuthal electric field affects the phase. In both cases, this affects the phase bunching of the electrons. It is convenient to rescale our normalized variables by

$$u \equiv \frac{2w}{\beta_{\perp 0}^2} = \frac{2}{\beta_{\perp 0}^2}(1 - \frac{\gamma}{\gamma_0}),$$

$$\zeta \equiv \frac{\beta_{\perp 0}^2}{2} Z = \pi \frac{\beta_{\perp 0}^2}{\beta_{\parallel 0}} \frac{z}{\lambda},$$

and normalize our fields with

$$F \equiv \frac{E_0}{B_0} \beta_{\perp 0}^{s-4} \frac{s^{s-1}}{s! 2^{s-1}} J_{m\pm s}(k_\perp R_e).$$

It is also possible to make the approximation

$$k_\perp r \approx s\frac{\gamma B_\perp}{\gamma_0} = s\beta_{\perp 0}(1 - \frac{2w - w^2}{\beta_{\perp 0}^2})^{1/2} = sp'_\perp.$$

These re-normalizations and the approximation alter equations (2.18) and (2.19) to the form

$$\frac{\partial u}{\partial \zeta} = 2\left(\frac{2^s s!}{s^s \beta_{\perp 0}^{s-1}}\right) F f(\zeta) \frac{p'_\perp}{\beta_{\perp 0}} J'_s(sp'_\perp)\sin\theta, \tag{2.20}$$

$$\frac{\partial \theta}{\partial \zeta} = \Delta - u - s\left(\frac{2^s s!}{s^s \beta_{\perp 0}^{s-1}}\right) F f(\zeta) \frac{\beta_{\perp 0}(1 - \beta_{\perp 0}^2 u/2)}{{p'_\perp}^2} J'_s(sp'_\perp)\cos\theta, \tag{2.21}$$

where $\Delta \equiv 2\delta_0 \beta_{\perp 0}^2$. We allow the normalization F for the field to be very complicated because under the condition that $\beta_{\perp 0}^2/2 \ll 1$, then $p'_\perp \approx (\beta_{\perp 0}^2 - 2w)^{1/2} = \beta_{\perp 0}(1-u)^{1/2}$. This condition permits a small argument expansion on the remaining Bessel function

$J_s'(x) = \frac{s^s}{2^s s!} x^{s-1}$. If we apply this expansion we can rewrite our differential equations as

$$\frac{\partial u}{\partial \zeta} = 2Ff(\zeta)(1-u)^{s/2}\sin\theta, \tag{2.22}$$

$$\frac{\partial \theta}{\partial \zeta} = \Delta - u - sFf(\zeta)(1-u)^{s/2-1}\cos\theta. \tag{2.23}$$

Finally, we can define our cavity length L by $k_\parallel = 2/L$ and rewrite the axial field profile from $f(z) = e^{-(k_\parallel z)^2}$ to $f(\zeta) = e^{-(2\zeta/\mu)^2}$, where $\mu \equiv \pi \frac{\beta_{\perp 0}^2}{\beta_{\parallel 0}} \frac{L}{\lambda}$.

We have constructed the coupled differential nonlinear equations of motion for a gyrating electron interacting with an electromagnetic field. These equations which describe the normalized transferred energy and phase of the electron are only functions of three parameters: the normalized field strength F, cavity length μ and detuning of the magnetic field Δ. However, Equations (2.22) and (2.23) only track the amount of energy that a single electron surrenders to the electromagnetic mode. Therefore, we need to verify that for various input boundary conditions the electrons will act coherently. The energy spread for the electrons at the input is very small allowing the electrons to have the same gyration frequency, but the phase around the gyrocenter is completely random ($\theta_0 = 0 \rightarrow 2\pi$). To calculate the actual efficiency of energy conversion for the device, we have to make sure that the stimulated emission is coherent for all of the electrons. This efficiency can be calculated by averaging over initial boundary conditions $\eta_\perp = \langle u(\zeta_{out}) \rangle_{\theta_0}$.

2.2.2 Analysis

The efficiency analysis for the conversion of energy from kinetic electron energy to electromagnetic radiation was performed by using a fourth-order Runge-Kutta algorithm and averaging the results for 32 electrons with uniform spacing in initial phase. For clarity, the results in Figure 2-5 and Figure 2-6 are shown as contour plots with variables F and μ and optimized for Δ. These plots are shown in this form because Δ is often the easiest parameter to vary, as the magnet can be charged to the desired strength. The spatial limits for the calculation were set at $\zeta = -\sqrt{3}\mu/2$ to $\sqrt{3}\mu/2$,

as this range is the commonly accepted cutoff point for the electric field of a tapered gyrotron oscillator.

In Figure 2-5, the contour plot for efficiency as a function of F and μ is shown for the first harmonic, and Figure 2-6 shows the contour plot for the second harmonic. It is possible that there are other peaks in efficiency for larger values of F and μ, but it is often desirable to operate at the smallest values of F and μ. This is because the longer the cavity, the more expensive the solenoidal magnet, and the larger the F, the greater current the electron gun must provide. Through power conservation, one can show that $F = \eta_{\perp}^2 I$, where I is the normalized current. This is the balance equation that specifies the current the electron gun must supply to the gyrotron. A direct expression for the actual current can be found, but that is beyond the scope of this thesis. The actual current expression is given in the literature [53].

It is also possible to show how the average efficiency changes as the electrons progress through the cavity, as shown in Figure 2-7. The cavity length for the simulation in Figure 2-7 is $\mu = 20$, but the field profile and electrons are tracked over a length $\zeta = -\sqrt{3}\mu/2$ to $\sqrt{3}\mu/2$. It should be noted that the peak efficiencies for the first harmonic $\eta_{\perp_1} = 0.72$ and the second harmonic $\eta_{\perp_2} = 0.71$ are in excellent agreement with published values [53, 123, 178].

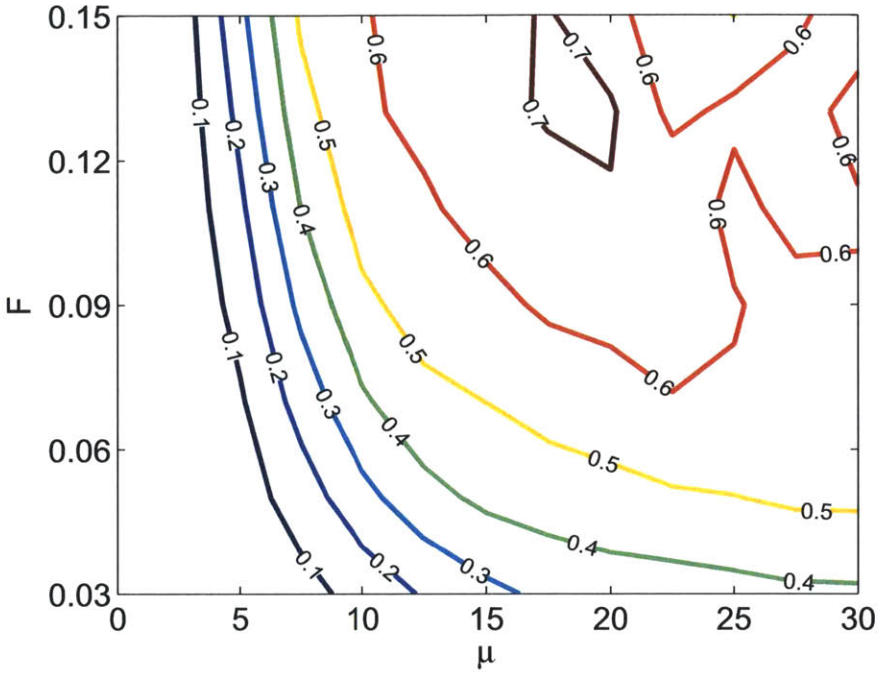

Figure 2-5: Contour plot for efficiency of the 1st harmonic interaction between a cavity with normalized field strength, F, and interaction length, μ.

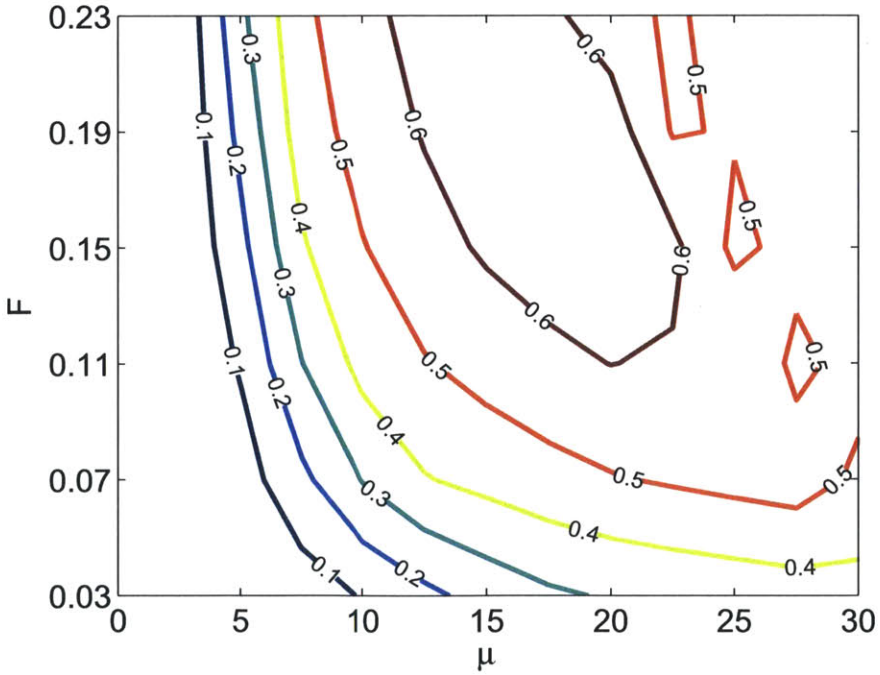

Figure 2-6: Contour plot for efficiency of the 2nd harmonic interaction between a cavity with normalized field strength, F, and length, μ.

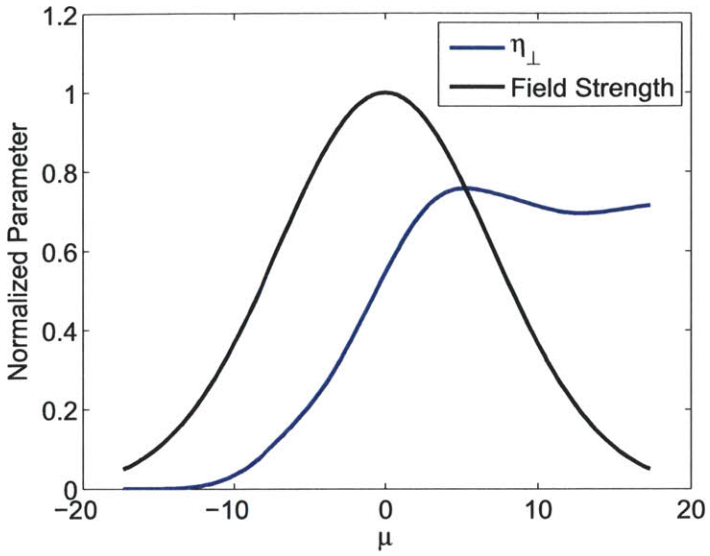

Figure 2-7: The fraction of electron energy that is extracted from the beam, averaged over 32 initial phases, as it passes through the cavity (blue line). Also shown is the normalized electric field profile in the cavity (black line) that interacts with the electron beam.

2.3 Theory of Gyrotron Amplifiers

Gyrotron amplifiers are driven by the interaction between the eigenmode of an interaction circuit (waveguide) and a mildly relativistic electron beam that is gyrating in a constant axial magnetic field. The dispersion diagram for the waveguide mode, Equation (2.9), and the electron beam, Equation (2.10), is shown at the top of Figure 2-8. The region of strongest coupling is when the frequency of the electromagnetic mode approaches the Doppler shifted cyclotron frequency. Shown at the bottom of Figure 2-8 is a simple schematic of a gyrotron amplifier interaction region with an annular electron beam guided through a circuit with a constant magnetic field normal to the direction of propagation for the electromagnetic wave. The MIG would be located to the left of the circuit and the collector to the right. As the beam enters the circuit, it interacts with the waveguide mode that is close to a harmonic of the frequency at which the electron gyrates around the magnetic field line. The electron beam surrenders some of its kinetic energy to the electromagnetic mode through stimulated emission. The circuit and magnetic field are tapered to terminate the

interaction. The electrons exit the circuit and are deposited on a metallic collector. The electromagnetic wave is extracted with an axial dielectric window or a Vlasov type launcher.

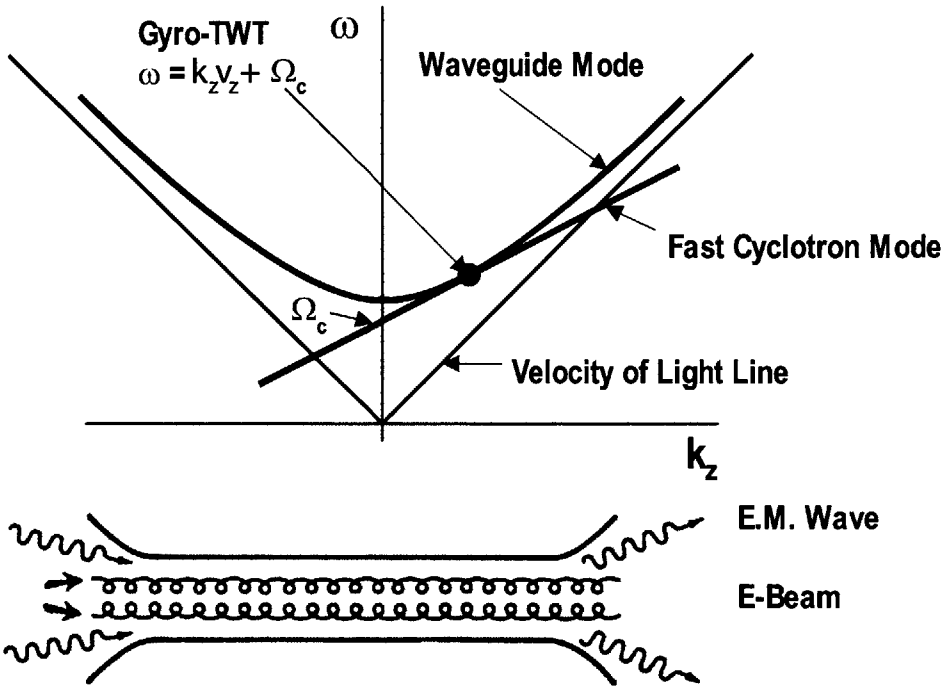

Figure 2-8: Dispersion diagram for a 1st harmonic gyrotron amplifier and a schematic of the interaction circuit where the electromagnetic wave couples to electron beam.

2.3.1 Nonlinear Equations of Motion

Similar to the method described previously for gyrotron oscillators, tracking single particle behavior and averaging over a group of particles with a uniform phase distribution leads to a set of self-consistent nonlinear equations that can describe the amplification process in a gyrotron amplifier. Excluding space charge effects, this method developed by Yulpatov [177] and later generalized by Nusinovich et al. [124] can also be simplified to produce a linear growth rate that is relatively easy to calculate. The equations of motion for an electron and the field amplitude are given by:

$$\frac{\partial w}{\partial z'} = -2\frac{(1-w)^{s/2}}{1-bw}\mathrm{Re}\left\{F'e^{-i\bar{\theta}}\right\} \tag{2.24}$$

$$\frac{\partial \bar{\theta}}{\partial z'} = \frac{1}{1-bw}\left\{-bw\bar{\Delta} + \bar{\mu}w + \frac{s}{(1-w)^{1-s/2}}\mathrm{Im}\left\{F'e^{-i\bar{\theta}}\right\}\right\} \tag{2.25}$$

$$\frac{\partial F'}{\partial z'} - i\bar{\Delta}F' = -I_0'\frac{1}{2\pi}\int_0^{2\pi}\frac{(1-w)^{s/2}}{1-bw}e^{i\bar{\theta}}d\bar{\theta}_0 \tag{2.26}$$

where w is the normalized electron energy, $\bar{\theta}$ is the normalized electron phase, $\bar{\theta}_0$ is the initial value of the normalized electron phase, F' is the normalized field amplitude, I_0' is the normalized current, $z' = kz$ is the normalized position, k is the wavenumber, s is the cyclotron harmonic and we define the normalized parameters

$$\begin{aligned}
b &= \frac{h\beta_{t0}^2}{2\beta_{z0}(1-h\beta_{z0})} \\
\bar{\mu} &= \frac{\beta_{t0}^2}{2\beta_{z0}}\frac{1-h^2}{1-h\beta_{z0}} \\
\bar{\Delta} &= \frac{\Delta}{\beta_{z0}} = \frac{1}{\beta_{z0}}\left(1 - s\frac{\mu}{\gamma_0} - h\beta_{z0}\right) \\
\mu &= \frac{eB_0}{m_e\omega} \\
h &= k_z/k.
\end{aligned}$$

Additionally, we note that k_z is the axial wavenumber, $\beta_{z0} = \frac{v_{z0}}{c}$, v_{z0} is the initial axial electron velocity, $\beta_{t0} = \frac{v_{t0}}{c}$, v_{t0} is the initial transverse electron velocity, γ is the relativistic mass factor, e is the electron charge, m_e is the electron mass and B_0 is axial DC magnetic field. In order to relate the normalized field amplitude to the waveguide modes

$$\vec{E} = \mathrm{Re}\left[A(z)\vec{E}_s(r_t)e^{i(\omega t - k_z z)}\right] \tag{2.27}$$

$$\vec{H} = \mathrm{Re}\left[A(z)\vec{H}_s(r_t)e^{i(\omega t - k_z z)}\right] \tag{2.28}$$

we need the relationship

$$F = \frac{1 - h\beta_{z0}}{\kappa\gamma_0\beta_{t0}\beta_{z0}} A' L_s(X, Y) \tag{2.29}$$

$$A' = \frac{eA}{m_e c\omega} \tag{2.30}$$

$$F' = \frac{\xi^{s-1}}{2^s(s-1)!} F e^{i\bar{\Delta}z'} \tag{2.31}$$

where $\kappa = k_t/k$, k_t is the transverse wavenumber, $\xi = \frac{\kappa p'_{t0}}{\mu}$, $p'_{t0} = \frac{p_{t0}}{m_e c}$ and p_{t0} is the initial transverse momentum. The normalized electron energy and phase are defined as

$$w = \frac{2(1 - h\beta_{z0})}{\beta_{t0}^2} \frac{\gamma_0 - \gamma}{\gamma_0} \tag{2.32}$$

$$\theta = s\Theta - (\omega t - k_z z) + \bar{\Delta}z' \tag{2.33}$$

$$\Theta = \mu \int_0^z p_z^{-1} dz' + \phi \tag{2.34}$$

where p_z is the axial momentum and ϕ defines the x and y momentum of the particle ($p_x = -p_\perp \sin(\phi)$ and $p_x = p_\perp \cos(\phi)$) at the entrance of the circuit. The current I, in amps, is given by

$$I_0 = \frac{e|I|}{mc^3} \frac{1 - h\beta_{z0}}{\gamma_0\beta_{z0}^2} \frac{2c}{k_t^2} \frac{|L_s^2|}{N_s} \tag{2.35}$$

$$I'_0 = [\frac{\xi^{s-1}}{2^s(s-1)!}]^2 I_0. \tag{2.36}$$

where $\frac{mc^3}{e} = 17$ kA, L_s is the Form Factor of a waveguide mode, describing its interaction with an electron beam, and N_s is the norm of a waveguide mode, accounting for the power in any given transverse cross section.

$$L_s = \left[\frac{k}{k_\perp}\left(\frac{\partial}{\partial \mathbf{X}} + i\frac{1}{|s|}\frac{\partial}{\partial \mathbf{Y}}\right)\right]^{|s|} \Psi(\mathbf{X}, \mathbf{Y}) \tag{2.37}$$

$$N_s = \frac{c}{4\pi} \int \{\mathbf{E}_s \times \mathbf{H}_s^* - \mathbf{H}_s \times \mathbf{E}_s^*\} \cdot \mathbf{z}_0 dS_\perp \tag{2.38}$$

where X and Y are the transverse coordinates of the electron guiding center. It is

very useful to define a coupling factor

$$\frac{|L_s^2|}{N_s} \equiv \text{Coupling Factor}, \tag{2.39}$$

which can be calculated numerically for different modes and beam radii to compare the strength of the interaction. For a cylindrical waveguide the normalized current reduces to

$$I_0 = \frac{e|I|}{mc^3}\frac{1-h\beta_{z0}}{\gamma_0\beta_{z0}^2}\frac{4\kappa^2}{h}\frac{J_{m\pm s}^2(k_t R_0)}{(\nu^2-m^2)J_m^2(nu)}. \tag{2.40}$$

2.3.2 Derivation of Linear Gain

If we take Equations (2.24)-(2.26), it is possible to linearize them in the small signal regime and derive a dispersion relation that will give the growth rate for a mode. To linearize the equations we Taylor expand and keep only first order perturbations. The first order terms of $w, \bar{\theta}, F'$ are

$$\frac{\partial w^{(1)}}{\partial z'} = -2(1 - sw^{(1)}/2 + bw^{(1)})\mathrm{Re}\left\{F'^{(1)}e^{-i\bar{\theta}_0}(1 - i\bar{\theta}^{(1)})\right\}, \tag{2.41}$$

$$\frac{\partial \bar{\theta}^{(1)}}{\partial z'} = -\bar{\Delta}bw^{(1)} + \bar{\mu}w^{(1)} + s\mathrm{Im}\left\{F'^{(1)}e^{-i\bar{\theta}_0}(1 - i\bar{\theta}^{(1)})\right\}, \tag{2.42}$$

$$\frac{\partial F'^{(1)}}{\partial z'} - i\bar{\Delta}F'^{(1)} = -I_0'\frac{1}{2\pi}\int_0^{2\pi}(1 - sw^{(1)}/2 + bw^{(1)})e^{i\bar{\theta}_0}(1 - i\bar{\theta}^{(1)})d\bar{\theta}_0. \tag{2.43}$$

Additional terms can be removed where $w^{(1)}$, $\bar{\theta}^{(1)}$ and $F'^{(1)}$ are multiplied because these are second order perturbations, yielding

$$\frac{\partial w^{(1)}}{\partial z'} = -2\mathrm{Re}\left\{F'^{(1)}e^{-i\bar{\theta}_0}\right\}, \tag{2.44}$$

$$\frac{\partial \bar{\theta}^{(1)}}{\partial z'} = (\bar{\mu} - \bar{\Delta}b)w^{(1)} + s\mathrm{Im}\left\{F'^{(1)}e^{-i\bar{\theta}_0}\right\}, \tag{2.45}$$

$$\begin{aligned}\frac{\partial F'^{(1)}}{\partial z'} - i\bar{\Delta}F'^{(1)} = -I_0'\frac{1}{2\pi}\Bigg\{&\left[\int_0^{2\pi}e^{i\bar{\theta}_{0n}}d\bar{\theta}_{0n} = 0\right] \\ &+ \int_0^{2\pi}(-i\bar{\theta}_n^{(1)} - sw_n^{(1)}/2 + bw_n^{(1)})e^{-i\bar{\theta}_{0n}}d\bar{\theta}_{0n}\Bigg\}.\end{aligned} \tag{2.46}$$

Assume the perturbations propagate as $e^{i\Gamma z'}$ and average w and $\bar{\theta}$ over all electrons:

$$\bar{w}^{(1)} = \int_0^{2\pi} w^{(1)} e^{i\bar{\theta}_{0n}} d\bar{\theta}_{0n} \tag{2.47}$$

$$\bar{\bar{\theta}}^{(1)} = \int_0^{2\pi} \bar{\theta}^{(1)} e^{i\bar{\theta}_{0n}} d\bar{\theta}_{0n} \tag{2.48}$$

$$i\Gamma\bar{w}^{(1)} = -F'^{(1)} \tag{2.49}$$

$$i\Gamma\bar{\bar{\theta}}^{(1)} = (\bar{\mu} - \bar{\Delta}b)\bar{w}^{(1)} + \frac{is}{2}F'^{(1)} \tag{2.50}$$

$$i\Gamma F'^{(1)} - i\bar{\Delta}F'^{(1)} = I_0'(i\bar{\bar{\theta}}^{(1)} - (b - s/2)\bar{w}^{(1)}) \tag{2.51}$$

To determine the value of Γ we take the determinant and set it equal to zero

$$\begin{vmatrix} i\Gamma & 0 & -1 \\ \bar{\mu} - \bar{\Delta}b & i\Gamma & \frac{is}{2} \\ -I_0'(b - s/2) & iI_0' & i\Gamma - i\bar{\Delta} \end{vmatrix} = 0,$$

$$-i\Gamma^3 + i\bar{\Delta}\Gamma^2 - i\Gamma I_0' s/2 + iI_0'(b - s/2)\Gamma + i(\bar{\mu} - \bar{\Delta}b)I_0' = 0. \tag{2.52}$$

Simplifying we find the linear gain dispersion relation:

$$\Gamma^3 - \bar{\Delta}\Gamma^2 - I_0'(s - b)\Gamma + (\bar{\mu} - \bar{\Delta}b)I_0' = 0. \tag{2.53}$$

The three roots of Γ correspond to the growth rates of the three waves that will couple with the electron beam and propagate as $e^{i\Gamma z'}$. The excitation of these three waves is referred to as an insertion loss because only one of the waves will result in a growing wave. The power that couples to the remaining two waves will either propagate without gain or be absorbed.

2.3.3 Analysis

The nonlinear equations of motion can be used to determine the energy extracted from the electron beam, i.e. $\eta_\perp$ the perpendicular efficiency. The analysis of the conversion

of kinetic electron energy in Equations (2.24)-(2.26) to electromagnetic radiation was performed by using a fourth-order Runge-Kutta algorithm and averaging the results for 32 electrons with uniform spacing in initial phase. For clarity, the result is shown as contour plots with variables $\delta = \bar{\Delta}/\sqrt{I_0'}$ and $\mu = \bar{\mu}/\sqrt{I_0'}$ in Figure 2-9. The circuit length was limited to $L = 10$ with an input field strength of $F_0 = 0.01$. The contours shown are for the maximum achieved efficiency over this length of the circuit. In Figure 2-10, the perpendicular efficiency is shown as a function of distance for the specific case of $\delta = 2.2$, $\mu = 6$ with a maximum achieved efficiency of $\eta_{\perp}^{max} = 0.63$. Figure 2-11 shows the particle phase for 16 electrons as they travel down the circuit for the same operational parameters. The particles only begin to bunch significantly around $L = 7$. Prior to this location the device is operating in a purely linear gain regime. The maximum in efficiency occurs close to $L = 8$, where the electron bunching is optimized.

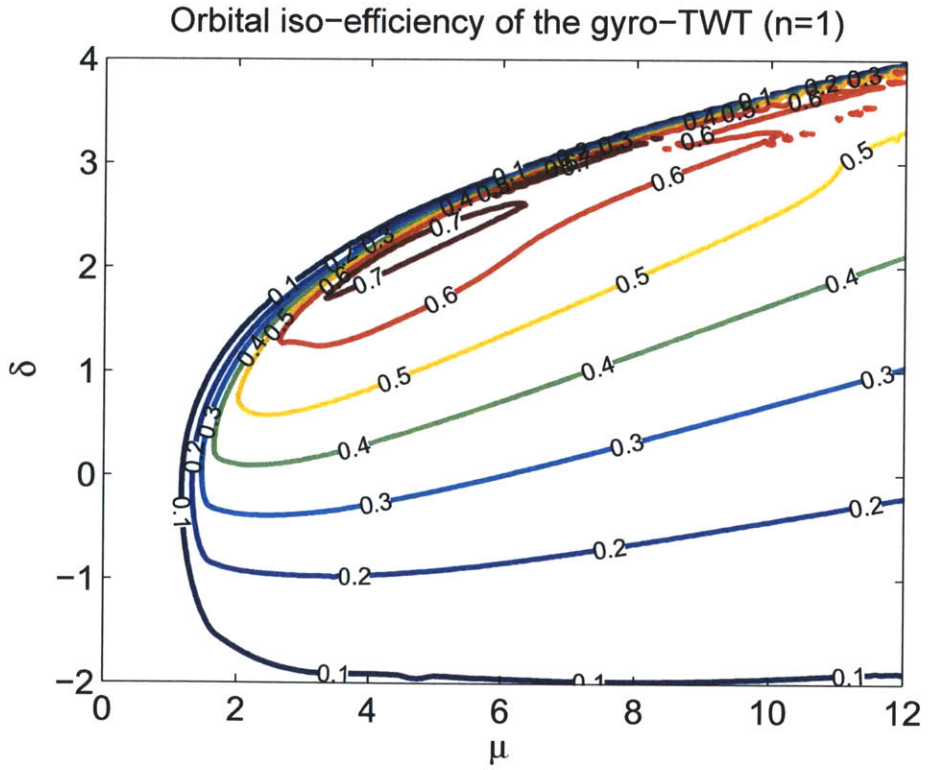

Figure 2-9: Contour plot for the perpendicular efficiency of the 1st harmonic interaction for a gyrotron amplifier. Results are in excellent agreement with [124].

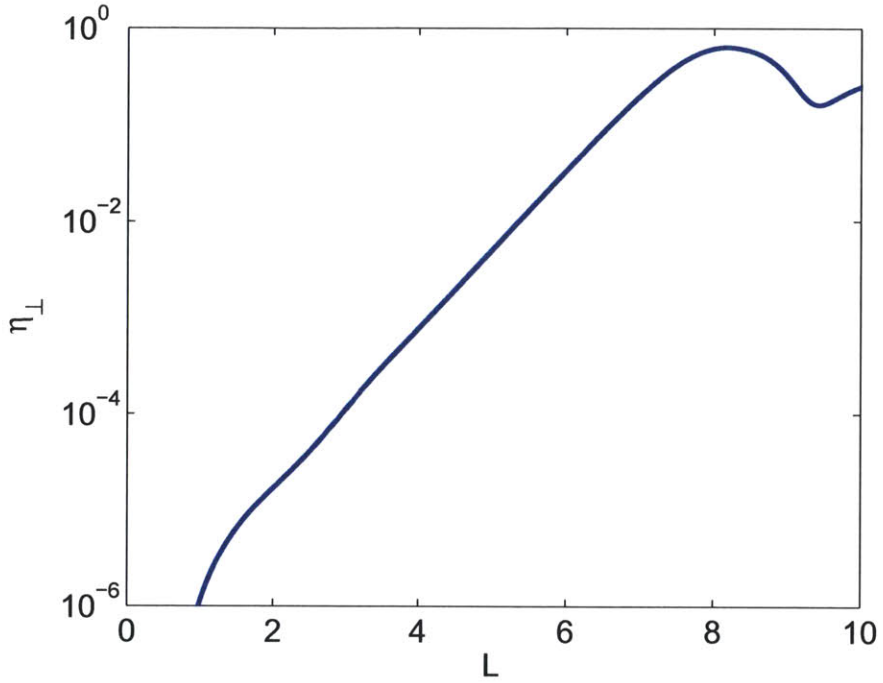

Figure 2-10: The perpendicular efficiency as a function of circuit length for $\Delta = 2.2$ and $\mu = 6$. A maximum efficiency of $\eta_\perp^{max} = 0.63$ is achieved.

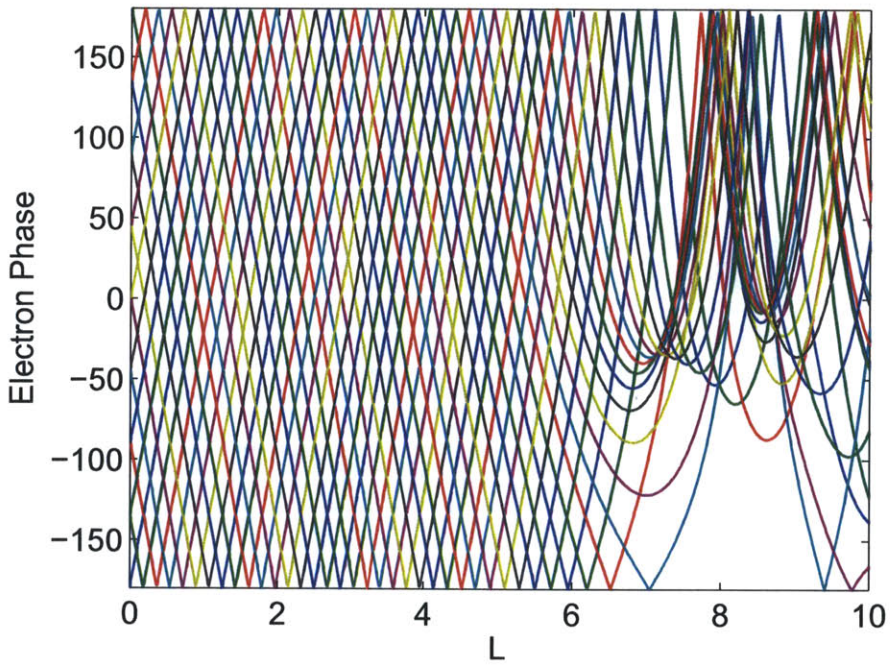

Figure 2-11: Electron orbital phase for 16 of the 32 electrons used in the simulation from Figure 2-10.

A comparison between the linear gain calculated using the linear theory in Equation (2.53) and the nonlinear theory Equations (2.24)-(2.26) is shown in Figure 2-12. The simulation is performed for the TE_{03} mode of a circular waveguide with a 2 mm radius and a 1.2 mm electron beam as a function voltage (10-18 kV) for an input frequency of 250 GHz. The electron beam current and $\alpha = \frac{v_t}{v_z}$ are varied linearly as a function of voltage from 0.3-0.4 A and $\alpha = 0.45 - 0.7$. The magnetic field is 8.7304 T, the circuit length is 167 cm (or 875 in normalized coordinates) and the input field strength is $F_0' = 4 \times 10^{-5}$. In Figure 2-12(a) we see the waveguide dispersion relation and the electron beam resonance condition that varies with increasing voltage from blue to green. In Figure 2-12(b) the perpendicular efficiency and the field amplitude are shown as a function of distance for 11.6 kV. The slope of $\eta_\perp$ is twice that of F' because $\eta_\perp \propto F'^2$. Figure 2-12(c) and (d) show the linear gain calculated from the linear and nonlinear equations and for all voltages tested the gain is in close agreement. The calculated μ, δ and I_0' are shown in Figure 2-12(e) as a function of voltage for the linear and nonlinear simulations. The values of μ and δ correspond to the parameters needed to determine $\eta_\perp$ from Figure 2-9. In Figure 2-12(f) the peak efficiency and the efficiency at the end of the circuit are shown. Note that the end efficiency is what would be observed experimentally. The peak efficiencies from Figure 2-12(f) correspond to those from Figure 2-9 between 11.2-16.8 kV for the appropriate μ and δ. Both above and below this range, the peak efficiency in Figure 2-12(f) is lower because the circuit is not long enough to reach saturation. Where the peak and end efficiency do not agree (11.7-16.3 kV), the amplification has saturated before the end of the circuit.

Waveguide attenuation can play a significant role in the operation of a gyrotron amplifier [99, 125]. Waveguide attenuation can be incorporated into the linear and nonlinear theory of the amplifier by introducing a complex term to k_z. Attenuation has a strong frequency dependence close to waveguide cutoff. A gyrotron amplifier typically operates ~3% from waveguide cutoff and the effect of attenuation will therefore be frequency dependent. The addition of loss results in complex values for the

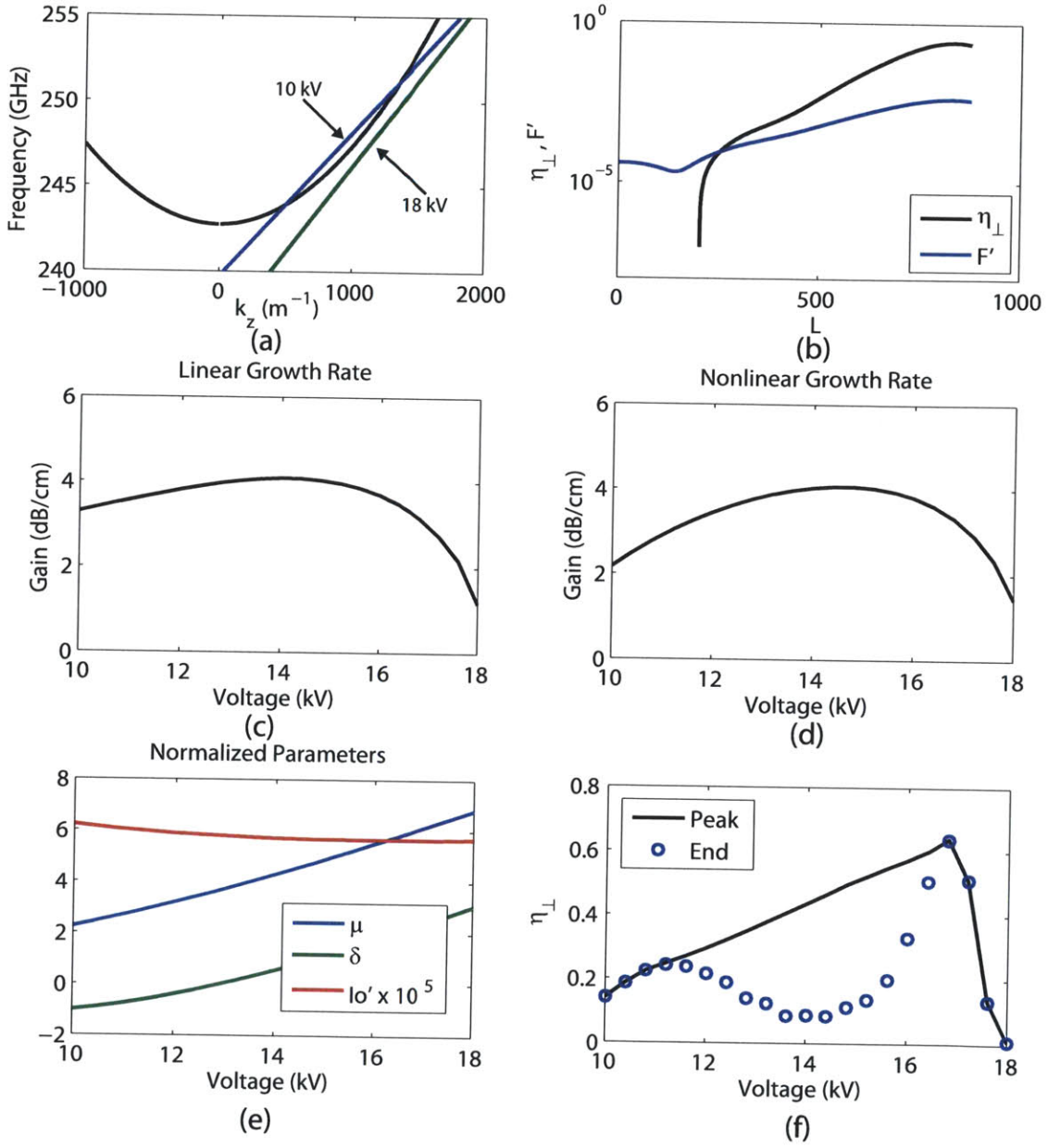

Figure 2-12: Comparison between linear an nonlinear simulations for identical operating conditions. (a) The limits of the electron beam resonance condition shown with blue and green lines. (b) The perpendicular efficiency and the field amplitude. The (c) linear and (d) nonlinear gain per cm for the corresponding (e) normalized parameters and (f) peak and exit efficiency.

three parameters which determine the growth rate Δ, $\bar{\mu}$ and b because h becomes complex. However, loss primarily affects Δ because $\mathrm{Im}\{\bar{\mu}, b\} \ll \mathrm{Im}\{\Delta\}$ while the real parts of these three parameters are on the same order of magnitude. Figure 2-13 shows a comparison between the linear growth rate for an amplifier with and without loss. The dispersion relation is shown in Figure 2-13(a) and the normalized parameters are shown in Figure 2-13(b). The loss per unit length is shown in Figure 2-13(f) as a function of frequency. These values were used because they correspond to expected values for the PBG waveguide. Figure 2-13(c) shows the linear gain with and without waveguide loss. The attenuation typically decreases the peak gain while increasing the bandwidth. The effect of attenuation on the three waves that couple to the electron beam can be seen in Figure 2-13(d), where Γ corresponds to a root of Equation (2.53). In Figure 2-13(d), the dots are without loss and the circles are with loss. Additionally, we note that as the detuning of the electron beam approaches zero the decrease in gain corresponds to 1/3 of the attenuation in dB, see Figure 2-13(e).

MAGY [34] is a self-consistent time-dependent code that can simulate both gyrotron oscillators and amplifiers, and it has been bench marked against many gyrotron experiments. The advantage of simulating an amplifier structure with MAGY is the inclusion of velocity spread for the electron beam and the ability to confirm that the device is stable from oscillations. However, in the absence of these two concerns MAGY should agree with the theory presented in Section 2.3. For a comparison we will use the system described in Figure 2-14(a) with the TE_{03} waveguide mode of a 2 mm circular waveguide and a 1.2 mm electron beam. The circuit length is 260 mm. The attenuation in the waveguide is set at 2 dB/cm. In Figure 2-14(b), we show a comparison for the linear growth rate between linear and nonlinear theory for fixed frequency, 250 GHz, while varying the magnetic field. MAGY is compared to the nonlinear theory in Figure 2-14(c), which also shows the dramatic effect of insertion loss that results from the coupling of the input wave into three different waves of which only one is amplified. Typically, circuit gain is shown as a function of frequency; however, Figure 2-14 demonstrates agreement independent of magnetic

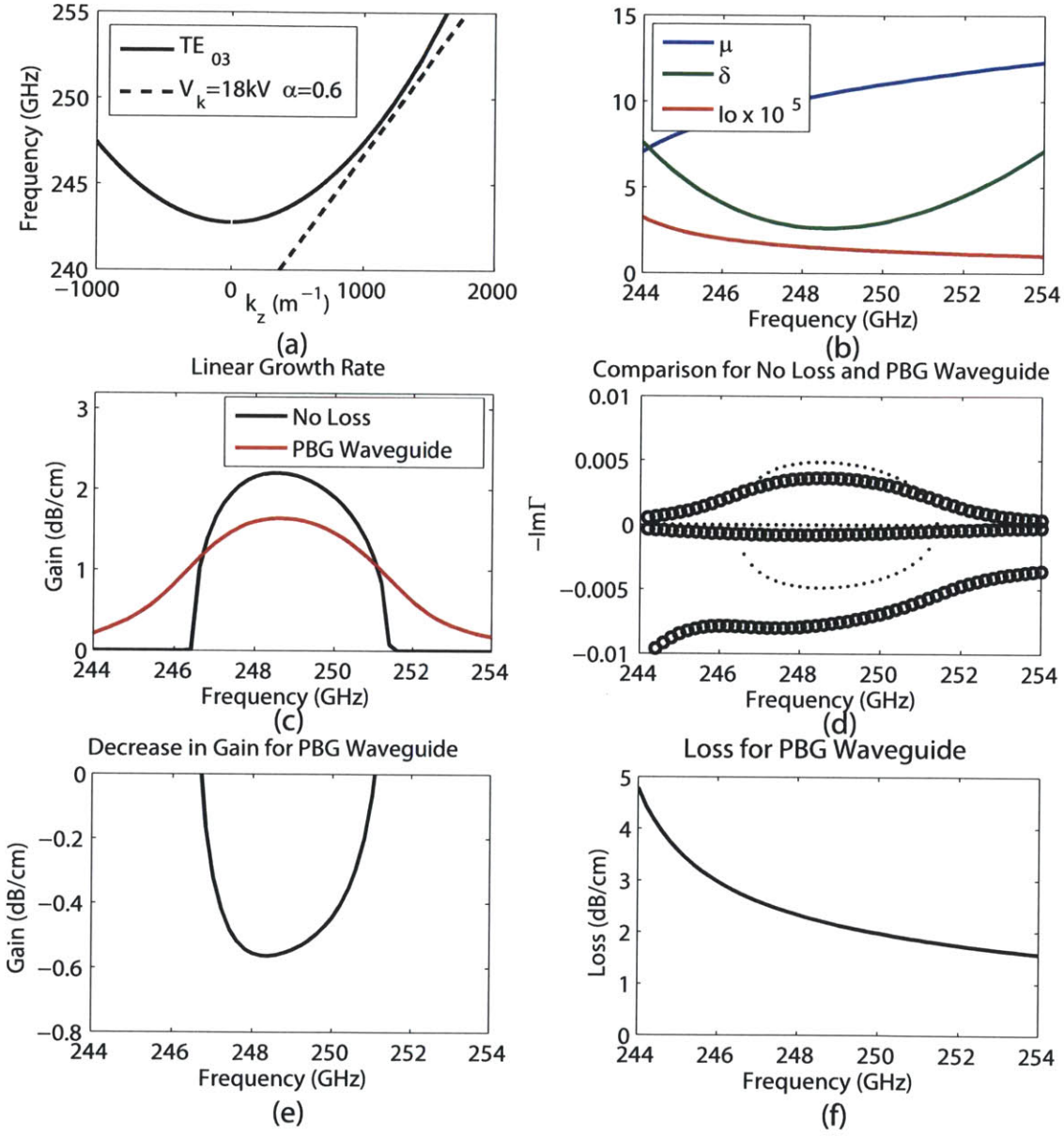

Figure 2-13: Effect of attenuation on the linear gain of a gyrotron amplifier as a function of frequency. The electron beam current is 0.3 A, the magnetic field is 8.7322 T and the beam radius is 1.2 mm.

field and provides some intuition with regards to how sensitive the amplifier is to the magnetic field. In Section 4.5, a comparison between MAGY and the nonlinear theory is shown as a function of frequency with excellent agreement observed. The results from MAGY were shifted by 0.012 T in order to produce agreement with the theory. The presence of this shift was confirmed under a variety of conditions (voltage, current, α, frequency, etc.) and it is highly repeatable. The source of this shift is unknown at present.

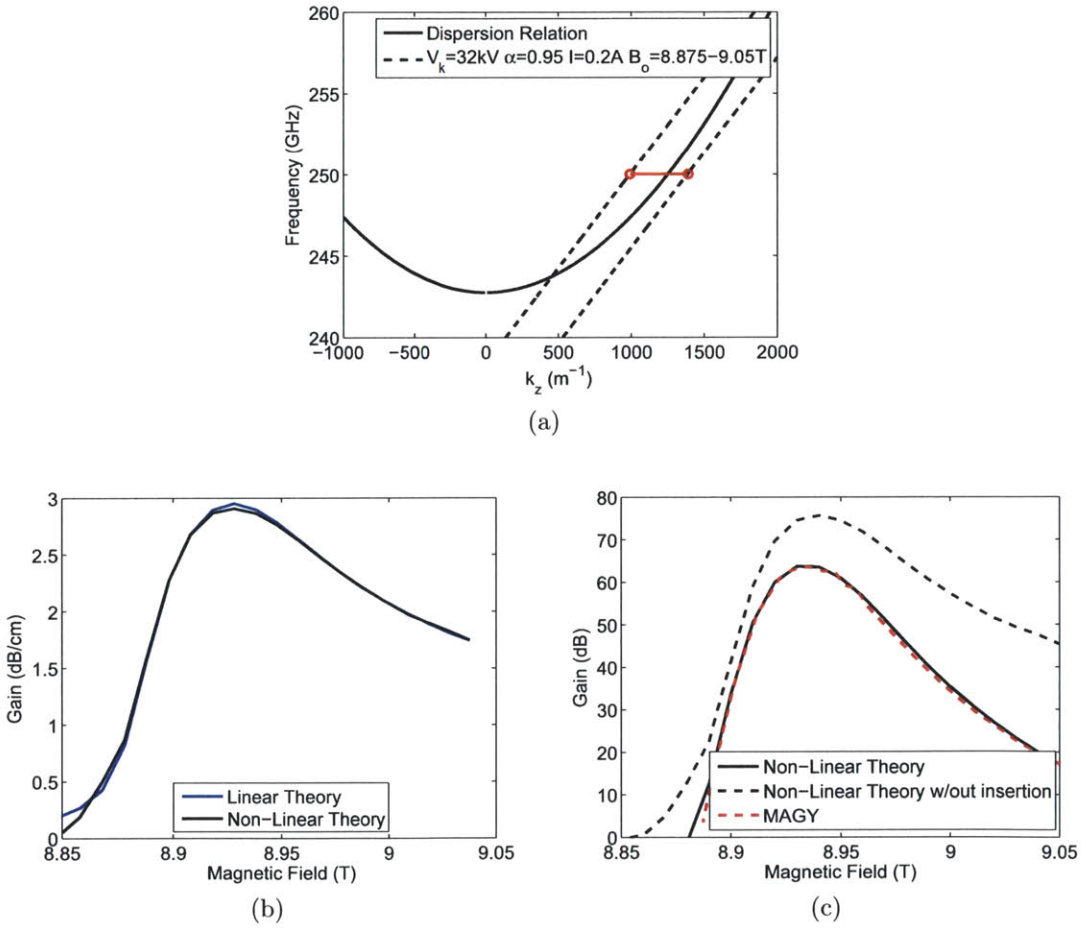

Figure 2-14: (a) Dispersion diagram for the system being analyzed. The magnetic field is varied while the frequency of amplification is held constant and labeled with a red line. (b) Comparison between the linear growth rate determined from linear and nonlinear theory. (c) Comparison between the circuit gain calculated using nonlinear theory and MAGY. The dashed black line shows the gain calculated from the linear growth rate for the same length of circuit. The large difference is due to the insertion loss incurred from coupling to the growing wave.

2.4 Conclusions

The nonlinear theory of operation for a gyrotron oscillator was derived, discussed and analyzed. Numerical simulations were performed that provided excellent agreement with published values. A general explanation for the operation of gyrotron oscillators and amplifiers was provided. The bunching mechanism for both fast and slow waves in a streaming electron plasma was presented. The nonlinear equations of motion in a gyrotron amplifier were presented. The linearized dispersion relation for amplification was derived. Numerical simulations were performed using the same techniques as the gyrotron oscillator and the results are consistent with published values. A comparison between linear and nonlinear theory shows that they produce nearly identical values for the linear gain of a device. However, effects from saturation and the achievable efficiency of a circuit require a nonlinear formalism. The effect of attenuation was also analyzed using linear and nonlinear theory. It was shown that, for zero detuning, the linear gain is decreased by one third of the attenuation. Finally, a comparison between the nonlinear theory and MAGY was shown to exhibit excellent agreement when including attenuation in the circuit. However, MAGY is required in order to include the effects of velocity spread .

Chapter 3

THz Waveguides: Theory and Experiment

3.1 Attenuation in Waveguides

Waveguide design and fabrication are critical for the successful implementation of this gyrotron amplifier. The amplifier requires diagnostics and mode converters using fundamental rectangular waveguide, Section 3.2; a PBG waveguide for the interaction circuit, Section 3.3 and corrugated waveguide for low-loss transmission from the source to the amplifier, Section 3.4. These waveguides require custom design and specialized fabrication because the frequency of operation for the amplifier (250 GHz) is above the range of typical commercial applications. The challenges imposed by the elevated frequency consist of smaller dimensions with tighter tolerances and increased ohmic losses. Ohmic losses are both mode and frequency dependent, which encourages the use of overmoded waveguide for transmission over long distances. However, design constraints often determine the use of fundamental mode waveguide. In either case, fabrication techniques can result in drastically increased attenuation. With only a low-power solid-state source ($\leq$ 35 mW) available as the driver for the amplifier, attenuation is a critical concern.

Attenuation in a waveguide is determined by analyzing the surface currents induced by the mode. In a circular waveguide, with cylindrical coordinates (ρ, θ, z), the electric and magnetic fields for TE_{mp} modes can be written as:

$$E_\rho = \frac{-i\omega\mu m}{k_c^2 \rho} A \cos(m\phi) \mathbf{J}_m(k_c\rho) e^{-ik_z z}, \tag{3.1}$$

$$E_\phi = \frac{i\omega\mu}{k_c} A \sin(m\phi) \mathbf{J}'_m(k_c\rho) e^{-ik_z z}, \tag{3.2}$$

$$E_z = 0, \tag{3.3}$$

$$H_\rho = \frac{-ik_z}{k_c} A \sin(m\phi) \mathbf{J}'_m(k_c\rho) e^{-ik_z z}, \tag{3.4}$$

$$H_\phi = \frac{-ik_z m}{k_c^2 \rho} A \cos(m\phi) \mathbf{J}_m(k_c\rho) e^{-ik_z z}, \tag{3.5}$$

$$H_z = A \sin(m\phi) \mathbf{J}_m(k_c\rho) e^{-ik_z z}, \tag{3.6}$$

where $k_c = \nu_{mp}/a$, ν_{mp} is the p$^{\text{th}}$ root of the m$^{\text{th}}$ order Bessel function and a is the waveguide radius. In order to calculate the attenuation constant (α_c), we must find the power propagating down the waveguide (P_0) and the power dissipated on the conducting walls (P_l) of the waveguide. The power propagating down the waveguide is found by integrating the Poynting vector over the cross-sectional surface of the waveguide

$$P_0 = \frac{1}{2}\mathbf{Re}\left\{ \int_{\rho=0}^{a} \int_{\phi=0}^{2\pi} \bar{E} \times \bar{H}^* \cdot \hat{z} \rho d\phi d\rho \right\} \tag{3.7}$$

where $\hat{z}$ is the direction of propagation. The dissipated power is found by integrating the surface current, J_s, on the surface of the waveguide at that cross section

$$P_l = \frac{R_s}{2} \int_{\phi=0}^{2\pi} |\bar{J}_s^2| a d\phi \tag{3.8}$$

where R_s is the surface resistivity and $|J_s|^2$ is given by the magnetic fields on the surface $[|H_\phi|^2 + |H_z|^2]$. Once P_0 and P_l are known, the attenuation constant can be defined as

$$\alpha_c = \frac{P_l}{2P_o} \tag{3.9}$$

where the field propagates as $e^{-\alpha_l z}$. Due to the surface currents and the propagation constant k_z, α_c is frequency and mode dependent. For waveguides with complicated geometries, such as a photonic band gap structure, it is not possible to analytically

calculate the attenuation constant because the fields of the mode are not well defined. One must use a numerical code, such as High Frequency Structure Simulator (HFSS), to observe how power propagates through the waveguide as a function of frequency.

3.2 Fundamental Rectangular Waveguide

The use of waveguide components in the THz band for communications, astrophysics and vacuum electronics has increased the demand of machining techniques for waveguide fabrication. Traditional machining, which requires drawing components, diffusion bonding, brazing, etc. is costly, complex and often not scalable to higher frequencies. Methods using lithographic processes with photoresist and silicon etching have demonstrated performance in the THz band [50, 49, 57, 101, 153, 167], but components produced using these techniques have high loss and are difficult to interface with standard waveguide components. With attenuation of 0.1 dB/λ [153] the best reported results in the WR-3 band have shown dramatic improvement, but remain significantly higher than traditional rectangular waveguide.

We present a new approach to the fabrication of waveguide components using direct machining with a CNC end mill. This method has demonstrated low loss, 0.2 dB/cm at 280 GHz for WR-3 waveguide as well as adaptability to structures with features on the order of 200 μm. This approach is a modification of the split-block machining process with the addition of a RF choke that runs parallel to the waveguide and rejects coupling to the TM_0 mode of the parallel plate waveguide produced by the split-block. These waveguide structures are easy to fabricate avoiding the use of lithographic processes, easily compatible with standard waveguide components and do not require permanent junctions such as diffusion bonding allowing for alteration of features after testing components.

3.2.1 Split-Block Choke

As the frequency of operation moves into the THz regime, losses in waveguide components increase due to surface resistivity and fabrication errors. The increase in

surface resistance with frequency requires the use of highly conductive metals for the inner surface of waveguide components. For many fabrication techniques this requires a final coating of the component with a highly conductive metal, which can lead to increased surface roughness or dimensional errors. Direct machining of highly conductive metals (copper, brass) removes any need for metallic plating of the fabricated component. The increase in frequency also causes the fabrication tolerances to become significant fractions of the wavelength. Gaps and mismatches are especially susceptible to the increase in frequency.

In the traditional approach to split-block fabrication a symmetric feature is fabricated onto two separate pieces which are joined [48, 118, 145, 137, 133, 139]. Split-block fabrication is easily integrated into the design of passive components as well as active ones. Ideally, this technique prevents coupling to the fundamental TM_0 mode of a parallel plate waveguide, as seen in Figure 3-1(a). The TM_0 mode would be excited by the H_z component of the rectangular waveguide, however H_z is at a null in the center of the waveguide and it is asymmetric about the null which limits its coupling to the symmetric TM_0 mode. However, this technique also requires very tight tolerances because, if the placement of the cut is asymmetric, the TM_0 mode can be excited resulting in drastically increased losses, as seen in Figure 3-2(a) for a $0.001''$ gap displaced from the center line by $0.0005''$. HFSS simulations for ideal copper rectangular waveguide with no gaps or fabrication errors is also shown in Figure 3-2(a). In order to prevent the excitation of the TM_0 mode, we propose the addition of two quarter wave steps to create an impedance mismatch and create a choke in the transverse direction for the entire length of the component, Figure 3-1(b). The addition of a choke to the split-block machining process reduces the accuracy which is required for a symmetric placement of the fabrication plane, as seen by the green line in Figure 3-2(a).

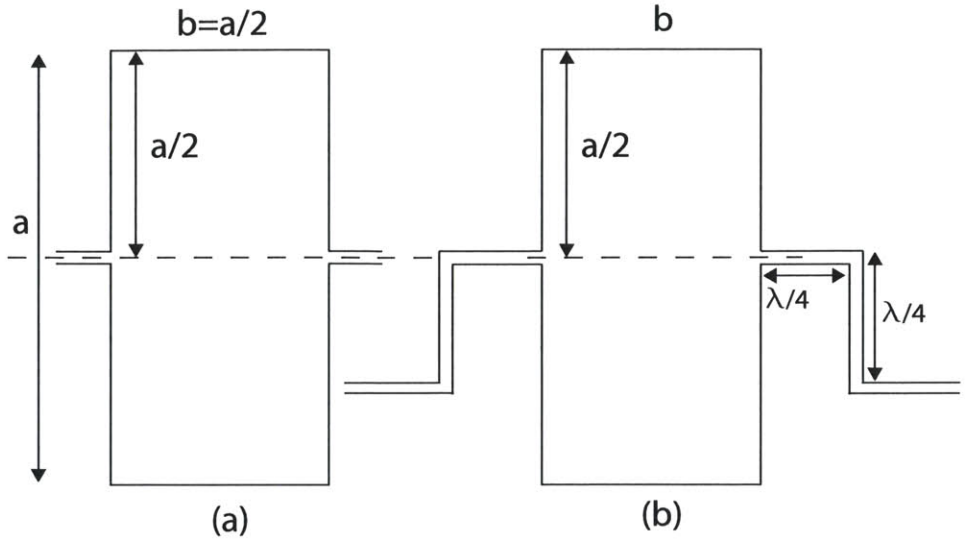

Figure 3-1: Cross section of waveguide for various fabrication techniques, where (a) is the split-block and (b) is the split-block choke.

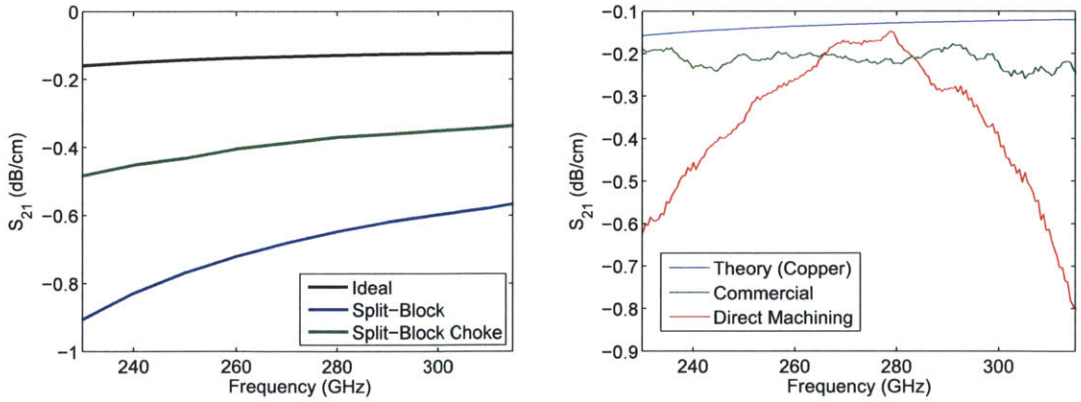

Figure 3-2: (a) HFSS simulations for the S_{21} of ideal copper straight waveguide and split-block and split-block choke copper waveguide with a 0.001″ gap displaced from the center line by 0.0005″. Losses increase dramatically when the central gap is displaced asymmetrically. (b) Measured S_{21} for straight waveguide.

3.2.2 Components

Straight Waveguide

Initial testing of the split-block choke fabrication technique was performed using sections of straight waveguide (1″, 2″ and 4″) machined in copper which could be compared to commercially available WR-3 waveguide (Aerowave, Inc.). Tests were performed using a vector network analyzer (Agilent E8363B) calibrated to perform S_{21} measurements. The measured loss per centimeter is shown in Figure 3-2(b) for both the commercial and split-block choke waveguide. Neither waveguide achieves the theoretical value for transmission, but both perform well over the WR-3 band. The direct machined waveguide shows improved performance in the central region of the band where the dimensions of the choke are exactly $\lambda/4$. This measurement demonstrates that direct machined waveguide can be quickly fabricated to a quality that is comparable with more specialized and costly fabrication techniques.

Directional Coupler

Three dB and 10 dB four-port directional couplers were designed and fabricated in order to test the precision of direct machining due to the small coupling slots required. Brass was used for the directional couplers, because it is easier to machine than copper. The coupler design targeted the 240-260 GHz band in both cases. The 3 dB coupler was designed with the aim of providing equal output power for ports 2 and 3 with 20 dB isolation for port 4. A four-slot design was selected where the gap between the two waveguide channels is 0.012″ and the slot width is 0.008″ with a spacing of 0.012″. Results for vector network analyzer (VNA) measurements are shown in Figure 3-3(a) and have excellent agreement with HFSS simulations that include ohmic losses but do not include the presence of the split-block choke. The flanges for ports 1 and 2/3 are separated by 2″ resulting in 1.5 dB of ohmic losses. Photographs of the four and two coupling slots for the 3 dB and 10 dB couplers are shown in Figure 3-3(b) and (c), respectively. The 10 dB coupler was designed with the two waveguide channels separated by 0.012″ a slot width of 0.008″ and a slot

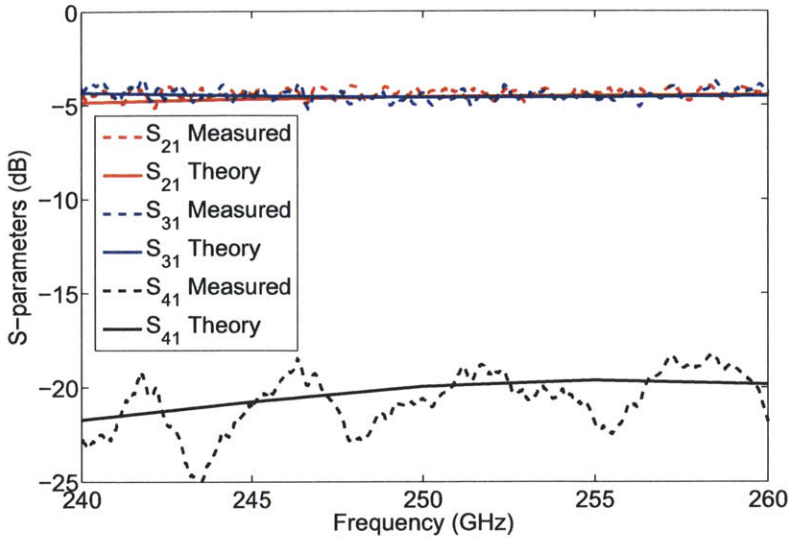

(a)

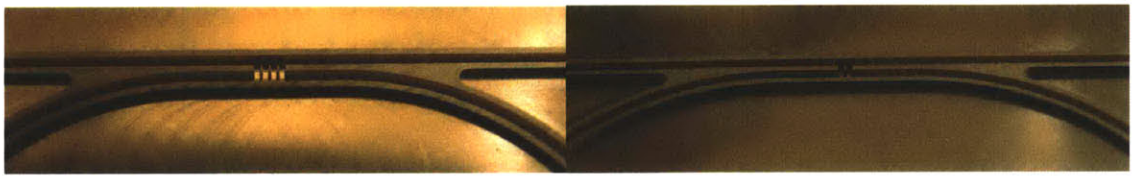

(b) (c)

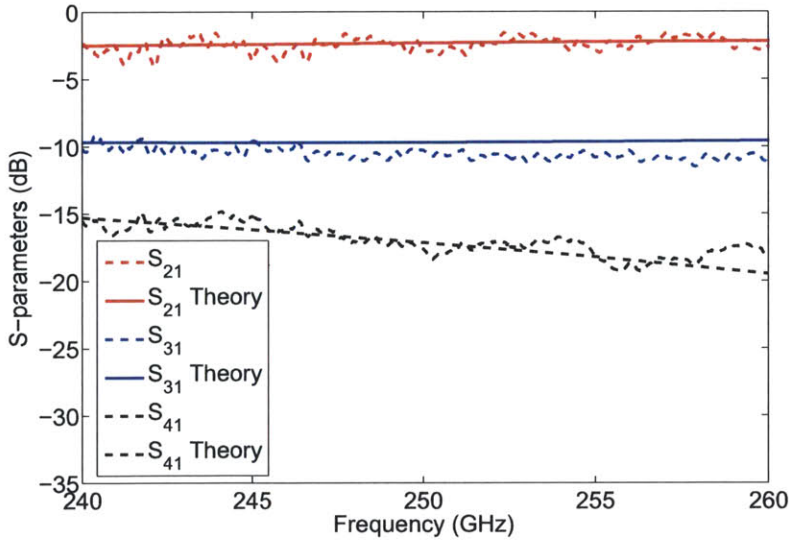

(d)

Figure 3-3: (a) Theory vs. measurement for the 3 dB directional coupler. (b) Photograph of the four-slot 3 dB directional coupler. (c) Photograph of the two-slot 10 dB directional coupler. (d) Theory vs. measurement for the 10 dB directional coupler.

spacing of 0.012″. Figure 3-3(d) shows excellent agreement with HFSS simulations.

3.3 PBG Waveguide

3.3.1 Photonic Band Gaps

In order for the gyrotron amplifier to operate correctly self-start oscillations, driven oscillations and BWOs must all be subdued. The traditional method for suppressing these oscillations consists of minimizing reflections in the amplifier circuit to lower the diffractive Q and placing severs (short sections of highly attenuating waveguide) to increase the start current for these oscillations. Both of these features are complicated to design and manufacture for very high frequency systems. Severs can also waste valuable space in the flat top of the magnetic field, thereby decreasing the performance of the amplifier. An alternate approach is to design an interaction circuit that has an attenuation constant that is highly frequency dependent to prevent oscillations at lower frequency modes and near cutoff for the operational mode.

An ideal interaction circuit would confine the operating mode with limited loss in the amplification region and have an attenuation constant that is very high for modes that are not of interest. Mode selective circuits can be made in a variety of ways (dielectric loading, confocal, PBG, etc.) that often have a detrimental impact on the mode of interest as well as additional complexity in fabrication. Finding a balance between the suppression of unwanted modes while minimizing losses of the desired mode is the key to developing a successful overmoded interaction circuit for a gyrotron amplifier.

It is possible to create a large variety of photonic band gap structures in one, two and three dimensions that support TE, TM and TEM waves. A photonic band gap of interest for gyrotron amplifiers needs to support a TE mode that will not diffract in the transverse direction with respect to the electron beam. Furthermore, if the circuit is to be overmoded, the lowest band gap for a given set of lattice constants should not extend to zero frequency. Taking these things into consideration, we have

selected a two dimensional triangular metallic lattice for the gyrotron amplifier, and it will be the only one discussed presently. A transverse cross section of a triangular lattice of metallic rods is shown in Figure 3-4. The properties of the lattice are governed by the radius, a, and spacing, b, of the rods. The fundamental unit cell is demarcated by a dashed line. The fundamental cell should be infinitely repeated to create a perfect PBG. However, a non-infinite lattice still exhibits the basic nature of the PBG with highly reflective bands, especially in the case of a metallic lattice. We begin by defining the conductivity profile of the lattice as

$$\sigma\left(\vec{x}_\perp + \vec{T}_{mn}\right) = \sigma\left(\vec{x}_\perp\right) \tag{3.10}$$

$$\vec{T}_{mn} = \left(m + \frac{n}{2}\right) b\hat{e}_x + \frac{\sqrt{3}}{2} nb\hat{e}_y \tag{3.11}$$

where b is the lattice spacing, m and n are integers and $\vec{x}_\perp = x\hat{e}_x + y\hat{e}_y$.

We will define our fields as a function of $\vec{x}_\perp$, z and t. Due to the symmetry and linearity of the system we can assume that the axial wave number, k_z, and the frequency, ω, are fixed. We write the Helmholtz wave equation as

$$\vec{\nabla}_\perp^2 \psi\left(\vec{x}_\perp\right) = \left(k_z^2 - \frac{\omega^2}{c^2}\right) \psi\left(\vec{x}_\perp\right) \tag{3.12}$$

with the boundary condition

$$\frac{\partial \psi}{\partial \vec{n}}|_S = 0 \tag{3.13}$$

where $\vec{n}$ is the vector normal to the metallic surface, S. The discrete array of metallic rods has a solution that can be written in Bloch form

$$\psi\left(\vec{x}_\perp + \vec{T}_{mn}\right) = \psi\left(\vec{x}_\perp\right) e^{i\vec{k}_\perp \cdot \vec{T}_{mn}} \tag{3.14}$$

where $\vec{k}_\perp = k_x\hat{e}_x + k_y\hat{e}_y$ is the transverse wave number, allowing us to solve the wave

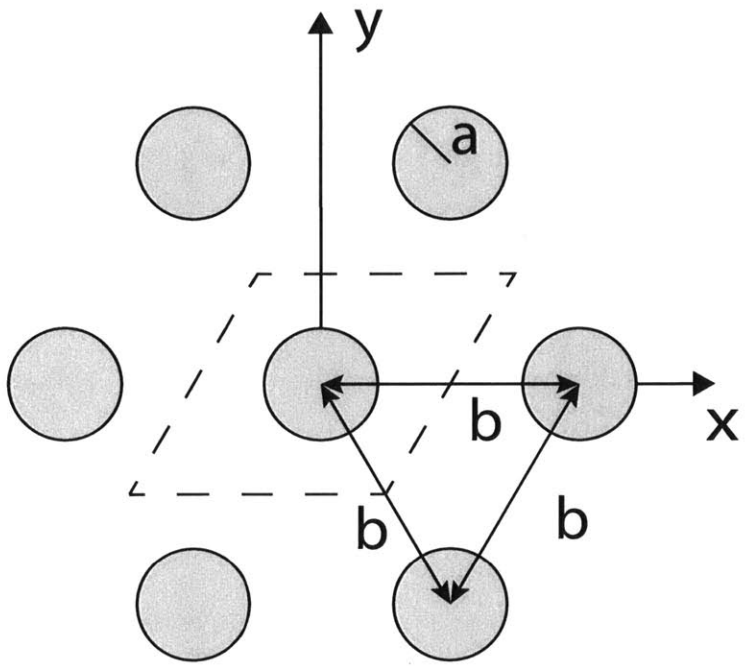

Figure 3-4: Triangular lattice of metallic rods. The fundamental unit cell is marked with a dashed line.

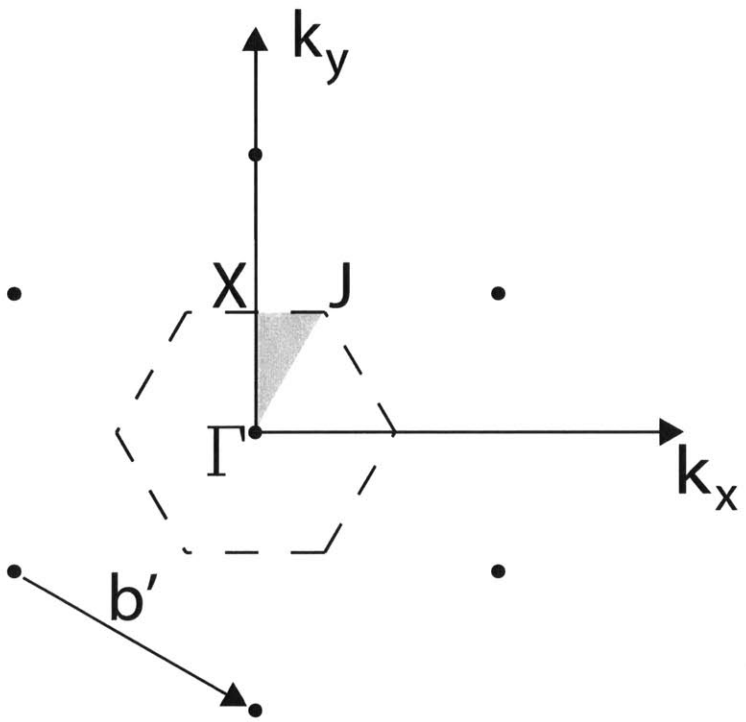

Figure 3-5: Reciprocal triangular lattice where $b' = \frac{4\pi}{\sqrt{3}b}$. The gray area is the irreducible Brillouin zone.

equation in the fundamental cell in Figure 3-4 given by

$$\left| x - \frac{y}{\sqrt{3}} \right| \leq \frac{b}{2}, |y| \leq \frac{\sqrt{3}}{4} b. \tag{3.15}$$

The discrete nature of the system also imposes periodic boundary conditions:

$$\psi\left(\frac{b}{2} + \frac{1}{\sqrt{3}}y, y\right) = e^{ik_x b}\psi\left(-\frac{b}{2} + \frac{1}{\sqrt{3}}y, y\right) \tag{3.16}$$

$$\psi\left(x, \frac{\sqrt{3}b}{4}\right) = e^{ik_x b/2 + ik_y\sqrt{3}b/2}\psi\left(x - \frac{b}{2}, -\frac{\sqrt{3}b}{4}\right). \tag{3.17}$$

Equation (3.14) imposes limits on the value of $\vec{k}_\perp$, shown as the Brillouin zone in Figure 3-5. The three special points Γ, X and J are at $\vec{k}_\perp = 0$, $\vec{k}_\perp = (2\pi/\sqrt{3}b)\hat{e}_y$ and $\vec{k}_\perp = (2\pi/\sqrt{3}b)(1/\sqrt{3}\hat{e}_x + \hat{e}_y)$.

One possible method to solve the wave equation in the unit cell area is using HFSS [146]. By imposing the proper boundary conditions, we can pre-select for TE modes and fully explore the possible k-space of the system. For any given $k_\perp$, there will be a corresponding phase advance across the unit cell. Perfect H boundaries are defined on the top and bottom of the unit cell to limit eigenmode solutions to TE modes. The wave number can be specified by creating a master/slave boundary as shown in Figure 3-6. The master/slave boundary defines the phase advance across the two orthogonal directions of the unit cell, thereby specifying the wave number. For example, traversing from the Γ point to the X point on Figure 3-5, k_x will always be zero, but $0 \leq k_y \leq 2\pi/\sqrt{3}b$. If we consider the periodic boundary conditions for this range of values, Equation (3.16) indicates that the phase shift $\phi_1 = 0$ from the master #1 to the slave #1 boundary and Equation (3.17) indicates there is a $0 \leq \phi_2 \leq \pi$ phase shift from the master #2 to the slave #2 boundaries in Figure 3-6. Performing the same analysis from X to J and J to Γ will complete the exploration of the Brillouin zone. The necessary values of k_x and k_y and the corresponding phases of the master/slave boundaries are listed in Table 3.1.

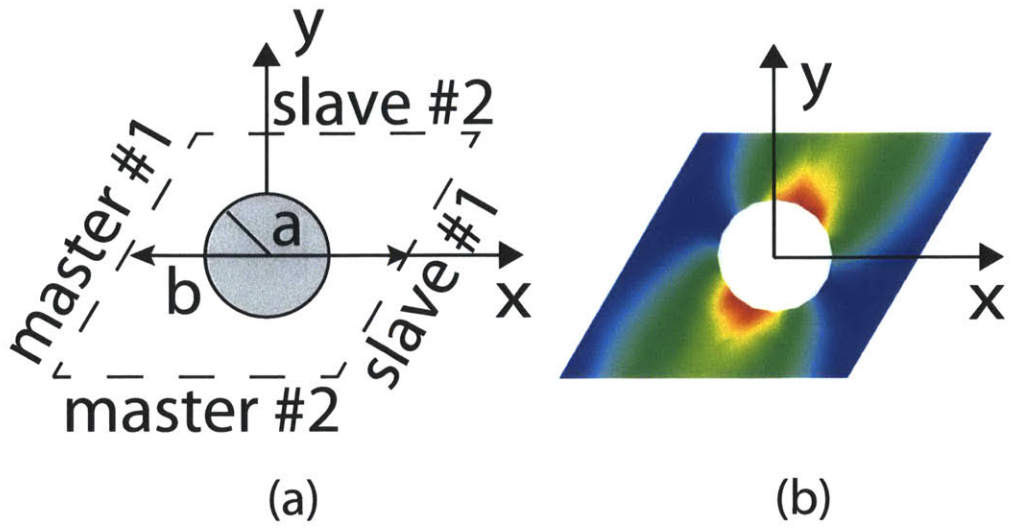

Figure 3-6: (a) Master/slave boundaries for the PBG unit cell and (b) the equivalent HFSS model with the complex magnitude of the electric field of the lowest order propagating mode for $a/b = 0.2$, $\phi_1 = \pi/9$ and $\phi_1 = 19\pi/18$.

Table 3.1: Simulation Parameters to Investigate Brillouin Zone

	k_x	k_y	ϕ_1	ϕ_2
Γ to X	0	$0 \rightarrow 2\pi/\sqrt{3}b$	0	$0 \rightarrow \pi$
X to J	$0 \rightarrow 2\pi/3b$	$2\pi/\sqrt{3}b$	$0 \rightarrow 2\pi/3$	$\pi \rightarrow 4\pi/3$
J to Γ	$2\pi/3b \rightarrow 0$	$2\pi/\sqrt{3}b \rightarrow 0$	$2\pi/3 \rightarrow 0$	$4\pi/3 \rightarrow 0$

The results of eigenmode simulations for $a/b = 0.2$ and the full range of values in Table 3.1 are shown in Figure 3-7. The 8 lowest order modes are plotted as a function of $k_\perp$ and normalized frequency. A photonic band gap is defined as a range of frequencies over which no mode has a solution. In Figure 3-7 we observe that a very small gap opens from $\omega b/c = 6.69$ to $\omega b/c = 6.75$. Figure 3-7 is in excellent agreement with results published by Smirnova et al. [151] using alternate methods. In Figure 3-8, the eigenmode frequencies are plotted for $a/b = 0.43$, which corresponds to the radius to spacing ratio of the design mode. In this figure, we can see three photonic band gaps for $\omega b/c = 5.35 \rightarrow 6.62$, $\omega b/c = 11.37 \rightarrow 12.12$ and $\omega b/c = 15.26 \rightarrow 16.93$.

Performing HFSS simulations over the full range of a/b it is possible to produce the global photonic band gap plot for a triangular lattice shown in Figure 3-9. This

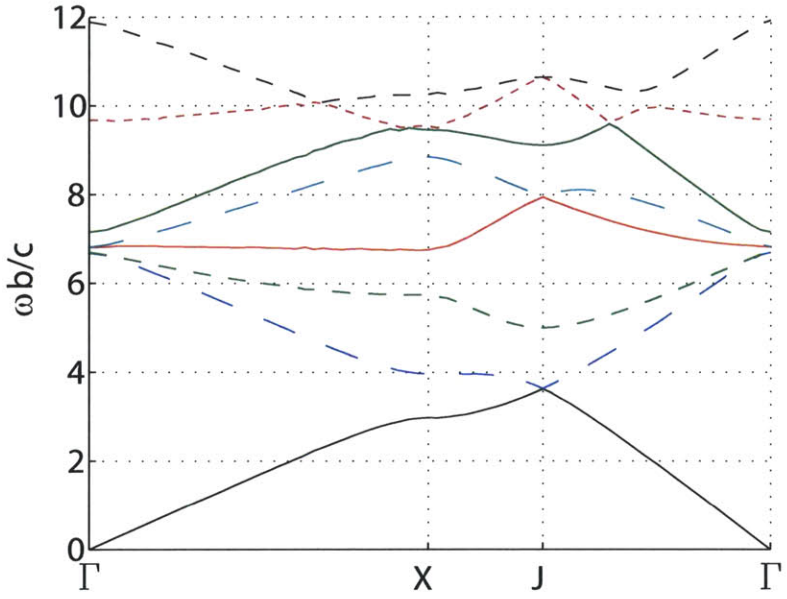

Figure 3-7: Normalized eigenmode frequencies as a function of $k_\perp$ for $a/b = 0.2$.

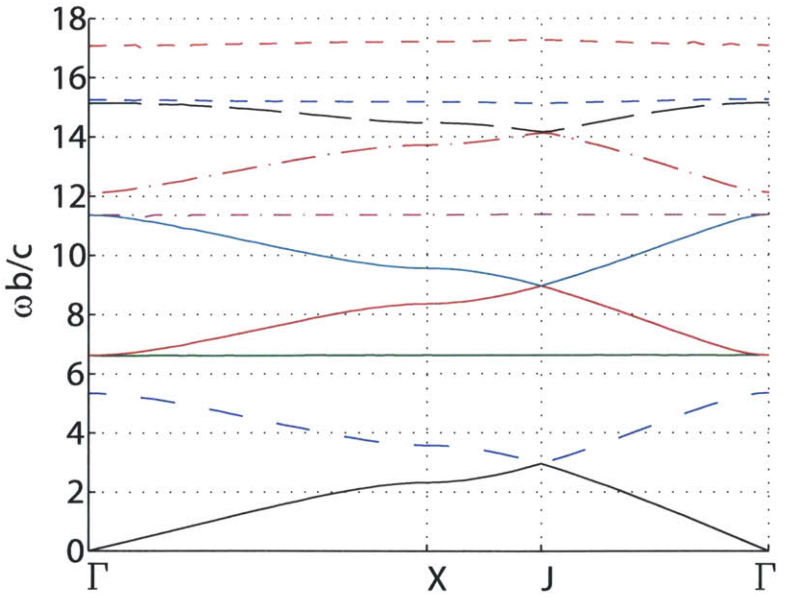

Figure 3-8: Normalized eigenmode frequencies as a function of $k_\perp$ for $a/b = 0.43$.

band gap plot is also in excellent agreement with results published by Smirnova et al. [151].

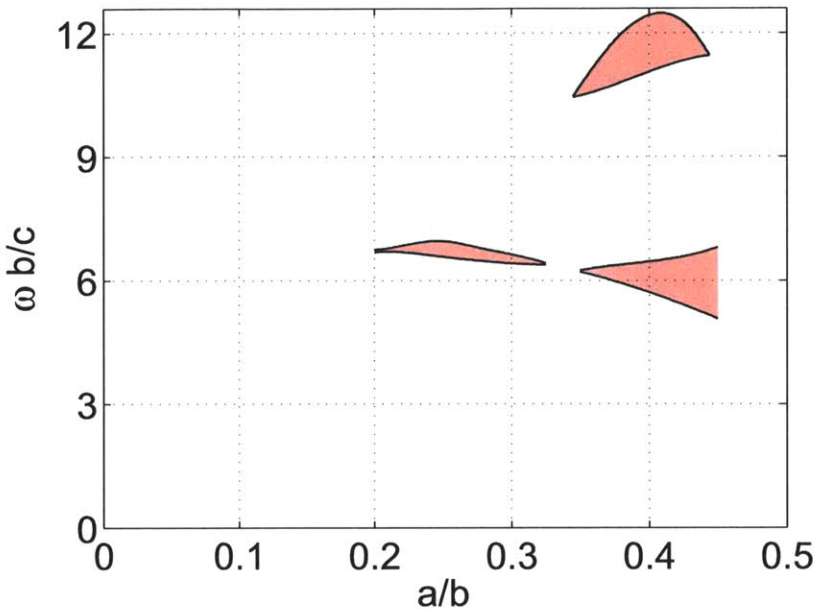

Figure 3-9: The global band gap plot for a triangular lattice, where a is the spacing and b is the diameter of the rod. The band gaps are marked by the red shaded region.

3.3.2 PBG Defect Modes

In order to transform the infinite PBG lattice into a waveguide, a certain number of rods must be removed to create a defect. This defect region acts as a waveguide where the direction of propagation is along the rod and the confinement in the transverse direction is provided by the PBG lattice. The number of rods in the transverse dimension does not need to be infinite, and it can be adjusted to provide the amount of attenuation desired. By removing rods, without any additional distortions to the lattice, the PBG defect created is hexagonal in shape. Therefore, the modes one expects to find in such a defect do not map directly to the eigenmodes of a circular waveguide. The eigenmodes of the hexagonal defect are related much more closely to the eigenmodes of a hexagonal waveguide. The eigenmodes of a hexagonal waveguide that have a six fold symmetry can be found by symmetrizing the solution of a

triangular waveguide [84, 94]. We can fully describe the electric and magnetic fields for a hexagonally symmetric TE_{mnl} mode by defining the axial magnetic field as

$$H_z = H_0 \left(\cos \frac{2l\pi}{\sqrt{3}a_e} y \cos \frac{2(m-n)\pi}{3a_e} x + \cos \frac{2m\pi}{\sqrt{3}a_e} y \cos \frac{2(n-l)\pi}{3a_e} x + \cos \frac{2n\pi}{\sqrt{3}a_e} y \cos \frac{2(l-m)\pi}{3a_e} x \right) \tag{3.18}$$

where H_0 is the amplitude, a_e is the edge length for on of the six waveguide edges and $l = -(m+n)$, m, n are integers. A comparison between hexagonal and PBG waveguide modes is shown in Figure 3-10. The edge length for the defect is $a_e = 2.4711$ mm. Figures 3-10 (a) and (b) are analytical calculations produced from the electric field determined from Equation (3.18). Figures 3-10 (c) and (d) are HFSS simulations with PML boundaries at the edge of the simulation. These simulations provide a diffractive quality factor (Q_{diff}) which is a measure of the modes confinement. The white circles are metallic rods with a perfect electrical conductor (PEC) surface and lattice constants of $a = 0.397$ mm and $a/b = 0.43$.

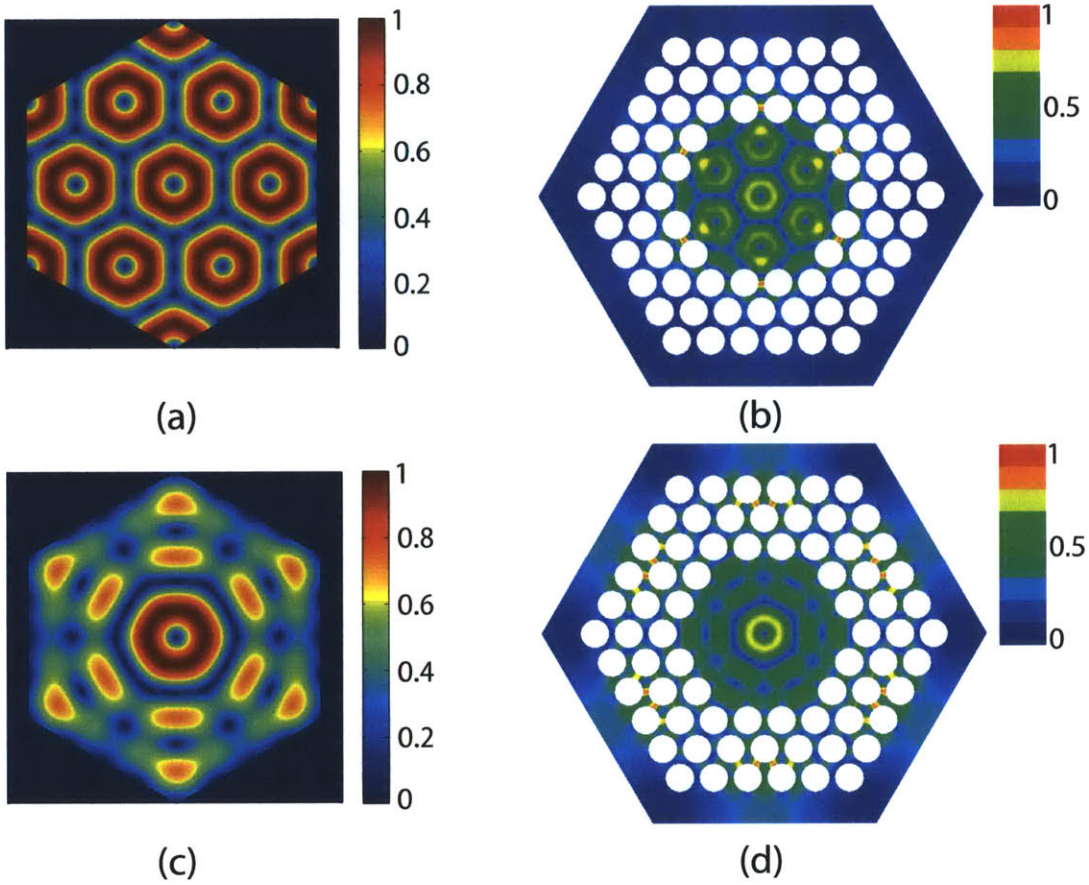

Figure 3-10: Comparison between electric field of hexagonal ((a) $TE_{0,3,-3}$ and (c) $TE_{1,2,-3}$) and PBG ((b) and (d)) waveguide modes. The cutoff frequency for each mode is (a) 242.6 GHz, (b) 242.7 GHz, (c) 214 GHz and (d) 212.1 GHz. The (b) operational PBG waveguide mode is well confined (Q_{diff}=1370) and (d) the lower order PBG waveguide mode is not confined (Q_{diff}=35).

3.4 Overmoded Corrugated Waveguide

Adapted from "Low-loss Transmission Lines for High-power Terahertz Radiation," by Emilio A. Nanni, Sudheer K. Jawla, Michael A. Shapiro, Paul P. Woskov and Richard J. Temkin, Journal of Infrared, Millimeter, and Terahertz Waves July 2012, Volume 33, Issue 7, pp 695-714. [113]

Applications of high-power Terahertz (THz) sources require low-loss transmission lines to minimize loss, prevent overheating and preserve the purity of the transmission mode. Concepts for THz transmission lines are reviewed with special emphasis on

overmoded, metallic, corrugated transmission lines. Using the fundamental HE_{11} mode, these transmission lines have been successfully implemented with very low-loss at high average power levels on plasma heating experiments and THz dynamic nuclear polarization (DNP) nuclear magnetic resonance (NMR) experiments. Loss in these lines occurs directly, due to ohmic loss in the fundamental mode, and indirectly, due to mode conversion into high order modes whose ohmic loss increases as the square of the mode index. An analytic expression is derived for ohmic loss in the modes of a corrugated, metallic waveguide, including loss on both the waveguide inner surfaces and grooves. Simulations of loss with the numerical code HFSS are in good agreement with the analytic expression. Experimental tests were conducted to determine the loss of the HE_{11} mode in a 19 mm diameter, helically-tapped, three meter long brass waveguide with a design frequency of 330 GHz. The measured loss at 250 GHz was 0.029 ± 0.009 dB/m using a vector network analyzer approach and 0.047 ± 0.01 dB/m using a radiometer. The experimental results are in reasonable agreement with theory. These values of loss, amounting to about 1% or less per meter, are acceptable for the DNP NMR application. Loss in a practical transmission line may be much higher than the loss calculated for the HE_{11} mode due to mode conversion to higher order modes caused by waveguide imperfections or miter bends.

3.4.1 Introduction

Transmission of high-power THz radiation has proved challenging due to the lossy nature of most fundamental mode transmission lines at these frequencies. Both material properties as well as machining tolerances contribute to the limitations imposed on fundamental rectangular or circular waveguide which is often the preferred approach at lower frequencies (GHz range). An overmoded approach to transmission lines has been demonstrated as an efficient and practical solution for high-power THz applications [174, 175, 54, 55, 31, 176, 56, 85]. The number of approaches to the design of overmoded transmission lines is quite extensive. Free space beaming techniques rely on propagation of a Gaussian beam via a series of mirrors and/or lenses [161, 11, 51]. This approach has low-loss but may have issues of safety and alignment stability. The

most common approach is the use of overmoded waveguides, in which the guide radius is much larger than the wavelength. Such waveguides can be corrugated metallic waveguides, dielectric waveguides or dielectric lined metallic waveguides. Free space beaming and corrugated waveguide are closely related, because the fundamental HE_{11} mode used in corrugated waveguides has a conversion efficiency of 98% [128] to the Gaussian beam which is used in quasi-optical transmission. Extensive reviews of the properties of overmoded waveguides have been published [24, 160] for sub-THz and megawatt power level transmission lines. High-power sub-THz transmission lines have been rigorously tested for use in electron cyclotron resonance heating (ECRH) of plasma experiments such as DIII-D [37], ASDEX [100] and LHD [87]. With further research being driven by ITER [61, 60, 65, 41], this remains an active area of interest. With overmoded transmission lines, ohmic losses play a greatly reduced role; however, special attention is required to sources of mode conversion caused by misalignments and offsets. Mode conversion to higher order modes results in increased losses, reflections and greatly reduced coupling of the THz radiation to the desired target or sample. Overmoded corrugated waveguides have been used in a variety of applications for the transmission of THz radiation for spectroscopic and plasma heating experiments. The HE_{11} mode is the most efficient waveguide propagation mode in an overmoded corrugated metallic waveguide with a diameter $\gg 2\lambda$, and having internal circumferential corrugations of rectangular shape with a depth of $\lambda/4$ at a pitch of at least 2.5 grooves per λ along the waveguide length [62, 58].

Low-loss broad band transmission lines are of great interest for low power THz spectroscopy and imaging [109, 64]. To overcome the extremely high losses of simple rectangular or circular waveguides, a variety of different methods are being investigated including dielectric coated metallic tubes [108], dielectric waveguides [106, 40], metallic wires [170], parallel metallic plates [107] and photonic crystals [77, 72]. Using dielectric lined metal waveguides, a loss of 1 dB/m has been achieved at frequencies above 1 THz [35]. Many of these techniques employ the use of overmoded waveguides and strive to find modes that can be efficiently coupled to free space THz beams. Currently, these techniques yield losses that are too high for continuous wave (CW)

systems with high average power and for systems with transmission lines on the order of multiple meters.

Electron cyclotron emission (ECE) diagnostics on plasma fusion experiments are now requiring the development of transmission lines in the THz band. ECE can be observed at either the fundamental or harmonics of the electron cyclotron frequency, $\omega = neB/m$, where m and e are the electron mass and charge, B is the magnetic field and $n = 1, 2, 3...$ is the harmonic number. With the magnetic field varying significantly within the fusion plasma, these diagnostics require broadband transmission lines for observation of ECE. Additionally, observation at harmonics of the electron cyclotron frequency provide the advantage of not receiving direct interference from the ECRH system that could be active. Frequency selective transmission line components have been developed for direct observation of ECE at ~140 GHz on the ECRH transmission line at TEXTOR [129]. Similar systems are under consideration for ASDEX [33] and ITER [78], which will require operation at higher frequencies. The ITER ECE diagnostic will operate independently of the ECRH transmission line and will observe emission from the plasma at frequencies as high as 0.35 THz [143, 13, 76].

In the THz range (>300 GHz), research into high-power (>10 W) transmission lines is being driven by dynamic nuclear polarization (DNP) nuclear magnetic resonance (NMR) experiments which require low-loss and a minimum of mode conversion [111]. For these experiments, the gyrotron and DNP magnets must be sufficiently far apart to avoid mutual field interference [174], requiring transmission of THz radiation over a distance of several meters [85]. It is not possible to use conventional single mode rectangular waveguides for transmission, since the ohmic loss in such guides would be prohibitive. Modern gyrotrons for DNP typically include internal mode converters [80, 15, 165, 141, 127] after the interaction region of the gyrotron to transform the THz radiation from the high order TE_{mn} mode in the cavity to a Gaussian beam. For gyrotrons without internal mode converters, alternate configurations can include quasi-optical mode converters external to the gyrotron [31] which produce Gaussian beams. The Gaussian beam then propagates through the dielectric output window of the gyrotron where it can be coupled either to a corrugated waveguide or

the quasi-optical setup. The linearly polarized Gaussian beam excites the linearly polarized HE_{11} mode in the waveguide [96]. Then it is convenient to transmit the HE_{11} mode to the sample under study with straight sections, miter bends and tapers of corrugated metallic waveguide.

As NMR experiments move to higher field, the frequency that must be transmitted extends further into the THz band. Due to the scaling of the groove size with wavelength, this requires smaller corrugations. Machining individual corrugations becomes increasingly difficult and expensive as the corrugation dimensions shrink with frequency. The machining process necessitates the assembly of many short sections of waveguide. To avoid these machining considerations, creating corrugations with stacked rings has been attempted [54]. Alternatively, tapping a single helical groove is more cost effective for making long sections of corrugated waveguide.

In this paper, we review the design of low-loss corrugated waveguides in Section 3.4.2; Section 3.4.3 derives the ohmic losses in corrugated waveguides; Section 3.4.4 describes simulations for the calculation of ohmic losses with non-ideal groove shapes; Section 3.4.5 describes the fabrication of helically-tapped corrugated waveguide; Section 3.4.6 presents ohmic loss measurements performed on corrugated waveguide; Section 3.4.7 is the summary and conclusions.

3.4.2 High-Power Low-Loss Corrugated Metallic THz Transmission Lines

Figure 3-11 shows a schematic of a corrugated metallic waveguide with rectangular grooves. The radius a is much larger than a wavelength λ. The corrugations are optimized when the groove depth $d \approx \lambda/4$, period $p \approx \lambda/3$ and groove width $w < p/2$. The corrugation tooth thickness is denoted by $t = p - w$. The radial coordinate r extends from the center line of the waveguide and the groove coordinate ξ originates from the base of the groove well. The axial coordinate z is parallel to the centerline.

The modes in a corrugated waveguide have been developed [58], with the lowest order mode being the HE_{11} hybrid mode. The transverse electric field profile near

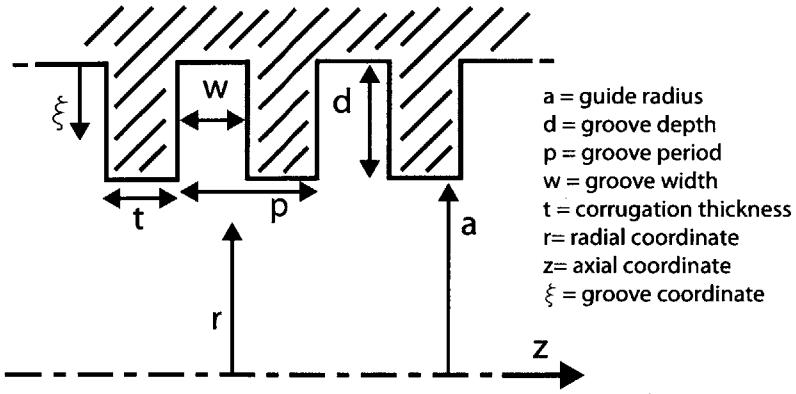

Figure 3-11: Illustration of a corrugated metallic waveguide which is optimized with a radius $a \gg \lambda$, groove depth $d \approx \lambda/4$, period $p \approx \lambda/3$ and groove width $w < p/2$.

the optimized groove depth $d \approx \lambda/4$ is given by:

$$E^{mn}(r,\phi) = (\chi_{mn}/a)\, J_m(\chi_{mn} r/a)\cos(m\phi) \tag{3.19}$$

where (r,ϕ) are the radial and angular coordinates and χ_{mn} is the n^{th} zero of the m^{th} order Bessel function J_m. For the HE_{11} mode $m = 0$, $n = 1$ and $\chi_{01} \approx 2.405$. This expression is valid when the corrugation depth is approximately one quarter wavelength and the radius a is much larger than the wavelength. For perfect excitation of the HE_{11} mode in the transmission line, the overall transmission line loss is expected to be dominated by losses at right angle bends, called miter bends, and by tilts and offsets in the fabrication and alignment of the waveguide components. The loss in a miter bend originates from diffraction effects and ohmic losses, with the fractional power loss from diffraction

$$P_{\text{Diffraction}} = 0.195\left(\frac{\lambda}{a\sin\theta}\right)^{3/2}, \tag{3.20}$$

ohmic losses in H-plane miter bends

$$P_{\text{Ohmic}} = \frac{4R_s\cos\alpha}{Z_0}, \tag{3.21}$$

and E-plane miter bends

$$P_{\text{Ohmic}} = \frac{4R_s}{Z_0\cos\alpha} \tag{3.22}$$

where R_s is the surface resistivity, Z_0 is the impedance of free space, θ is the bend angle and α is the angle of incidence [160, 59]. Fabrication of overmoded corrugated waveguide components requires careful consideration of machining tolerances at the waveguide connections. Tilts and axial offsets can lead to the coupling of the input THz beam to higher order modes of the waveguide, which gives rise to mode conversion losses, resulting in an increase of ohmic losses or decreased coupling to the sample of interest. The fractional power loss due to mode conversion [128, 160] for an axial offset, Δa, is

$$P_{\text{Offset}} = 2.7\left(\frac{\Delta a}{a}\right)^2, \tag{3.23}$$

and for a tilt, $\Delta\theta$, is

$$P_{\text{Tilt}} = 4.2\left(\frac{a \cdot \Delta\theta}{\lambda_0}\right)^2. \tag{3.24}$$

While these are significant sources of loss, in practice the loss may be dominated by the imperfections and poor coupling of the THz beam entering the transmission line, resulting in the excitation of higher order modes. This is a result of the non-Gaussian output beam either from the source or upon insertion of an unmatched output beam (due to tilts and offsets) into the waveguide, leading to high losses in the transmission line [41].

Figure 3-12(a) shows the transmission line used in a 250 GHz DNP NMR system [174]. The main transmission line is a 22 mm diameter (a = 11 mm) metallic corrugated waveguide made of aluminum. The individually machined corrugations are optimized with $d \approx \lambda/4$ (0.3 mm), $w = 0.3$ mm and $p = 0.4$ mm. Two 0.254 m waveguide sections, fifteen 0.124 m waveguide sections and one 0.064 m directional coupler block were assembled with outer diameter clamps to achieve the desired waveguide length. The difference between the measured and theoretical loss is discussed in detail in Section 3.4.6. The estimated ohmic loss in the overmoded waveguide of Figure 3-12(a) is less than 10^{-3}m^{-1}. The loss for the 22 mm diameter waveguide portion of the transmission line of Figure 3-12(a) was measured to be less than 1% per meter

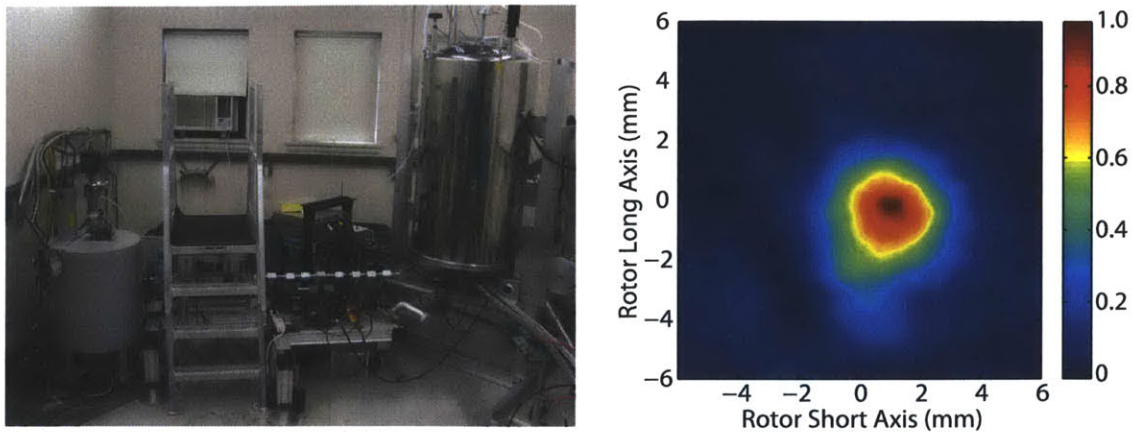

Figure 3-12: (a) The 250 GHz transmission line connecting the gyrotron output (left) to the NMR spectrometer (right). (b) The measured Gaussian beam emitted from the end of an 8 mm corrugated waveguide and radiated to a distance of 12 mm from the waveguide end.

[174].

A directional coupler is used for measuring forward and reverse power on the transmission line shown in Figure 3-12(a). A smaller diameter waveguide is necessary for the probe inside the DNP NMR magnet due to limited space. The transition to smaller diameter can be performed with waveguide tapers or mirrors. Bends in the transmission line may be accomplished using a miter bend in the waveguide or using a mirror box. The transmission line of Figure 3-12(a) has only one right angle bend, and it is implemented using two mirrors. The mirrors also match the beam from the 22 mm waveguide into the 8 mm waveguide in the NMR probe. Due to losses induced by imperfections in the Gaussian beam quality of the gyrotron and by errors in the alignment of the components of the transmission line, the transmission efficiency from the gyrotron output window to the sample is typically in the 50-80% range [174, 112] measured at the 8 mm corrugated waveguide output that radiates onto the sample. Figure 3-12(b) is an image of the beam radiated to the sample distance of 12 mm from the end of the corrugated waveguide recorded using a Spiricon Pyrocam III pyroelectric detector.

The transmission line shown in Figure 3-12 is only one example of successful transmission lines used in DNP NMR research. Recently, a 13 m transmission line

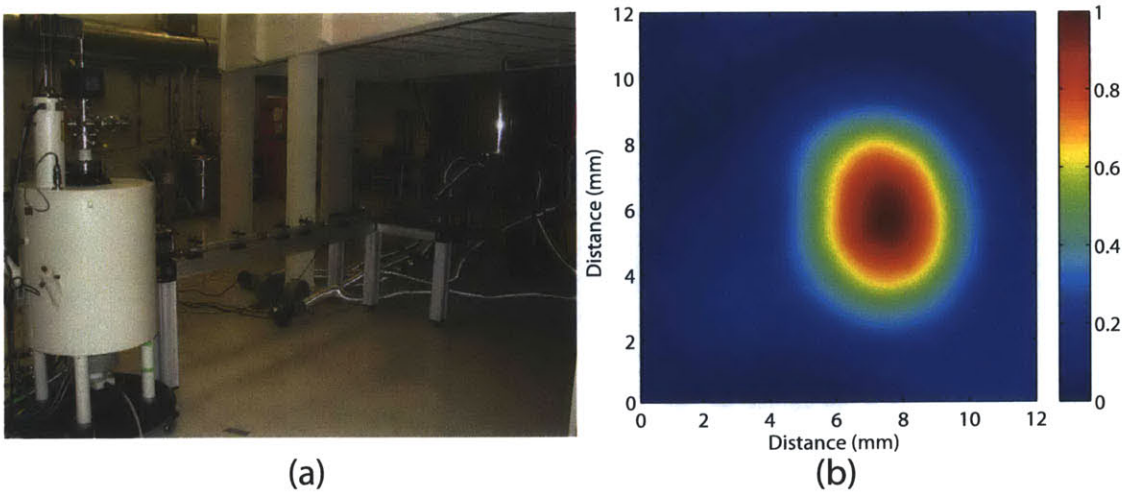

Figure 3-13: (a) The 460 GHz transmission line connecting the gyrotron output (left) to the NMR spectrometer (right). (b) The measured Gaussian beam emitted from the end of a 19 mm ID corrugated waveguide and radiated to a distance of 100 mm from the waveguide end.

using corrugated waveguides and switches has been successfully implemented on a 260 GHz gyrotron system for DNP NMR [55, 31]. A fully optical (mirror) transmission line using a mirror relay line has also recently been implemented for a DNP NMR spectrometer system [126]. Another overmoded smooth-walled waveguide has been successfully implemented at 395 GHz [105] with 55% transmission on a 28 mm diameter waveguide to the base of the DNP magnet and 7% of the output power delivered to the sample. A recently implemented 460 GHz transmission line for DNP applications [175, 155, 154] has been tested with 40% transmission of power to the sample. The 460 GHz transmission line, shown in Figure 3-13(a), is constructed using the same techniques as the 250 GHz transmission line, shown in Figure 3-12(a), and consists of a 6 m long, 19 mm diameter corrugated waveguide, which is tapered to a diameter of 4.6 mm once it reaches the probe. The field pattern shown in Figure 3(b) was measured using a Spiricon Pyrocam III pyroelectric detector positioned 100 mm from the aperture of the waveguide at the center point between the gyrotron magnet and NMR spectrometer. Future research will concentrate on making these transmission lines simpler and more efficient.

3.4.3 Theory of Ohmic Losses in Corrugated Waveguides

Selection of waveguide radius and groove dimensions has severe effects on the ohmic loss in corrugated waveguides, requiring careful understanding of the source of attenuation in these waveguides. Here we derive an analytical formula for the attenuation coefficient of a corrugated metallic waveguide with ideal rectangular grooves. The result was obtained by integrating the field equations over the groove surfaces to obtain the ohmic loss. The electric and magnetic fields of the HE mode at $r = a$ are [58]

$$\vec{E}\left(r=a,\phi\right)=\vec{e}_{01}=-\left(\frac{Z_0}{\pi}\right)^{1/2}\frac{\chi_m}{ka^2}\left[\hat{r}\frac{1}{Z}-j\hat{z}\right]\sin\phi \tag{3.25}$$

$$\vec{H}\left(r=a,\phi\right)=\vec{h}_{01}=-\left(\frac{1}{Z_0\pi}\right)^{1/2}\frac{\chi_m}{ka^2}\left[\hat{\phi}\frac{\sin\phi}{Z}-j\cos\phi\hat{z}\right] \tag{3.26}$$

where the unit vectors for $r/\phi/z$ are $\hat{r}/\hat{\phi}/\hat{z}$, Z_0 is the impedance of free space, $Z = \frac{w}{p}\tan kd$ is the approximate impedance seen at the corrugated surface, $k = 2\pi/\lambda$ is the wavenumber, $\chi_m = \chi_{01}\left(1 - 1/2kaZ\right)$ [62] and $ka \gg 1$. To calculate the attenuation constant for the waveguide we integrate the ohmic losses over the groove shape of one period [46, 47]

$$\alpha=\frac{R_s}{2}\frac{1}{p}\iint\left(|H_\phi|^2+|H_z|^2\right)dsd\phi \tag{3.27}$$

where ds denotes the surface of the groove, $R_s = \sqrt{\pi\mu\rho f}$ is the surface resistivity, μ is the permeability, f is the frequency, ρ is the bulk resistivity and α has units of Np/m. In the traditional approach, we can rewrite Equation (3.27) in terms of the fields from Equation (3.26) and integrate over a flat surface which is represented by the approximate impedance [58]

$$\alpha=\frac{R_s}{2}\frac{1}{p}\int_0^{2\pi}\int_0^{p}\left(|h_\phi|^2+|h_z|^2\right)adzd\phi. \tag{3.28}$$

The result is given by [58]

$$\alpha=\frac{R_s}{2Z_0}\frac{{\chi_m}^2}{k^2a^3}\left(\frac{1}{(w/p)^2\tan^2kd}+1\right). \tag{3.29}$$

To improve this calculation, the integral in Equation (3.27) should be performed over the entire surface of the groove, where Equation (3.26) is not strictly valid. In [46] this is remedied by using a spatial harmonics representation for the fields inside the waveguide and an infinite set of resonant modes inside the corrugations. Alternatively, we allow for H_ϕ to be at a maximum and $E_z = 0$ at the base of the groove ($\xi = 0$) for $d \approx \lambda/4$. To satisfy boundary conditions we take $H_\phi = h_\phi \frac{\cos k\xi}{\cos kd}$ for $0 \leq \xi \leq d$. For the z component it is sufficient to calculate the loss on the surface $r = a$ where $H_z = h_z$, which is the same approach used in the impedance approximation method. This leads to the integration

$$\alpha = \frac{R_s}{2}\frac{1}{p}\left[\iint \left| h_\phi \frac{\cos k\xi}{\cos kd}\right|^2 ds d\phi + ap\int_0^{2\pi} |h_z|^2 d\phi\right]. \tag{3.30}$$

If we separate Equation (3.30) into the different surfaces of the rectangular groove

$$\begin{aligned}\alpha = \tfrac{R_s}{2}\tfrac{1}{p} \quad \Bigg[& 2\int_0^{2\pi}\int_0^{d} \left|h_\phi \tfrac{\cos k\xi}{\cos kd}\right|^2 a d\xi d\phi + \int_0^{2\pi}\int_0^{w} \left|h_\phi \tfrac{1}{\cos kd}\right|^2 a dz d\phi \\ & + \int_0^{2\pi}\int_0^{t} |h_\phi|^2 a dz d\phi + ap\int_0^{2\pi} |h_z|^2 d\phi\Bigg]\end{aligned} \tag{3.31}$$

and perform the integrations, the attenuation is given by

$$\alpha = \frac{R_s}{2Z_0}\frac{{\chi_m}^2}{k^2a^3}\left[\frac{1}{Z^2p}\left(2\frac{1}{\cos^2 kd}\left(\frac{d}{2} + \frac{1}{2k}\sin kd\cos kd\right) + \frac{w}{\cos^2 kd} + t\right) + 1\right], \tag{3.32}$$

which can be further simplified in terms of the expression given by

$$\alpha = \frac{R_s}{2Z_0}\frac{{\chi_m}^2}{k^2a^3}\left(\frac{1 - \frac{t}{p}\sin^2(kd) + \frac{d}{p} + \frac{1}{kp}\sin(kd)\cos(kd)}{(1 - t/p\,)^2\sin^2(kd)} + 1\right). \tag{3.33}$$

Equation (3.33) shows that the loss increases as the square of the mode index χ_m. Thus, mode conversion into high order modes, with large χ_m, can contribute to greatly enhanced loss on a transmission line. A comparison between (3.29) (dashed black line) and (3.33) (solid black line) is shown in Figure 3-14 for the HE_{11} mode with rectangular corrugations, $a = 9.5$ mm, $d = 0.227$ mm, $p = 0.3175$ mm, $t/p = 0.5$ and ideal brass conductivity. The figure shows attenuation in dB/m which can be

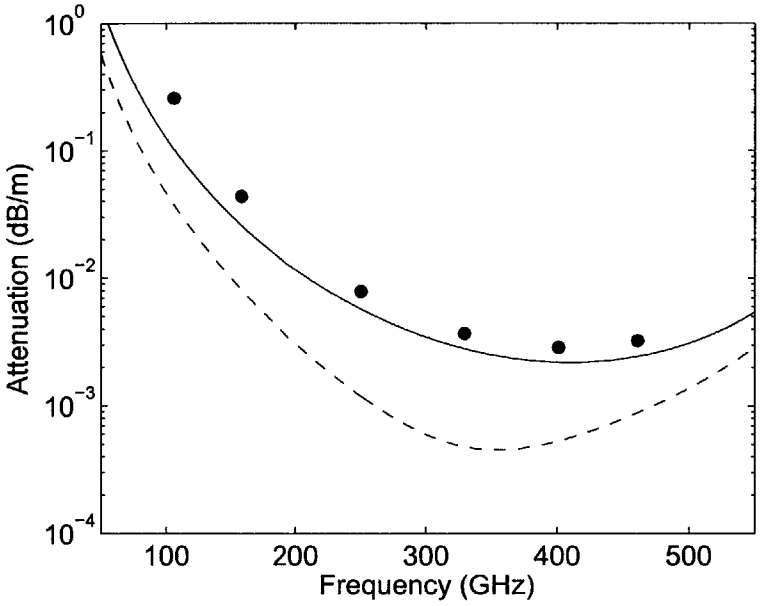

Figure 3-14: Ohmic losses in overmoded circular corrugated waveguide for rectangular brass (conductivity 1.56×10^7 mhos/m) corrugations as predicted by our theory (solid line) and the impedance approximation method (dashed line). Numerical simulations with HFSS are shown with blue dots.

obtained from the attenuation in Np/m multiplied by 8.686. As d approaches $\lambda/4$, a significant difference develops between Equation (3.29) (dashed line) and Equation (3.33) (solid line) because the contribution from h_ϕ goes to zero in Equation (3.29) and losses internal to the corrugations are not accounted for as in Equation (3.33). It should be noted that for the special case of $d = \lambda/4$, the expression in Equation (3.33) is equivalent to the expression for loss given by Dragone [62]

$$\alpha = \frac{R_s}{2Z_o}\frac{{\chi_{m}}^2}{k^2a^3}\left(\frac{1-\frac{t}{p}+\frac{\lambda}{4p}}{(1-t/p)^2}+\alpha_2\right) \tag{3.34}$$

where $\alpha_2 \approx 1$ for groove shapes with $t/p > 0.1$.

3.4.4 Simulations in HFSS

In order to verify the analytical calculations predicting extremely low-loss propagation of the HE_{11} mode in corrugated waveguides, we have employed HFSS. Measurement

of the propagation loss for the HE_{11} mode at the optimum wavelength is dominated by experimental error from the presence of higher order modes or the experimental setup. Additionally, the fabrication of the corrugated waveguide can lead to non-ideal groove geometries that are trapezoidal, triangular or sinusoidal, instead of rectangular which are not accounted for in Equation (3.33). Proper simulation of these highly overmoded waveguides has proved difficult due to the large physical size and very small power loss involved. However, the idealized physical geometry of a linear corrugated waveguide is highly symmetric. In the direction perpendicular to propagation, the HE_{11} mode has fourfold symmetry, and in the direction of propagation, the waveguide is symmetric over the geometry of one groove. Using HFSS with the proper symmetry conditions and applying a phase advance along the direction of propagation, the HE_{11} mode can be analyzed for a variety of groove shapes and frequencies. The magnitude of the electric field in the transverse plane of the corrugated waveguide and at a variety of frequencies is shown in Figure 3-15. As seen in Figure 3-15, the profile of the HE_{11} mode is significantly distorted when the frequency of operation is not well matched to the corrugation depth, in close agreement with [46]. The distortion in the field profile is due to the frequency dependent impedance of the corrugation leading to increased ohmic losses at lower frequencies. At the $\lambda/4$ condition, the HE_{11} mode is linearly polarized with the direction of the electric field labeled in Figure 3-15(d). As the frequency is lowered, the HE_{11} mode becomes distorted and is no longer linearly polarized, which would lead to mode conversion if coupling into the transmission line with a Gaussian beam, effectively limiting the bandwidth of the transmission line. The ohmic losses determined by the HFSS computer modeling for the rectangular groove shape (blue dots) are shown in Figure 3-14 and are consistent with our model (solid line).

The machining process for the corrugations can lead to deviations from the ideal rectangular groove shape. These deformations, in the form of trapezoidal, sinusoidal and triangular groove shapes, were found to increase ohmic losses for the corrugated waveguide. Similar deformations also affect the loss on grooved surfaces for diffrac-

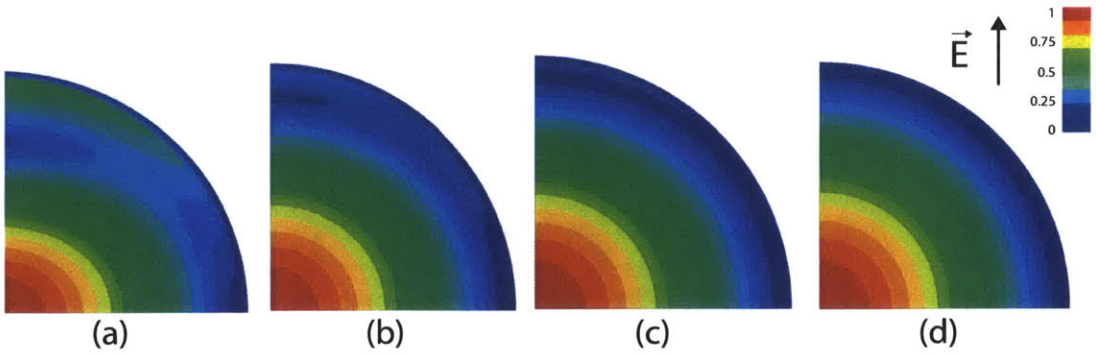

Figure 3-15: The magnitude of the electric field from HFSS simulations for one period of a rectangular corrugation with $a = 9.5$ mm, $d = 0.227$ mm, $p = 0.3175$ mm, $t/p = 0.5$ and ideal brass conductivity at (a) 105 GHz, (b) 158 GHz, (c) 250 GHz and (d) 330 GHz.

tion gratings and polarizers [138]. Numerical simulations were performed for the groove shapes shown in Figure 3-16(a). The increase in ohmic losses for non-ideal groove shapes results from two effects: alteration of the fields on the surface of the groove and decrease of the effective groove depth relative to the actual depth causing an adjustment to the impedance approximation. Expanding the groove shape in a Fourier series and comparing the weight of the first Fourier term accurately predicts which groove shapes result in higher ohmic losses. Adjusting the groove depth can be used to compensate for the transmission losses for non-rectangular shapes. The effective depth of the grooves (shown in Figure 3-16(a)) is listed in Table 3.2 for various corrugation shapes.

Table 3.2: Corrugation Shape Depth Correction

Shape	$d_{\text{effective}}$ (normalized)
Rectangular	1.00
Trapezoidal	0.733
Triangular	0.565
Sinusoidal	0.785

The ohmic losses calculated from the analytical theory and HFSS are shown in Figure 3-16(b), with the rectangular (blue dots), trapezoidal (red triangles), sinusoidal (green diamonds) and triangular (black squares) groove shapes. The theoretical attenuation calculated with HFSS of the rectangular groove shapes is in very good

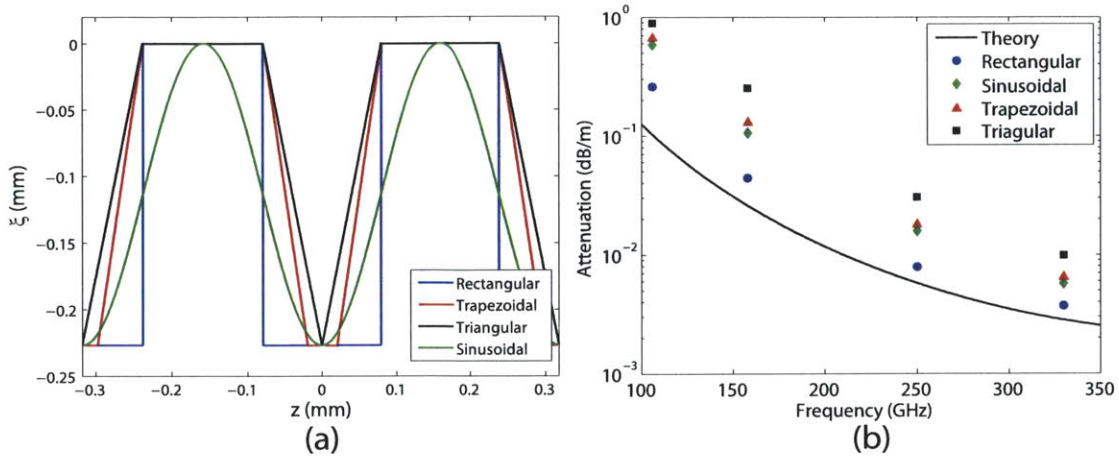

Figure 3-16: (a) Groove shapes simulated in HFSS with $d = 0.227$ mm and $p = 0.3175$ mm given in the groove coordinate system (ξ, z) used in Fig. 1. (b) Ohmic losses in corrugated waveguide simulated in HFSS compared to the impedance approximation method.

agreement with the analytical model (black line). Variations to the groove shape result in increased ohmic losses for the same frequency. As predicted in Table 3.2 and shown in Figure 3-16(b), the trapezoidal and sinusoidal grooves show similar levels of ohmic losses, with the triangular shape resulting in the largest increase of attenuation.

3.4.5 Fabrication of Helically-Tapped Transmission Line Components

As the frequency of the waves on the transmission line moves further into the THz regime, fabrication of individual corrugations becomes more difficult and expensive, requiring special tools and dedicated setups [61], but could be performed with relative ease using a helical tap. However, the groove shape in a helically-tapped waveguide does not produce the ideal rectangular groove shape and could result in increased ohmic losses. The simulations discussed in the previous section indicate that there are acceptable non-rectangular groove shapes which a helical tap is capable of tapping. To test this approach, a 4.5 m long transmission line optimized for operation at 330 GHz was constructed from fifteen 19 mm ID 300 mm long brass tubing sections tapped

with an 80 grooves per inch (3.15/mm) tap. Brass was chosen as the waveguide material due to its hardness for fine machining and good conductivity. The tap thread before and after machining and the resulting corrugations were examined under magnification as shown in Figure 3-17(a). The corrugations mirror the shape of the cutting thread looking approximately trapezoidal and with the cut groove narrower than the wall between. The depth of the cutting thread wore down about 10% over the course of fabrication. Images of the grooves indicate $d = 0.227$ mm, $p = 0.318$ mm and $t = p/2$. The trapezoidal groove shape in Figure 3-17(a) corresponds to the trapezoidal groove shown in Figure 3-16(a) and simulated in Figure 3-16(b). Polarization rotation, which is a concern for helically-grooved waveguide, becomes less of an issue at higher frequencies because of the inverse frequency squared scaling. The rotation angle in radians can be estimated by

$$\psi \cong \left(\frac{2.405}{ka}\right)^3 \frac{Lp}{\lambda a} \text{ (radians)} \tag{3.35}$$

where L is the waveguide length[58]. For our waveguide parameters, the rotation is estimated as 0.1°/m at 330 GHz, which is not sufficient to cause a problem for DNP experiments.

The theoretical prediction for offset and tilt losses calculated using Equation (3.23) and Equation (3.23) for a single joint of our transmission line is shown in Figure 3-17(b). Errors in successive joints will increase the offset and tilt losses. Even with relatively large offsets (black line) a very modest power loss would be observed; however, the setup is extremely sensitive to tilts (dashed and dashed/dotted lines). To mitigate these effects, collars are placed at each waveguide joint which provide concentricity and angular alignment.

3.4.6 Straight Waveguide Measurements

The predicted loss in a straight section of waveguide is extremely low, limiting the possible experimental methods for measuring the loss. To aid in this process, mea-

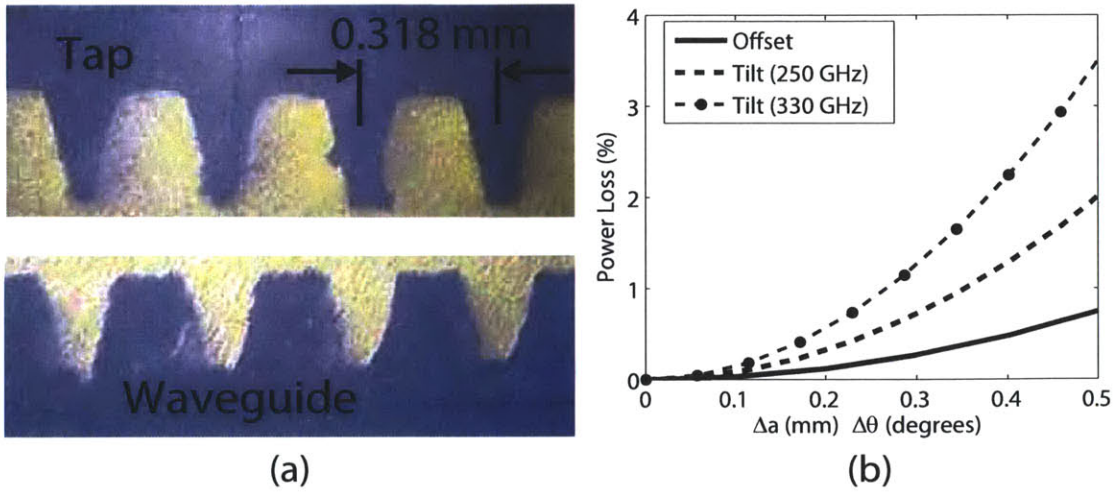

Figure 3-17: (a) Photos of the 330 GHz tap and waveguide cross sections. Chips from cutting are present on the second tap tooth from left. (b) Theoretical prediction of power loss due to axial offset (black line) and tilts (dashed and dashed/dotted lines) at waveguide junctions for the 19 mm diameter 330 GHz corrugated waveguide.

surements were taken using a vector network analyzer (VNA) around 250 GHz due to the availability in our laboratory of a high quality fundamental rectangular waveguide to 19 mm ID corrugated waveguide transition. The HE_{11} mode was obtained from the VNA WR-3 fundamental rectangular waveguide by a series of waveguide components consisting of a rectangular to circular transition, a smooth to corrugated waveguide transition, a corrugated conical horn, and an acrylic up-taper to the 19 mm ID corrugated waveguide. In a previous measurement [89], the mode content produced by this setup was determined with great accuracy. The VNA (Agilent E8363B with millimeter-wave VNA extender V03VNA2-T/R) setup for transmission line losses and radiated field measurements is shown in Figure 3-18(a) with the VNA extender head and up-tapers in the lower left of the photo. At the other end of the waveguide there is an automated beam profile scanner. A schematic of this setup is shown in Figure 3-18(b) with the scanner replaced by a removable short or load. A 2 m section of straight waveguide was used to bring the HE_{11} mode from the launcher to the scanner setup. The magnitude and phase of the radiated beam were recorded for spatial scans at 70, 100 and 130 mm distances from the waveguide aperture. Two methods, a phase retrieval code [88] and direct magnitude/phase measurements, showed that

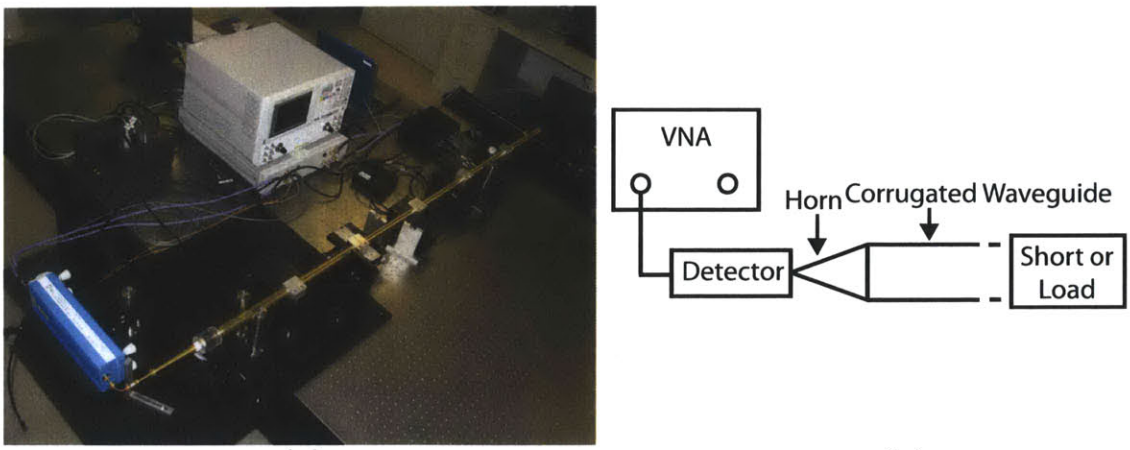

Figure 3-18: (a) VNA setup for 330 GHz waveguide transmission line loss measurements. (b) Schematic of the setup for transmission line losses with removable short or load.

an HE_{11} mode purity of 94.2±0.3% was generated at 250 GHz. The detailed mode content of the microwave fields in the corrugated waveguide is listed in Table 3.3 with the decomposition performed using a linearly polarized basis set [96] where the LP_{01} mode is the linearly polarized HE_{11} mode. The large HE_{11} mode content allows the use of this setup to perform transmission loss measurements to test the quality of the transmission line and to make a comparison to the theoretical and numerical calculations from Section 3.4.3 and Section 3.4.4.

Table 3.3: Modes at the Aperture of the Corrugated Waveguide

	Power				Phase (radians)		
LP_{mn}	n = 1	n = 2	n = 3	LP_{mn}	n = 1	n = 2	n = 3
m = 0	0.942	0.040	0.003	m = 0	-1.69	-1.77	0.06
m = 1	0.007	<0.001	<0.001	m = 1	2.11	-	-
m = 2	0.004	<0.001	<0.001	m = 2	1.42	-	-

Validation of the theoretical calculation for the loss was accomplished with two methods to measure transmission losses. In the first method, a heterodyne radiometer and liquid nitrogen cooled blackbody (Eccosorb) were used to measure insertion losses relative to thermal noise over the band 248±4 GHz using techniques previously described [174]. The attenuation in the waveguide was determined by comparing the

relative intensity of the receiver noise measurement with the addition of waveguide sections, up to a total of 3 m. In the second method, a VNA was used to perform calibrated S_{11} measurements to determine the ohmic loss in the system [95]. The S_{11} measurements entailed short and matched load (radiation into free space) measurements for every added section of the overmoded waveguide. Reflection measurements are preferable to transmission for measuring very small losses over a distance of several meters because the measurement setup for the detector can remain immobile while sections of waveguide are added. This removes a significant source of error introduced by flexing cables and making connections. Several challenges present themselves when performing S_{11} measurements in the overmoded waveguide including Fabry-Pérot resonances caused by small mismatches and mode beating. Fabry-Pérot effects were removed by taking measurements over the 240 - 260 GHz range and filtering the oscillations on the measured signal. The treatment for mode beating, if the HE_{11} mode is dominant, can be generalized to express the relationship between the detected power and the relative phase of various higher order modes with respect to the HE_{11} mode. With 94.2% of the power in the HE_{11} mode, the beating can be described by

$$P_D = \left| A_{01} e^{-\alpha_{01} z} + A_{\mathrm{HOM}} e^{i(\phi_{\mathrm{HOM}})} e^{-\alpha_{\mathrm{HOM}} z} \right|^2 \tag{3.36}$$

where P_D is the detected power, A_{mn} is the amplitude given in Table 2, α_{mn} is the attenuation constant and HOM designates the higher order mode index that is being considered. The relative phase, $\phi_{\mathrm{HOM}} = 2L\left(k_{01z} - k_{\mathrm{HOM}z}\right)$, between the modes is determined by the phase of the reconstructed mode content, shown in Table 3.3, back propagated to the measurement plane for the straight waveguide measurements. The measured and calculated P_D for the system is shown in Figure 3-19. The calculated P_D is based on the power and phase in the 5 lowest higher order modes, with the attenuation in the waveguide as the only free variable, and is determined from the best fit between the measured and calculated transmitted power.

The transmission as a function of length for the straight waveguide measurements,

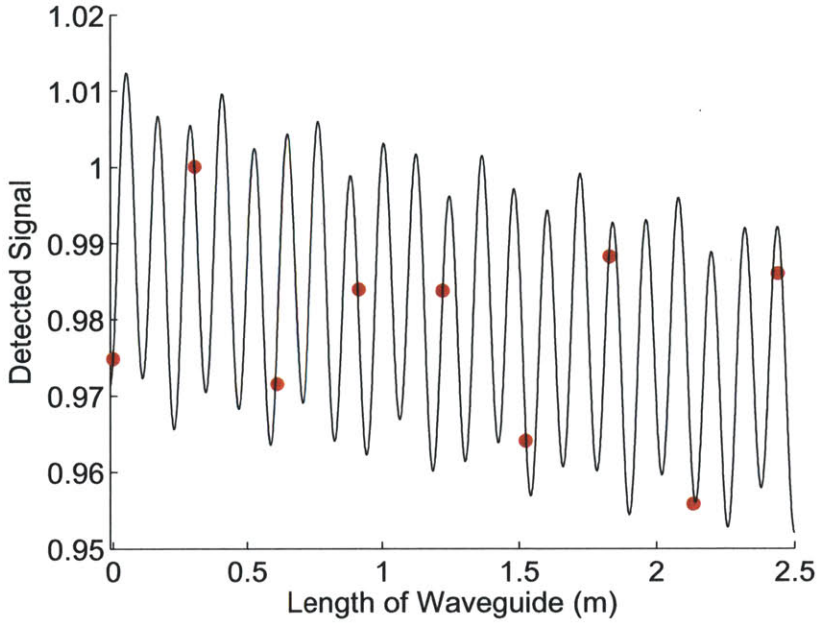

Figure 3-19: Predicted (black line) and measured (red dot) signal from the VNA as a function of waveguide length.

which is computed from the S_{11} measurements [176, 95], is shown in Figure 3-20(a). Measurements in Figure 3-20(a) were independently repeated 5 times, with the mean of the measurements shown with black dots and one standard deviation is marked with error bars for each added section of waveguide. The attenuation, α, is determined by a best fit for $e^{-\alpha z}$. The measured insertion losses, plotted in Figure 3-20(b), are 0.047 ± 0.01 and 0.029 ± 0.009 dB/m for the radiometer and VNA, respectively. The measurements are in reasonable agreement with one another and with the theoretical estimate. The difference between the VNA measurement and HFSS model can be explained by adjusting the bulk resistivity by a factor of 2 (or $\sqrt{2}$ for the surface resistance). The resulting losses of $\sim$3% for the complete 4.5 m straight waveguide length are acceptable for the intended application. Consequently, using a tap to save fabrication costs of corrugated waveguide does not cause the quality of the waveguide to suffer, with deeper groove depth compensating for the non-ideal rectangular shape.

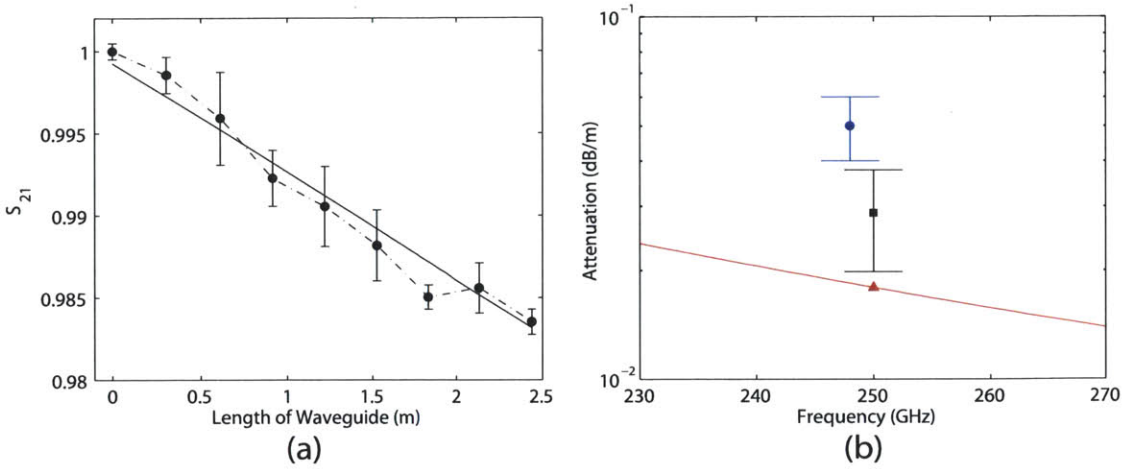

Figure 3-20: (a) Measured transmission through 19 mm ID corrugated waveguide at 250 GHz as a function of waveguide length. (b) HE_{11} waveguide transmission loss measurements (blue dot: radiometer, black square: vector network analyzer) and HFSS model (red triangle and line: trapezoidal groove) for ideal brass conductivity and $a = 9.5$ mm.

3.4.7 Discussion and Conclusions

The transmission of THz radiation over significant distances has proven to be a challenge for systems requiring high efficiencies. Additional problems have surfaced when considering high-power THz radiation where ohmic losses or mode conversion can lead to physical damage to the transmission line or load. Overmoded corrugated waveguides have proved to be a reliable technique with regards to their low-loss nature and ability to handle high-powers. Corrugated waveguides routinely achieve losses below 0.01 dB/m for the lowest order HE_{11} mode. However, their overmoded nature requires precise excitation and very accurate physical alignment of the transmission line to avoid severe mode conversion which leads to increased ohmic losses and a poorer beam quality output. Additionally, corrugated waveguides do have a large, but limited bandwidth due to the frequency-dependent nature of the corrugations. Frequencies far below the optimized condition of $d \approx \lambda/4$ experience increased ohmic losses and the HE_{11} mode is no longer linearly polarized. Bragg reflections occur for higher frequencies when $d \approx n\lambda/2$, where $n = 1, 2, 3...$ is an integer. At frequencies well above 1 THz overmoded corrugated waveguides remain an unproven technology. However, with a minimum reported loss of 1 dB/m alternate forms of transmission

lines above 1 THz, have not achieved comparable low-losses. With improved machining and the availability of free space Gaussian beams, overmoded corrugated waveguides could extend into this regime. Corrugated waveguides that require individual machining of grooves are costly and complex when frequencies approach the THz range. However, helically-tapped waveguides are much simpler to fabricate and have corrugations that are very effective in low-loss transmission. Typical designs for overmoded corrugated waveguides operate with similar corrugation dimensions with $d \approx \lambda/4$, $p \approx \lambda/3$ and $t \approx p/2$. We can write Equation (3.28) as

$$\alpha = \frac{\lambda^{1.5}}{a^3} C_{\mathrm{OM}} \tag{3.37}$$

where we took $R_S \propto 1/\sqrt{\lambda}$ and C_{OM} is a constant, shown in Table 3.4 for a variety of metals, scaled from the measurements on the brass corrugated waveguide presented in this paper.

Table 3.4: Normalized Attenuation Coefficient for Metallic Corrugated Waveguide

	C_{OM} (NP $\cdot$ m$^{0.5}$)	C_{OM} (dB $\cdot$ m$^{0.5}$)
Brass	3.94×10^{-5}	3.42×10^{-4}
Al	3.11×10^{-5}	2.70×10^{-4}
Copper	2.03×10^{-5}	1.76×10^{-4}

From this expression it is evident that these waveguides become more favorable at higher frequencies as the wavelength gets shorter. With their behavior being extremely dependent on the waveguide radius, it is also possible to drastically improve performance for long transmission lines with larger diameter waveguide. Additionally, this expression provides a realistic expectation for the HE_{11} mode loss on a transmission line. We should also note that for both the TE_{10} mode in rectangular waveguide and TE_{11} mode in circular waveguide the attenuation has a starkly different dependence, $\alpha \propto \lambda^{-0.5}/a$, where a is the long dimension in rectangular waveguide and the radius in circular waveguide. As frequencies push into the THz regime, these modes require prohibitively large cross sections for many applications to maintain a reasonable attenuation coefficient. An alternative is to use the TE_{01} mode in smooth-walled

circular waveguides which has a similar dependence to the HE_{11} mode, but this mode is difficult to couple to free space Gaussian beams.

Transmission of THz radiation is a growing area of research due to the increasing availability of THz sources capable of producing a megawatt of average power in the near-THz and 10-100 W in the THz band. The ohmic losses in corrugated waveguides are well understood, with good agreement between theory, simulation and experiments. High quality Gaussian beams that couple efficiently to the HE_{11} mode of the corrugated waveguide are a requirement for low-loss operation. The higher order mode content of the transmission line can produce increased ohmic losses on straight waveguide sections and reduced performance of components such as miter bends and tapers. Overmoded corrugated transmission lines with high average powers have been successfully implemented on plasma fusion experiments and DNP NMR experiments up to 0.46 THz, and this study shows that they will continue to be of value at higher frequencies.

Chapter 4

PBG Gyrotron Amplifier Design

4.1 Introduction

Studies have shown how the promise of high gain and high-output power in gyrotron amplifiers is limited by the strong forward and backward wave gyrotron oscillations near the waveguide cutoff [20]. Fundamental mode interaction circuits with distributed loading were demonstrated to suppress the gyrotron backward wave oscillations (gyro-BWO) and forward wave oscillations near the waveguide cutoff [43]. Operation in fundamental modes is not feasible at high frequencies, such as 250 GHz, where the radius of the interaction structure would be on the order of a fraction of a millimeter. This results in high ohmic losses that can lead to thermal damage and reduced gain. It also presents a significant challenge in transporting an electron beam over long distances (~300 mm) without causing beam interception on the waveguide walls. Operation in higher order modes poses its own problems with gyro-BWOs in lower order modes. To prevent these oscillations, a mode selective interaction circuit with distributed loss that is easy to manufacture is highly desirable.

One candidate mode for an amplifier at 250 GHz would be the TE_{03} mode of a circular waveguide. The azimuthal symmetry of the TE_{03} mode would provide a strong coupling to the electron beam. However, for this circuit the danger of oscillations from lower order modes is easily seen in Figure 4-1, where the dispersion relation for several modes in a cylindrical waveguide is plotted. The Doppler shifted resonance

condition in Figure 4-1 is plotted for parameters that would yield a strong interaction centered at 250 GHz with broad bandwidth. Where the resonance condition intercepts with other modes, oscillations are possible. A forward wave oscillation with the TE_{23} mode or a gyro-BWO with the TE_{81} and TE_{42} modes are the most significant threat. Clever selection of electron beam parameters, the inclusion of severs or distributed loading can increase the start current for oscillations, but any realistic design must have an interaction circuit that directly addresses the presence of lower order modes.

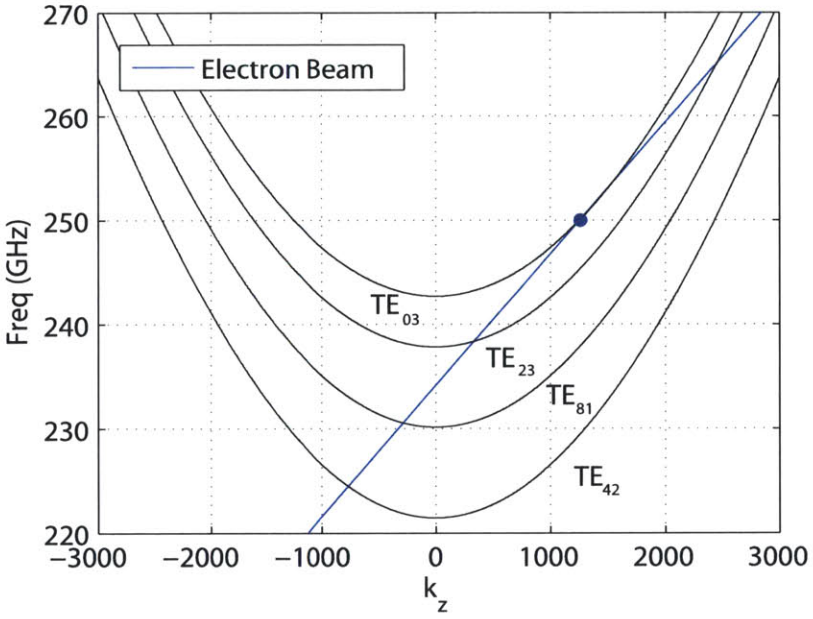

Figure 4-1: Dispersion relation for a circular waveguide with a 2 mm radius and the Doppler shifted cyclotron resonance condition for the electron beam.

The design of a 250 GHz gyrotron TWT amplifier with a circuit gain exceeding 50 dB that focuses on the presence of lower order modes is presented in this chapter. The amplifier uses a novel PBG interaction circuit with mode selective properties. The PBG interaction structure confines a TE_{03}-like mode with comparable interaction efficiency to a circular waveguide operating in the TE_{03}, while providing lower-order mode suppression and attenuation via distributed loss along the entire interaction circuit. The design of the input and output coupler for the PBG interaction circuit

will also be discussed in this chapter.

4.2 PBG Interaction Circuit

The interaction circuit is the most sensitive component in the entire design process and in large part defines the standards that other elements of the gyrotron amplifier must meet. The interaction region is limited to the flat top length of the magnetic field, defined by the 0.1% deviation of the magnetic field from its peak value (300 mm). In order for the amplifier to interact efficiently with the electron beam, the beam must undergo a phase bunching process that results from its interaction with an electromagnetic field, described in Section 2.3. After the phase bunching process is complete, a majority of the power that will be extracted from the beam is produced in a few centimeters. It is important to quickly terminate the interaction with the beam to prevent reabsorption of microwave power. The selected PBG waveguide is a novel interaction structure for gyrotron amplifiers that is highly mode selective and has strong coupling with the electron beam resulting in high interaction efficiency.

A variety of geometries have been studied to find suitable mode confinement and frequency dependent characteristics. The circuit is based on a PBG composed of a two dimensional triangular lattice of metal rods with a central defect. It will be shown that it can meet the requirements of mode selectivity and high interaction efficiency. The 2D triangular lattice PBG, including lattice-defect waveguide modes, is described in Section 3.3. The advantage of using this PBG structure is that its band gap structure is favorable for suppression of lower order modes. With the proper lattice constants the PBG can confine electromagnetic radiation at 250 GHz while suppressing both higher and lower frequencies. The dimensions of the lattice are tuned so that the lattice acts as a strong reflector in a narrow band of frequencies around the operating mode. A defect is created in the lattice by removing some rods, allowing a higher order mode to be confined with a high diffractive quality factor (Q_{diff}), Section 3.3.2. Other modes that can exist in the defect either at higher or lower frequencies suffer significant losses because of the partially transparent lattice [151]. A PBG gyrotron

oscillator has already been demonstrated confirming the advantages of such a circuit in overmoded operation [149].

The band gap plot corresponding to the 2D triangular lattice in Figure 3-4 is shown in Figure 4-2, where the shaded enclosed regions are the band gaps of the lattice. An electromagnetic wave of a given frequency will be perfectly reflected by an infinite lattice with corresponding lattice constants a and b that reside in a band gap. If the frequency does not reside in the band gap the wave will be partially or fully transmitted through the lattice. The design point for the experiment at 250 GHz is marked with a red dot. The lower edge of the gap was selected because this maximizes the suppression of lower order modes which are the most likely to oscillate.

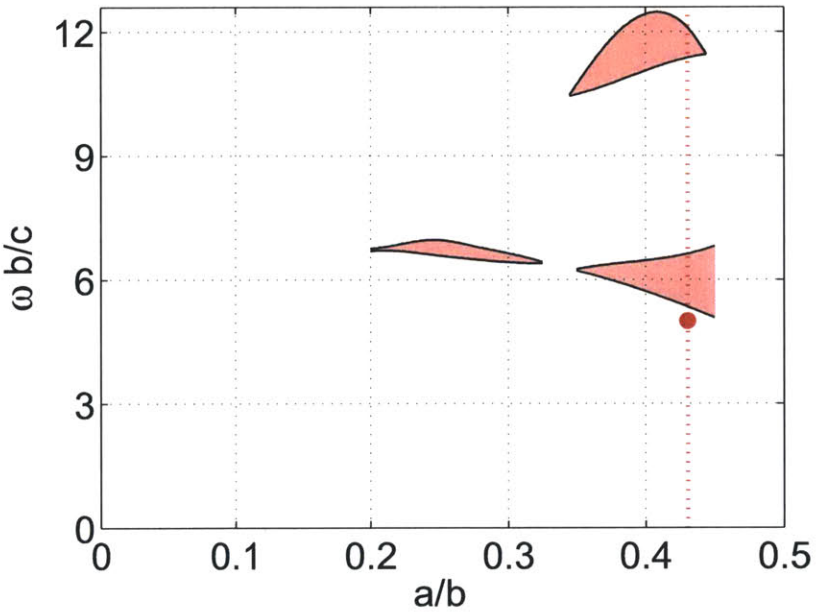

Figure 4-2: The global band gap plot with the operational spacing of $a/b = 0.43$ is marked with a dashed red line. The TE_{03} mode for a finite lattice with three rods removed is marked with a red point.

One difficulty of using a PBG structure is finding a mode that will interact well with an electron beam. By removing a number of rods a defect region is created in the lattice, whereby a mode can be confined. Starting with the central location and removing three concentric rows of rods a TE_{03}-like mode can be excited, Figure 4-4. This mode is similar to the TE_{03} mode in a circular waveguide, Figure 4-3. These

structures were simulated using the eigenmode solver in HFSS to find the modes at cutoff. In Figure 4-3, the TE_{03} mode is plotted in a circular waveguide with a radius of $a = 2$ mm and it has a cutoff frequency of $f_c = k_\perp c/2\pi = \nu_{03}c/2a\pi = 242.7$ GHz, where $\nu_{03} = 10.17347$. This waveguide has many lower order modes that could easily spark oscillations in particular the TE_{23}, TE_{81} and TE_{42}. The corresponding TE_{03}-like mode confined by a PBG waveguide is shown in Figure 4-4 with cutoff at 242.68 GHz. The PBG lattice constants of $\omega b/c = 4.87$ and $a/b = 0.43$ provide the appropriate amount of confinement and suppression of other modes. The diameter of the defect region is approximately the same size as the circular waveguide. Unlike the TE_{03} mode in a circular waveguide, the main mechanism for attenuation is not ohmic losses but diffractive radiation through the lattice, due to the finite extent of the lattice. This should minimize the amount of ohmic heating on the metallic rods and will require the addition of lossy material after the lattice to absorb the stray radiation.

Using a combination of eigenmode simulations with phase advance boundary conditions and driven modal simulations in HFSS, the attenuation in the waveguide as a function of frequency was calculated, as shown in Figure 4-5. With a loss of -2 dB/cm at 250 GHz we have a reasonable amount of attenuation in the waveguide. Diffractive radiation results in -1.7 dB/cm of loss and ohmic loss contributes to -0.3 dB/cm of loss. Additionally, HFSS simulations indicate lower order modes are not supported in the PBG waveguide.

HFSS can also be used to calculate the coupling between a waveguide mode and the electron beam. The normalized coupling factors [123] from Equation (2.39) for the TE_{03} mode in a circular and PBG waveguide are plotted relative to each other in Figure 4-6. The region of interest is the second maximum in the coupling factor because an electron beam radius of less than 1 mm is impractical for this experiment. For an electron beam radius of 1.1 mm the normalized coupling factor for the PBG waveguide is 48% compared to a circular waveguide. The decrease in the normalized coupling factor between the electron beam and the PBG waveguide mode is accept-

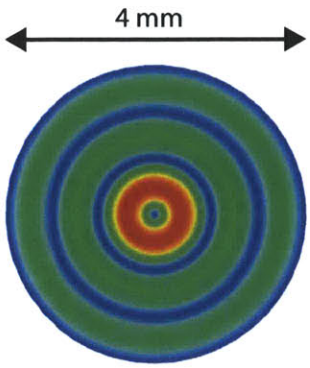

Figure 4-3: The magnitude of the electric field for the TE_{03} mode of a circular waveguide.

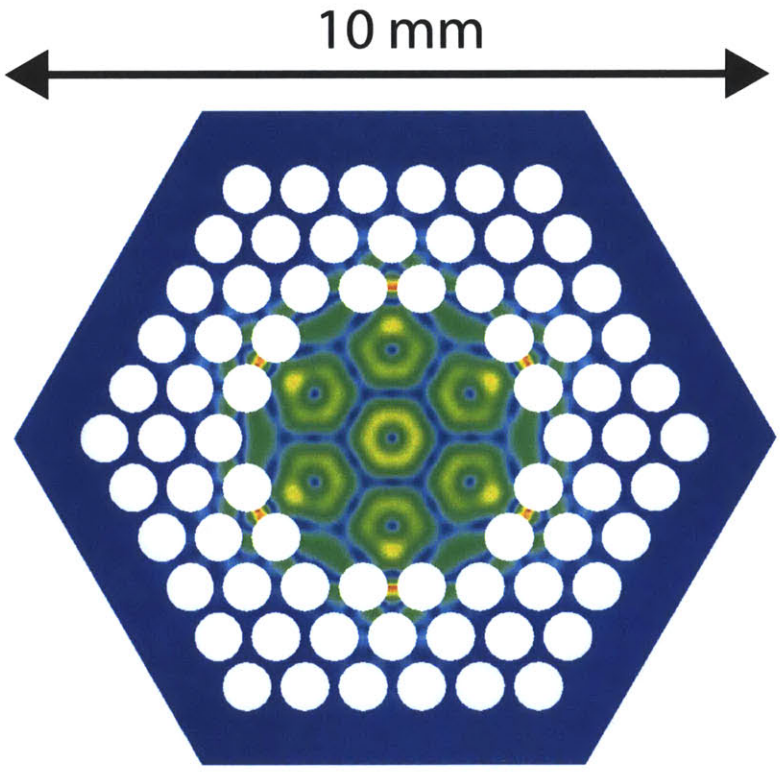

Figure 4-4: The magnitude of the electric field for the TE_{03}-like mode confined in a PBG composed of a triangular lattice of metal rods.

able considering the additional advantages of the PBG waveguide. Furthermore, the interaction between the electron beam and a waveguide mode can be increased by adjusting electron beam parameters. The normalized coupling factor of the PBG waveguide is almost constant between 1-1.2 mm allowing for some variation in the electron beam radius without impacting the coupling.

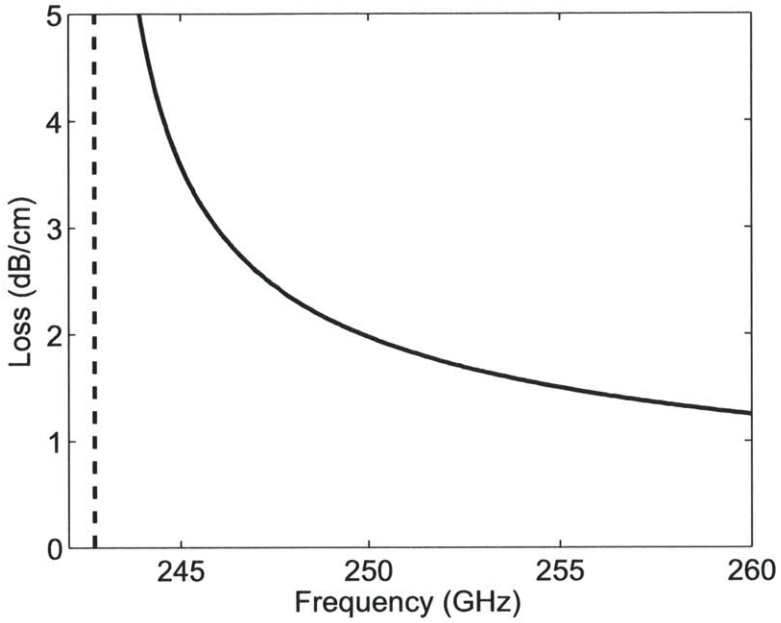

Figure 4-5: Attenuation as a function of frequency for the TE_{03}-like mode.

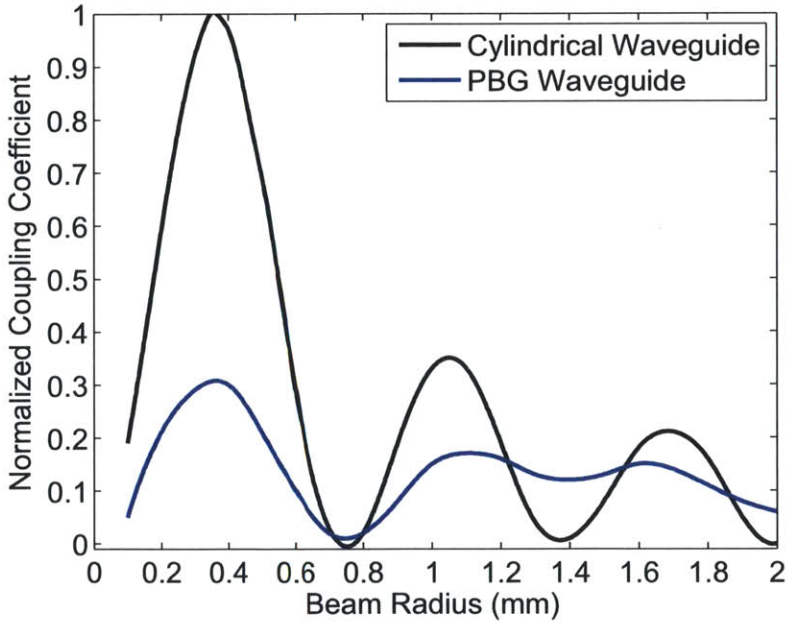

Figure 4-6: Normalized coupling coefficient comparison for a circular waveguide and the PBG waveguide. The electron beam radius for the gyrotron amplifier will be 1.1 mm.

4.3 Input Coupler

The input coupler must efficiently convert the driver signal from the TE_{10} mode of a fundamental rectangular waveguide into the operational mode of the amplifier. The operational mode of the amplifier is very similar to the TE_{03} mode in a circular waveguide. Therefore, the proposed method for the efficient excitation of the amplifier is the use of a wraparound coupler for a small section of circular waveguide, with a radius that corresponds to the same cutoff frequency of the PBG waveguide, that mates directly to the PBG structure.

A wraparound coupler works by exciting a standing wave in a rectangular resonant ring that wraps around the circular waveguide. Wraparound couplers have been previously demonstrated to work well up to W-band [39]. Coupling slots are placed at nulls in the electric field of the ring resonator to induce currents in a circular waveguide that will excite the TE_{03} mode. Once the mode is excited in the circular waveguide, as much energy as possible should be directed towards the interaction region. A down-taper is placed on one side of the coupling slots to direct the mode towards the PBG structure. The down-taper reduces the size of the circular waveguide until it goes below cutoff for the TE_{03} mode. This reflects the power traveling towards the electron gun without producing mode conversion. An additional benefit of having a down-taper is that the electron gun is protected from high power radiation in the TE_{03} mode that could be generated if the amplifier begins to oscillate. Simulations of the structure were run in HFSS using driven modal simulations with an input waveport on the rectangular waveguide leading to the wraparound coupler. An output waveport was placed at the end of 5 mm of PBG structure and a short cylindrical section. This allows the S-parameters to account only for the pure TE_{03} content of the waveguide. An electric field symmetry plane was used to reduce simulation time as the geometry is symmetric. The schematic of the wraparound coupler as it was modeled in HFSS is shown in Figure 4-7(a). In Figure 4-7(b)-(d) the evolution of the magnitude of the electric field is shown as it propagates down the coupler. The wave

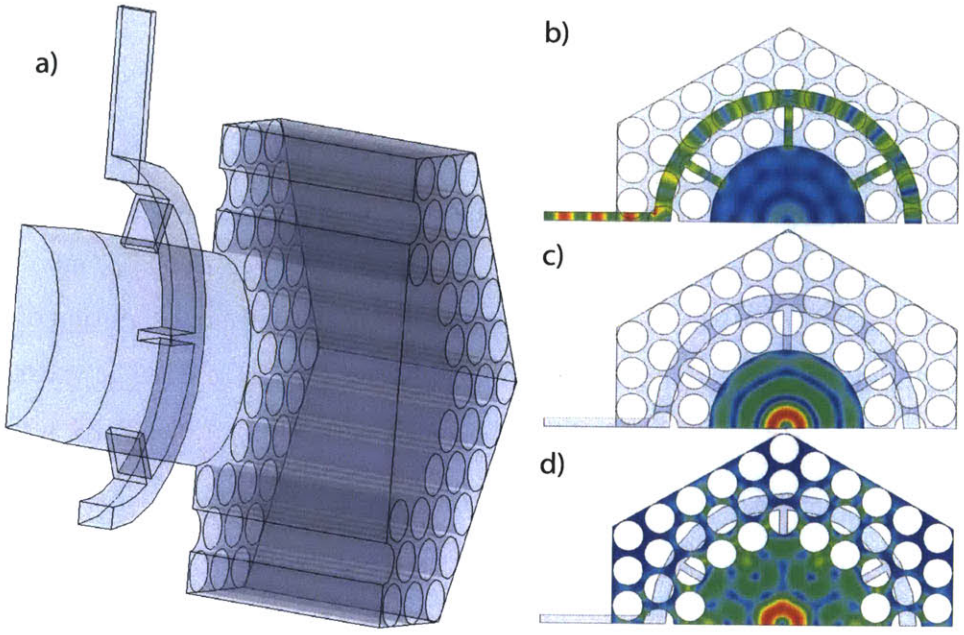

Figure 4-7: (a) Cross section of the input coupler with the components (from left to right) down-taper, wraparound, circular waveguide and PGB waveguide. The magnitude of the electric field at 250 GHz shown in (b) the wraparound, (c) the circular waveguide and (d) the PBG waveguide.

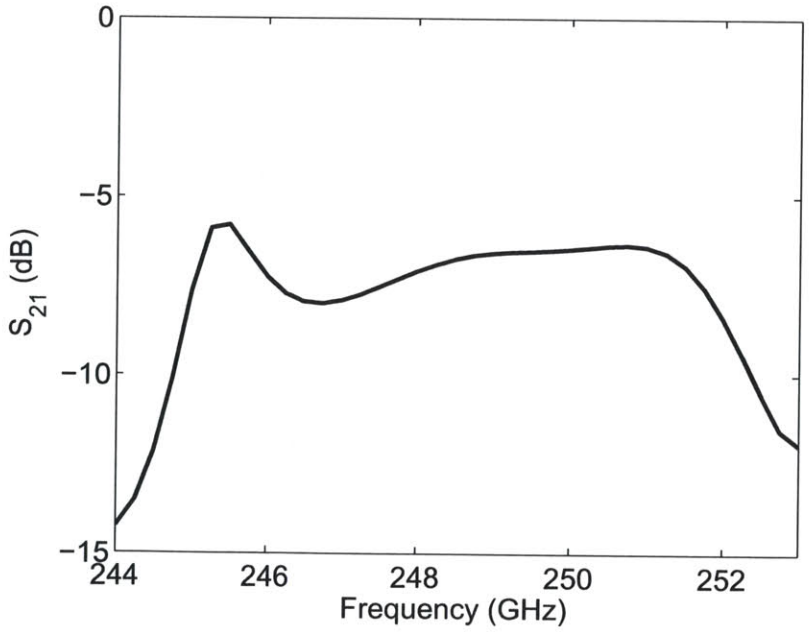

Figure 4-8: S-parameters for the wraparound input coupler simulated in HFSS.

begins by forming a standing wave in the resonant ring that then couples into the circular waveguide where the TE_{03} mode is formed. After propagating into the PBG waveguide, the TE_{03} mode changes into a form that is very similar to the result in Figure 4-4. The S-parameters of the coupler are shown in Figure 4-8. S_{21} is measured after the wave has propagated into the PBG waveguide. The coupler converts more than 30% of the power into a forward propagating wave over 4 GHz of bandwidth.

4.4 Output Coupler

Power extraction from the amplifier must meet two criteria: minimum reflections into the interaction circuit and a radiation pattern that will couple into a transmission line. As a first stage of the output coupler, the near cutoff interaction circuit is enlarged to lower the cutoff frequency, decreasing the interaction with the electron beam and minimizing reflections. This component, referred to as an up-taper, was designed using CASCADE to minimize reflections in the operational range of the amplifier with dimensions shown in Figure 4-9. The final radius of the waveguide, $a = 3.175$ mm was selected so that the bounce angle would be $\theta_B \approx 38°$ determined by

$$\sin(\theta_B) = (\nu_{nm}/ka)\,. \tag{4.1}$$

After the up-taper, the TE_{03} mode can either be extracted axially or it can be mode converted into a Gaussian beam and be extracted radially. The axial configuration is simplest, but not optimal for pulsed-DNP experiments as they require transmission of the signal to the NMR test stand and coupling into the sample [17]. If the output of the gyrotron amplifier is a Gaussian beam it can be efficiently coupled to a corrugated waveguide with low-loss transmission over a distance of several meters. Gaussian beams are also easily coupled to the sample with tapers or lenses [112]. The Gaussian beam mode converter can be designed by considering the quasi-optical nature of the 250 GHz signal and decomposing the waveguide mode into a series of rays

that propagate at a bounce angle based on the radius of the waveguide, Figure 4-10. If the waveguide was terminated these rays would radiate outward radially permitting a parabolic mirror to reflect them as a plane wave. In order to limit the direction of the radiation the termination is not a smooth cut, but a notch in the waveguide that allows all of the exiting plane waves to radiate cylindrically into a half-space [158]. The length of the cut is determined by the bounce angle to be

$$L_{\text{cut}} = 2a\sqrt{1-(m/\nu_{nm})^2}\cot(\theta_B). \tag{4.2}$$

For these dimensions $L_{\text{cut}} \approx 8.2$ mm. A parabolic mirror is used to collect these rays and form a plane wave. The waist of the beam formed by the parabolic mirror needs to match the output 19 mm diameter corrugated waveguide of the gyrotron amplifier. The waist needed for matching is $\sim$ 6.1 mm; however, the corrugated waveguide is located some distance from the parabolic mirror and the waist of the beam will expand. Simulations in HFSS were performed to determine the 3.4 mm focal length of the parabolic mirror. A second cylindrical mirror with transverse focusing was also used to provide better matching to the corrugated waveguide. The HFSS simulations shown in Figure 4-11 produced a 93% Gaussian with beam waists of w_x =5.8 mm and w_y =5.6 mm at the edge of the simulation. The beam should expand to the correct dimension by the aperture of the corrugated waveguide.

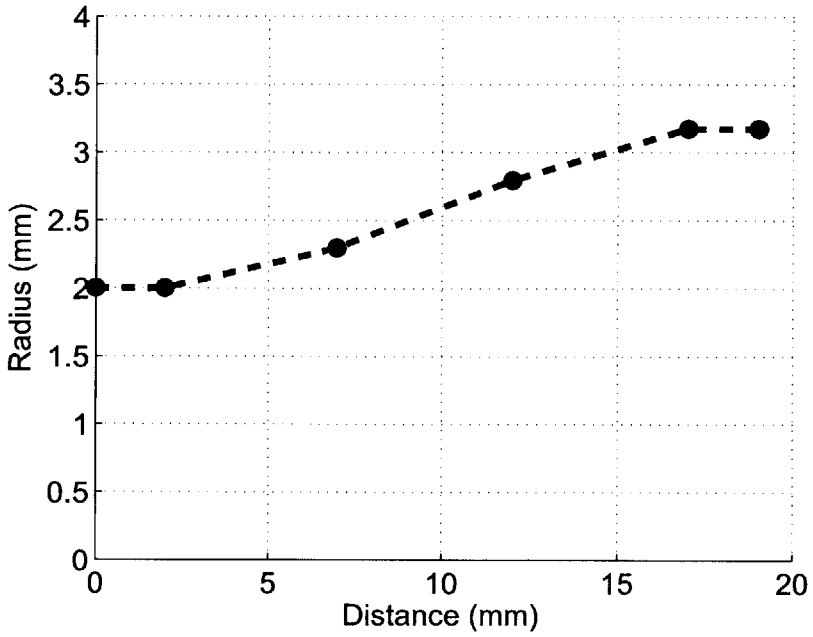

Figure 4-9: Dimensions of the up-taper simulated in CASCADE and HFSS.

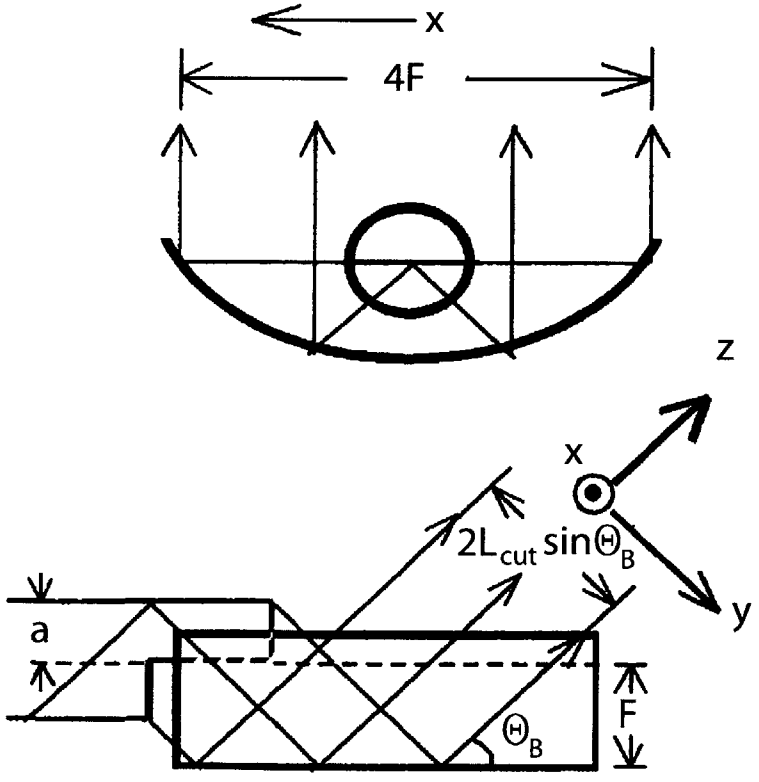

Figure 4-10: Ray tracing diagram for a step cut launcher and the first parabolic mirror, adapted from [127].

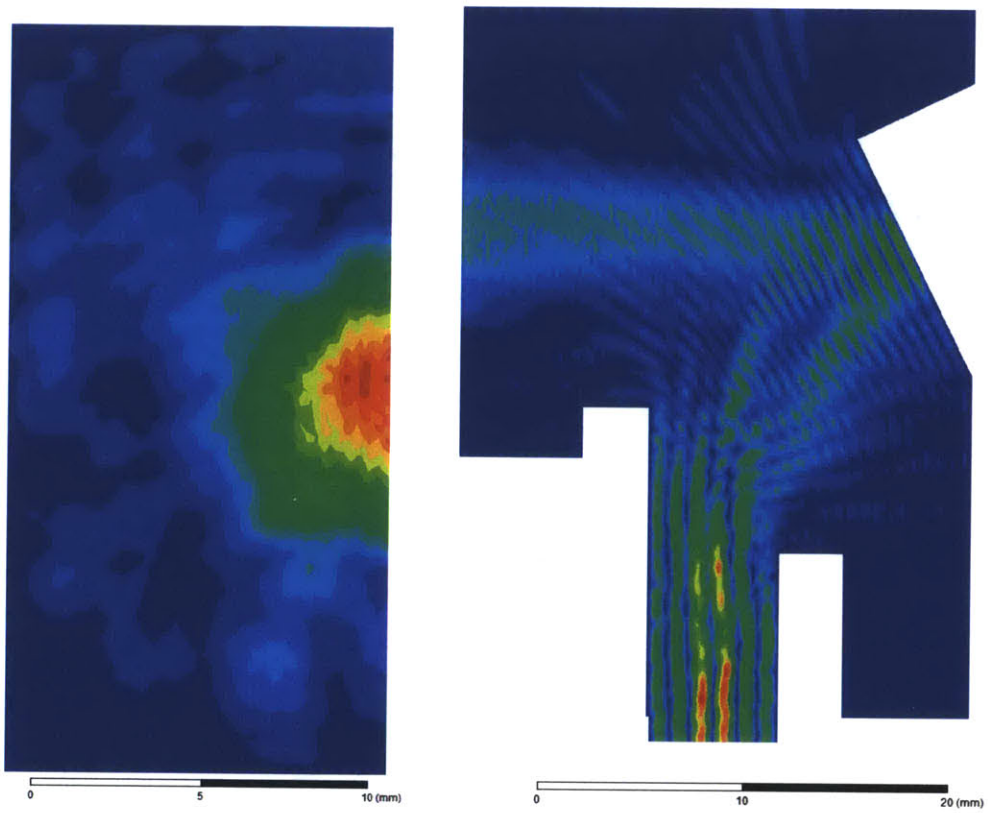

(a) (b)

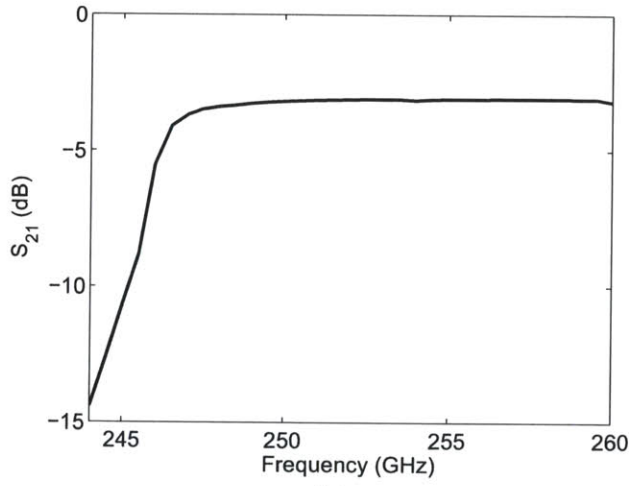

(c)

Figure 4-11: (a) The electric field of the Gaussian beam produced by the quasi-optical mode converter simulated in HFSS. (b) Side view of the mode converter with step-cut launcher, parabolic mirror and cylindrical steering mirror shown in the outline. (c) Combined performance of the up-taper and the step-cut launcher for converting the TE_{03} mode into the HE_{11} mode.

4.5 Linear and Nonlinear Simulations

In the limit of small signal gain, the equations of motion for the electrons in a gyrotron amplifier, Equations (2.24)-(2.26), can be linearized [124] to produce the dispersion relation in Equation (2.53). Using this small signal dispersion relation in combination with the normalized coupling coefficient, loss parameters for the PBG circuit, and S-parameters for circular to PBG waveguide junctions calculated in HFSS it is possible to calculate the single pass and round trip gain for the device. The linear growth rate is extremely dependent on the electron beam parameters and needs to be optimized to maximize the circuit gain and bandwidth.

It is easiest to achieve large bandwidths when the amplifier is slightly detuned from a grazing condition with the waveguide dispersion relation, Figure 4-12. The further the grazing condition is from the cutoff frequency the larger the bandwidth, but the lower the gain. There are also several disadvantages that come with operating too close to cutoff. First, a strong interaction between the wave and the electron beam close to cutoff increases the possibility of self start oscillations. Second, waveguide dispersion limits the gyrotron amplifier's ability to amplify short pulses. For these reasons the amplifier's bandwidth is centered at 250 GHz, which is 3% above cutoff. There are also some advantages to lowering the linear growth rate (for a fixed attenuation constant) in order to make a high-gain amplifier while avoiding driven oscillations. If the growth rate is relatively small, a long circuit will be required to achieve the desired gain of more than 50 dB. For a driven oscillation to occur, the round-trip gain must be greater than 0 dB, meaning a wave that is amplified, reflected from the end of the interaction region, propagates to the start of the circuit and is reflected again has increased in energy. If the gain per cm, including loss, is approximately equal to the attenuation per cm, it is easier to suppress the driven oscillation. With an attenuation of -2 dB/cm at 250 GHz a linear growth rate of 2.5-3 dB/cm meets this condition. The linear growth rate is allowed to be slightly higher than the attenuation for two reasons. First, the addition of velocity spread will lower the gain per centimeter. Second, the output of the amplifier is optimized for transmission,

Table 4.1: Design Operating Parameters

Beam voltage, V_0	32 kV
Beam current, I_0	1.0 A
Beam pitch factor, α	0.75
Beam Radius	1.1 mm
Input power	1 mW
Max Output power	1 kW
Center Frequency	250 GHz
Peak Magnetic Field	8.818 T
Operating Mode	PBG TE_{03}-like
Perpendicular Velocity Spread	3-5%
Circuit Length	260 mm

so only a small fraction of the amplified signal is reflected. Taking these things into consideration, the optimized electron beam parameters that were calculated for this structure are listed in Table 4.1.

Figure 4-13 shows the linear growth rate as a function of frequency for the TE_{03}-like mode in a PBG waveguide calculated using Equation (2.53) and the parameters in Table 4.1. These operational parameters provide a reasonable growth rate, a very large bandwidth and a weak interaction close to the cutoff frequency. As was mentioned previously, the normalized coupling factor is considerably lower for the PBG waveguide compared to a circular waveguide, but it has a limited impact on the growth rate.

After determining the operating parameters which yield the desired linear growth rate, nonlinear simulations are performed to determine the impact of insertion loss and saturation. The results for nonlinear simulations using Equations (2.24)-(2.26) and the parameters in Table 4.1 are shown in Figure 4-13 and Figure 4-14. Figure 4-13 shows that the linear growth rate for both linear and nonlinear simulations is in excellent agreement. Figure 4-14 is the circuit gain we would expect from a 260 mm circuit, where the effect of insertion loss (coupling the electromagnetic wave to the

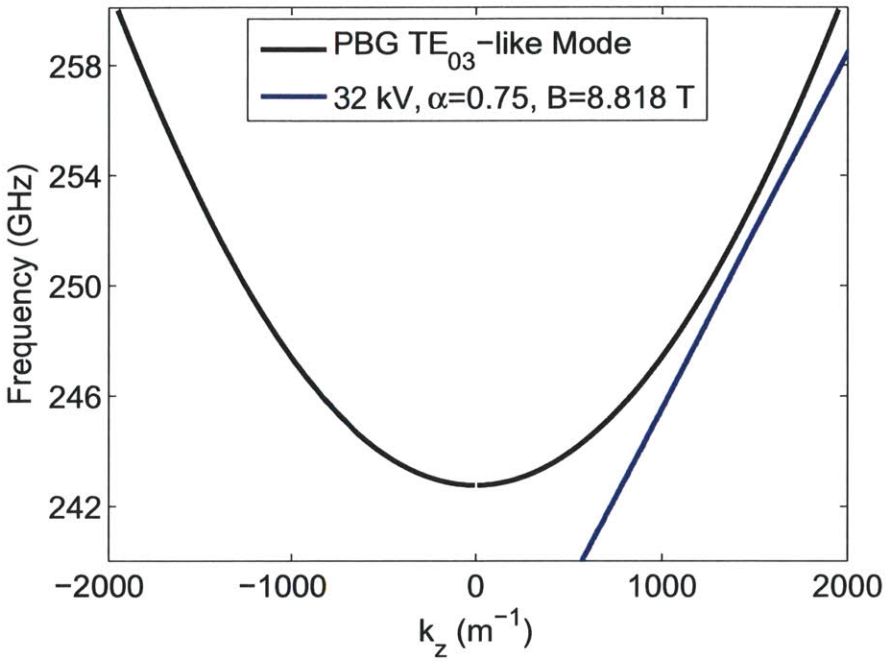

Figure 4-12: Dispersion relation for the parameters in Table 4.1.

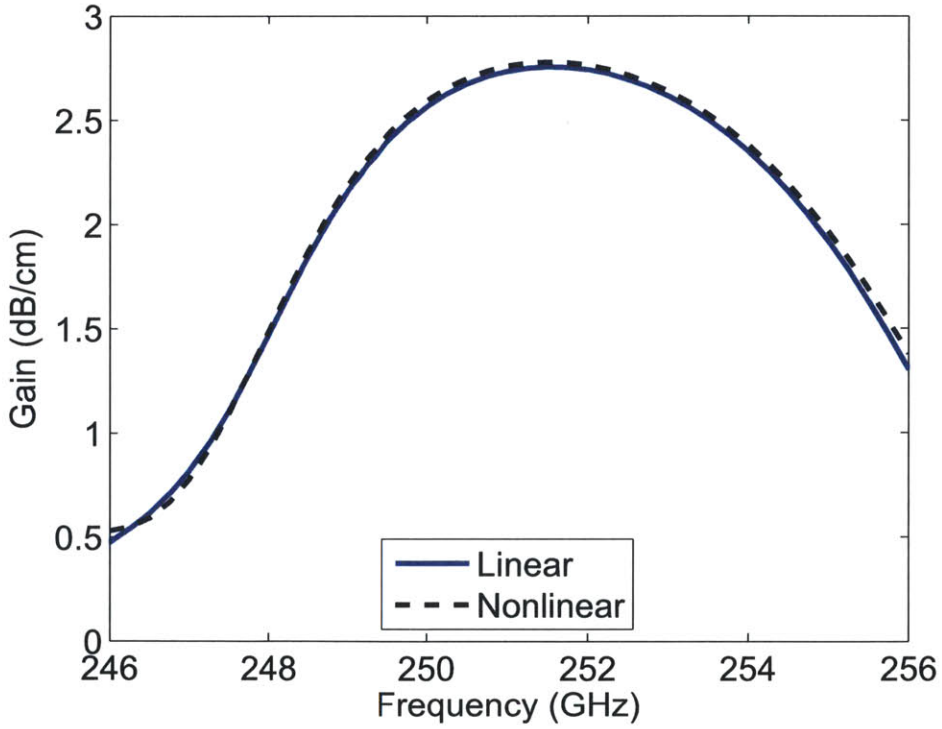

Figure 4-13: Linear gain in dB/cm from linear and nonlinear theory.

electron beam) can be seen when comparing the dashed black line and the black line. The dashed black line is calculated from the linear growth rate in db/cm in Figure 4-13 and multiplied by the circuit length. As the electron beam approaches zero detuning, $\Delta = 0$, in the center of the bandwidth the insertion loss approaches -9 dB. Additionally, saturation was not observed in the nonlinear simulations for these parameters.

In order to include the effects of the electron beam's perpendicular velocity spread and the possibility of oscillations, MAGY [34], a nonlinear, self-consistent simulation code, was used. This software is the most common package used for the design of gyrotron oscillators and amplifiers, and has shown good experimental agreement for both cases [34, 92]. In Figure 4-14, the gain in dB is shown for the nonlinear theory and simulations using MAGY. For no velocity spread MAGY and the nonlinear theory are in excellent agreement. A practical electron gun should be able to achieve 3-5% perpendicular velocity spread, as will be shown in Section 5.3. The electron beam in the MAGY simulations presented includes 0%, 3% and 5% velocity spread and is otherwise identical to the parameters listed in Table 4.1. The frequency dependent characteristics of the structure that are calculated using HFSS were implemented in MAGY. MAGY simulations require the use of a circular waveguide and the geometry cannot be altered to take into account the PBG. To account for this, the electron beam was placed at a slightly larger radius (1.2 mm) where it would have the same coupling coefficient as the PBG mode (1.1 mm), see Figure 4-6. To achieve the correct attenuation constant, the conductivity of the waveguide in the interaction region was altered to match the values in Figure 4-5. The circuit in MAGY also includes an up-taper designed using CASCADE to minimize reflections, discussed in Section 3.7. The input power for the numerical simulations was 1 mW. Agreement between linear theory and MAGY is excellent, with both cases showing approximately 3 GHz of bandwidth. The center frequency of the MAGY simulations is lowered slightly as the velocity spread increases due to the impact of velocity spread, which is more severe on higher frequencies.

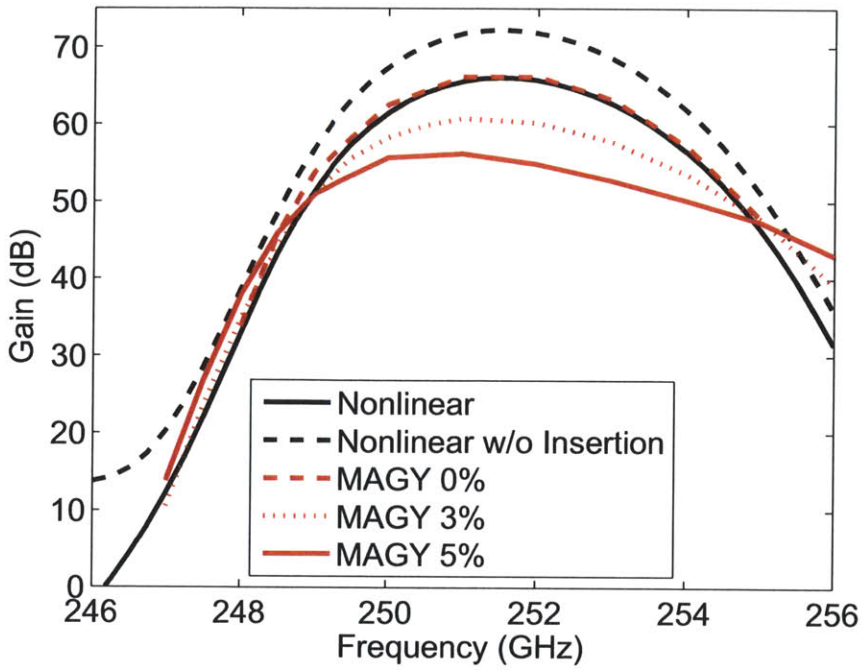

Figure 4-14: The circuit gain for the device calculated from the nonlinear theory compared to results from MAGY for a 260 mm circuit with 0%, 3% and 5% perpendicular velocity spread.

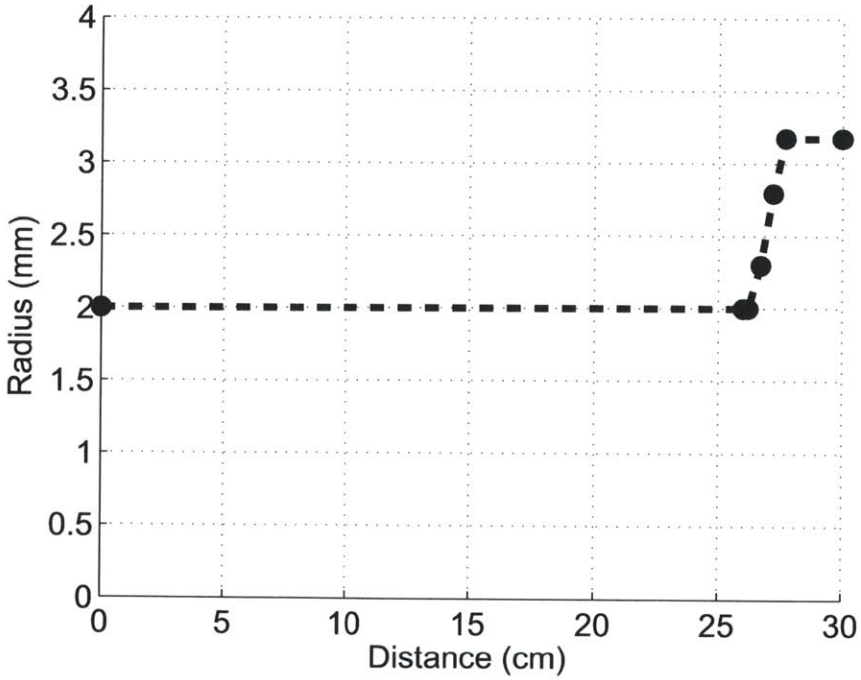

Figure 4-15: Dimensions of circuit simulated in MAGY.

The output power of the amplifier for a 1 mW input and for saturated operation is shown in Figure 4-16. For an input of 1 mW, the amplifier produces more than 1 kW of peak output power. The saturated output power, defined as the peak output power observed independently of input power, shows that the amplifier is operating on the edge of the saturated regime. The input power required to reach saturation in Figure 4-16 is shown in Figure 4-17. Figure 4-18 shows the input versus output power curve for 252 GHz. Below 1 mW of input power the amplifier exhibits linear behavior and above 1 mW the gain falls rapidly as the output of the amplifier saturates.

Alternate operational parameters for the electron beam can also lead to high gain and large bandwidths. For the same conditions given in Table 4.1, with the exclusion of magnetic field and α, two alternate design points, with dispersion relations shown in Figure 4-19, are presented in Figure 4-20 and Figure 4-21. The first case, for an $\alpha = 0.5$, requires a slightly lower magnetic field in order to maximize the gain. The decrease in α lowers the start current for oscillations in the operational mode which allows the electron beam resonance condition to overlap with the waveguide dispersion relation. The lower α allows for a very wide bandwidth of interaction with a small decrease in the gain. This could be compensated for by raising the electron beam current. In practice, the bandwidth will be limited by the presence of velocity spread which will impact the gain more severely at higher frequencies. The second case, for an $\alpha = 1$, requires a small increase in the magnetic field; however, a significant gap is needed between the electron beam resonance condition and the waveguide dispersion relation to prevent oscillations. Figure 4-21 does not present results for 0% velocity spread in MAGY because these conditions would lead to an oscillation. The higher α leads to a limited bandwidth of operation and requires amplification at frequencies closer to cutoff. However, the gain and bandwidth are less sensitive to velocity spread making this a good option if the velocity spread from the electron gun is high.

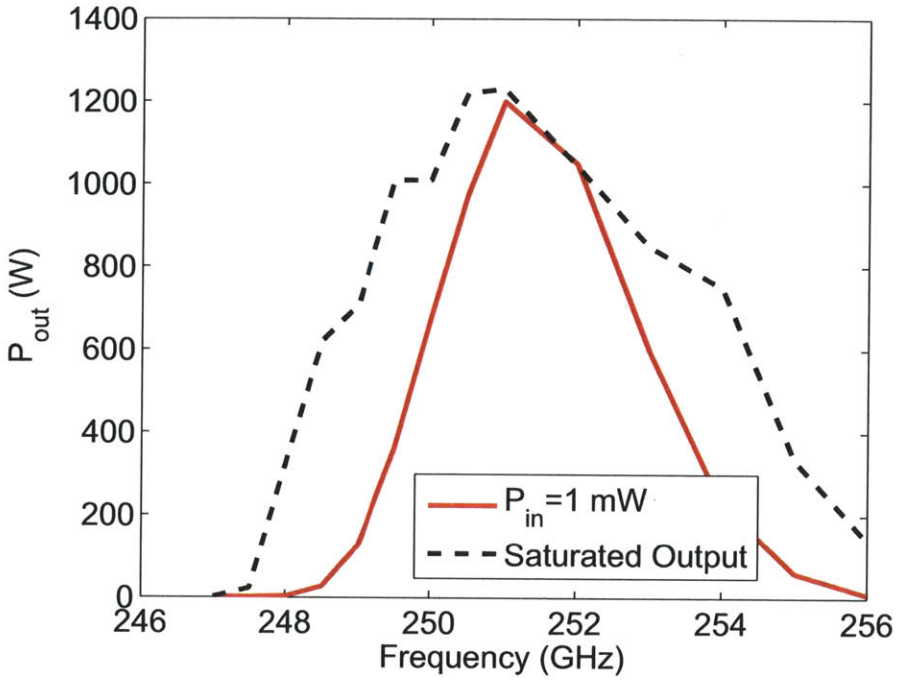

Figure 4-16: Output power as a function of frequency simulated with MAGY using a 32 kV, 1 A electron beam with 3% $v_\perp$ spread.

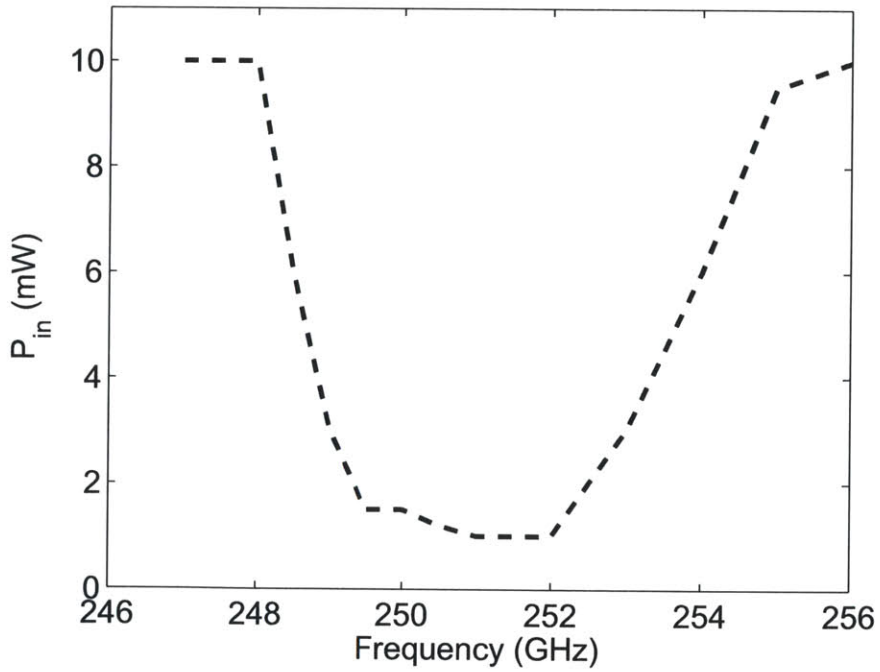

Figure 4-17: Input power as a function of frequency required to reach saturation in Figure 4-16.

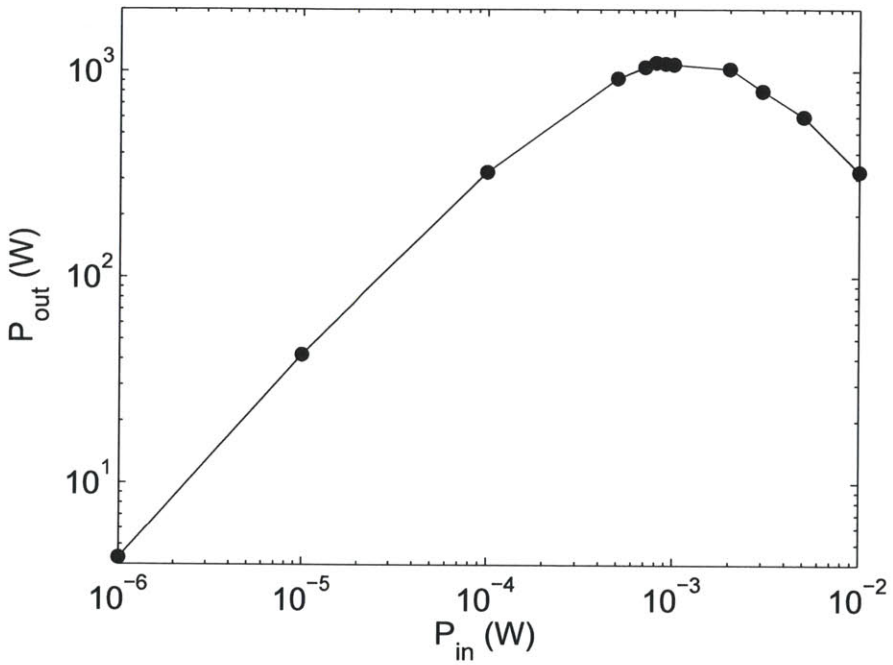

Figure 4-18: Output power as a function of the input power for 252 GHz for a 32 kV, 1 A electron beam with 3% $v_\perp$ spread.

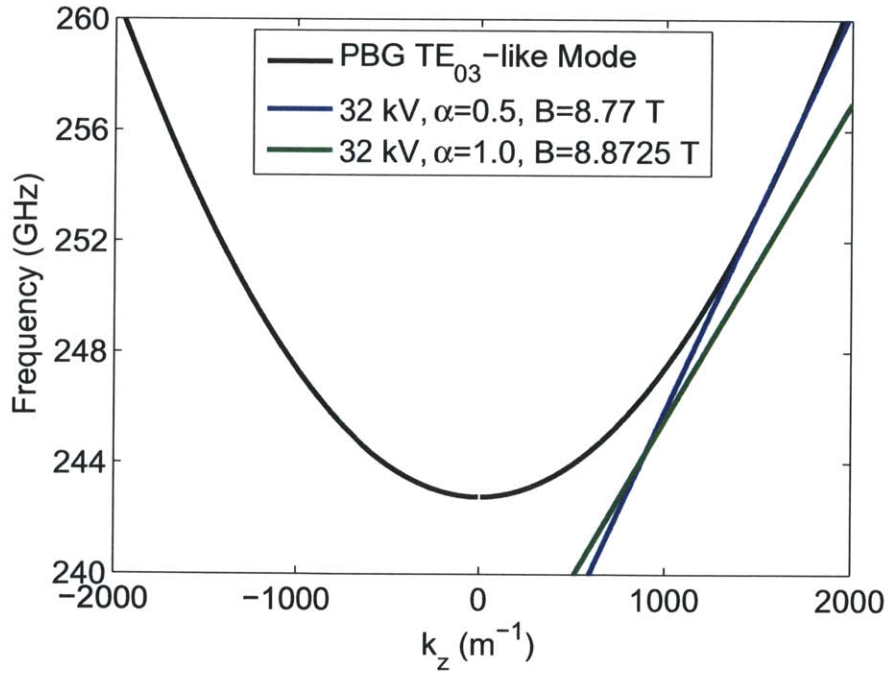

Figure 4-19: Dispersion relation for the parameters in Table 4.1.

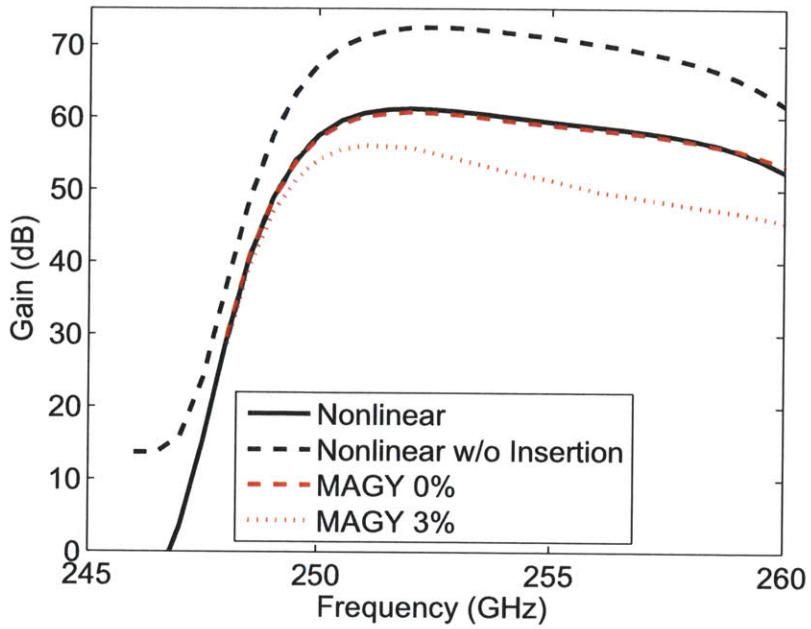

Figure 4-20: The circuit gain calculated from the nonlinear theory compared to results from MAGY with 0% and 3% perpendicular velocity spread. Operational parameters correspond to Table 4.1 with the exception of $\alpha = 0.5$ and $B_0 = 8.77$ T. The electron beam resonance condition is shown in Figure 4-19 (blue line).

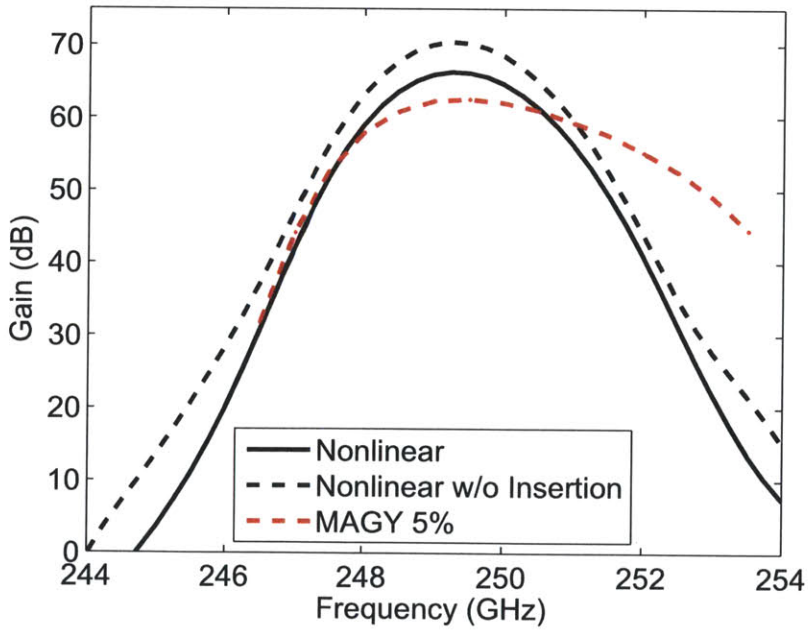

Figure 4-21: The circuit gain calculated from the nonlinear theory compared to results from MAGY with 5% perpendicular velocity spread. Operational parameters correspond to Table 4.1 with the exception of $\alpha = 1$ and $B_0 = 8.8725$ T. The electron beam resonance condition is shown in Figure 4-19 (green line).

4.6 Conclusions

The complete design of a novel 250 GHz gyrotron amplifier based on a PBG interaction circuit has been presented. This design relies on the frequency dependent distributed loss provided by the interaction circuit to suppress both forward and backward wave oscillations from lower order modes. Linear theory and nonlinear simulations have shown reasonable operational parameters and circuit length will provide the desired gain and bandwidth. With 60 dB of amplification and 3 GHz of bandwidth, the design meets the requirements of pulsed-DNP experiments. A wraparound input coupler with more than 30% power transmission from fundamental waveguide to the PBG will provide the required mode conversion from the solid state source to the amplifier circuit. The output coupler for the gyrotron amplifier will consist of an up-taper optimized to minimize reflections and a step-cut launcher which produces a 93% Gaussian beam coupled into a corrugated waveguide.

Chapter 5

Experimental Setup

An experimental test stand was assembled during the course of this work for the operation of the gyrotron amplifier. The integration of several major pieces of equipment was required including a high-voltage modulator, high-field magnet, electron gun, water-water heat exchanger, water-air heat exchanger, etc. While these items do not fall directly within the scope of this research project, their operation was often the limiting factor in the progress of this work. The full experimental setup required to operate the gyrotron amplifier can be seen in Figure 5-1. The He compressor for the superconducting magnet, the liquid-liquid heat exchanger to cool the He compressor, the air-cooled chiller for the high-voltage modulator and the air-cooled oil bath for the electron gun are not pictured in Figure 5-1.

5.1 High-Voltage Modulator

The pulsed high-voltage modulator, Figure 5-2, was provided by Scandinova Systems AB and was used to bias the electron gun. The modulator operates with a maximum voltage of 50 kV for a 10 μs pulse length and a maximum repetition rate of 5 Hz. The modulator provides connections for both the cathode and mod-anode lead with CA-1 Claymount receptacles. The voltage for the mod-anode is set by a resistive bridge with multiple tap settings. The measured flat top of the of the pulse is $\pm 0.5\%$ for 8 μs into a 10 kΩ low-inductance resistive load connected to the modulator with

a 2 m Claymount L3 cable (145 pF/m). The pulse shape from the modulator is extremely sensitive to the capacitance and inductance of the load. The additional capacitance from the electron gun (~120 pF) and the long cable required to reach the electron gun (4 m) resulted in severe distortion of the pulse shape. To correct the pulse shape, additional inductance was added to the internal cables that connect the switching modules to the high-voltage transformer. The grounded shielding on both the cathode and mod-anode leads was removed to limit the cable capacitance. The flatness of the pulse into the gyrotron load was limited to $\pm 0.5\%$ for 6 μs, as seen in Figure 5-3. The high-voltage modulator includes two internal capacitive voltage divider (CVD) probes for voltage and current transformer probes located internal to the unit on the high voltage side of the transformer. The traces for these probes are labeled in Figure 5-3 as Scandinova Voltage and Current. Also shown in Figure 5-3 is the electron beam current, which was measured on the gyrotron collector grounding cable with a Rogowski coil and the mod-anode voltage, which was measured with a CVD probe on the mod-anode lead.

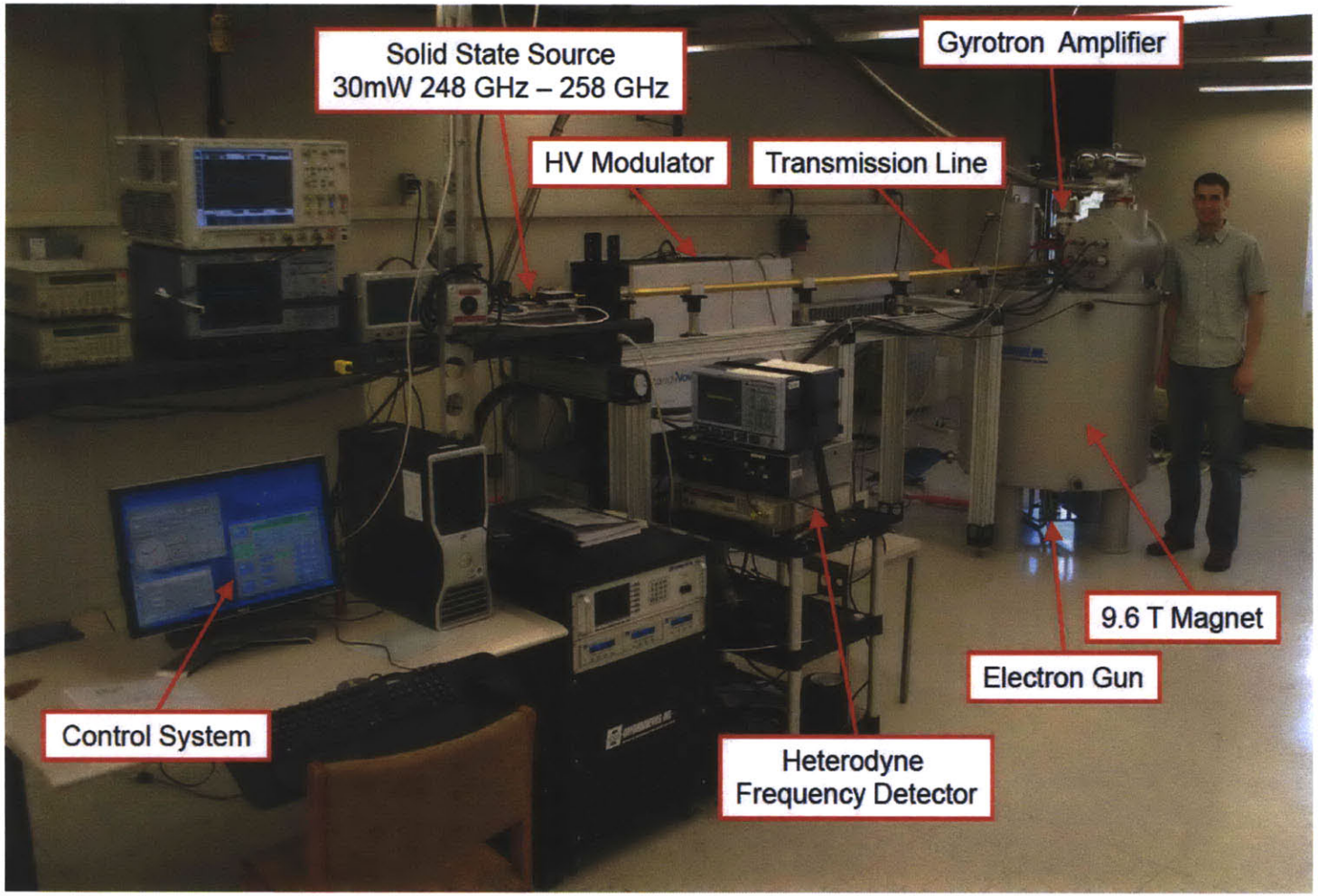

Figure 5-1: The 250 GHz gyrotron amplifier laboratory setup.

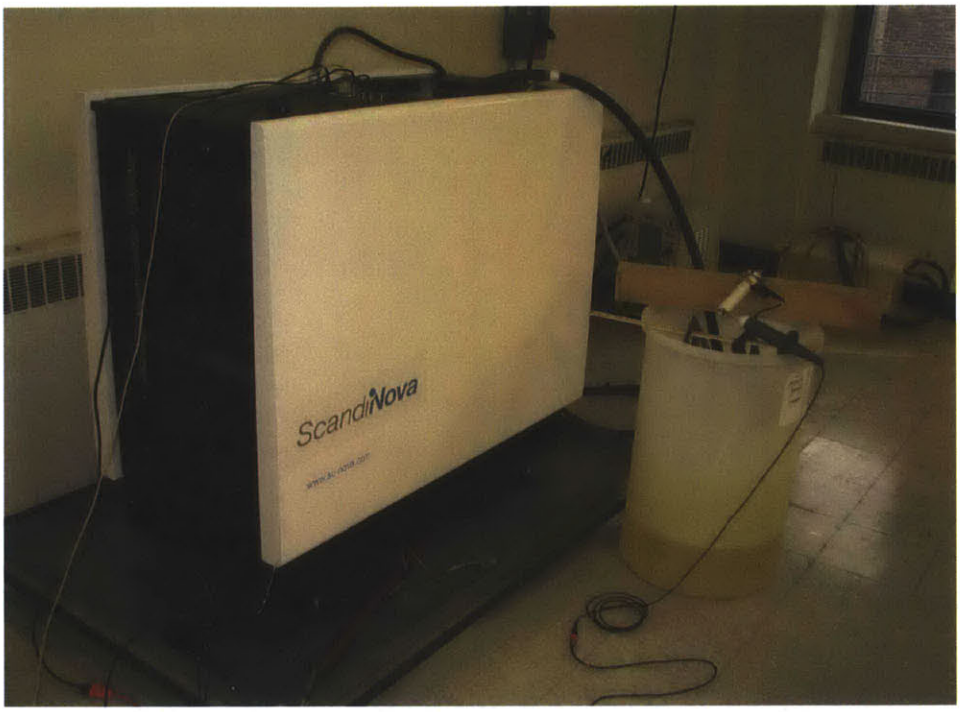

Figure 5-2: Scandinova Systems AB high-voltage modulator during initial testing with a 10 kΩ low-inductance resistive load terminating the cathode lead. The mod-anode lead is terminated with an open and is being monitored by the high-voltage CVD probe.

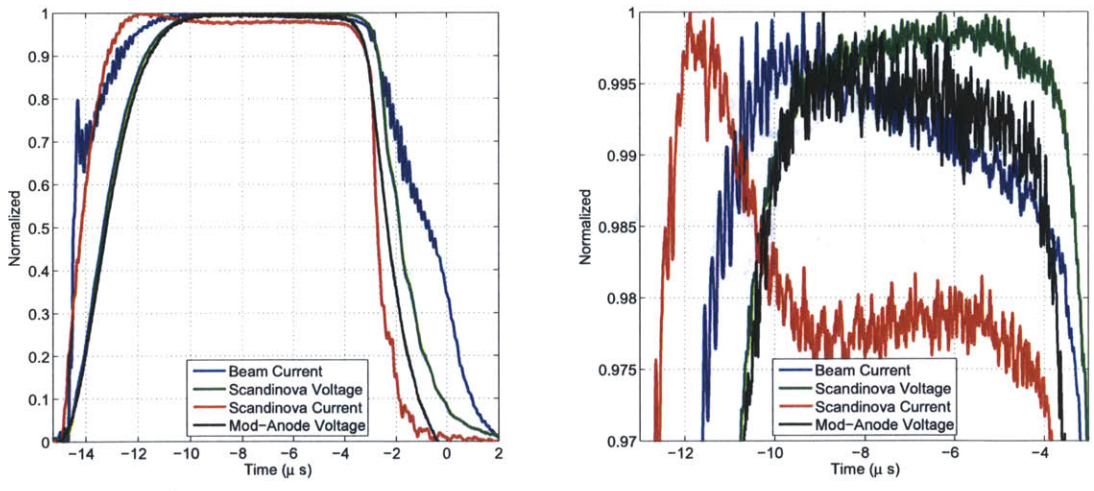

Figure 5-3: High-voltage modulator pulse into the gyrotron load. The pulse was set to -5 kV on the cathode with the mod-anode tap at 45% of the cathode voltage. The peak electron beam current was ~100 mA.

5.2 Superconducting Magnet

A 9.6 T superconducting magnet supplied by Cryomagnetics, Inc. was used for this experiment. The superconducting magnet has a 300 mm, 0.1% homogenous axial field. This is a major requirement for gyrotron amplifiers where the achievable gain is directly impacted by the interaction length. The magnet system includes a second independent superconducting gun coil used for making adjustments to the axial field profile at the electron gun emitter location. The magnet is suspended in a vacuum-jacketed liquid-helium bath. In order to prevent helium loss, the magnet includes a helium recondenser mounted on top of the magnet. A schematic of the magnet is shown in Figure 5-4 and an installation photo is shown in Figure 5-5. During installation, the magnet underwent four training quenches at progressively higher currents, Figure 5-6. It was determined that these quenches were a result of ice (N_2, H_2O) formation between coils or shifts in coils during transport. The magnet chamber was cycled to room temperature, pumped with a turbomolecular pump and recooled. After this procedure, the full rated field was successfully achieved.

The design axial magnetic field is shown in Figure 5-7 with the local magnetic field in the electron gun region shown in Figure 5-8. Black dots in both figures mark the location of the electron beam emitter. The effect of the gun coil can be seen in Figure 5-8, with $\pm$ 25% of the rated gun coil current shown in the plots.

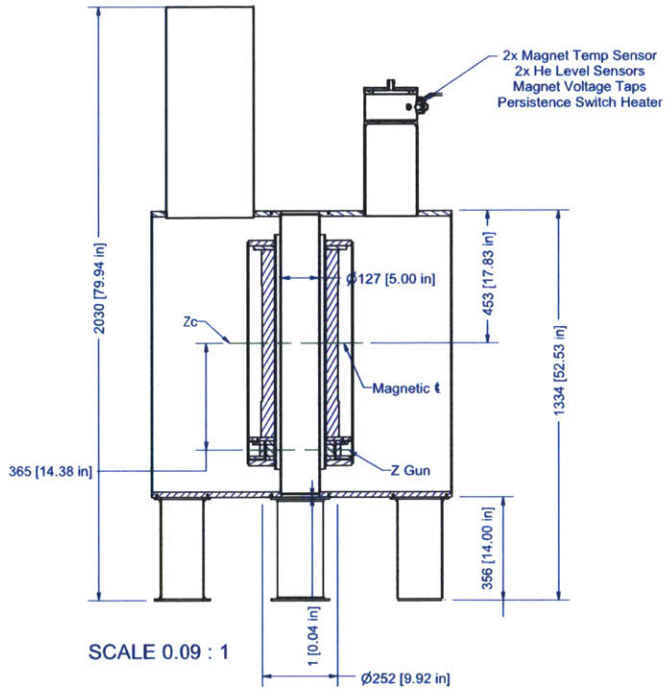

Figure 5-4: Cross-sectional CAD drawing of the 9.6 T magnet.

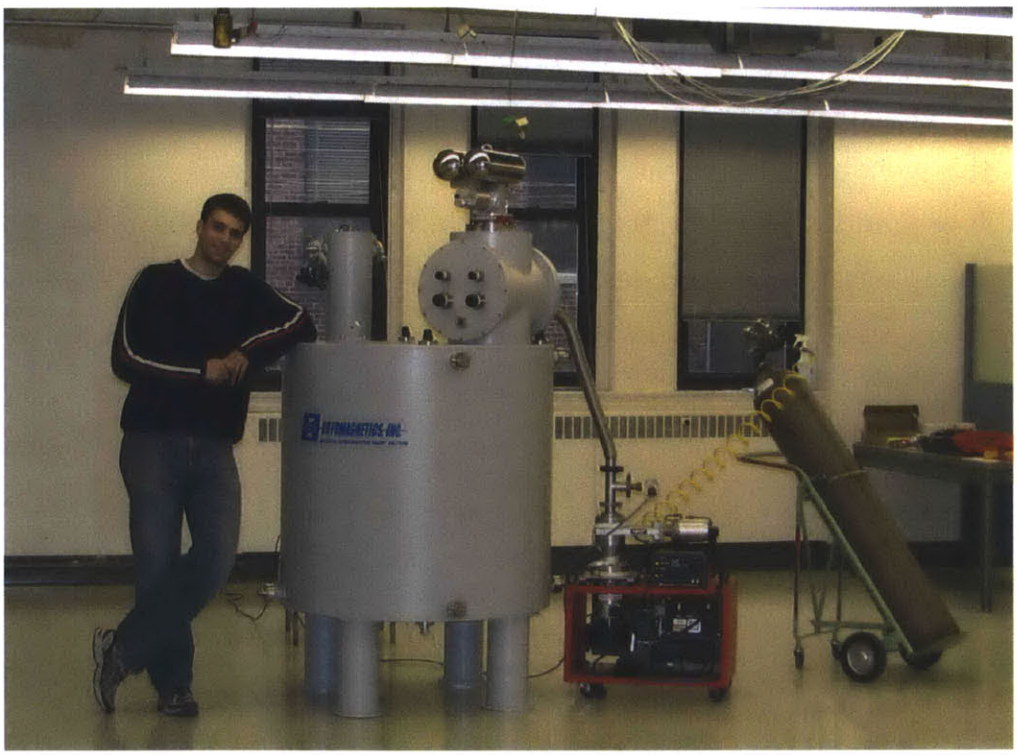

Figure 5-5: The Cryomagnetics, Inc. 9.6 T magnet. The turbo-molecular pump is connected to the vacuum jacket for the liquid-He bath.

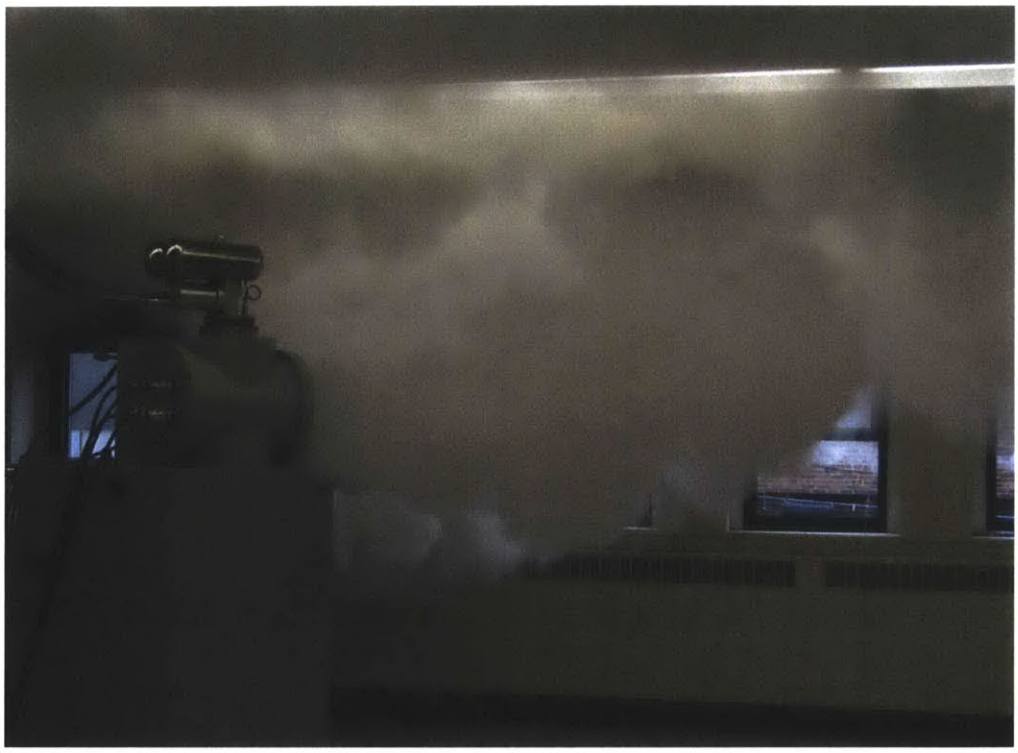

Figure 5-6: Helium gas being vented from the magnet during a training quench.

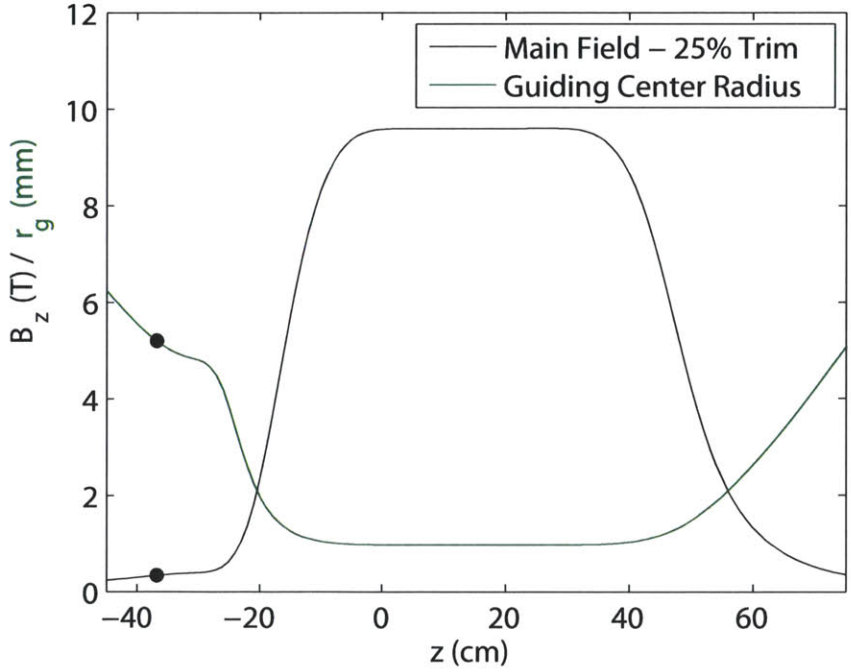

Figure 5-7: The magnetic field plotted as a function of distance used to model the electron gun performance. The guiding center radius is also plotted along the axis of the magnet.

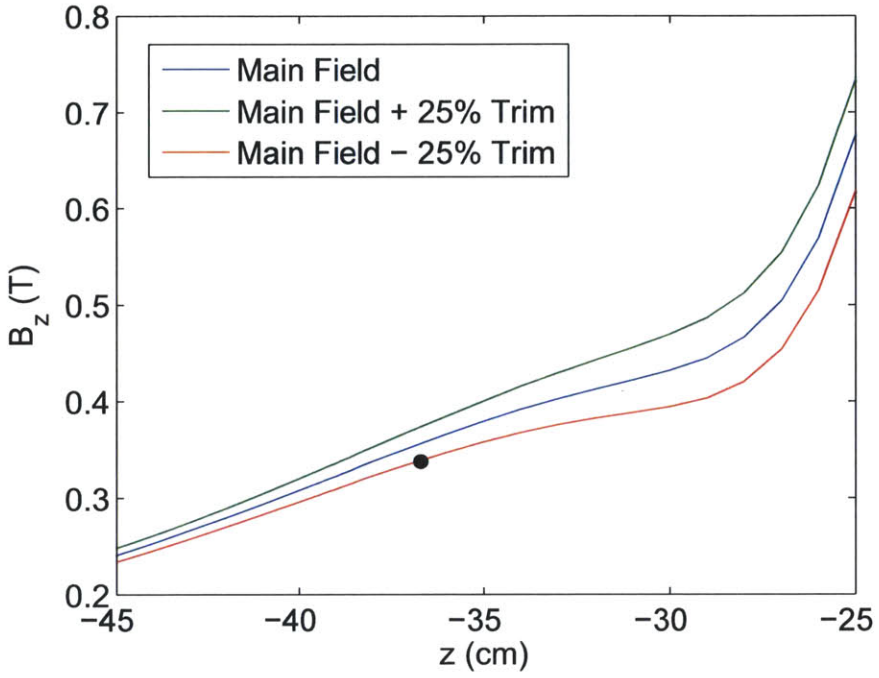

Figure 5-8: The main magnetic field with the gun coil magnet at 0% and ±25% of the rated current.

5.3 Electron Gun

The electron gun must meet very specific requirements in order for the amplifier circuit to operate successfully because the interaction efficiency is highly dependent on the beam quality. In a standard electron gun, a large electric field extracts electrons from an annular ring on the cathode. The extraction of electrons occurs by heating the cathode and applying a large potential bias between the cathode and anode. The electric field between the cathode and anode is partially transverse to the static axial magnetic field at the cathode. The transverse component causes the electrons to begin gyrating. The electrons undergo compression as they enter the higher intensity magnetic field area. The static magnetic field also prevents the electrons from being intercepted by the anode which is before the interaction region. There can be either one (diode) or two (triode) anodes in the electron gun. The triode configuration increases the beam quality by creating extraction and acceleration regions. Additionally, the ability to modify the voltage on the first anode (mod-anode) provides increased control over the static electric field profile allowing the user to vary the velocity pitch factor, $\alpha = v_\perp/v_z$, of the electron beam. This is of great importance in the operation of the gyrotron amplifier as it allows the user to tune the operating region by raising or lowering the main magnetic field and adjusting the α accordingly to reach grazing condition. The electron gun was designed using the simulation code MICHELLE [135, 136]. Initial design parameters for the electron gun configuration were calculated using equations based on conservation of angular momentum and adiabatic electron motion.

Using the design equations given in [14] a first order design was found by specifying the main design parameters: current, voltage, main magnetic field, compression and α. Experience has shown [120] that a slope of 50° (between the axis of symmetry and the emitter surface) for the emitter produces the highest quality beams with an acceptable beam width. The basic gun design parameters can be plotted as a function of the mean emitter radius as shown in Figure 5-9. In order to minimize the maximum electric field and decrease the width of the emitter strip, a large compression factor is

Table 5.1: Electron Gun Parameters

Electron Gun	Preliminary Parameters
Type	Triode
Beam Voltage	35 kV
Beam Current	2 A
Max Current Density	5 A/cm^2
Beam Radius	1.0 mm
Velocity Pitch Factor, α	0.75
Perpendicular Velocity Spread	$\leq$ 3%
Cathode Radius	5.2 mm
Compression Ratio	25
Magnetic Field at Gun	0.4 T
Electric Field at Gun	$\leq$ 100 kV/cm
Cathode - Main Anode Voltage	15 kV

favorable. The practical limit for the compression factor is approximately 25; setting this as the criteria we arrive at a mean emitter radius of 5.2 mm. The remaining design parameters are marked as black dots in Figure 5-9.

The initial drawing of the triode electron gun using the design parameters from Figure 5-9 for a cathode slope of 50° was optimized using MICHELLE to minimize the perpendicular velocity spread. MICHELLE also verified the performance of the electron gun over a range of beam voltage (up to 50 kV) and mod-anode voltage to ensure that the electron gun would have the desired tunability. The final CAD drawing of the electron gun is shown in Figure 5-10. The mean emitter radius, emitter strip width, cathode slope and cathode-to-anode spacing correspond to the design parameters shown in Figure 5-9. The drawing of the electron gun includes the cathode (blue line), emitter (teal line), mod-anode (red line), the anode or common (green line) and dielectric spacers (purple line). The full CAD drawing as modeled extends to the right until the beginning of the interaction circuit, and the electron gun is cylindrically symmetric about the black line. The electron gun placement was determined using the magnetic field profile of the 9.6 T magnet. The emitter strip is located 366.8 mm before the beginning of the flat top of the magnetic field. One important consideration is that the magnetic field is monotonically increasing from

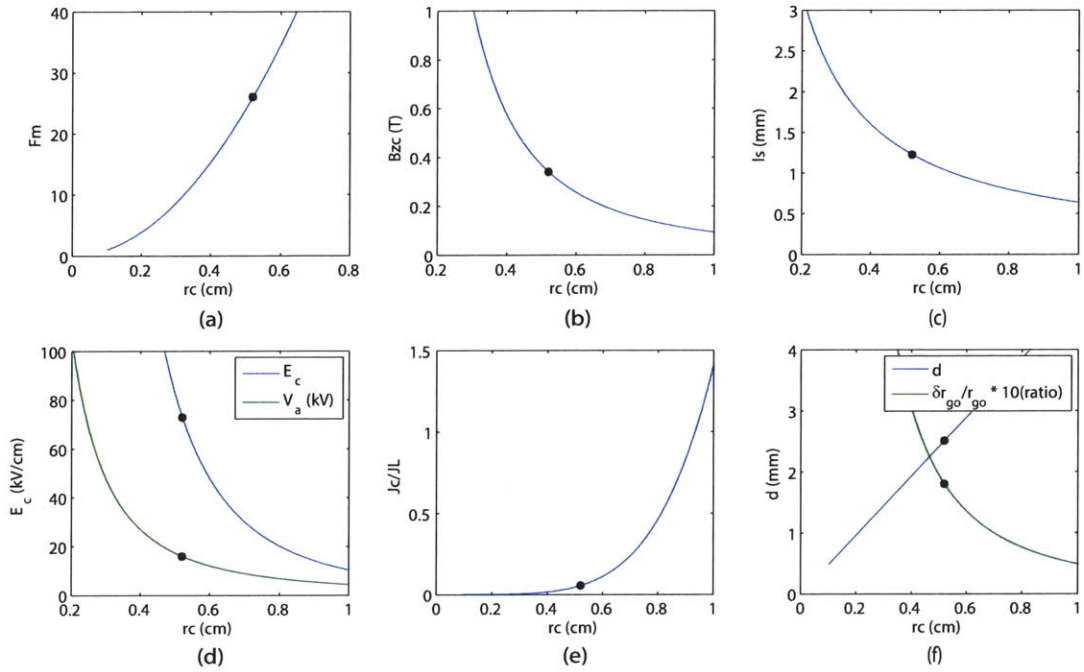

Figure 5-9: Gun parameters calculated using equations derived by Baird and Lawson for a 32 kV, 2 A beam and 50° cathode tilt. The (a) compression, (b) magnetic field at the emitter, (c) emitter width, (d) maximum electric field and cathode to mod-anode potential, (e) Langmuir space charge, and (f) cathode to mod-anode spacing, d, and guiding center spread are plotted versus the mean emitter radius. Black dots mark the selected design values.

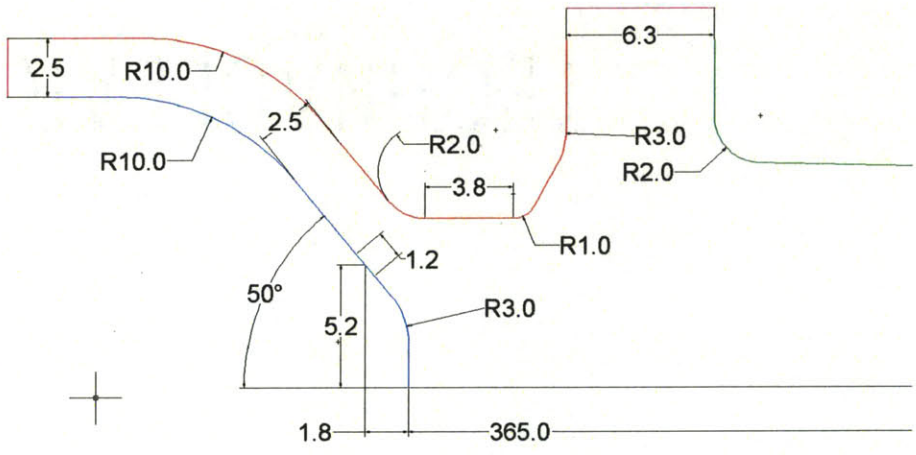

Figure 5-10: Schematic of the electron gun design with all units in mm unless otherwise marked.

the emitter location to the flat top. The magnetic field used to model the electron gun and the guiding center radius is plotted in Figure 5-7. The guiding center radius is monotonically decreasing as it approaches the flat top of the magnetic field. In Figure 5-7 the flat top of the magnetic field extends from 0 to 300 mm. The location of the electron gun is marked with a black dot. For the current design, the magnetic field uses an internal gun coil at 25% of its rated current to decrease the magnetic field at the cathode. It is possible that during operation the gun location could be changed, requiring an adjustment of the current in the gun coil to maintain the compression and ensure a proper guiding center radius. The magnetic field $\pm 25\%$ of the rated current of the gun coil is shown in Figure 5-8. The magnetic field at the cathode for the optimized electron gun is marked with a black dot.

The physical location of the electron gun resides within the 5″ magnet bore. A side view of the 9.6 T Cryomagnetics, Inc. magnet is shown in Figure 5-4. The emitter strip will be located 10 mm into the bore of the magnet. The electron gun will be encased in a metallic housing to provide a grounding plane allowing for the option of moving the electron gun without affecting the grounding plane by the presence of the inner wall of the magnet bore.

The optimal design parameters of the electron gun consist of a 2 A beam with a cathode voltage of -32 kV, a mod-anode voltage of -18 kV, and an anode voltage of 0 V. The electric field produced under these conditions is shown in Figure 5-11(a) with a comfortable maximum of 65.1 kV/cm. The potential lines and particle trajectories under the same conditions are show in Figure 5-11(b). Two distinct regions can be observed in the electron gun. The first stage extracts the electrons with the field produced by the mod-anode and is approximately one cyclotron orbit in length. The α and velocity spread are primarily determined in this section. The accelerating region occurs after the first complete cyclotron orbit where the electrons pass over potential lines that are transverse to their motion.

The triode electron gun designed using MICHELLE produces the desired beam pitch factor of 0.75 with a velocity spread of less than 2% for a 32 kV, 2 A beam

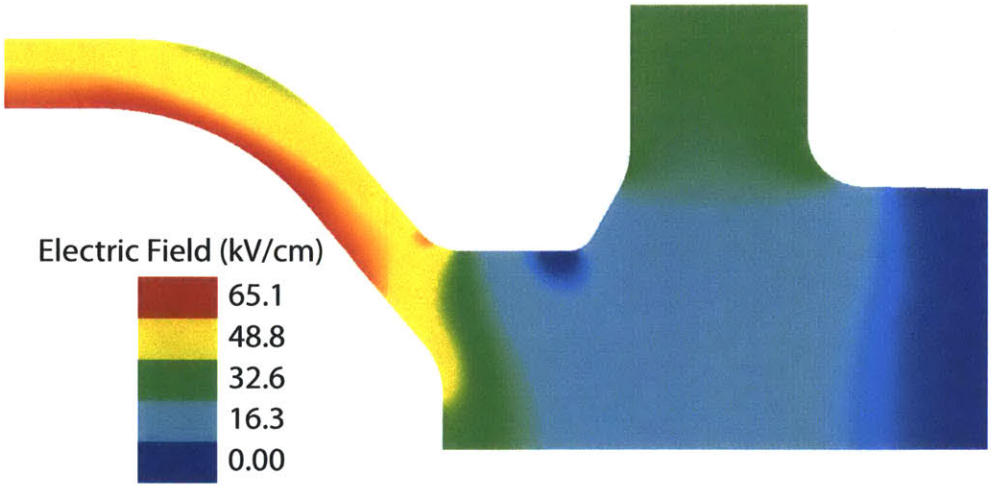

(a)

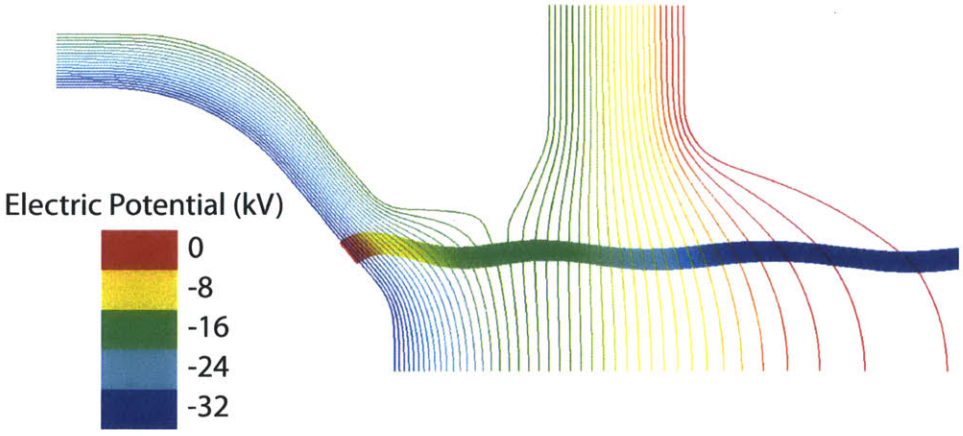

(b)

Figure 5-11: (a) Electric field distribution for the cathode at -32 kV, mod-anode at -18 kV and anode at ground. (b) Electric potential lines and particle trajectories for the cathode at -32 kV, mod-anode at -18 kV and anode at ground. Gun coil at 25% of rated current.

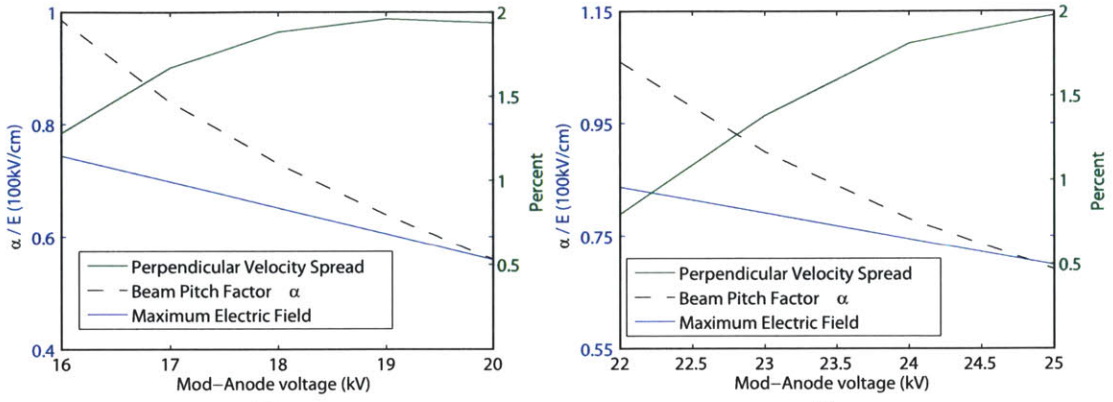

(a)

(b)

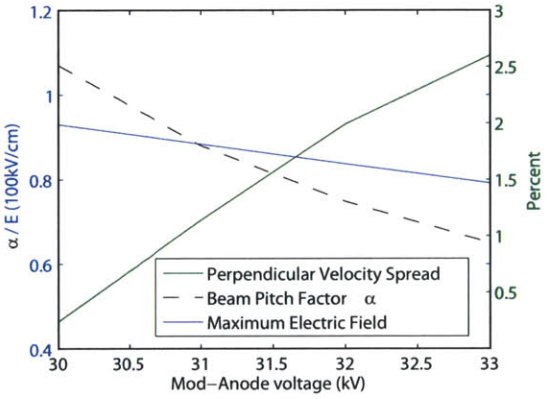

(c)

Figure 5-12: (a) Operational parameters for the electron gun at 32 kV, (b) 40 kV, and (c) 50 kV. Gun coil at 25% of rated current.

and 18 kV mod-anode voltage, as shown in Figure 5-12(a). The electron gun was also investigated over a large range of mod-anode and beam voltages. Results in Figure 5-12(a)-(c) indicate that this design is capable of producing an α of 0.75 for beam voltages as high as 50 kV with a velocity spread of ~2%. The velocity spread in the constructed electron gun will be greater due to surface roughness effects and machining errors and could rise to as much as ~5%. The final design consists of a cathode with a 50° tilt that can comfortably produce a 2 A beam (current density of 5 A/cm^2 at the emitter). The gun coil will provide additional tunability of the beam pitch factor and aid in the suppression of velocity spread. From 32-50 kV varying the mod-anode voltage to be 50-66% of the cathode voltage varies the beam from an α of 1-0.6 without ever exceeding the 96 kV/cm limit or reflecting electrons.

Once the electron optics were designed, the electron gun was fabricated by Communications and Power Industries, Inc. (CPI). Photographs of the emitter undergoing bell jar testing can be seen in Figure 5-13. The emitter is being heated during this testing and is visible as the section that is glowing red.

Activation of the electron gun was performed using an AC power supply for the filament and a DC power supply to bias the cathode and anode. The cathode was supplied with a maximum of $V_{\text{rms}}^{\text{AC}} = 8.52$ V and $I_{\text{rms}}^{\text{AC}} = 2.47$ A. After this initial activation the filament supply was replaced with a DC filament supply. **Special care must be taken when using a DC filament power supply because improper wiring will lead to permanent damage by shorting of the filament. As shown in the schematic from Figure 5-14, the cathode filament must be biased negatively with respect to the cathode assembly.** The cathode was supplied with a maximum of $V_{\text{peak}}^{\text{DC}} = 8.68$ V and $I_{\text{peak}}^{\text{DC}} = 2.50$ A. The cathode was deemed sufficiently activated when it achieved 1.2 mA of emission with an 80 V bias. After testing the electron gun with a DC filament power supply, the electron gun was connected with the high-voltage modulator which uses a DC filament power supply and can generate pulses from 2-50 kV for a duration of 10 μs. The I-V curve for the activated cathode is shown in Figure 5-15. A space-charge limited regime is observed up to a 1 kV bias voltage where the current emitted is proportional to $V^{3/2}$. After

this the cathode switches to a temperature limited regime. The emission from the electron gun can be controlled by varying the current provided by the filament supply, altering the emission in the temperature limited regime.

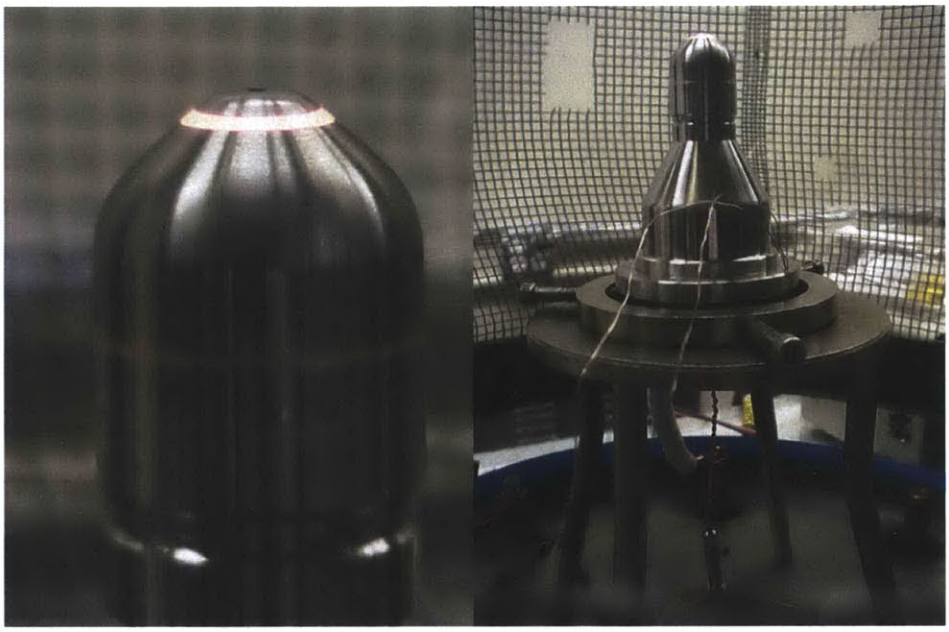

(a) (b)

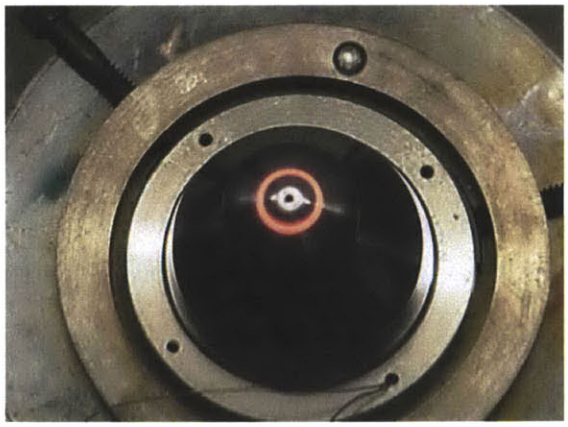

(c)

Figure 5-13: Bell jar tests conducted at CPI, Inc., courtesy of Kevin Felch. (a) Side view of the emitter and cathode. (b) Side view of the mounted cathode. (c) Top view of the cathode and emitter.

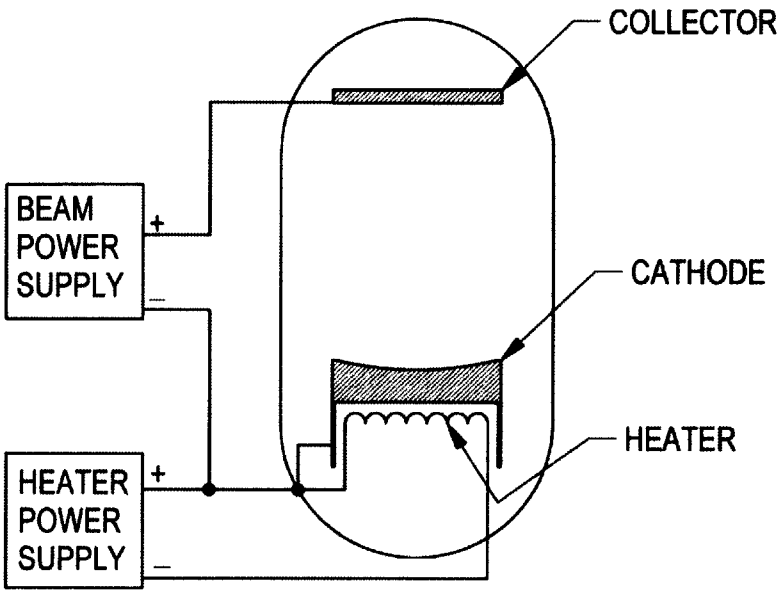

Figure 5-14: Correct wiring schematic for a heater power supply. Figure adapted from Spectra-Mat, Inc., Technical Bulletin TB-200 - C05/10.

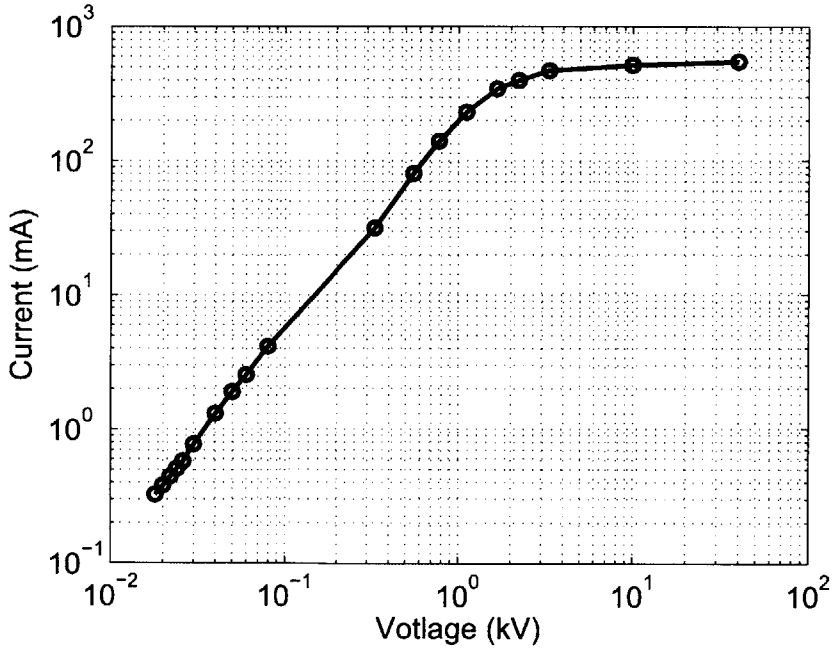

Figure 5-15: I-V characteristics for the electron gun measured during the activation of the cathode. The filament heater was set to 4.44 A on the high-voltage modulator GUI. Points below 100 V were measured using a DC bias.

5.4 Solid-State Driver

The driver for this experiment is a Virginia Diodes, Inc. (VDI) solid-state Amplifier / Multiplier Chain (AMC) with a rated performance of >30 mW in a ~4 GHz band centered at 252.5 GHz and with >10 mW over 10 GHz tuning band. Measured output power is shown in Figure 5-16(a) and the driver is shown in Figure 5-16(b). The output power was measured using a calorimeter head calibrated using a known laser source. The reflection coefficient of the calorimeter head at 250 GHz was measured using a vector network analyzer.

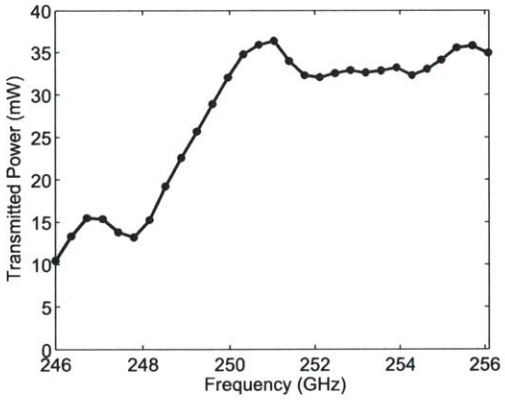

(a)

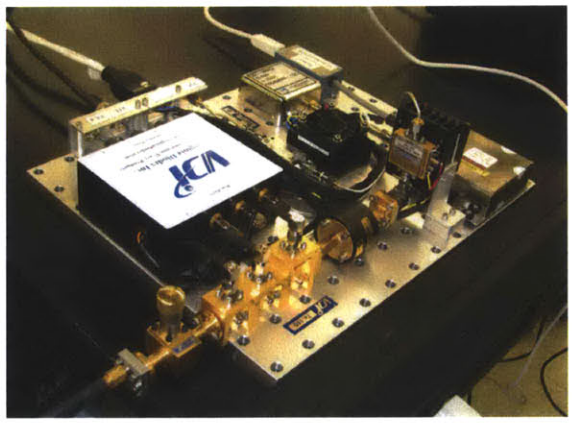

(b)

Figure 5-16: (a) Measured power delivered by the transmission line to WR-3 waveguide that will be coupled to the TE_{03} wraparound structure. (b) VDI solid state driver connect to a variable attenuator and a Pacific Millimeter detector diode used for signal of frequency measurements.

5.5 Control Software

The high-voltage modulator is controlled by a program that allows for adjustments to pulse length, peak voltage, repetition rate and heater current. Interlocks for arcing, water cooling and vacuum pressure are hardwired to the modulator trigger and filament heater power supply. The high-voltage modulator control software is shown in Figure 5-17(a).

The temperature of the He compressor that cools the superconducting magnet is monitored and recorded by LabVIEW. The He compressor is cooled by a water-to-water heat exchanger that is connected to the building chilled water supply. The thermal load of the He compressor is approximately 8.5 kW. In the event of a decrease in cooling capacity, the operation of the He compressor is cycled to limit the loss of liquid He from the magnet cryostat. For the compressor, the maximum safe point for operation is 29 °C. If the temperature exceeds the safe point, the compressor shuts down for 10 minutes minimum and does not return to operation until the temperature has lowered to an acceptable value. Figure 5-17(b) shows the monitoring and recording interface for the He compressor. A separate LabVIEW panel (not shown) controls the on/off status of the compressor based on the temperature.

The pressure in the vacuum vessel is monitored and recorded using a LabVIEW program, Figure 5-17(c), that communicates with a DATAQ DAQ card. The pressure is sampled at a 5 Hz and displayed. The pressure is recorded every minute in normal operation ($< 10^{-8}$ Torr). If the pressure exceeds 10^{-8} Torr, the entire previous minute of data is recorded.

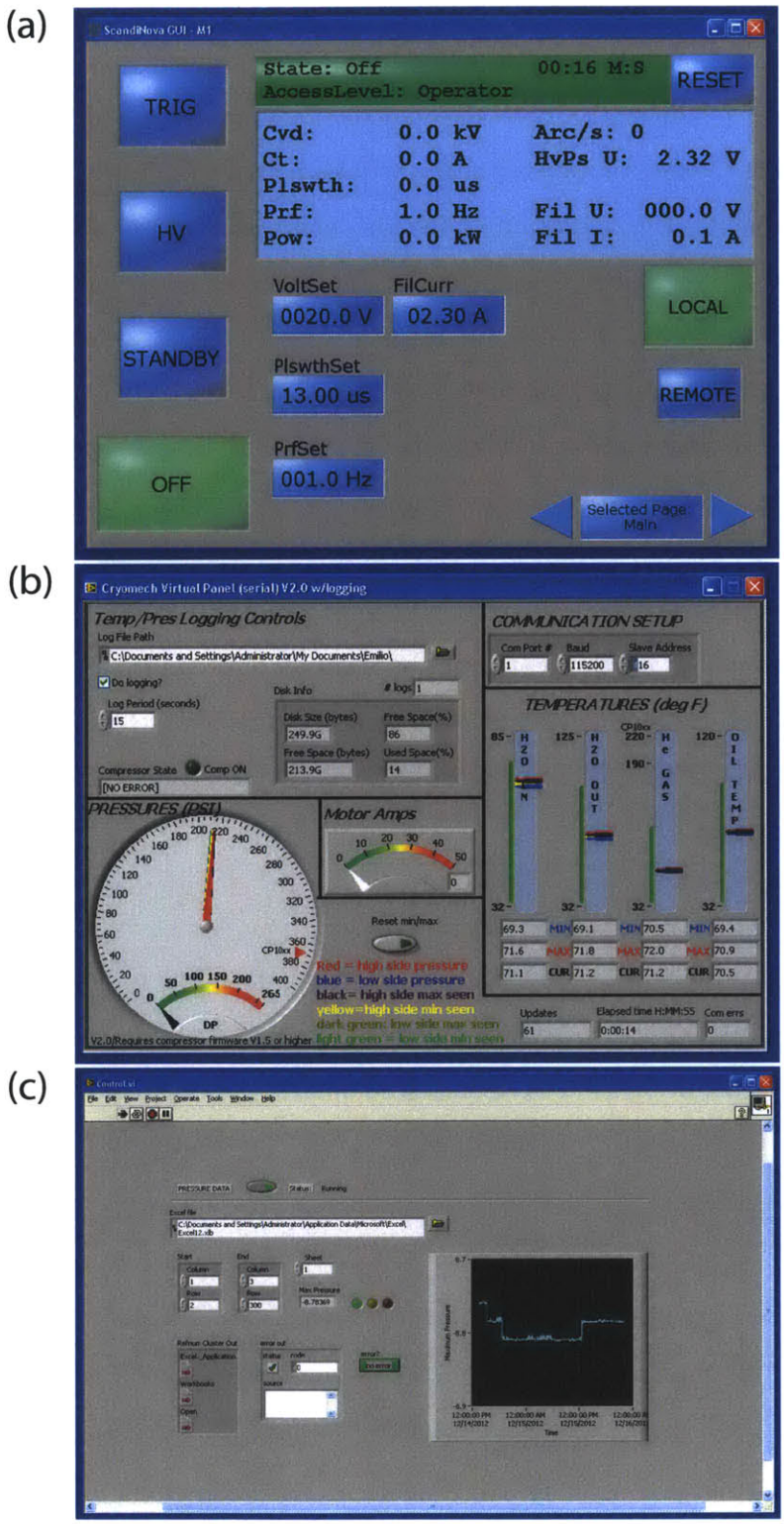

Figure 5-17: Various programs used to operate the gyrotron amplifier.

5.6 Heterodyne Frequency Detection

Microwave diodes are commonly used as detectors and mixers up to the THz band. For both applications, the nonlinearity of the diode is used to frequency convert the gyrotron amplifier frequency, f_{RF}, to a range of frequencies that can be detected by an oscilloscope. The I-V characteristics of a diode can be expressed as:

$$I(V) = I_s \left(e^{\alpha V} - 1\right) \tag{5.1}$$

where $\alpha = e/mkT$, T is the temperature, k is Boltzmann's constant, m is the ideality factor, e is the electron charge and I_s is the saturation current [102]. Assuming the diode voltage to be $V = V_0 + v$, where V_0 is the DC bias and v is a small AC signal, we can Taylor expand Equation (5.1) and rewrite the induced current as

$$I(V) = I_0 + i = I_0 + \frac{v}{R_{\mathrm{eff}}^{[1]}} + \frac{v^2}{2R_{\mathrm{eff}}^{[2]}} + \cdots \tag{5.2}$$

where

$$\left.\frac{d^j I}{dV^j}\right|_{V_0} = \frac{\alpha^{j-1}}{R_{\mathrm{eff}}^{[1]}} = \frac{1}{R_{\mathrm{eff}}^{[j]}} \tag{5.3}$$

I_0 is the DC bias current, i is the small signal current, j is an integer and $R_{\mathrm{eff}}^{[j]}$ is the effective resistivity.

If the diode is being used as a detector it will be excited with a signal $v(t) = v_{\mathrm{RF}} \cos(\omega_{\mathrm{RF}} t)$. The easiest signal to observe would be a DC bias induced at the diode by this small AC signal. Through our small signal analysis we see that the first order term is linear in v and would produce no DC bias. From the second order term, the only DC signal produced by the RF signal is

$$i_{\mathrm{DC}} = \frac{v_{\mathrm{RF}}^2}{4R_{\mathrm{eff}}^{[2]}}. \tag{5.4}$$

Note that the induced current from the RF signal in Equation (5.4) is linearly proportional to the RF power. This is referred to as *square-law* behavior and it is the typical

range of operation because it produces a distortion free signal. With too strong of an input power, the signal begins to saturate.

If the diode is being used as a mixer it will be excited with a signal $v(t) = v_{\mathrm{LO}}\cos(\omega_{\mathrm{LO}}t) + v_{\mathrm{RF}}\cos(\omega_{\mathrm{RF}}t)$, which is a combination of the RF signal and a local oscillator (LO) frequency, f_{LO}. In this case, we are interested in detecting a mixed signal that is lower in frequency and will allow us to determine the unknown f_{RF}. The first order term in Equation (5.2) that is linear in v will not produce any mixing, so, once again, we look at the second order term. The lowest-frequency non-DC signal produced is

$$i_{\mathrm{IF}} = \frac{v_{\mathrm{RF}}v_{\mathrm{LO}}}{2R_{\mathrm{eff}}^{[2]}}\cos((\omega_{\mathrm{RF}} - \omega_{\mathrm{LO}})t). \tag{5.5}$$

The frequency of this signal, known as the intermediate frequency f_{IF}, is used to determine f_{RF}.

A heterodyne receiver system, with the schematic shown in Figure 5-18, was used to perform frequency measurements for oscillations and amplification. The output of the gyrotron amplifier, f_{RF}, propagates along a corrugated waveguide to a corrugated horn antenna terminated with a receiver diode. Down-conversion of the signal at the diode to f_{IF} is performed by mixing the gyrotron amplifier signal with the n^{th} harmonic of f_{LO}.

For a given f_{IF}, there are two LO frequencies $f_{\mathrm{LO,upper}}$ and $f_{\mathrm{LO,lower}}$ that can result in the same f_{IF}:

$$f_{\mathrm{IF}} = f_{\mathrm{RF}} - nf_{\mathrm{LO,lower}}, \tag{5.6}$$

$$f_{\mathrm{IF}} = nf_{\mathrm{LO,upper}} - f_{\mathrm{RF}}. \tag{5.7}$$

Combining both equations, one can find the operating mixer harmonic n in order to obtain the unknown f_{RF}:

$$n = \frac{2f_{\mathrm{IF}}}{f_{\mathrm{LO,upper}} - f_{\mathrm{LO,lower}}}. \tag{5.8}$$

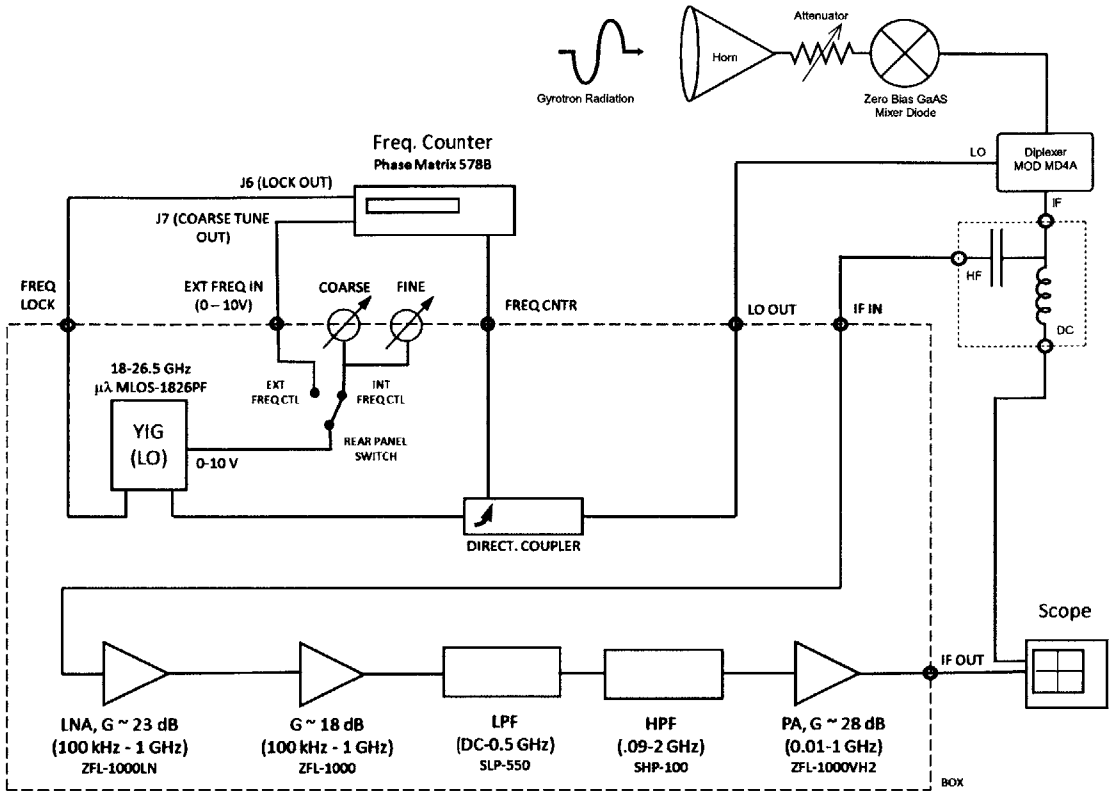

Figure 5-18: Schematic of the heterodyne receiver system for frequency measurement, adapted from [162].

The mixer diode utilized in this setup is either a Pacific Millimeter Products WR-3 harmonic mixer, model HM, or a WR-3 detector diode, model HD. The zero bias GaAs diode can detect a maximum input power of +20 dBm; however, the response of this *square-law* detector is only linear up to -20 dBm with ~3 dB of compression in sensitivity per decade of increased power. The ideal sensitivity of the diode is 150 mV/mW when operated as a detector. The mixer diode is connected to a Pacific Millimeter Products diplexer, model MD4A. The LO signal is provided by a Micro Lambda Wireless YIG oscillator, model MLOS-1826PF, voltage tunable over 18-26.5 GHz. The typical operational LO power provided to the mixer is +6 dBm and can be a maximum of +15 dBm. The combined RF and LO power at the mixer should not exceed +20 dBm. The LO frequency is measured by a Phase Matrix frequency counter, model 578B. This frequency counter has an automatic source locking capability able to stabilize the frequency of the electronically tunable YIG

oscillator. After the down-conversion, the IF signal is amplified and filtered from 100-500 MHz. The signal is Fourier transformed in order to determine the spectral content, which can be performed in real time by using an oscilloscope. The induced current of the harmonic mixer diode requires a DC return path. This can be provided by an inductor to ground or a diode bias circuit. Monitoring the self biasing of the diode on the DC channel allows one to confirm that an adequate amount of LO power is being supplied. Typically, 100-500 mV are observed on the DC component of the IF channel when the LO power is on. The heterodyne frequency detector is pictured in Figure 5-1, depicting from top to bottom, the oscilloscope, the LO and IF filter and amplifier, and the frequency counter.

Chapter 6

Experimental Results

A high-power gyrotron amplifier centered at 250 GHz has been designed, constructed and tested [110, 115, 116, 117, 114]. The design of the gyrotron amplifier was presented in Chapter 4. This gyrotron amplifier, Figure 5-1, will be used with a 380 MHz pulsed-DNP/EPR spectrometer. This is the highest frequency achieved for a gyrotron amplifier, and it has demonstrated the highest gain for a vacuum electron device above 94 GHz. At 32 kV and 350 mA, the gyrotron amplifier operates with peak small signal gain of 38 dB at 247.7 GHz. The instantaneous -3 dB bandwidth of the amplifier at peak gain is 0.4 GHz. For this operating point, a peak output power of 45 W has been measured. The output power is not saturated but is limited by the 7.5 mW of available input power. Additionally, the amplifier can be tuned for operation from 245-256 GHz. This chapter discusses the experimental results taken over a wide range of parameters, 15-30 kV and 0.25-0.5 A, which show good agreement with a theoretical model in the small signal regime. The theoretical model incorporates cold test measurements for the transmission line, input coupler, PBG waveguide and mode converter.

6.1 Solid Model

A cross section of the solid model for the gyrotron amplifier is shown in Figure 6-1. The electron beam in Figure 6-1 travels from the electron beam emitter on the left to

the collector on the right. The insert at the bottom of the figure shows a magnified view of the interaction region for the electron beam and the electromagnetic wave. The 300 mm flat field of the magnet includes everything between the wraparound coupler and the Vlasov launcher. The main limiting factors for the design of the vacuum vessel were set by the 5″ magnet warm bore diameter; the vertical orientation for the gun; a limiting height of 78″ in order to insert/remove the gyrotron under vacuum; input and output ports for the microwave signal; and good conduction for the vacuum pumps.

The electron gun designed at MIT, Section 5.3, and fabricated by Communications and Power Industries, Inc. was terminated with a 2-3/4″ Conflat (CF) flange. The maximum outer diameter of the electron gun was 4.73″. A high-voltage interface was designed to provide connections for the cathode, mod-anode and heater filament in oil to prevent electrical breakdown. The high-voltage interface was designed such that it does not need to be dismounted in order to remove the gyrotron amplifier from the magnet bore. This allows the oil tank inside the interface to remain sealed during maintenance.

In order to take advantage of the full bore size, a custom step transition in the external vacuum vessel was included between the electron beam tunnel and the amplifier insert. To increase the effective pumping speed at the electron gun, many slots were placed in the beam tunnel prior to the step transition. The electron beam tunnel is inserted prior to connecting the electron gun to the vacuum vessel and cannot be removed without removing the electron gun. A molybdenum electron beam scraper is found at the end of the electron beam tunnel. A misalignment of the electron beam with respect to the main magnetic field results in interception at the scraper.

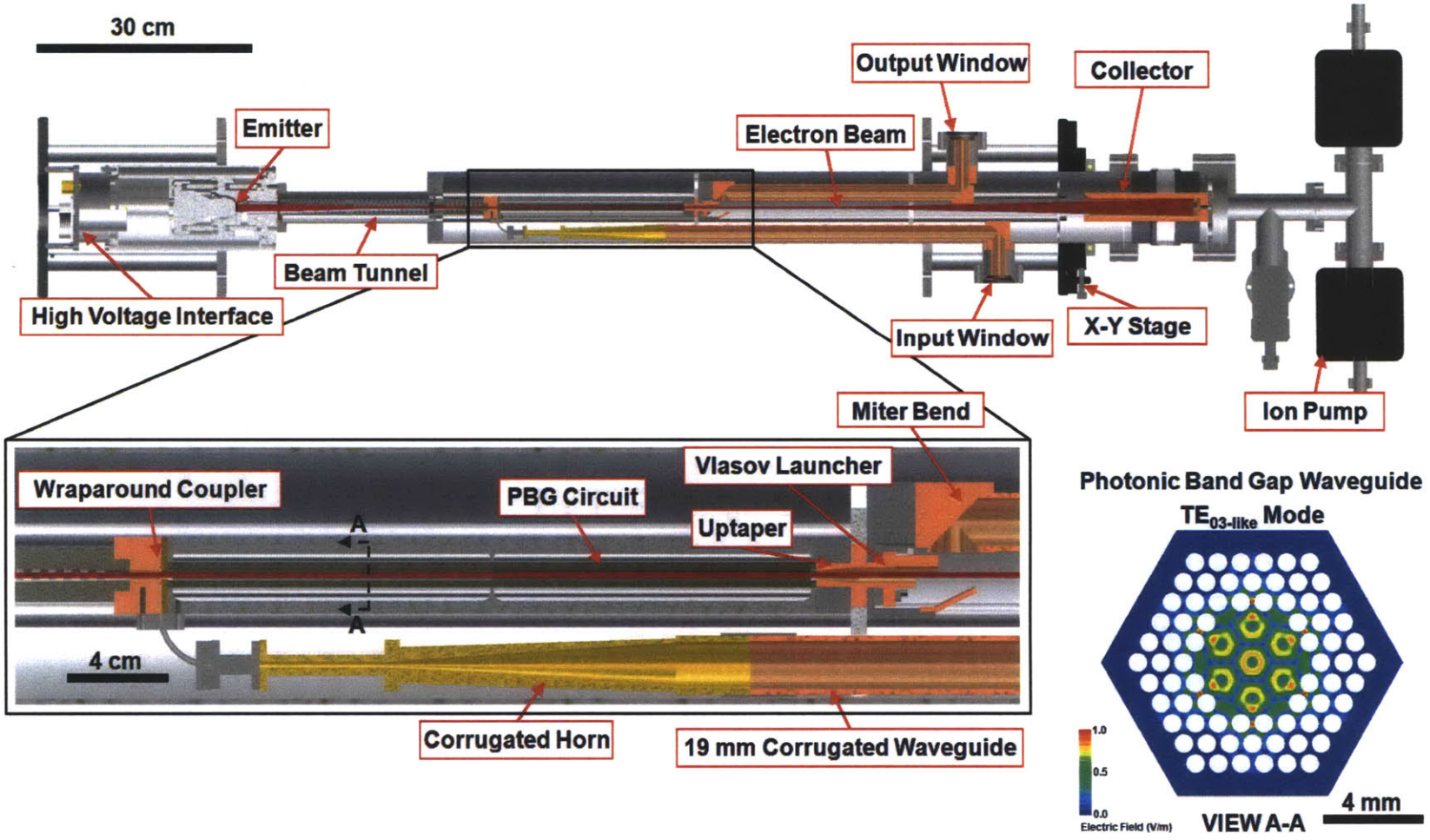

Figure 6-1: Autodesk Inventor solid model of the gyrotron amplifier.

All components which are used to guide the microwave signal, collectively referred to as the amplifier insert, are assembled from the collector side of the vacuum vessel. The amplifier insert includes the input transmission line, input coupler, interaction circuit, Vlasov launcher and output transmission line. This insert is fully removable from the collector side, which allows for changes to be made rapidly and without removing the entire gyrotron amplifier from the magnet. Due to the long distance between the solid-state driver and the amplifier, a 19 mm diameter helically-tapped overmoded corrugated waveguide was used to bring the driver signal to the input coupler. The wraparound input coupler requires a fundamental WR-3 waveguide connection. A corrugated horn transition from HE_{11} to WR-3 TE_{10} was included inside the vacuum vessel at the termination of the overmoded waveguide. The wraparound coupler, PBG waveguide and Vlasov launcher are assembled together as a stack with alignment provided by cylindrical inserts, if concentricity was the only requirement, or stainless steel alignment rods, if concentricity and azimuthal orientation were required. The alignment rods are threaded at both ends to provide axial compression for the stack. The stack is supported by a beam tunnel extension which can be removed to adjust the axial position of the circuit.

After the circuit, the microwaves are mode converted using a Vlasov launcher and then a steering mirror couples the Gaussian beam into an overmoded helically-tapped corrugated waveguide. This includes two miter bends forming a periscope output transverse to the electron beam. A non-axial output window was selected due to the additional length that would have been required, in addition to increased ease of use given the vertical orientation of the amplifier. A copper collector is suspended from a flange after the input/output windows and a ceramic break, which allows for independent monitoring of body and collector current. An all-metal valve and two 20 L/s ion pumps are located after the collector. A X-Y alignment stage on the collector side of the magnet was designed to both support the vacuum vessel and provide precision alignment for the electron beam. Axial alignment is provided on the gun side of the magnet from the HV interface support rods. These rods have replaceable ring extensions that allow for axial alignment in specific increments.

Additional X-Y alignment is available with adjustments to the support rods; however, this is very limited because of the 0.27″ difference between the diameter of the electron gun and the magnet bore. All custom fabrication for this experiment was performed at the MIT central machine shop, with the exclusion of the electron gun.

6.2 Cold Tests

6.2.1 Wraparound Coupler and Launcher

As components were fabricated for the amplifier, measurements for characterization were performed using a VNA (Agilent E8363B with Millimeter Wave VNA extender V03VNA2-T/R). Initial testing focused on the input coupler combined with the Vlasov launcher to test the power coupled through these passive components before the addition of the PBG circuit. The fabricated wraparound coupler and Vlasov step-cut launcher with mirrors and a miter bend were assembled, Figure 6-2, and tested with a comparison between the measured and calculated S_{21} shown in Figure 6-3. The power radiated from the miter bend was coupled back into WR-3 waveguide for the VNA detector using a corrugate-horn HE_{11} to WR-3 TE_{10} mode converter connected to the miter bend. The same mode converter was used to detect the amplified signal on a diode during the operation of the amplifier. PBG waveguide sections of 20 mm and 40 mm that mate with the wraparound coupler were cold tested, with a measured loss of -1.8 dB/cm for the TE_{03}-like mode at 250 GHz in good agreement with simulations. The cold test structure for the PBG waveguide measurements is shown in Figure 6-4.

6.2.2 Overmoded Transmission Line

A 19 mm inner diameter corrugated waveguide and two horns are used to efficiently couple the microwave source to the circuit. The measured radiation pattern of the

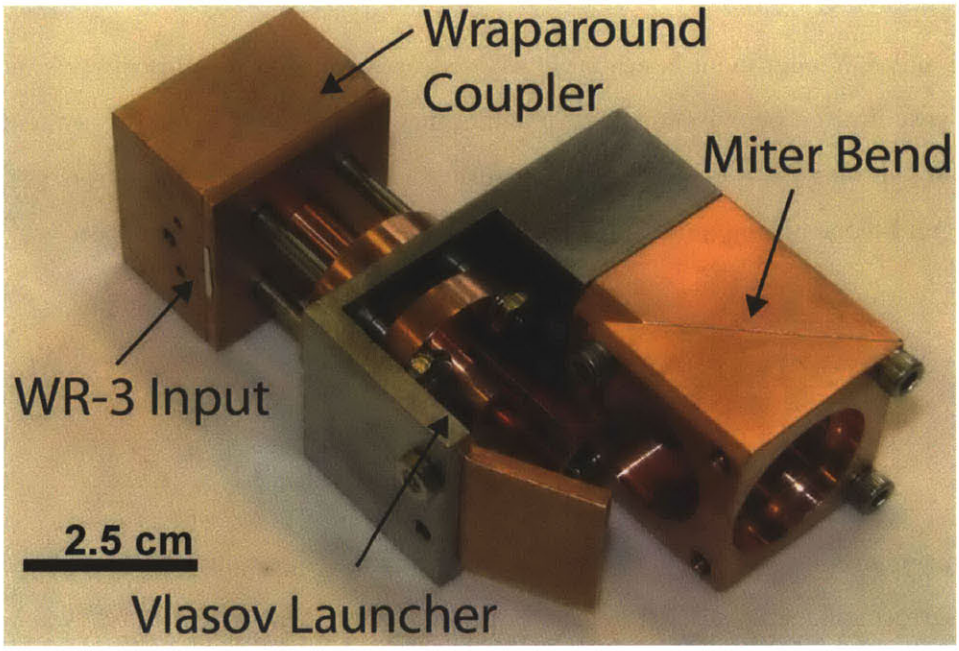

Figure 6-2: Assembled structure used in the cold tests for the TE_{03} wraparound coupler, up-taper and step-cut launcher.

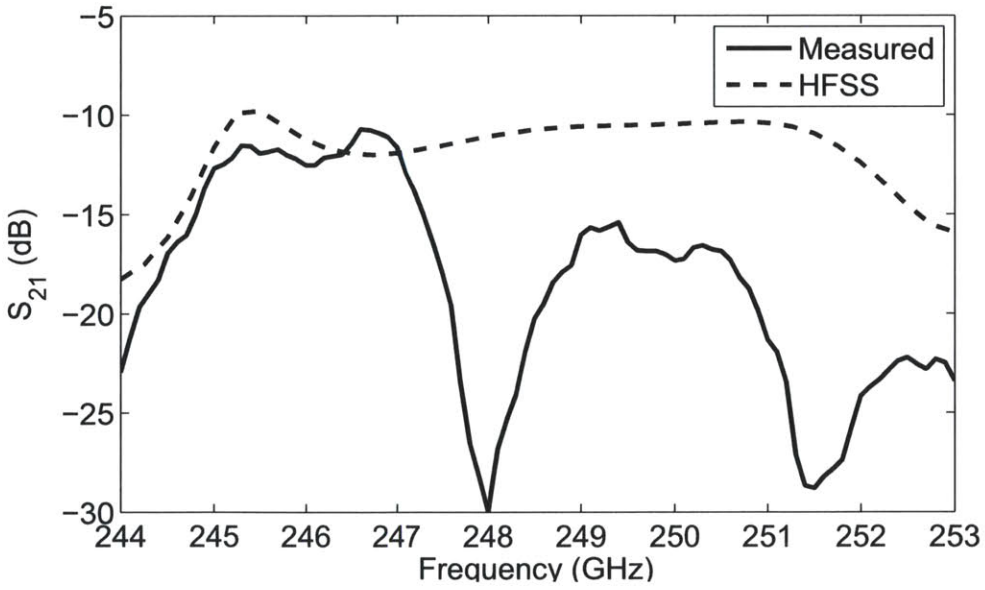

Figure 6-3: Measured and calculated S_{21} for the TE_{03} wraparound structure, up-taper and step-cut launcher. A corrugated horn was used to detect the radiated beam and couple it to the network analyzer.

horns at 250 GHz has a 94±0.3% HE_{11} mode content [89]. Six meters of brass over-moded helically-tapped corrugated waveguide were fabricated for the transmission line connecting the solid-state source to the gyrotron amplifier (3.5 m) and for the output of the gyrotron amplifier (2.5 m). The helical tap allowed for fabrication of sections as long as 24 inches, greatly increasing the accuracy of the alignment of the transmission line. The helical grooves are slightly trapezoidal with a depth of 0.33 mm and a period of 0.4 mm allowing for optimized performance at 250 GHz. The measured loss in the operational band for 4 m of transmission line, shown in Figure 6-5, was measured to be 1.4%.

6.2.3 Component Calibration

The transmission line windows for the input and output arm of the vacuum vessel were provided by MPF Products, Inc. The 1.4″ diameter quartz windows were brazed into 2-3/4″ CF flanges and had a measured thickness of 0.133″. The window was specified as UV grade fused silica. The windows were tested using the VNA and the 250 GHz corrugated horns that were employed on the input transmission line. The measured S_{21} is shown in Figure 6-6(a). The theory curve which fits the measurements is for d=0.1335″ and $\epsilon = 3.98$ in good agreement with previous measurements of other quartz samples [162]. To protect the solid-state source from spurious oscillations, a WR-5 isolator was placed immediately after the driver. A WR-5 isolator was selected because it is available commercially from Radiometer Physics GmbH. Two WR-3 to WR-5 transitions were used to mate the source and corrugated horn to the isolator. The S_{21} for the forward/reverse orientation of the isolator and both WR-3 to WR-5 transitions is shown in Figure 6-6(b). A Custom Microwave, Inc. WR-3 variable attenuator was used to protect the receiver diode during operation of the amplifier and to vary the input power delivered to the amplifier. The attenuation is controlled by a micrometer with the calibration shown in Figure 6-7(a) and the test setup shown in Figure 6-7(b).

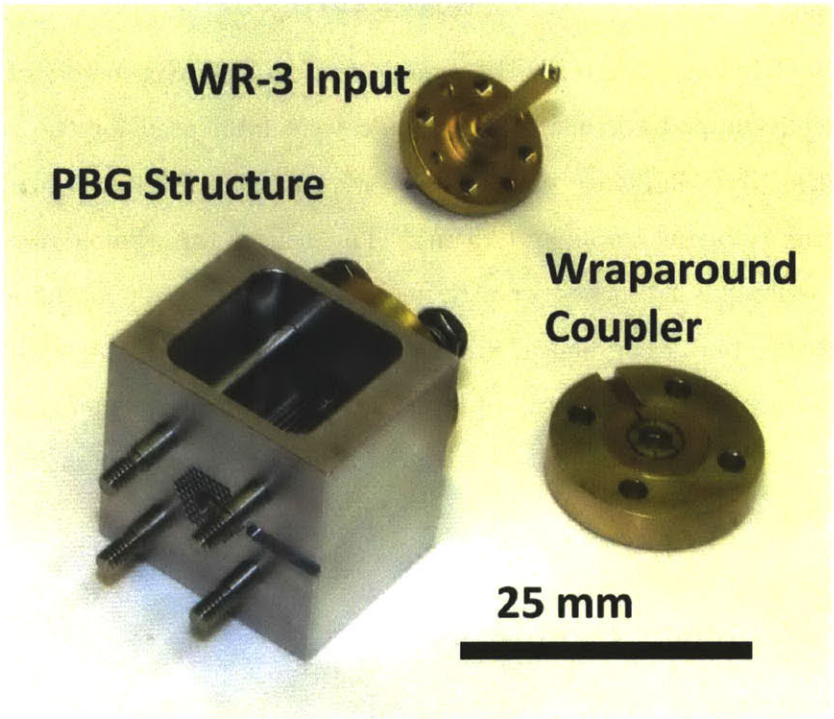

Figure 6-4: Structure used in the cold test of the PBG waveguide.

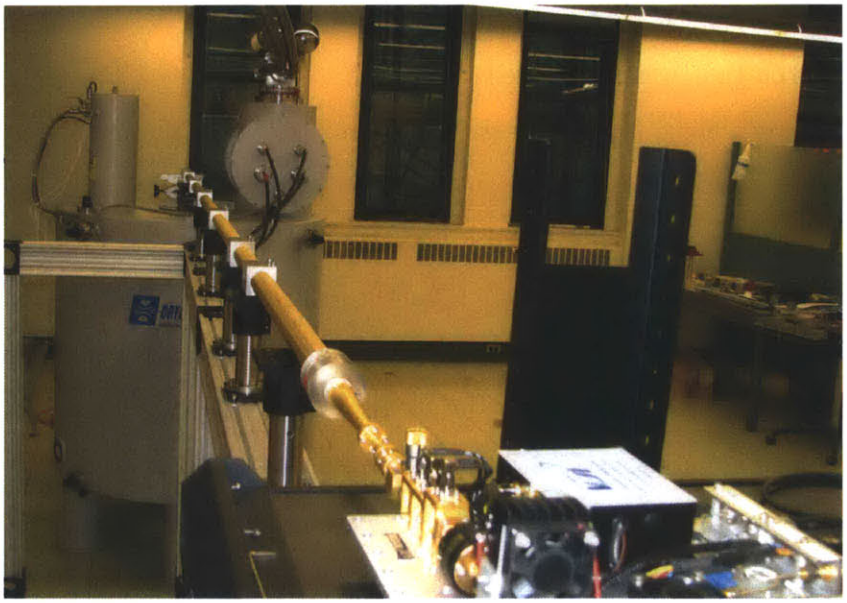

Figure 6-5: Setup for testing a 4 m helically-tapped corrugated waveguide with a 250 GHz source (bottom right). Also shown, the 9.6 T magnet that was used for the gyrotron amplifier (top left).

A Gentec-EO Pyroelectric Joulemeter Probe that is capable of measuring the total energy produced during the amplified pulse with 100 nJ accuracy was calibrated using a 140 GHz extended interaction oscillator (EIO) with a known power output and a 2 μs pulse. A calibrated variable attenuator was used to adjust the power level seen by the Joulemeter and a detector diode. The calibration for the Joulemeter is shown in Figure 6-8(a). These measurements were also confirmed using a 140 GHz solid-state source that produces 120 mW peak power. The pulse length of the solid state source was varied from 2-30 μs with no observable effect on the Joulemeter calibration. Figure 6-8(b) shows the diode and Joulemeter signal used to produce the calibration curve in Figure 6-8(a). The diode trace (solid line) shows a 2 μs pulse at five levels of attenuation and the corresponding (matching color) Joulemeter trace (dashed line). The diode voltage is not linear with the Joulemeter and it must be scaled to account for compression, discussed in Section 5.6, because the input power level to the diode is greater than -20 dBm. The compression was confirmed by the use of the calibrated variable attenuator.

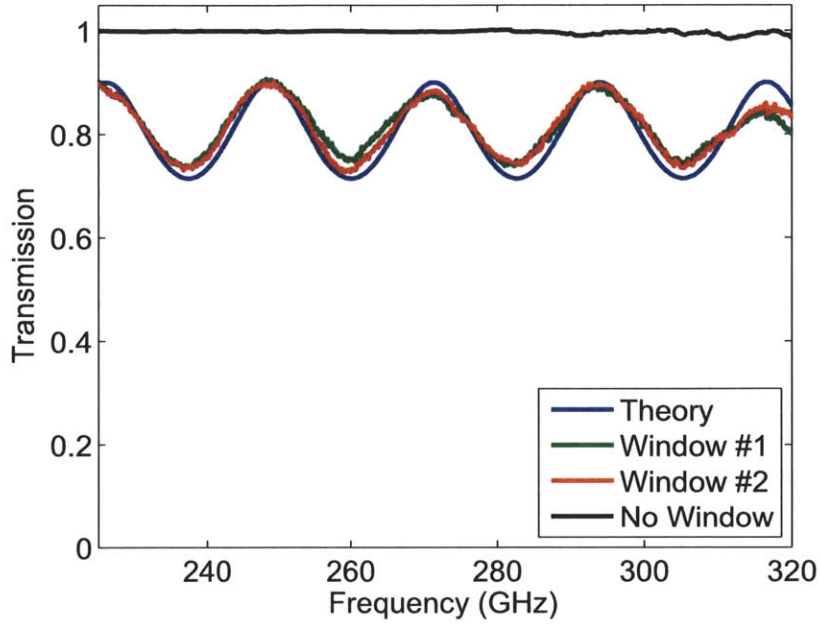

(a)

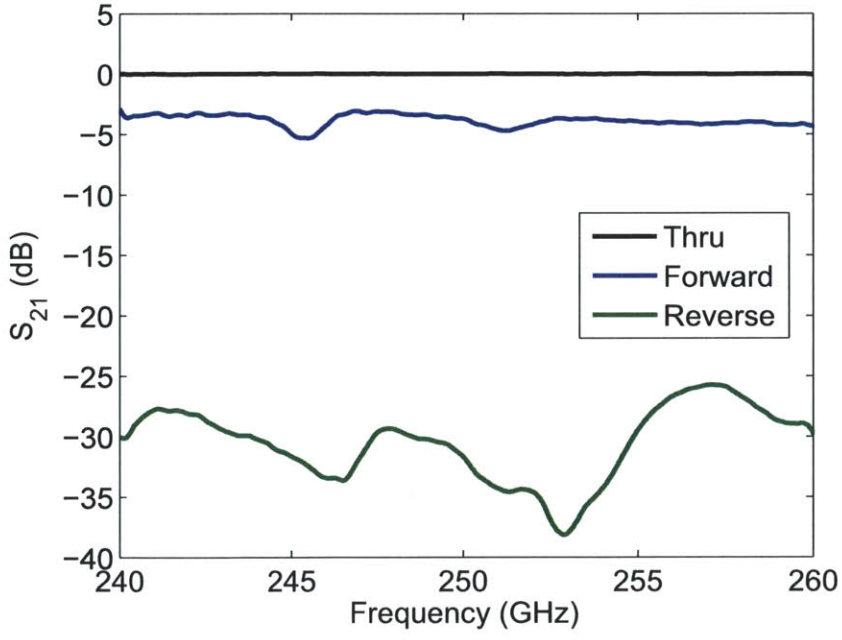

(b)

Figure 6-6: (a) VNA measurements for the Quartz windows purchased from MPF. (b) S_{21} for the forward and reverse direction of the isolator as a function of frequency. The thru measurement is the baseline connection between the two millimeter wave extender heads used by the VNA to reach the 220-330 GHz band.

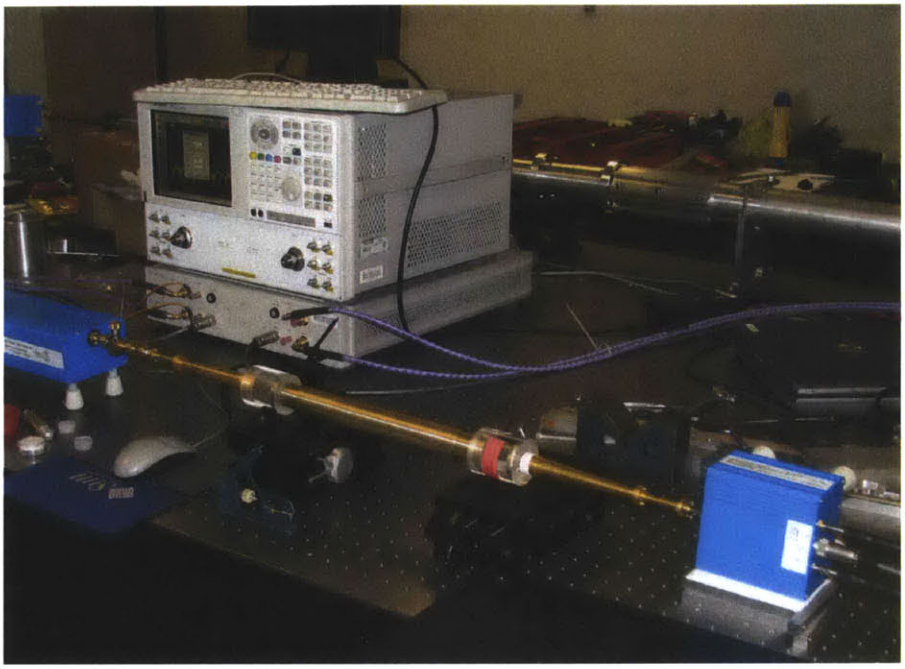

(a)

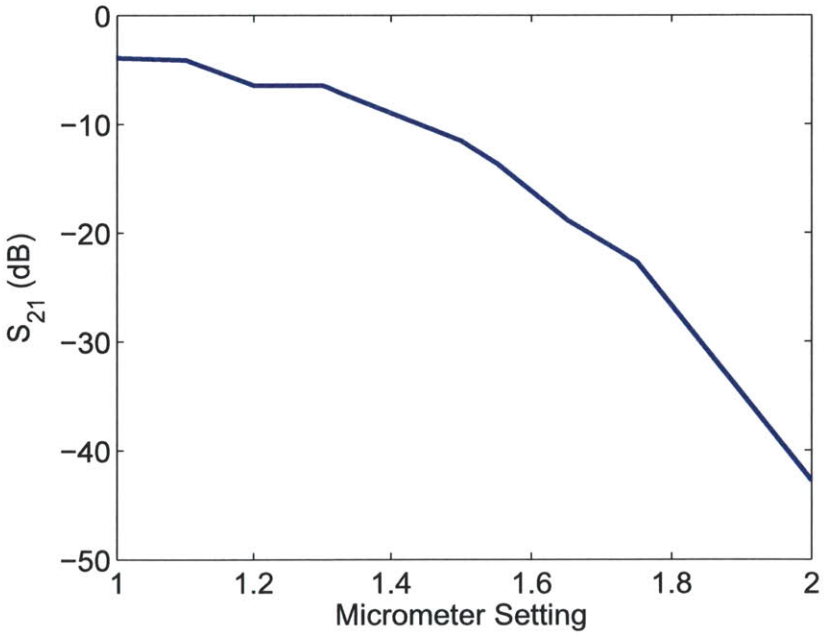

(b)

Figure 6-7: (a) The VNA setup during the testing of the variable attenuator and the corrugated horns. (b) S_{21} for the attenuator as a function of the micrometer setting. A minimum attenuation of 4 dB was observed due to this component.

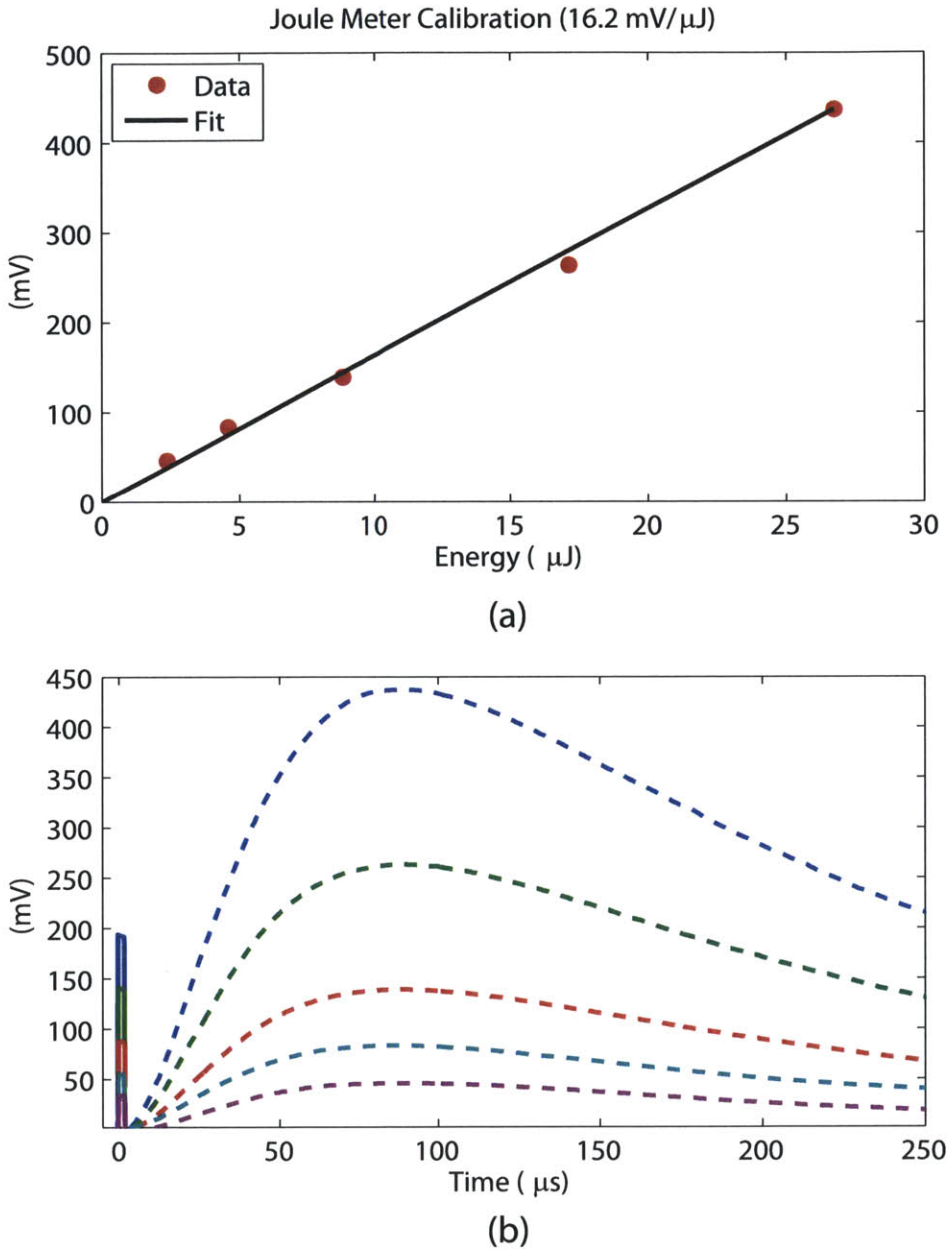

Figure 6-8: (a) Pulse energy vs. Joulemeter output voltage. Measured values produced using a 140 GHz EIO with various levels of attenuation. A linear fit of the data corresponds to a sensitivity of ~16 mV/μJ. (b) Oscilloscope trace produced by the Joulemeter and a detector diode for various attenuator settings recorded simultaneously. The solid lines are the detector diode and the dashed lines correspond to the Joulemeter.

6.3 Assembly

The components internal to the vacuum interface were individually cleaned with acetone followed by ethanol. If the components were considered difficult to clean due to corrugations, slots, bolt holes or required delicate handling, they were cleaned with acetone and then ethanol in a heated sonicator. These troublesome components were also baked, prior to assembly, in a separate vacuum chamber to ensure that they reached a temperature $\geq$150 °C. After baking individual components, the various sections of the amplifier (beam tunnel, amplifier insert, collector) were assembled. Various stages of the PBG amplifier insert are shown in Figure 6-9 and Figure 6-10. The entire amplifier, with the exclusion of the electron gun, was baked at 150 °C until the pressure stabilized at 3×10^{-7} Torr. The electron gun was excluded because this prevented potentially dangerous compounds from collecting on the emitter surface of the electron gun. After the bake was completed, the vacuum vessel was back-filled with nitrogen and the electron gun was attached. The completed gyrotron amplifier is shown in Figure 6-11.

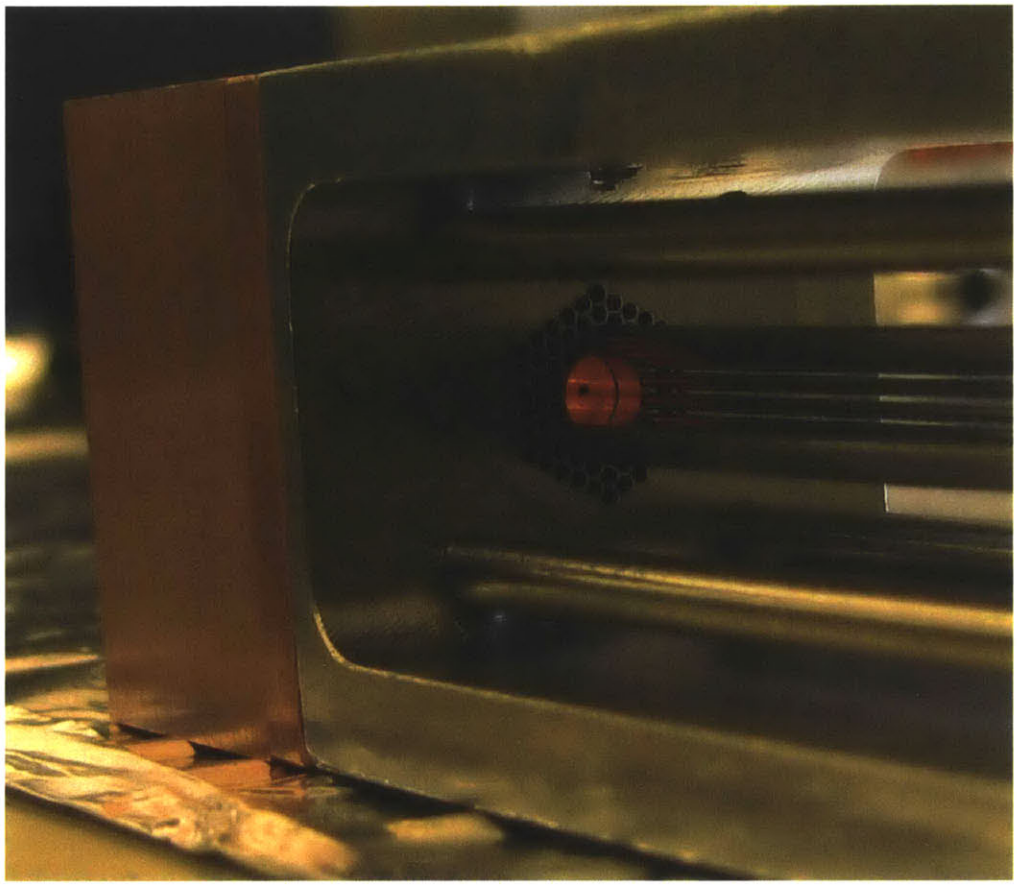

(a)

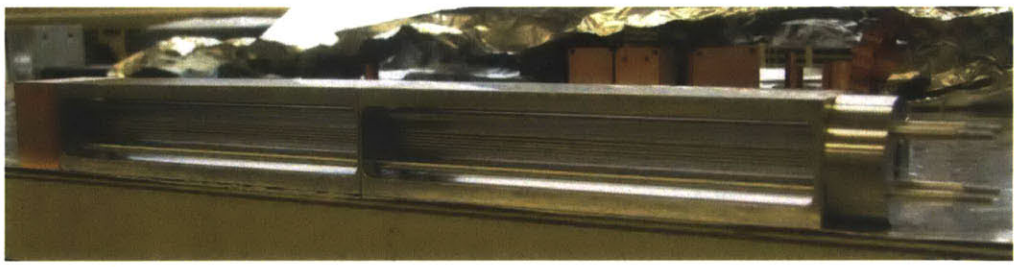

(b)

Figure 6-9: (a) Wraparound coupler (copper) mated to the stainless steel support structure for the PBG rods. One of the coupling slots is visible on the inner surface of the circular copper waveguide. Several rods from the first row of the PBG have been inserted. (b) Fully assembled PBG circuit prior to the connection of the Vlasov launcher.

(a) (b)

Figure 6-10: (a) Fully assembled amplifier insert with the input corrugated waveguide on the right and the output on the left. (b) Close-up of the corrugated horn mated to the wraparound coupler and PBG circuit which is supported by the final section of the slotted beam tunnel. Venting holes for the first section of the beam tunnel and the electron gun are visible on the mounting plate (bottom) around the slotted beam tunnel.

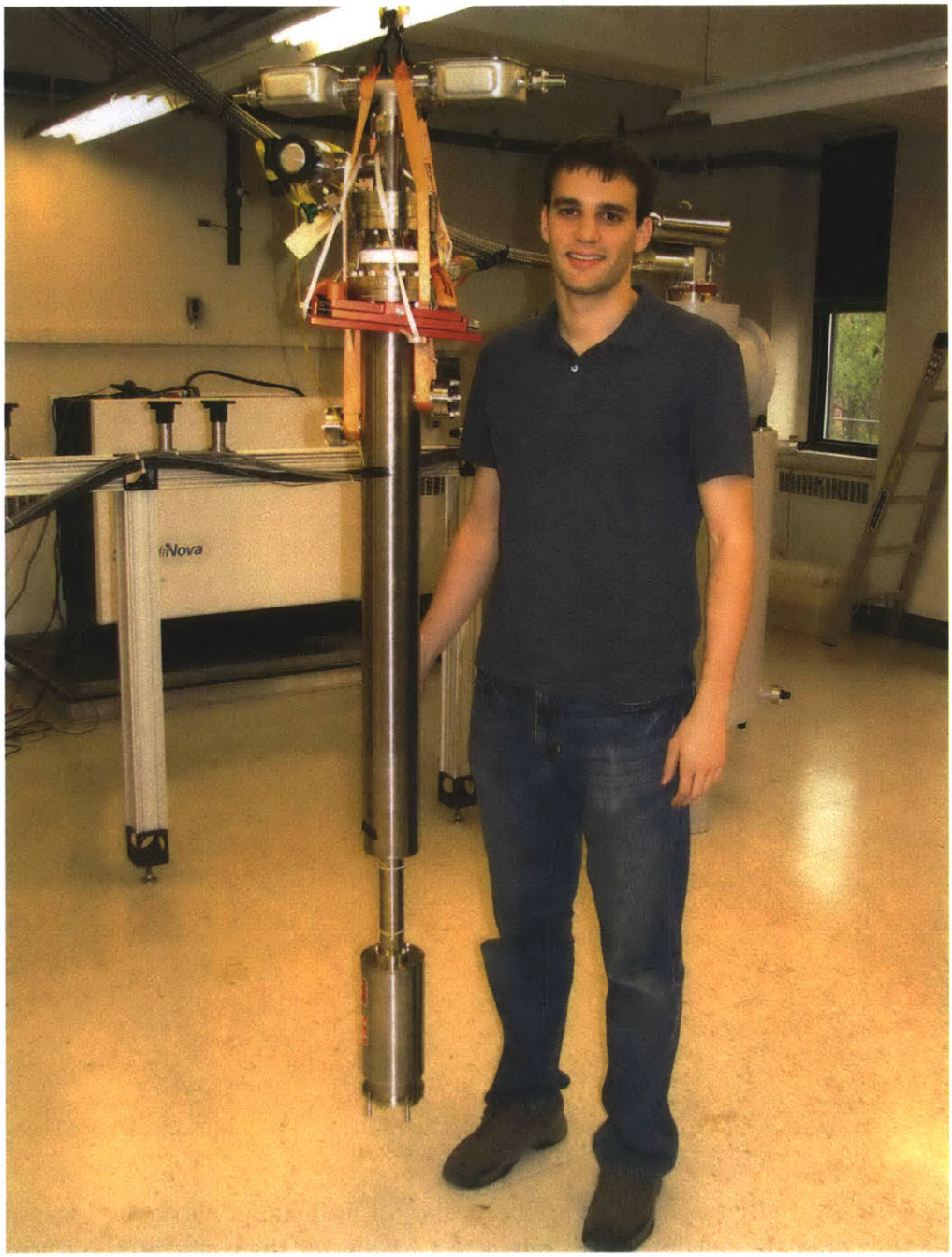

Figure 6-11: The Fully assembled amplifier insert immediately prior to insertion into the magnet bore.

6.4 Gyrotron Amplifier Results

The gyrotron amplifier, with the design described in Chapter 4 and the experimental setup described in Chapter 5, was tested over a wide range of parameters to find its optimized performance. The following section describes the results achieved during this investigation, of which the primary concern was determining the peak output power and hence the gain of the device. Additionally, properties (instantaneous bandwidth, linearity, spectral purity, output pattern, etc.) which are important to the practical implementation of the amplifier were investigated.

Power measurements were performed using two separate methodologies. The first approach entailed the use of a HD Pacific Millimeter zero-bias GaAs diode, calibrated on a CW solid-state source at 250 GHz in conjunction with a calibrated WR-3 variable attenuator to measure the peak power produced by the amplified pulse. The second approach was the use of a Gentec-EO Pyroelectric Joulemeter Probe that is capable of measuring the total energy produced in the pulse with 100 nJ accuracy, Section 6.2.3.

A typical amplified pulse measured at the output of the gyrotron using the detector diode is shown in Figure 6-12. The pulse is amplified during the entire 6 μs flat top of the voltage pulse. This pulse was recorded at 245.9 GHz, 31.6 kV, 0.14 A and 8.77 T.

Due to the large bandwidth provided by the input coupler, the operational frequency of the amplifier can be tuned from 245-256 GHz by varying the operational parameters (i.e. electron beam voltage, beam pitch factor and magnetic field) from 11.5-33.1 kV, 160-460 mA and 8.54-8.92 T. The peak power measured over the course the experiment is shown in Figure 6-13 as a function of frequency. A peak power of 45 W was measured at 247.7 GHz for 32 kV and 350 mA. With an input power of 7.5 mW, the gain for this operating point was 38 dB. The output power tends to be higher closer to cutoff because of the increase in interaction efficiency with the electromagnetic wave. Eventually, the power weakens close to cutoff due to the limited power available from the solid-state source, Figure 5-16(a). The notches in the power spectrum are related to the coupling efficiency of the source to the PBG circuit and

arise primarily from the wraparound coupler, Figure 6-3.

6.4.1 Output Beam Pattern

One of the novel aspects found in the 250 GHz gyrotron amplifier is the use of an internal mode converter in conjunction with a corrugated waveguide periscope. The internal mode converter, Figure 6-4, transforms the TE_{03}-like mode of the PBG circuit into a Gaussian beam which propagates with high efficiency in corrugated waveguides [113]. The periscope that is internal to the vacuum interface allows the mode converter to be located immediately after the circuit, which limits the excitation of performance-limiting oscillations. The Gaussian beam that exits the amplifier will allow for efficient transmission to the pulsed-DNP/EPR spectrometer [174]. The measured radiated pattern from the amplifier during operation is shown in Figure 6-14. The output pattern was recorded using a 2D automated scanner with a cut WR-3 waveguide probe terminated with a detector diode. The measured pattern is 92.4% Gaussian with beam waists of $w_x = 6.6$ mm and $w_y = 6.8$ mm. The simulated output beam pattern from HFSS is shown in Figure 6-15. The simulated pattern is 93% Gaussian with beam waists of $w_x = 5.8$ mm and $w_y = 5.6$ mm. As mentioned in Section 4.4, the beam waist is smaller in the simulation because the waist will expand until it reaches the aperture of the corrugated waveguide. This is the first successful demonstration of a periscoped waveguide internal to a gyrotron. Similar approaches for efficient power extraction are being considered for MW gyrotrons [119].

6.4.2 Frequency Measurements

In order to confirm the gyrotron amplifier is operating correctly, frequency measurements were taken to determine the spectral purity of the amplified pulse. Frequency measurements were performed using the heterodyne frequency detector described in Section 5.6. Under ideal conditions, the amplified pulse will preserve the frequency spectrum produced by the solid-state source. Several sources of noise could result

in increased bandwidth for the pulse including noise from the driver, noise from the electron beam, the inherent bandwidth of the pulse, waveguide dispersion or dispersion from the gain spectrum. For the long pulse experiments that were conducted, waveguide and gain dispersion were not a noticeable factor. Additionally, solid-state drivers are very low noise and the electron beam itself was not observed to make any contribution to the frequency spectrum bandwidth. For stable amplification, the spectral bandwidth given by the Fourier transform should be on the order of 180 kHz because the input signal is amplified over the flat top of the pulse (6 μs),.

A comparison between the measured frequency spectrum for an oscillation and amplification is shown in Figure 6-16. The frequency spectrum for an oscillation tends to be much broader (~10 MHz) than amplification because the oscillation frequency is very sensitive to fluctuations in voltage, axial mode competition and the unstable nature of oscillations during the start-up phase. When the microwave signal is the result of amplification, a stable discrete peak is produced and the measured frequency corresponds to the driver output. The frequency is confirmed by measuring the LO and IF frequency for both the upper and lower side bands. In Figure 6-16(b), the driver frequency is adjusted by 24 MHz resulting in corresponding shifts in the observed IF frequency for a fixed LO.

The frequency spectrum of the pulse is shown on a logarithmic scale in Figure 6-17(a) along with the background noise when the driver is turned off but the high voltage is pulsed. In Figure 6-17, the oscilloscope trace is shown for the amplified gyrotron signal down-converted from $f_{RF} = 253.632$ GHz to a Fourier transform peak at $f_{IF} = 300$ MHz for $f_{LO,upper} = 19.487$ GHz and the 13$^{\text{th}}$ mixer harmonic (n). The noise present in the baseline (off) signal, green line Figure 6-17(a), is due to noise from the receiver setup. Noise from the YIG LO, which is amplified through the IF channel, is the primary contributor to the baseline signal. The measured bandwidth for the 6 μs amplified pulse was 220 kHz, as shown in Figure 6-17(b). This spectrum is slightly larger than the theoretical prediction for an ideal square pulse, which is explained by the difference in the shape of the pulse envelope.

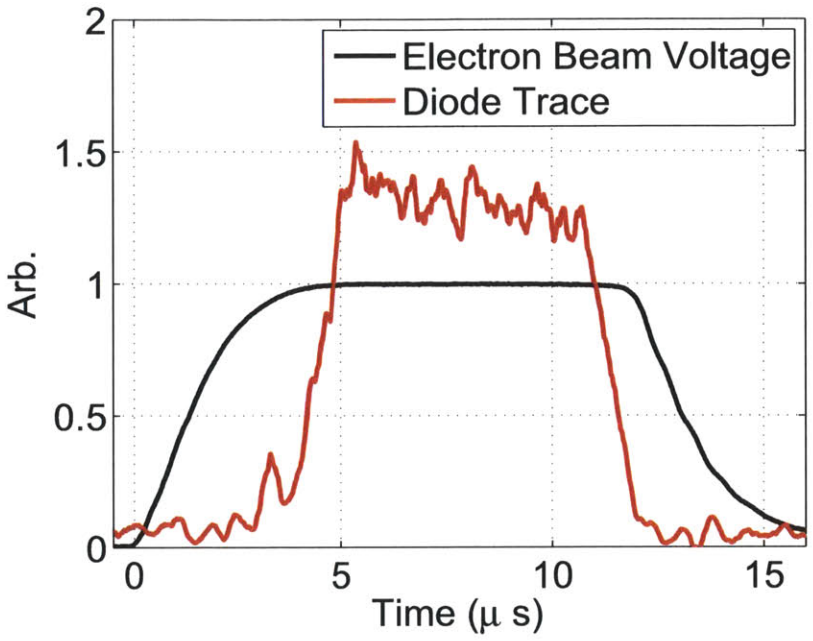

Figure 6-12: Diode trace measured at the gyrotron amplifier output and the corresponding high voltage pulse.

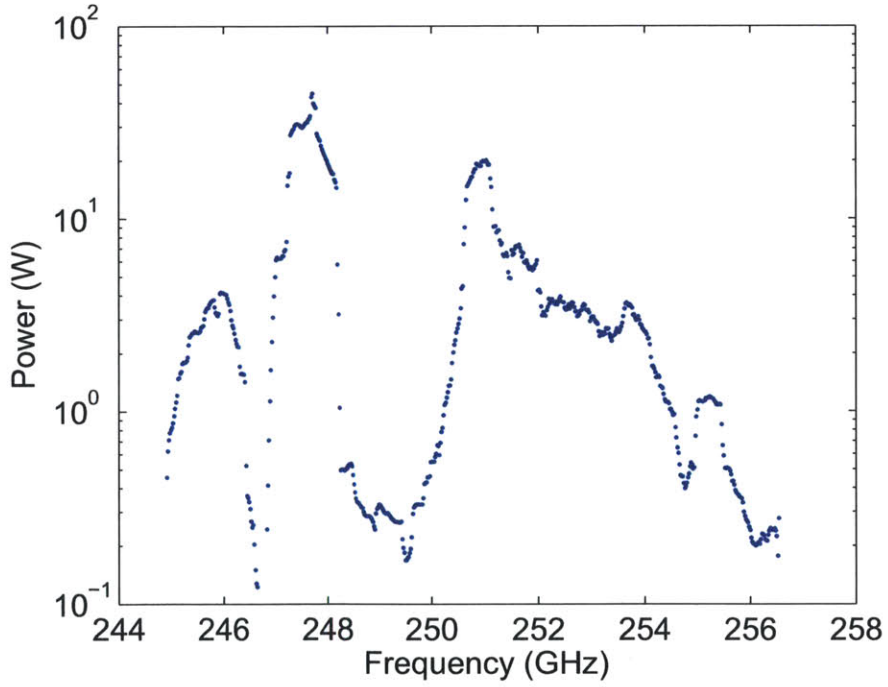

Figure 6-13: Maximum power recorded as a function of frequency while varying the operating parameters from from 11.5-33.1 kV, 160-460 mA and 8.54-8.92 T.

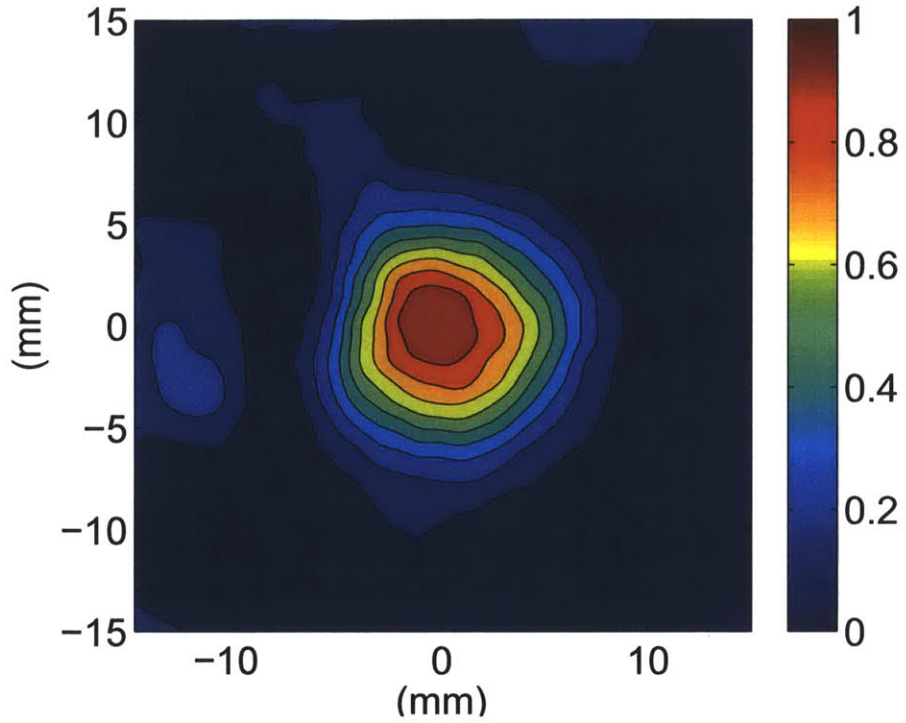

Figure 6-14: The radiated field pattern of the amplifier at 247.7 GHz measured after 2 m of 19 mm diameter corrugated waveguide and radiated 60 mm in free space.

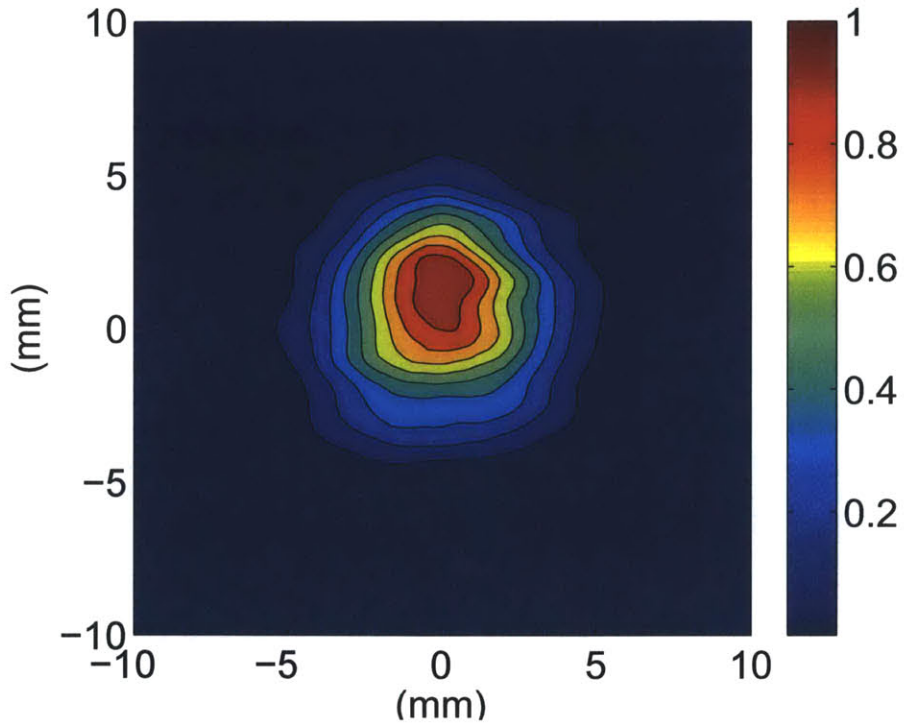

Figure 6-15: Simulated output beam pattern from HFSS.

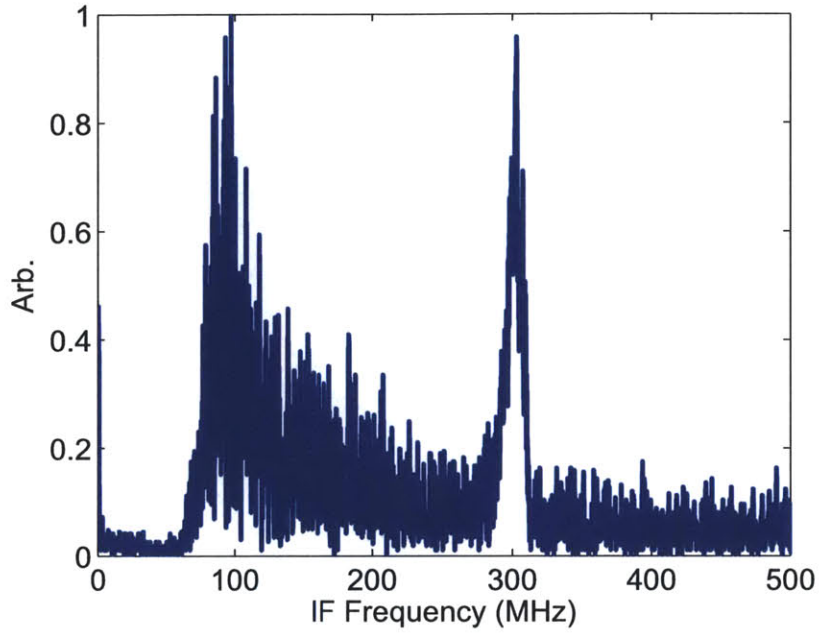

(a)

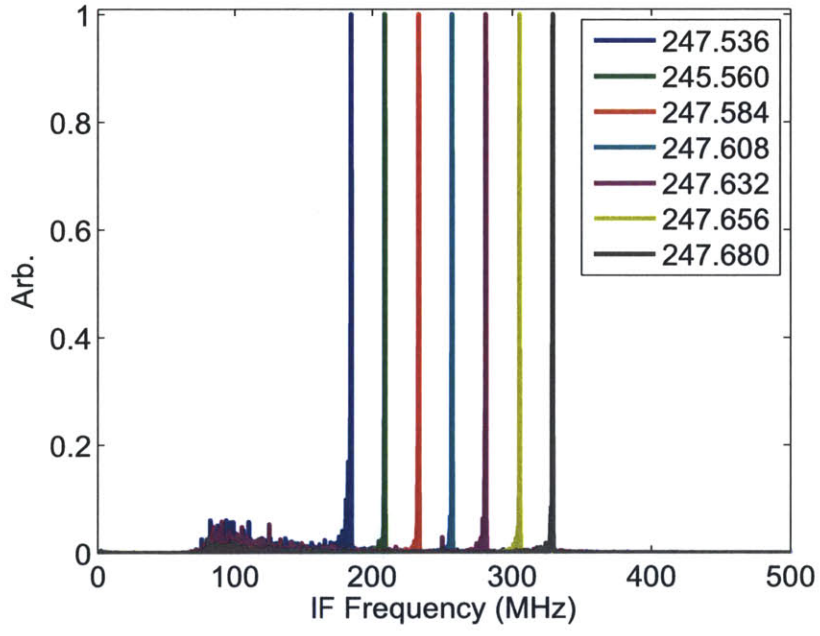

(b)

Figure 6-16: (a) Down-converted spectrum of an oscillation at 244.1 GHz. The spectrum of the oscillation is centered at an IF frequency of 300 MHz. (b) Down-converted spectrum of amplification for a variety of frequencies with a fixed LO frequency, 19.073 GHz, resulting in a shift for the observed IF frequency peak.

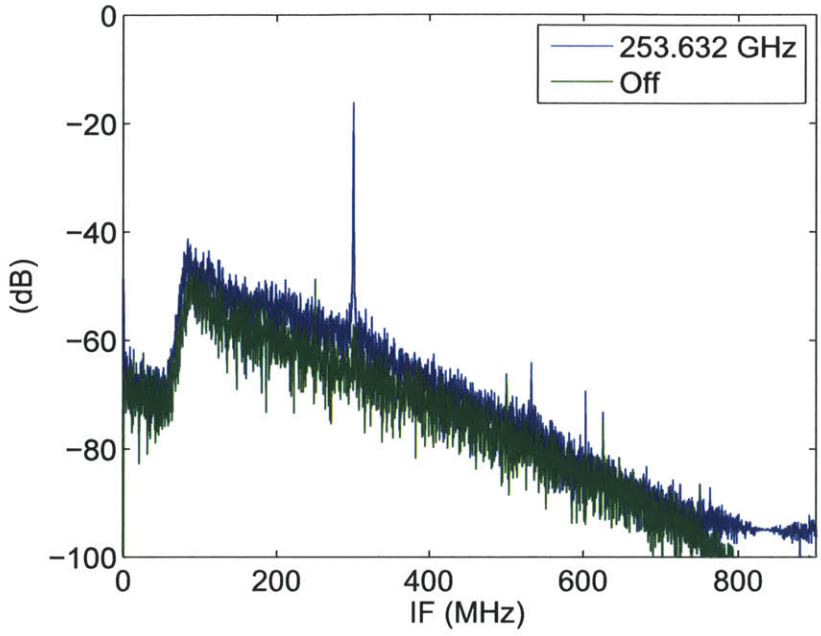

(a)

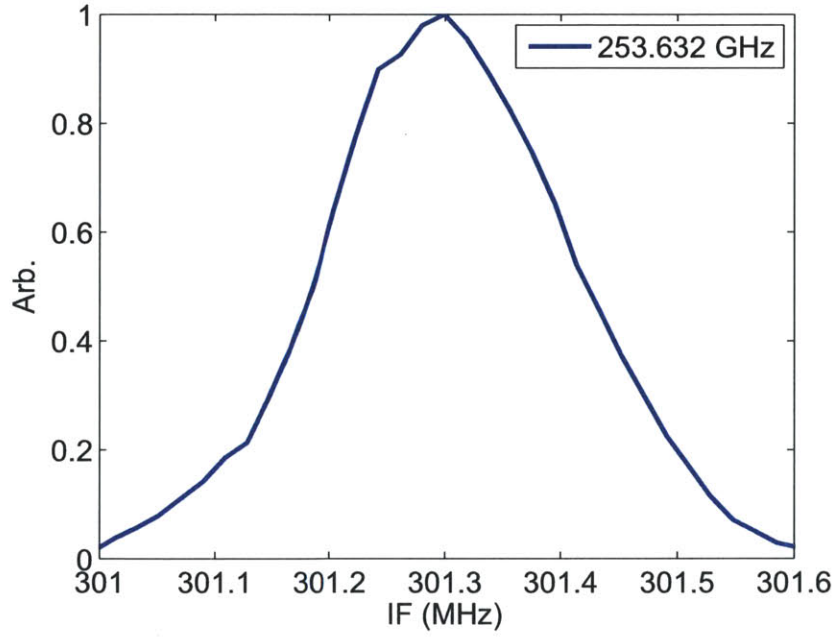

(b)

Figure 6-17: (a) Down-converted spectrum of amplification at 253.632 GHz for the 13^{th} harmonic lower side band with LO=19.487 GHz. Also shown is the recorded noise spectrum during the voltage pulse when the RF driver is off. (b) A zoom of the measured signal showing the narrow bandwidth of the amplified pulse.

6.4.3 Instantaneous Bandwidth

The instantaneous bandwidth was measured by maintaining all operational parameters for the device constant except for the input frequency of the solid-state driver. In general, it was observed that the amplifier had two modes of operation: lower in frequency, close to cutoff, modest bandwidth, high gain and high-output power or higher in frequency, far from cutoff, modest gain and wide bandwidths. Figure 6-18 shows the instantaneous bandwidth for two operating points that demonstrate the two modes of operation. The high-gain operating point produced 38 dB of gain, 45 W of output power and a 3 dB bandwidth of 0.4 GHz at 247.7 GHz. The wide-bandwidth operating point had a peak gain of 24 dB and output power of 4.4 W with a 4.5 GHz bandwidth at 253 GHz. This behavior of the amplifier is explained by the operating points proximity to cutoff. As the frequency approaches cutoff, the interaction strength between the electron beam and the electromagnetic wave increases because of the decreased group velocity. However, the rate of change for the group velocity increases limiting the bandwidth of interaction. An additional effect is observed from the design of the input wraparound coupler which has better coupling close to cutoff.

A theoretical model of the gyrotron amplifier was developed for comparison with measurements. This theoretical model is based on the nonlinear theory, described in Section 2.3, to predict the strength and bandwidth of the interaction between the electron beam and the TE_{03}-like PBG mode; and MAGY in order to incorporate the impact of velocity spread. The model includes the cold test measurements from Section 6.2 to incorporate losses from the input coupler, transmission line, windows and launcher. The basic strength of the beam-wave interaction is determined by the main operating parameters for the electron beam, i.e. magnetic field, voltage, and current. MICHELLE simulations of the electron gun, Section 5.3, are used as an initial estimate of the α and electron beam radius. The nonlinear theory is used to calculate the bandwidth of the interaction and small adjustments, within the experimental error, were made to the α value in order to better match the measured bandwidth. Then, these parameters are used with MAGY in order to determine the effect of

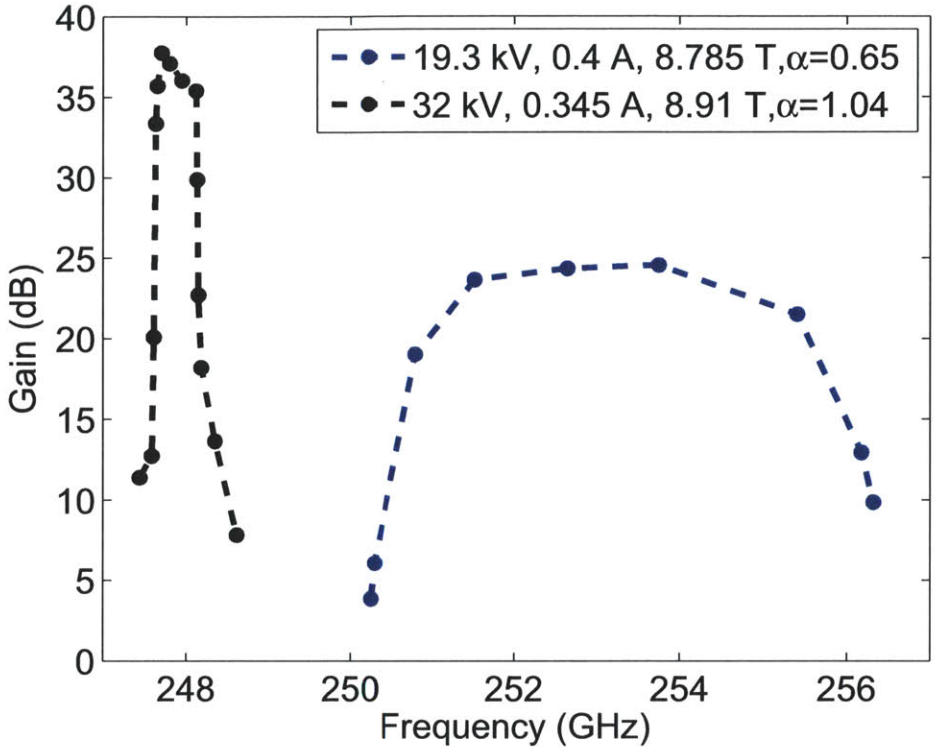

Figure 6-18: High-gain operating point which provides peak output power of 45 W and 38 dB of gain with a 0.4 GHz bandwidth and the wide-bandwidth operating point with 4.5 GHz of tunability and 24 dB of Gain.

velocity spread. The initial estimate of the velocity spread is also determined from the MICHELLE simulations. Velocity spread has a detrimental impact on the gain which increases with frequency. Additionally, the impact of velocity spread is increased when the electron beam parameters result in a $|\Delta| > 0$ as compared to a $\Delta \approx 0$. The effect of attenuation in the PBG waveguide is included in both the nonlinear and MAGY simulations. The device gain is calculated after including the losses from coupling into and out of the circuit. The losses from coupling into and out of the circuit are quite significant, as can be seen in Figure 6-3. The best coupling was measured at -12 dB around 247 GHz, but this is located close to the cutoff of the circuit which results in limited bandwidth. Additionally, the performance of the solid-state driver begins to decrease below 250 GHz, Figure 5-16. A large power hole is observed in the input coupler at 248 GHz. Above 250 GHz the best coupling is -16 dB which also suffered from limited bandwidth in the experiment. For wide bandwidth, the

amplifier was operated above 252 GHz where the input coupling is approximately flat at -25 dB. It was observed in the experiment that all operating points were limited to a circuit gain of ~50 dB before the onset of operational mode oscillations.

Figure 6-19 presents the results of this analysis for three different wide-bandwidth operating points. All cases show good agreement in terms of bandwidth and gain. The velocity spread used in the simulation is very close to the predicted value from the MICHELLE calculations, indicating that the electron gun is performing well. Figure 6-20 presents the results for three different high-gain operating points with the gain exceeding 30 dB. The predicted gain is in good agreement with the measured values; however, the predicted bandwidths do not agree as well. This is believed to be due to additional coupling losses that are not accounted for in the model and may have resulted from misalignments on the input or output transmission line.

6.4.4 Linear Gain

One critical aspect for the successful implementation of the amplifier in a pulsed-DNP/EPR spectrometer is the linearity of gain with variation of input power. Saturation (nonlinear gain) will result in signal distortion limiting the pump/probe signal power and decreasing the spectrometer's performance. To measure the linearity of the amplifier, the WR-3 variable attenuator, characterized in Section 6.2.3, was used to alter the signal intensity from the input as the output power was measured. Figure 6-21 demonstrates that, for two different operating points, as the input signal strength is attenuated the amplifier gain remains unaffected. The straight and dashed black lines in Figure 6-21(a) correspond to a linear gain of 35 dB and 25 dB, respectively. When the amplifier was operating with optimized parameters, saturation was not observed due to a lack of input power.

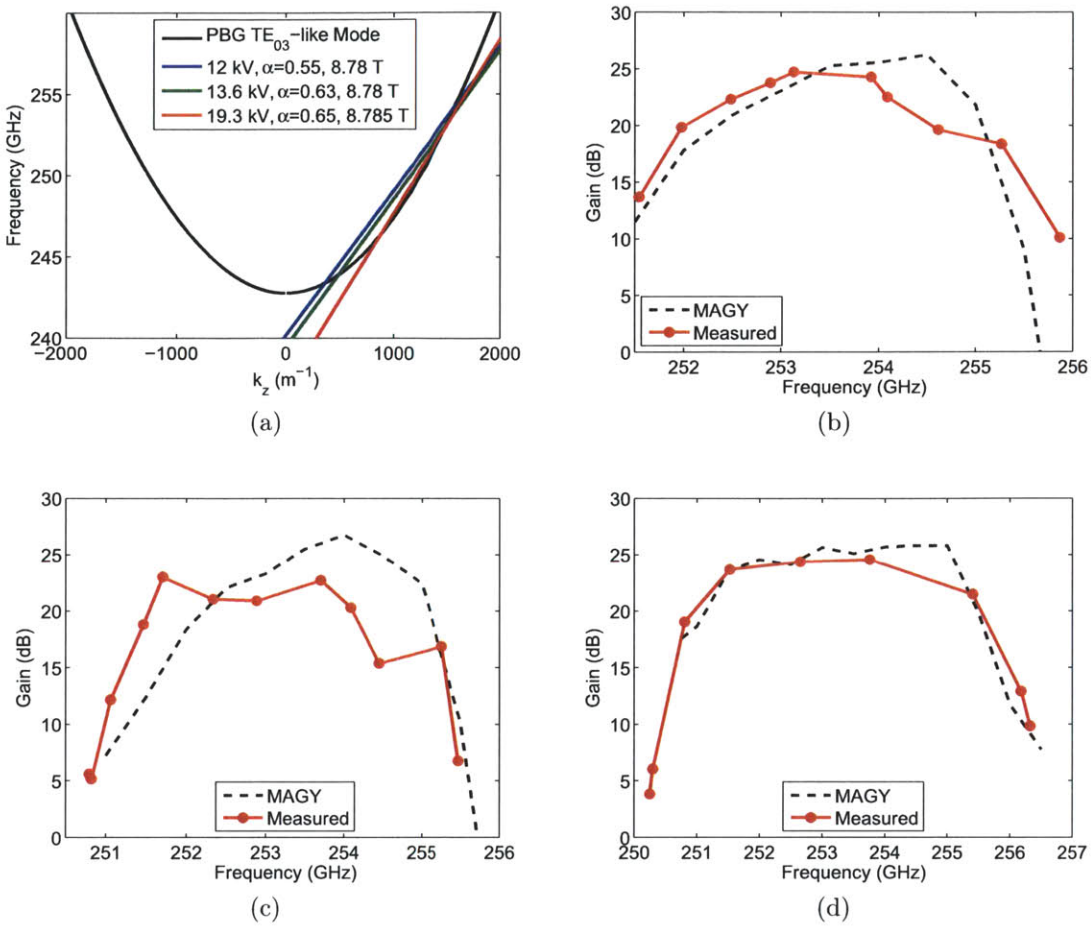

Figure 6-19: (a) Dispersion relation for three wide-bandwidth operating points with (b) 12 kV, 8.78 T, 0.46 A and 2% velocity spread; (c) 13.6 kV, 8.78 T, 0.42 A and 2.5% velocity spread; (d) 19.3 kV, 8.785 T, 0.4 A and 2% velocity spread.

6.4.5 Effect of Current and Voltage Variations

The amplifier's performance is very sensitive to the voltage and current of the electron beam. The electron beam voltage, for a fixed magnetic field, determines the frequency range over which it is possible to interact with the electron beam. In Figure 6-22, all parameters were held constant with the exception of voltage and, consequently, a weak variation of α and the electron beam current. The input frequency of the driver was fixed at 250.824 GHz and the electron beam current reached 320 mA at the maximum voltage of 20.75 kV. These parameters were determined to produce the maximum observable gain before the onset of oscillations. After reaching the

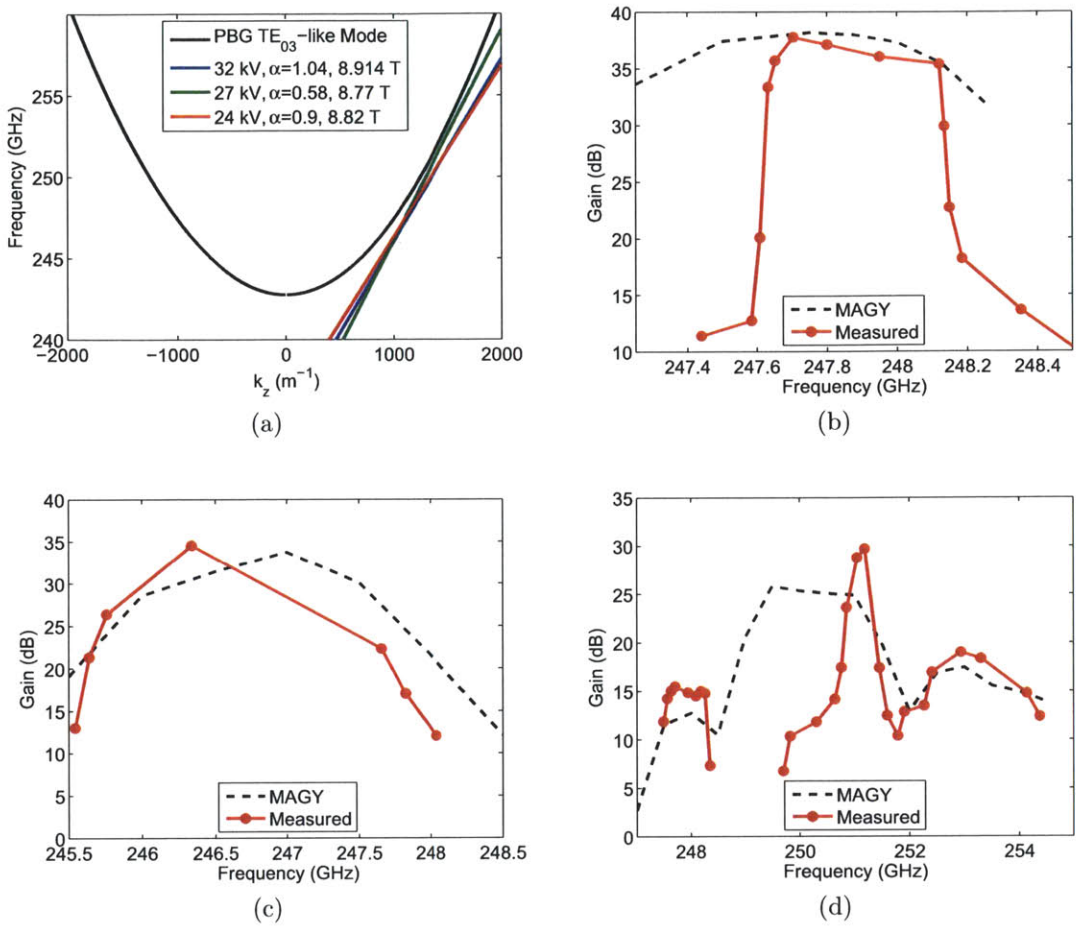

Figure 6-20: (a) Dispersion relation for three high-gain operating points with (b) 32 kV, 8.914 T, 0.345 A and 2.5% velocity spread; (c) 24 kV, 8.82 T, 0.225 A and 4% velocity spread; (d) 27 kV, 8.77 T, 0.25 A and 2% velocity spread.

maximum achievable gain the voltage was lowered and the output power was recorded. As seen the Figure 6-22, amplification can only be observed over a 1.75 kV range and has a very strong dependence on the voltage. For these parameters the amplification decreases monotonically with lower voltages because $\Delta < 0$ and Δ is decreasing with the voltage resulting in a weaker interaction. Increasing the voltage further results in an operational mode oscillation.

Under slightly different conditions we can observe a non-monotonic variation for the device gain with voltage. In Figure 6-23, the gain is once again shown as a function of voltage for the input frequency of 253.632 GHz. However, the current

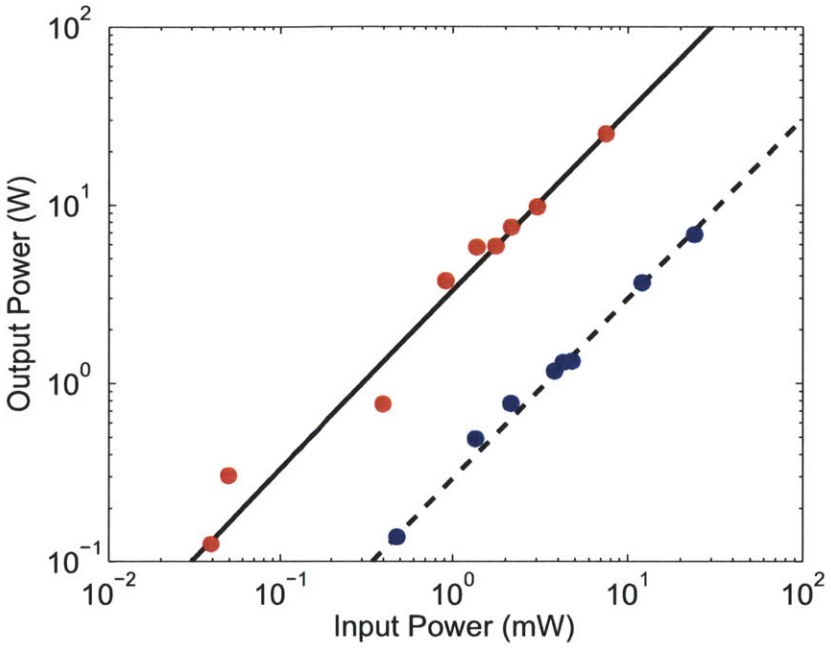

(a)

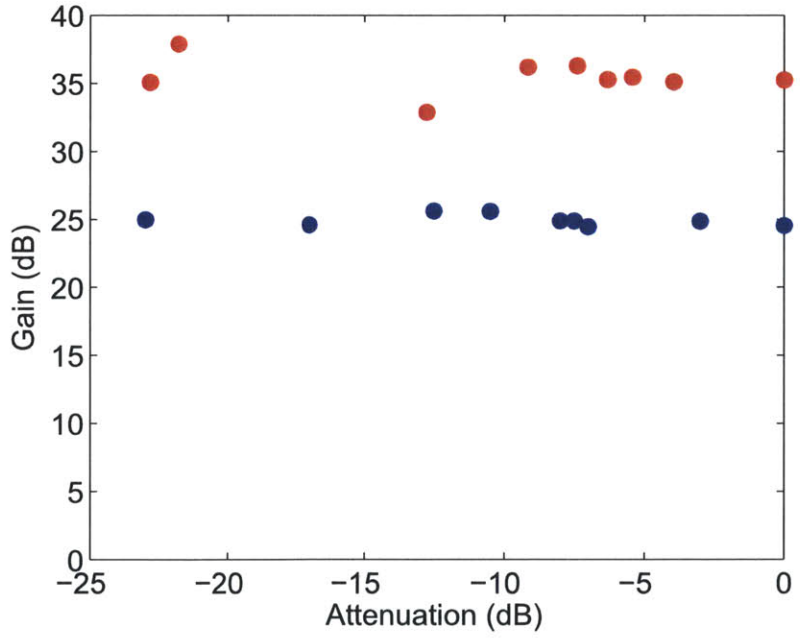

(b)

Figure 6-21: (a) Input power vs. output power for an input frequency of (red dots) 247.8 GHz at 32.6 kV, 320 mA and 8.9 T; (blue dots) 250.464 GHz at 20.4 kV, 370 mA and 8.83 T. (b) The corresponding gain as a function of the attenuation applied to the input signal using a variable attenuator.

is not high enough to trigger an oscillation with increasing voltage. As the voltage is increased the electron beam resonance is such that $\Delta > 0$ and is increasing with voltage. This results in a rapid decrease in the gain for the 15-16 kV range. Below 15 kV, the electron beam resonance coupling to the waveguide is increasing, but the system saturates because Δ is approaching zero resulting in a limited interaction efficiency due to saturation, as shown in Figure 2-9. This results in the rapid decrease in gain below 14.5 kV. The second peak in gain below 13 kV is the result of saturated amplification that is being overdriven, which causes fluctuations of the output power. While it may seem surprising to observe saturation with 23 dB of gain, the input coupling loss at this frequency is approximately -25 dB, which indicates a circuit gain of ~50 dB. Additionally, for the lower voltages in the plot, Δ is approaching zero, which is not the optimal condition for amplification.

A similar study can be performed by fixing all parameters and observing the increase in gain as a function of electron beam current. In this scenario, we know from Equation (2.53) that, once the gyrotron is able to amplify, the gain should grow as $(I - I_0)^{1/3}$, where I_0 is the threshold for amplification. In Figure 6-24, the measured and predicted device gain for the amplifier is shown as a function of current. Increasing the current further in the experiment resulted in an operational mode oscillation. These operational parameters are similar to the highest voltage case in Figure 6-22; however, the increase in α results in a $\Delta > 0$, and while the maximum current is lower, the achieved gain is higher.

In Figure 6-25, various operational voltage settings are held constant as a function of current. As the current is increased the beam-wave interaction increases, reaching a maximum level of gain, beyond which the amplifier oscillates in the operational mode. The performance at the low and high voltage are severely limited by the high current and high α, respectively. The theory curves for both Figure 6-24 and Figure 6-25 follow the $(I - I_0)^{1/3}$ dependence after it is shifted to account for input and output coupling losses.

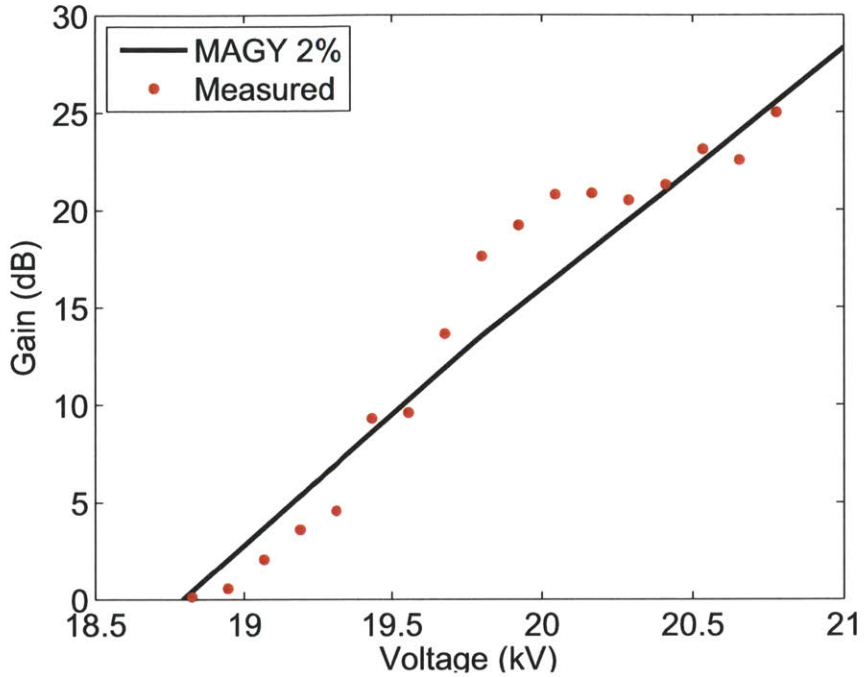

Figure 6-22: Gain as a function of the electron beam voltage for a magnetic field of 8.78 T, 250.824 GHz, $\alpha \approx 0.50 \rightarrow 0.65$ and $300 \rightarrow 320$ mA. The measured values (red dots) are compared with simulations in MAGY for 2% velocity spread (black line).

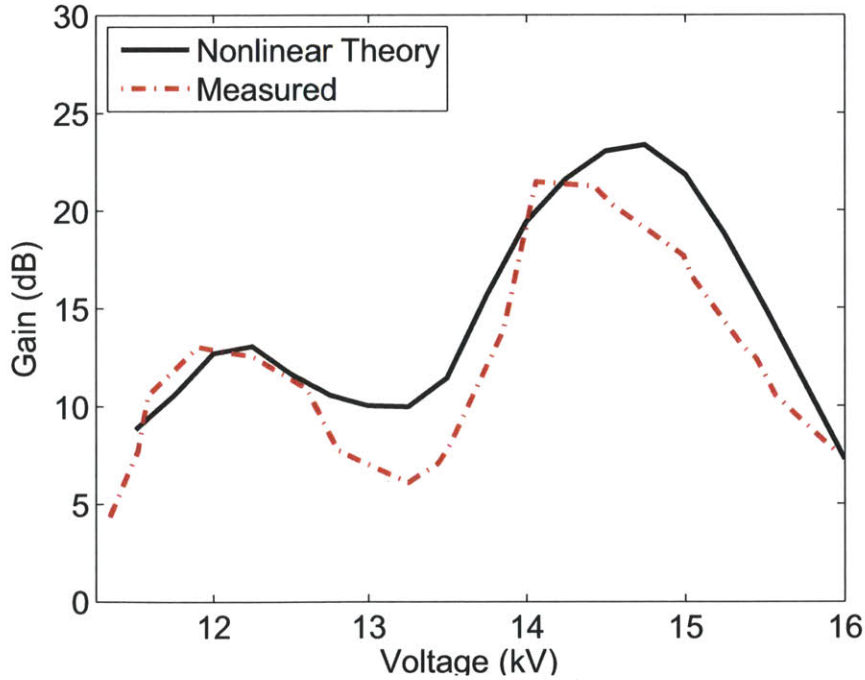

Figure 6-23: Gain as a function of the electron beam voltage for a magnetic field of 8.78 T, 253.632 GHz, $\alpha \approx 0.70 \rightarrow 0.80$ and $305 \rightarrow 355$ mA. The measured values (red line) are compared with the nonlinear theory (black line).

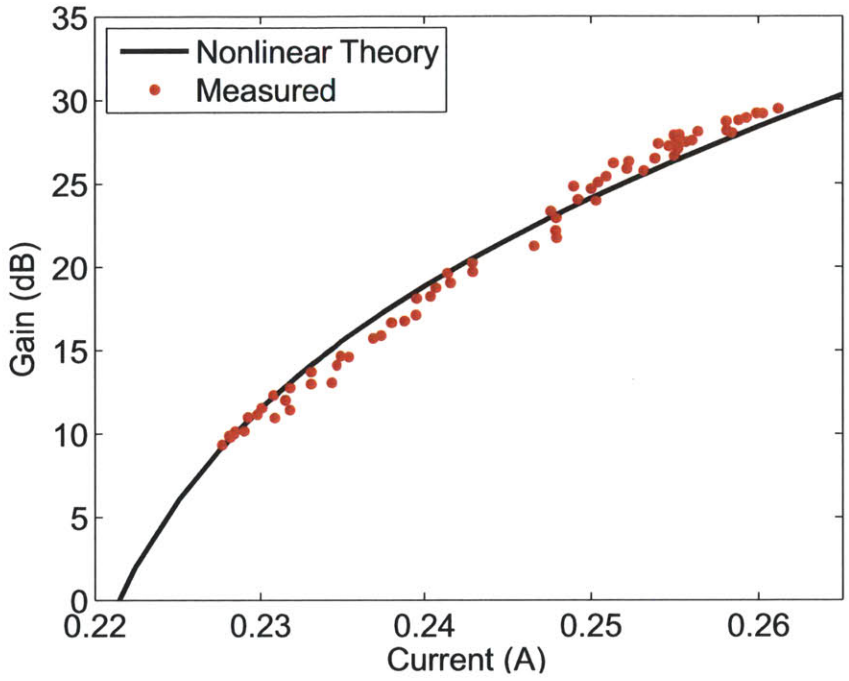

Figure 6-24: Gain as a function of the electron beam current for 21.2 kV, 251.04 GHz, 8.78 T, $\alpha = 0.84$. The measured values (red dots) are compared with the nonlinear theory (black line).

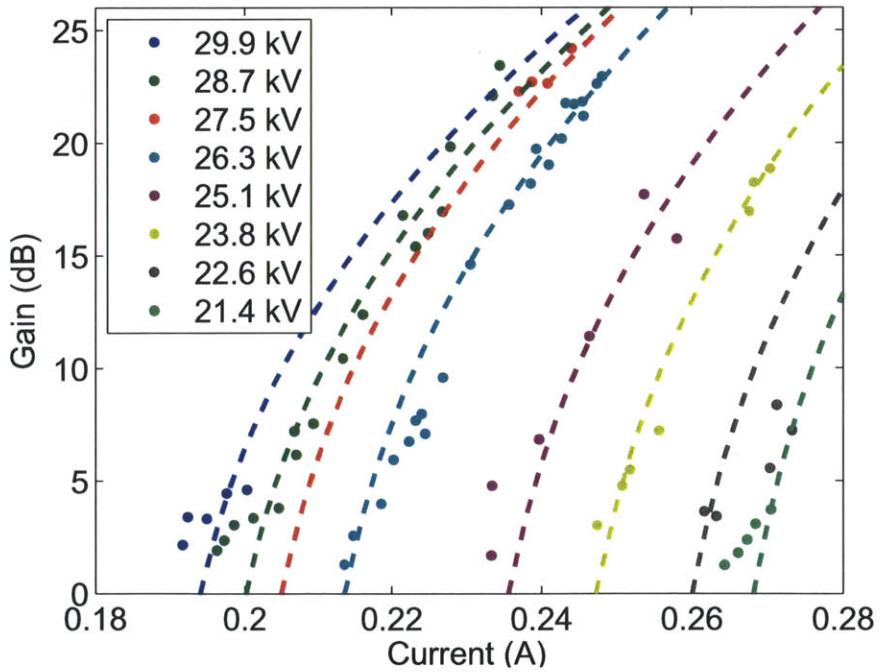

Figure 6-25: Gain as a function of the electron beam current for various voltages, 251.04 GHz, 8.82 T and $\alpha \approx 0.77 \rightarrow 0.99$. The measured values (dots) are compared with the nonlinear theory (dashed lines).

6.4.6 Future Improvements

During the course of this experiment, the primary limiting factor in the performance of the amplifier, in terms of gain and bandwidth, was the wraparound coupler. For this reason, it was determined that an improved input coupler should be investigated. The first approach taken was improving the fabrication and design of the wraparound coupler. The dimensions of the coupling slots and the length of the gun-side down-taper were adjusted to increase bandwidth and coupling efficiency. Additional focus was given to the fabrication of the coupler which had previously proved challenging. The split-block choke technique, which was initially demonstrated with the previous wraparound coupler, was further investigated with the fabrication of straight waveguide using copper and directional couplers using brass, Section 3.2.1. During this process, it was observed that brass components demonstrated more repeatable results, and it is believed that this is because brass is stronger and more brittle. However, brass is not safe for use with a thermionic cathode. In addition to making the new coupler design with OFHC copper, glidcop AL-60 copper was also used. Both materials were used because damage to the CNC endmill resulting in fabrication errors was a concern with using harder materials for the wraparound coupler. The results of HFSS simulations and VNA measurements from the improved coupler are shown in Figure 6-26. One of the two OFHC copper wraparounds fabricated demonstrated the best performance. While the glidcop wraparound couplers demonstrated almost identical performance, they were slightly worse than the best OFHC coupler.

An alternate approach to using a wraparound coupler was also investigated. This method involved the use of a Vlasov launcher on the input of the PBG circuit. There are several advantages to using a Vlasov style input: primarily, the increased bandwidth of the launcher and the fact that it does not require a gun side down-taper, which can reflect spurious modes lowering the oscillation start current. With a Vlasov input, limited performance close to cutoff and the large size of the launcher are of concern. The Vlasov input was easily fabricated, as it is almost identical to the output with the exception of the support structure. Figure 6-27 shows a photograph of the

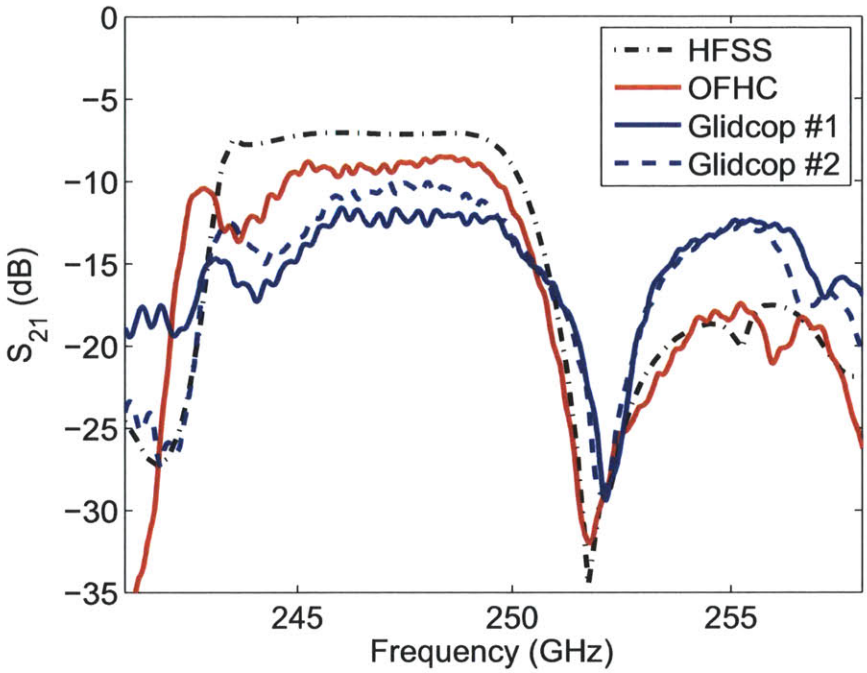

Figure 6-26: New wraparound input coupler design and testing.

Vlasov input and output under test using a VNA. The results of HFSS simulations and measurements are shown in Figure 6-28. The measurement of the Vlasov input is in good agreement with the simulation with some deviation close to cutoff where it becomes increasingly sensitive to misalignments. The Vlasov input demonstrates excellent coupling efficiency above 250 GHz.

Overall, the Vlasov input coupler seems to be better suited for the operation of the gyrotron amplifier. The bandwidth and coupling are both improved when compared to the wraparound coupler. The frequency range over which the Vlasov launcher works seems better suited to the large bandwidth regime which holds distinct advantages for the intended application. One final major advantage of the Vlasov input is that it does not have a gun-side down-taper, eliminating reflection of microwaves in the operational mode raising the start current for oscillations.

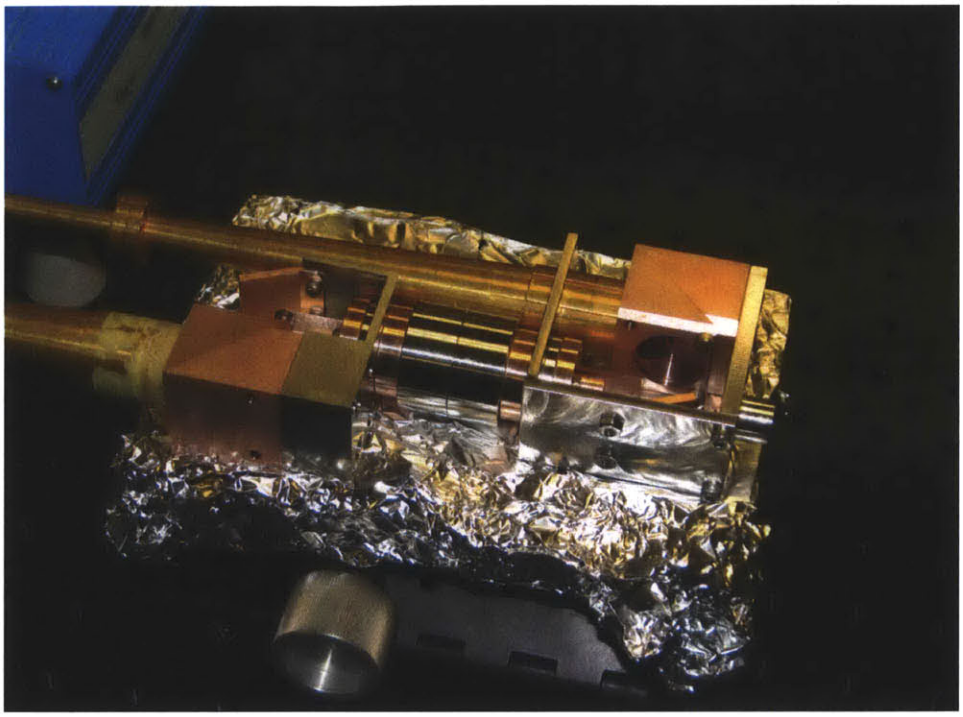

Figure 6-27: Photograph of the combined Vlasov launcher input and output under test using a VNA.

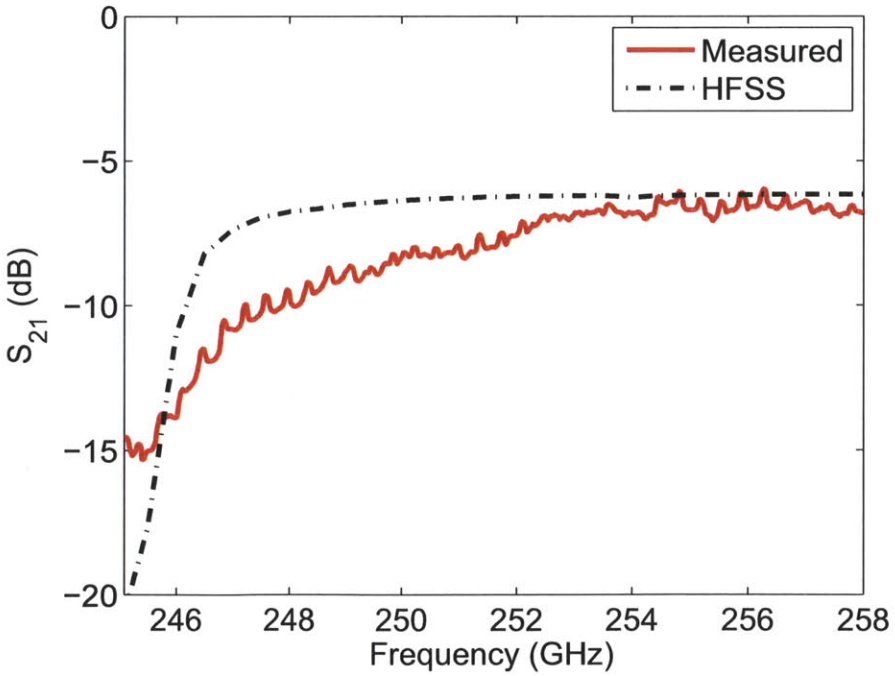

Figure 6-28: Comparison between theory and experiment for a combined Vlasov launcher input and output.

Chapter 7

Conclusions

The theoretical and experimental investigation of a novel gyrotron TWT amplifier at 250 GHz was presented in this thesis. The development of this gyrotron amplifier is notable for several major advances. At present, there are no other amplifiers in this frequency range that are capable of producing either high gain or high-output power. This experiment achieved the highest frequency of operation for a gyrotron amplifier. With 38 dB of gain and 45 W this is the highest gain observed above 94 GHz and the highest output power achieved above 140 GHz by any vacuum electron device; here we exclude free electron lasers powered by accelerators [9, 130]. It also has an instantaneous bandwidth as large as ~2% of its operational frequency which will allow for the investigation of short pulse amplification. The design of the amplifier is scalable to higher frequencies because the circuit geometry is easy to fabricate and allows for overmoded operation. Only direct machining was required for fabricating all of the microwave components in the amplifier. The amplifier's performance was not limited by the presence of oscillations in lower order modes clearly demonstrating the advantage of a PBG interaction circuit. With the achieved power levels, this amplifier has opened up the possibility for exciting new research in the field of pulsed-DNP NMR.

The gyrotron amplifier designed and tested in this thesis has achieved a peak small signal gain of 38 dB at 247.7 GHz, with a 32 kV, 0.35 A electron beam and a 8.9 T magnetic field, Section 6.4. The instantaneous -3 dB bandwidth of the amplifier at

peak gain is 0.4 GHz. A peak output power of 45 W has been measured. The output power is not saturated but is limited by the 7.5 mW of available input power. The amplifier can be tuned for operation from 245-256 GHz. With a gain of 24 dB and centered at 253.25 GHz, the widest instantaneous -3 dB bandwidth of 4.5 GHz was observed for a 19 kV, 0.305 A electron beam. To achieve stable operation at these high frequencies, the amplifier uses a novel PBG interaction circuit. The PBG interaction circuit confines the TE_{03}-like mode which couples strongly to the electron beam. The PBG circuit provides stability from oscillations by supporting the propagation of TE modes in a narrow range of frequencies, allowing for the confinement of the operating TE_{03}-like mode while rejecting the excitation of oscillations at lower frequencies. Experimental results taken over a wide range of parameters, 15-30 kV and 0.25-0.5 A, show good agreement with a theoretical model. The theoretical model incorporates cold test measurements for the transmission line, input coupler, PBG waveguide and mode converter; and it is compared to the instantaneous bandwidth of various operating points in Section 6.4.3. The theoretical model was tested against variations in current and voltage in Section 6.4.5. The amplifier output produces a Gaussian beam that is compatible with transmission on a corrugated waveguide in the HE_{11} mode. The measured pattern is 92.4% Gaussian with beam waists of $w_x = 6.6$ mm and $w_y = 6.8$ mm. This output beam will facilitate the integration of the amplifier on a NMR spectrometer.

During the course of this work significant efforts were made to improve the performance of THz waveguides, Chapter 3. Three areas of interest were investigated: improved fabrication of fundamental rectangular waveguide, PBG waveguides for overmoded operation and the improved theory and fabrication of corrugated waveguides. Fundamental rectangular waveguide offers significant advantages for basic microwave components such as bends, tapers, twists, etc.; however, the integration of these components in the THz band with more complicated structures such as directional couplers, mode converters, etc., has proved challenging. The novel split-block choke technique, presented in Section 3.2, is competitive with commercially available products while allowing for easy integration with more complicated structures. The

fabrication technique is rapid and reliable while allowing for optical inspection of the waveguide surfaces without damaging the structure which is not usually feasible with other fabrication techniques. Metallic PBG waveguides were investigated in Section 3.3 and demonstrated to be feasible in the THz band. The first observation was made that the modes that are excited in the hexagonal defect region correspond to hexagonal waveguide modes, not circular waveguide modes. Rapid fabrication of overmoded corrugated waveguides was presented in Section 3.4 with simulations and measurements demonstrating that helical tapping does not have a detrimental effect on the propagation of the HE_{11} mode. The theory for calculating the loss in a corrugated waveguide was improved and shown to match HFSS simulations over a large frequency range, greatly exceeding the optimized $\lambda/4$ condition for the groove depth.

Future studies on the performance of the amplifier and alterations to the circuit design could yield improved results. One area that could provide the most immediate benefit is the improvement of the input coupler as discussed in Section 6.4.6. Two viable options for replacing the existing input coupler have been fabricated and cold tested. Compared to the current input coupler, the new wraparound coupler demonstrates improved performance, but the Vlasov input seems to be the superior option in terms of coupling, bandwidth and limiting reflections.

Alterations to the PBG circuit to provide non-uniform distributed loading could also improve the performance of the amplifier. Different sections of the PBG circuit could be made with progressively more rows of rods providing increased confinement and decreased attenuation. Non-uniform loading can provide the same or improved suppression of oscillations in the operational mode while limiting the losses in the final sections of the circuit. This selective attenuation has a dramatic effect on the output power by limiting losses when the amplified field is at its strongest.

The large bandwidths observed from this gyrotron amplifier will allow for the amplification of very short pulses. Previously, pulses as short as 400 ps with pulse broadening and 1 ns without broadening, were investigated using a 140 GHz gyrotron amplifier [93]. This amplification was well described using the cold dispersion of the waveguide mode and gain bandwidth of the amplifier. With the achieved bandwidths

reported in this thesis it is conceivable that pulses as short as 250 ps could be amplified without broadening. This previously unexplored region could yield interesting results that would require a more complete physical explanation involving the coupled dispersion relation of the electron beam and electromagnetic wave.

Throughout the design of this experiment, special consideration was taken into account with regards to the implementation of the amplifier for its intended application. The output power, output beam pattern, instantaneous bandwidth, spectral purity and shot-to-shot stability of the amplified pulse meet the basic requirements for the implementation of this device on a pulsed-DNP spectrometer. While further investigation will be required for this integration to be achieved, the gyrotron amplifier as presented in this thesis has created the possibility for this to become a reality.

Bibliography

[1] A. Abragam and M. Goldman. Principles of dynamic nuclear polarisation. *Reports on Progress in Physics*, 41(3):395, 1978.

[2] A. Abragam and W. G. Proctor. A novel method of dynamic polarization of atomic nuclei in solids. *CR Acad. Sci*, 246, 1959.

[3] M. Afeworki, R. A. Mckay, and J. Schaefer. Selective observation of the interface of heterogeneous polycarbonate polystyrene blends by dynamic nuclear-polarization C-13 NMR-spectroscopy. *Macromolecules*, 25(16):4084 4091, 1992.

[4] M. Afeworki, R. A. Mckay, and J. Schaefer. Dynamic nuclear-polarization enhanced nuclear-magnetic-resonance of polymer-blend interfaces. *Materials Science and Engineering a-Structural Materials Properties Microstructure and Processing*, 162(1-2):221 228, 1993.

[5] M. Afeworki and J. Schaefer. Mechanism of DNP-enhanced polarization transfer across the interface of polycarbonate/polystyrene heterogeneous blends. *Macromolecules*, 25:4092 4096, 1992.

[6] M. Afeworki and J. Schaefer. Molecular dynamics of polycarbonate chains at the interface of polycarbonate/polystyrene heterogeneous blends. *Macromolecules*, 25:4097 4099, 1992.

[7] M. Afeworki, S. Vega, and J. Schaefer. Direct electron-to-carbon polarization transfer in homgeneously-doped polycarbonates. *Macromolecules*, 25:4100 4106, 1992.

[8] Ü. Akbey, W. T. Franks, A. Linden, S. Lange, R. G. Griffin, B. van Rossum, and H. Oschkinat. Dynamic nuclear polarization of deuterated proteins. *Angewandte Chemie International Edition*, 49(42):7803 7806, 2010.

[9] S. L. Allen, C. J. Lasnier, B. Felker, M. Fenstermacher, S. W. Ferguson, S. Fields, E. B. Hooper, S. Hulsey, M. Makowski, J. Moller, et al. Generation of high power 140 GHz microwaves with an FEL for the MTX experiment. In *Particle Accelerator Conference, 1993., Proceedings of the 1993*, pages 1551 1553. IEEE, 1993.

[10] J. H. Ardenkjær-Larsen, B. Fridlund, A. Gram, G. Hansson, L. Hansson, M. H. Lerche, R. Servin, M. Thaning, and K. Golman. Increase in signal-to-noise ratio of 10,000 times in liquid-state NMR. *Proceedings of the National Academy of Sciences of the United States of America*, 100(18):10158 10163, 2003.

[11] B. D. Armstrong, D. T. Edwards, R. J. Wylde, S. A. Walker, and S. Han. A 200 GHz dynamic nuclear polarization spectrometer. *Physical Chemistry Chemical Physics*, 12(22):5920 5926, 2010.

[12] V. A. Atsarkin. Dynamic polarization of nuclei in solid dielectrics. *Soviet Physics Solid State*, 21:725 744, 1978.

[13] M. E. Austin et al. ITER ECE: plans and challenges. In *Proceedings of the Fifteenth Joint Workshop on Electron Cyclotron Emission and Electron Cyclotron Resonance Heating: Yosemite National Park, California, USA*, pages 170 177, 2009.

[14] J. M. Baird and W. Lawson. Magnetron injection gun (MIG) design for gyrotron applications. *International Journal of Electronics*, 61(6):953 967, 1986.

[15] V. S. Bajaj, C. T. Farrar, M. K. Hornstein, I. Mastovsky, J. Vieregg, J. Bryant, B. Elena, K. E. Kreischer, R. J. Temkin, and R. G. Griffin. Dynamic nuclear polarization at 9T using a novel 250 GHz gyrotron microwave source. *J. Mag. Res.*, 160:85 90, 2003.

[16] V. S. Bajaj, M. K. Hornstein, K. E. Kreischer, J. R. Sirigiri, P. P. Woskov, M. L. Mak-Jurkauskas, J. Herzfeld, R. J. Temkin, and R. G. Griffin. 250 GHz CW gyrotron oscillator for dynamic nuclear polarization in biological solid state NMR. *Journal of Magnetic Resonance*, 189(2):251 279, 2007.

[17] A. B. Barnes, G. De Pa pe, P. C. A. van der Wel, K. N. Hu, C. G. Joo, V. S. Bajaj, M. L. Mak-Jurkauskas, J. R. Sirigiri, J. Herzfeld, R. J. Temkin, and R. G. Griffin. High-field dynamic nuclear polarization for solid and solution biological NMR. *Applied Magnetic Resonance*, 34(3):237 263, 2008.

[18] A. B. Barnes, E. Markhasin, E. Daviso, V. K. Michaelis, E. A. Nanni, S. Jawla, E. L. Mena, R. DeRocher, A. Thakkar, P. Woskov, et al. Dynamic nuclear polarization at 700 MHz/460 GHz. *Journal of Magnetic Resonance*, 224:1 7, 2012.

[19] A. B. Barnes, E. A. Nanni, J. Herzfeld, R. G. Griffin, and R. J. Temkin. A 250 GHz gyrotron with a 3 GHz tuning bandwidth for dynamic nuclear polarization. *Journal of Magnetic Resonance*, 221:147 153, 2012.

[20] L. R. Barnett, J. M. Baird, Y. Y. Lau, K. R. Chu, and V. L. Granatstein. A high gain single stage gyrotron traveling-wave amplifier. In *1980 International Electron Devices Meeting*, volume 26, pages 314 317, 1980.

[21] B. N. Basu. *Electromagnetic theory and applications in beam-wave electronics.* World Scientific Pub. Co. Inc., 1996.

[22] L. R. Becerra, G. J. Gerfen, R. J. Temkin, D. J. Singel, and R. G. Griffin. Dynamic nuclear polarization with a cyclotron resonance maser at 5 T. *Physical Review Letters*, 71(21):3561 3564, 1993.

[23] M. Bennati, C. T. Farrar, J. A. Bryant, S. J. Inati, V. Weis, G. J. Gerfen, P. Riggs-Gelasco, J. Stubbe, and R. G. Griffin. Pulsed electron-nuclear double resonance (ENDOR) at 140 GHz. *Journal of Magnetic Resonance*, 138(2):232 243, 1999.

[24] P. Bhartia and I. J. Bahl. *Millimeter wave engineering and applications.* John Wiley and Sons, Inc., New York, NY, 1984.

[25] M. Blank, P. Borchard, S. Cauffman, and F. Felch. Broadband W-band gyrotron amplifier development. In *2006 International Conference on Infrared Millimeter Waves and Terahertz Electronics*, page 198. IEEE, 2006.

[26] M. Blank, P. Borchard, S. Cauffman, and K. Felch. Demonstration of a broadband W-band gyro-TWT amplifier. In *2005 IEEE International Conference on Plasma Science*, page 112, 2005.

[27] M. Blank, P. Borchard, S. Cauffman, and K. Felch. Design and demonstration of W-band gyrotron amplifiers for radar applications. In *Joint 32nd International Conference on Infrared and Millimeter Waves and 15th International Conference on Terahertz Electronics.*, pages 364 366. IEEE, 2007.

[28] M. Blank, P. Cahalan, K. Felch, B. G. Danly, B. Levush, D. Pershing, K. T. Nguyen, and J. P. Calame. Demonstration of a wide-band 94 GHz gyrotwystron amplifier. In *Plasma Science, 2003. The 30th International Conference on*, page 256. IEEE, 2003.

[29] M. Blank, B. G. Danly, B. Levush, J. P. Calame, K. Nguyen, D. Pershing, J. Petillo, T. A. Hargreaves, R. B. True, A. J. Theiss, et al. Demonstration of a 10 kW average power 94 GHz gyroklystron amplifier. *Physics of Plasmas*, 6:4405, 1999.

[30] M. Blank, K. Felch, B. G. James, P. Borchard, P. , T. S. Chu, H. Jory, B. G. Danly, B. Levush, J. P. Calame, et al. Development and demonstration of high-average power W-band gyro-amplifiers for radar applications. *Plasma Science, IEEE Transactions on*, 30(3):865 875, 2002.

[31] A. A. Bogdashov, V. I. Belousov, A. V. Chirkov, G. G. Denisov, S. Y. Kornishin, and E. M. Tai. Transmission line for 258 GHz gyrotron DNP spectroscopy. In *Infrared Millimeter and Terahertz Waves (IRMMW-THz), 2010 35th International Conference on*, pages 1 2, 2011.

[32] D. R. Bolton, P. A. S. Cruickshank, D. A. Robertson, and G. M. Smith. Sub-nanosecond coherent pulse generation at millimetre-wave frequencies. *Electronics Letters*, 43(6):43–44, 2007.

[33] W. A. Bongers et al. Magnetic island localization for NTM control by ECE viewed along the same optical path of the ECCD beam. *Fusion Science and Technology*, 55(2):188 203, 2009.

[34] M. Botton, T. M. Antonsen Jr, B. Levush, K. T. Nguyen, and A. N. Vlasov. MAGY: a time-dependent code for simulation of slow and fast microwave sources. *IEEE Transactions on Plasma Science*, 26(3):882 892, 1998.

[35] B. Bowden, J. A. Harrington, and O. Mitrofanov. Low-loss modes in hollow metallic terahertz waveguides with dielectric coatings. *Applied Physics Letters*, 93(18):181104, 2008.

[36] V. L. Bratman, A. W. Cross, G. G. Denisov, W. He, A. D. R. Phelps, K. Ronald, S. V. Samsonov, C. G. Whyte, and A. R. Young. High-gain wide-band gyrotron traveling wave amplifier with a helically corrugated waveguide. *Physical Review Letters*, 84(12):2746 2749, 2000.

[37] R. W. Callis, W. P. Cary, R. Ellis, Y. A. Gorelov, H. J. Grunloh, J. Lohr, J. J. Peavy, R. I. Pinsker, D. Ponce, and R. Prater. The 6 MW, 110 GHz ECH system for the DIII-D tokamak. In *Plasma Science, 2002. The 29th IEEE International Conference on*, page 294, 2002.

[38] T. R. Carver and C. P. Slichter. Polarization of nuclear spins in metals. *Physical Review*, 92:212 213, 1953.

[39] T. H. Chang, C. H. Li, C. N. Wu, and C. F. Yu. Exciting circular temn modes at low terahertz region. *Applied Physics Letters*, 93(11):111503 111503, 2008.

[40] L. Chen, H. C., T. Kao, J. Lu, and C. Sun. Low-loss subwavelength plastic fiber for terahertz waveguiding. *Opt. Lett.*, 31(3):308 310, 2006.

[41] E. Choi, M. Shapiro, J. Sirigiri, and R. Temkin. Calculation of radiation from a helically cut waveguide for a gyrotron mode converter in the quasi-optical approximation. *Journal of Infrared, Millimeter and Terahertz Waves*, 30(1):8 25, 2009.

[42] K. R. Chu. The electron cyclotron maser. *Reviews of Modern Physics*, 76(2):489 540, 2004.

[43] K. R. Chu, H. Y. Chen, C. L. Hung, T. H. Chang, L. R. Barnett, S. H. Chen, and T. T. Yang. Ultrahigh gain gyrotron traveling wave amplifier. *Physical Review Letters*, 81(21):4760 4763, 1998.

[44] K. R. Chu, A. T. Drobot, H. H. Szu, and P. Sprangle. Theory and simulation of the gyrotron traveling wave amplifier operating at cyclotron harmonics. *IEEE Transactions on Microwave Theory and Techniques*, 28(4):313 317, 1980.

[45] K. R. Chu and J. L. Hirshfield. Comparative study of the axial and azimuthal bunching mechanisms in electromagnetic cyclotron instabilities. *Physics of Fluids*, 21:461, 1978.

[46] P. J. B. Clarricoats and A. D. Olver. *Corrugated horns for microwave antennas*. IEEE Electromagnetic Waves Series. Institution of Electrical Engineers, 1984.

[47] P. J. B. Clarricoats, A. D. Olver, and S. L. Chon. Attenuation in corrugated circular waveguides. I - Theory. *Institution of Electrical Engineers, Proceedings*, 122(11):1173 1179, 1975.

[48] C. E. Collins, J. W. Digby, R. D. Pollard, R. E. Miles, G. M. Parkhurst, J. M. Chamberlain, D. P. Steenson, N. J. Cronin, L. S. Karatzas, and J. W. Bowen. W-band measurements of 100 μm height micro-machined air-filled rectangular waveguides. In *Microwave Symposium Digest, 1997., IEEE MTT-S International*, volume 3, pages 1439 1442. IEEE, 1997.

[49] C. E. Collins, R. E. Miles, J. W. Digby, G. M. Parkhurst, R. D. Pollard, J. M. Chamberlain, D. P. Steenson, N. J. Cronin, S. R. Davies, and J. W. Bowen. A new micro-machined millimeter-wave and terahertz snap-together rectangular waveguide technology. *Microwave and Guided Wave Letters, IEEE*, 9(2):63 65, 1999.

[50] C. E. Collins, R. E. Miles, R. D. Pollard, D. P. Steenson, J. W. Digby, G. M. Parkhurst, J. M. Chamberlain, N. J. Cronin, S. R. Davies, and J. W. Bowen. Technique for micro-machining millimetre-wave rectangular waveguide. *Electronics Letters*, 34(10):996 997, 1998.

[51] P. A. S. Cruickshank, D. R. Bolton, D. A. Robertson, R. I. Hunter, R. J. Wylde, and G. M. Smith. A kilowatt pulsed 94 GHz electron paramagnetic resonance spectrometer with high concentration sensitivity, high instantaneous bandwidth, and low dead time. *Review of Scientific Instruments*, 80(10):103102, 2009.

[52] B. G. Danly, M. Blank, J. P. Calame, B. Levush, K. T. Nguyen, D. E. Pershing, R. K. Parker, K. L. Felch, B. G. James, P. Borchard, et al. Development and testing of a high-average power, 94-GHz gyroklystron. *Plasma Science, IEEE Transactions on*, 28(3):713 726, 2000.

[53] B. G. Danly and R. J. Temkin. Generalized nonlinear harmonic gyrotron theory. *Physics of Fluids*, 29(2):561, 1986.

[54] E. de Rijk, A. Macor, J. P. Hogge, S. Alberti, and J. P. Ansermet. Note: Stacked rings for terahertz wave-guiding. *Review of Scientific Instruments*, 82(6):066102, 2011.

[55] G. Denisov, A. Chirkov, V. Belousov, A. Bogdashov, et al. Millimeter wave multi-mode transmission line components. *Journal of Infrared, Millimeter and Terahertz Waves*, 32(3):343–357, 2011.

[56] V. Denysenkov, M. J. Prandolini, M. Gafurov, D. Sezer, B. Endeward, and T. F. Prisner. Liquid state DNP using a 260 GHz high power gyrotron. *Physical Chemistry Chemical Physics*, 12(22):5786–5790, 2010.

[57] J. W. Digby, C. E. McIntosh, G. M. Parkhurst, B. M. Towlson, S. Hadjiloucas, J. W. Bowen, J. M. Chamberlain, R. D. Pollard, R. E. Miles, D. P. Steenson, et al. Fabrication and characterization of micromachined rectangular waveguide components for use at millimeter-wave and terahertz frequencies. *Microwave Theory and Techniques, IEEE Transactions on*, 48(8):1293–1302, 2000.

[58] J. L. Doane. *Propagation and mode coupling in corrugated and smooth-walled circular waveguides*, volume 13 of *Infrared and Millimeter Waves*. New York, Academic Press, 1985.

[59] J. L. Doane and C. P. Moeller. HE_{11} mitre bends and gaps in a circular corrugated waveguide. *International Journal of Electronics*, 77(4):489, 1994.

[60] J. L. Doane and R. A. Olstad. Transmission line technology for electron cyclotron heating. *Fusion Science and Technology*, 53(1):39–53, 2008.

[61] J.L. Doane. Design of circular corrugated waveguides to transmit millimeter waves at iter. *Fusion science and technology*, 53(1):159–173, 2008.

[62] C. Dragone. Attenuation and radiation characteristics of the HE_{11} - mode. *Microwave Theory and Techniques, IEEE Transactions on*, 28(7):704–710, 1980.

[63] K. L. Felch, B. G. Danly, H. R. Jory, K. E. Kreischer, W. Lawson, B. Levush, and R. J. Temkin. Characteristics and applications of fast-wave gyrodevices. *Proceedings of the IEEE*, 87(5):752–781, 1999.

[64] G. Gallot, S. P. Jamison, R. W. McGowan, and D. Grischkowsky. Terahertz waveguides. *J. Opt. Soc. Am. B*, 17(5):851–863, 2000.

[65] F. Gandini, T. S. Bigelow, et al. The ECH transmission line for ITER. *Fusion Science and Technology*, 59(4):709–717, 2011.

[66] A. V. Gapanov. Addendum izvestia. *Izv. VUZ. Radiofizika*, 2:450–462, 1959.

[67] A. V. Gaponov. Interaction of helical electron beams with the electromagnetic field in a waveguide. *Radiotekh. I Elektron.*, 10:1414–1153, 1961.

[68] G. J. Gerfen, L. R. Becerra, D. A. Hall, R. G. Griffin, R. J. Temkin, and D. J. Singel. High-frequency (140 GHz) dynamic nuclear-polarization - polarization transfer to a solute in frozen aqueous-solution. *Journal of Chemical Physics*, 102(24):9494–9497, 1995.

[69] N. S. Ginzburg, I. V. Zotova, A. S. Sergeev, I. V. Konoplev, A. D. R. Phelps, A. W. Cross, S. J. Cooke, V. G. Shpak, M. I. Yalandin, and S. A. Shunailov. Experimental observation of cyclotron superradiance under group synchronism conditions. *Physical Review Letters*, 78(12):2365 2368, 1997.

[70] M. Y. Glyavin, A. G. Luchinin, and G. Y. Golubiatnikov. Generation of 1.5-kW, 1-THz coherent radiation from a gyrotron with a pulsed magnetic field. *Physical Review Letters*, 100(1):15101, 2008.

[71] M. Goldman. *Spin Temperature and Nuclear Magnetic Resonance in Solids.* Oxford University Press, London, 1970.

[72] M. Goto, A. Ouema, H. Takahashi, S. Ono, and N. Sarukura. Teflon photonic crystal fiber as terahertz waveguide. *Japanese Journal of Applied Physics*, 43(2B):L317 L319, 2004.

[73] V. L. Granatstein, R. K. Parker, and C. M. Armstrong. Vacuum electronics at the dawn of the twenty-first century. *Proceedings of the IEEE*, 87(5):702 716, 1999.

[74] R. G. Griffin and T. F. Prisner. High field dynamic nuclear polarization - the renaissance. *Physical Chemistry Chemical Physics*, 12(22):5737 5740, 2010.

[75] M. K. Haldar and A. H. Beck. Simple derivation of the expression for the synchronous field in circular cylindrical cavity gyrotrons. *Electronics Letters*, 15:487, 1979.

[76] G. R. Hanson, J. B. Wilgen, T. S. Bigelow, S. J. Diem, and T. M. Biewer. Analysis of the ITER low field side reflectometer transmission line system. *Rev. Sci. Instrum.*, 81:10D920, 2010.

[77] A. Hassani, A. Dupuis, and M. Skorobogatiy. Porous polymer fibers for low-loss terahertz guiding. *Opt. Express*, 16(9):6340 6351, 2008.

[78] M. A. Henderson et al. Overview of the ITER EC upper launcher. *Nuclear Fusion*, 48(5):054013, 2008.

[79] M. K. Hornstein. *A continuous-wave second harmonic gyrotron oscillator at 460GHz.* PhD thesis, Massachusetts Institute of Technology, 2005.

[80] M. K. Hornstein, V. S. Bajaj, R. G. Griffin, K. E. Kreischer, I. Mastovsky, M. A. Shapiro, J. R. Sirigiri, and R. J. Temkin. Second harmonic operation at 460 GHz and broadband continuous frequency tuning of a gyrotron oscillator. *Electron Devices, IEEE Transactions on*, 52(5):798 807, 2005.

[81] M. K. Hornstein, V. S. Bajaj, R. G. Griffin, and R. J. Temkin. Continuous-wave operation of a 460-ghz second harmonic gyrotron oscillator. *Plasma Science, IEEE Transactions on*, 34(3):524 533, 2006.

[82] K.-N. Hu, V. S. Bajaj, M. M. Rosay, and R. G. Griffin. High frequency dynamic nuclear polarization using mixtures of TEMPO and Trityl radicals. *J. Chem. Phys.*, 126:044512, 2007.

[83] K.-N. Hu, H.-H. Yu, T. M. Swager, and R. G. Griffin. Dynamic nuclear polarization with biradicals. *J. Am. Chem. Soc.*, 126(35):10844 10845, 2004.

[84] Y. Huang. Conducting triangular chambers for EMC measurements. *Measurement Science and Technology*, 10(3):L21, 1999.

[85] T. Idehara, K. Kosuga, L. Agusu, R. Ikeda, I. Ogawa, T. Saito, Y. Matsuki, K. Ueda, and T. Fujiwara. Continuously frequency tunable high power sub-THz radiation source gyrotron FU CW VI for 600 MHz DNP-NMR spectroscopy. *Journal of Infrared, Millimeter and Terahertz Waves*, 31(7):775 790, 2010.

[86] T. Idehara, K. Yoshida, N. Nishida, I. Ogawa, M. L. Pereyaslavets, and T. Tatsukawa. CW operation of a submillimeter wave gyrotron (gyrotron FU IV) for high stability of the output frequency. *International Journal of Infrared and Millimeter Waves*, 19(6):793 801, 1998.

[87] H. Idei, S. Kubo, et al. Electron cyclotron heating scenario and experimental results in LHD. *Fusion Engineering and Design*, 53(1-4):329 336, 2001.

[88] S. Jawla, J. P. Hogge, S. Alberti, T. Goodman, B. Piosczyk, and T. Rzesnicki. Infrared measurements of the rf output of 170-GHz/2-MW coaxial cavity gyrotron and its phase retrieval analysis. *Plasma Science, IEEE Transactions on*, 37(3):414 424, 2009.

[89] S. K. Jawla, E. A. Nanni, M. A. Shapiro, P. P. Woskov, and R. J. Temkin. Mode content determination of terahertz corrugated waveguides using experimentally measured radiated field patterns. *Plasma Science, IEEE Transactions on*, 40(6):1530 1537, 2012.

[90] C.-G. Joo, K.-N. Hu, J.A. Bryant, and R. G. Griffin. In situ temperature jump high-frequency dynamic nuclear polarization experiments: Enhanced sensitivity in liquid-state NMR spectroscopy. *J. Am Chem. Soc*, 128:9428 9432, 2006.

[91] C. D. Joye, M. A. Shapiro, J. R. Sirigiri, and R. J. Temkin. Demonstration of a 140-GHz 1-kW confocal gyro-traveling-wave amplifier. *IEEE Transactions on Electron Devices*, 56:818 827, 2009.

[92] H. J. Kim, E. A. Nanni, M. A. Shapiro, J. R. Sirigiri, and R. J. Temkin. Experimental measurement of picosecond pulse amplification in a 140 GHz gyro-TWT. In *2010 IEEE International Vacuum Electronics Conference*, pages 193 194, 2009.

[93] H. J. Kim, E. A. Nanni, M. A. Shapiro, J. R. Sirigiri, P. P. Woskov, and R. J. Temkin. Amplification of picosecond pulses in a 140-GHz gyrotron-traveling wave tube. *Physical Review Letters*, 105(13):135101, 2010.

[94] V. V. Komarov. Eigenmodes of regular polygonal waveguides. *Journal of Infrared, Millimeter and Terahertz Waves*, 32(1):40 46, 2011.

[95] E. J. Kowalski, E. A. Nanni, M. A. Shapiro, J. R. Sirigiri, R. J. Temkin, T. S. Bigelow, and D. A. Rasmussen. Measurement of loss in high power 170 GHz gyrotron transmission lines. In *Vacuum Electronics Conference (IVEC), 2010 IEEE International*, pages 335 336, 2010.

[96] E. J. Kowalski, D. S. Tax, M. A. Shapiro, J. R. Sirigiri, R. J. Temkin, T. S. Bigelow, and D. A. Rasmussen. Linearly polarized modes of a corrugated metallic waveguide. *Microwave Theory and Techniques, IEEE Transactions on*, 58(11):2772 2780, 2010.

[97] K. Kreischer, C. Farrar, R. Griffin, R. Temkin, and J. Vieregg. A 250 GHz gyrotron for NMR spectroscopy. In *Plasma Science, 2000. The 27th IEEE International Conference on*, page 198, 2000.

[98] K. Kuriki, O. Shapira, S. D. Hart, G. Benoit, Y. Kuriki, J. F. Viens, M. Bayindir, J. D. Joannopoulos, and Y. Fink. Hollow multilayer photonic bandgap fibers for nir applications. *Opt. Express*, 12(8):1510 1517, 2004.

[99] Y. Y. Lau, K. R. Chu, L. Barnett, and V. L. Granatstein. Gyrotron travelling wave amplifier: II. Effects of velocity spread and wall resistivity. *International Journal of Infrared and Millimeter Waves*, 2(3):395 413, 1981.

[100] F. Leuterer, M. Beckmann, H. Brinkschulte, F. Monaco, M. Münich, F. Ryter, H. Schütz, L. Empacher, G. Gantenbein, W. Förster, et al. Experience with the ECRH system of ASDEX-Upgrade. *Fusion Engineering and Design*, 53(1-4):485 489, 2001.

[101] V. M. Lubecke, K. Mizuno, and G. M. Rebeiz. Micromachining for terahertz applications. *Microwave Theory and Techniques, IEEE Transactions on*, 46(11):1821 1831, 1998.

[102] S. A. Maas. *Microwave mixers*. Artech House Publishers, Norwood, MA, 1986.

[103] T. Maly, G. T. Debelouchina, V. S. Bajaj, K.-N. Hu, C.-G. Joo, M. L. Mak-Jurkauskas, J. R. Sirigiri, P. C. A. van der Wel, J. Herzfeld, R. J. Temkin, and R. G. Griffin. Dynamic nuclear polarization at high magnetic fields. *J. Chem. Physics*, 128:052211, 2008.

[104] Y. Matsuki, T. Maly, O. Ouari, H. Karoui, F. Le Moigne, E. Rizzato, S. Lyubenova, J. Herzfeld, T. Prisner, P. Tordo, and R. Griffin. Dynamic nuclear polarization with a rigid biradical. *Angewandte Chemie*, 121(27):5096 5100, 2009.

[105] Y. Matsuki, H. Takahashi, K. Ueda, T. Idehara, I. Ogawa, M. Toda, H. Akutsu, and T. Fujiwara. Dynamic nuclear polarization experiments at 14.1 T for solid-state NMR. *Physical Chemistry Chemical Physics*, 12(22):5799 5803, 2010.

[106] R. Mendis and D. Grischkowsky. Plastic ribbon THz waveguides. *J. Appl. Phys.*, 88:4449, 2000.

[107] R. Mendis and D. M. Mittleman. An investigation of the lowest-order transverse-electric (TE_1) mode of the parallel-plate waveguide for THz pulse propagation. *J. Opt. Soc. Am. B*, 26(9):A6–A13, 2009.

[108] O. Mitrofanov and J. A. Harrington. Dielectric-lined cylindrical metallic THz waveguides: mode structure and dispersion. *Opt. Express*, 18(3):1898 1903, 2010.

[109] O. Mitrofanov, R. James, F. A. Fernandez, T. K. Mavrogordatos, and J. A. Harrington. Reducing transmission losses in hollow THz waveguides. *Terahertz Science and Technology, IEEE Transactions on*, 1(1):124 132, 2011.

[110] E. A. Nanni. Design of a 250 GHz gyrotron amplifier. Master's thesis, Massachusetts Institute of Technology, 2010.

[111] E. A. Nanni, A. B. Barnes, R. G. Griffin, and R. J. Temkin. THz dynamic nuclear polarization NMR. *Terahertz Science and Technology, IEEE Transactions on*, 1(1):145 163, 2011.

[112] E. A. Nanni, A. B. Barnes, Y. Matsuki, P. P. Woskov, B. Corzilius, R. G. Griffin, and R. J. Temkin. Microwave field distribution in a magic angle spinning dynamic nuclear polarization NMR probe. *Journal of Magnetic Resonance*, 210(1):16 23, 2011.

[113] E. A. Nanni, S. K. Jawla, M. A. Shapiro, P. P. Woskov, and R. J. Temkin. Low-loss transmission lines for high-power terahertz radiation. *Journal of Infrared, Millimeter and Terahertz Waves*, 33:605 714, 2012.

[114] E. A. Nanni, S. M. Lewis, M. A. Shapiro, and R. J. Temkin. A 250 GHz photonic band gap gyrotron amplifier. *Bulletin of the American Physical Society*, 57, 2012.

[115] E. A. Nanni, M. A. Shapiro, J. R. Sirigiri, and R. J. Temkin. 14.4: Design of a 250 GHz photonic band gap gyrotron amplifier. In *Vacuum Electronics Conference (IVEC), 2010 IEEE International*, pages 317 318. IEEE, 2010.

[116] E. A. Nanni, M. A. Shapiro, and R. J. Temkin. Progress on a 250 GHz photonic band gap gyrotron traveling wave tube. In *Infrared, Millimeter and Terahertz Waves (IRMMW-THz), 2011 36th International Conference on*, pages 1 2. IEEE, 2011.

[117] E. A. Nanni, M. A. Shapiro, and R. J. Temkin. A 250 GHz photonic band gap gyrotron traveling wave amplifier. In *Vacuum Electronics Conference (IVEC), 2012 IEEE Thirteenth International*, pages 413 414. IEEE, 2012.

[118] G. Narayanan, N. Erickson, and R. Grosslein. Low cost direct machining of terahertz waveguide structures. In *Tenth International Symposium on Space Terahertz Technology*, volume 1, page 516, 1999.

[119] J. M. Neilson, D. Tax, W. Guss, S. Jawla, E. Kowalski, M. Shapiro, and R. Temkin. Design and test of an internal coupler to corrugated waveguide for high power gyrotrons. In *Vacuum Electronics Conference (IVEC), 2012 IEEE Thirteenth International*, pages 117 118. IEEE, 2012.

[120] K. Nguyen, B. Danly, B. Levush, M. Blank, R. True, K. Felch, and P. Borchard. Electron gun and collector design for 94-GHz gyro-amplifiers. In *Particle Accelerator Conference, 1997. Proceedings of the 1997*, volume 3, 1997.

[121] K. T. Nguyen, J. P. Calame, D. E. Pershing, B. G. Danly, M. Garven, B. Levush, and T. M. Antonsen Jr. Design of a Ka-band gyro-TWT for radar applications. *IEEE Transactions on Electron Devices*, 48(1):108 115, 2001.

[122] T. Notake, T. Saito, Y. Tatematsu, A. Fujii, S. Ogasawara, L. Agusu, I. Ogawa, T. Idehara, and V. N. Manuilov. Development of a novel high power sub-THz second harmonic gyrotron. *Physical Review Letters*, 103(22):225002, 2009.

[123] G. S. Nusinovich. *Introduction to the Physics of Gyrotrons.* Johns Hopkins University Press, 2004.

[124] G. S. Nusinovich and H. Li. Theory of gyro-travelling-wave tubes at cyclotron harmonics. *International Journal of Electronics*, 72(5):895 907, 1992.

[125] G. S. Nusinovich, O. V. Sinitsyn, and A. Kesar. Linear theory of gyro-traveling-wave-tubes with distributed losses. *Physics of Plasmas*, 8:3427, 2001.

[126] I. Ogawa, T. Idehara, M. Myodo, H. Ando, D. Wagner, and M. Thumm. Development of a quasi-optical transmission system for gyrotron application as a radiation source. In *Infrared Millimeter Waves and 14th International Conference on Terahertz Electronics, 2006. IRMMW-THz 2006. Joint 31st International Conference on*, pages 552 552, 2006.

[127] I. Ogawa, T. Idehara, M. Pereyaslavets, and W. Kasparek. Design of a quasi-optical system converting the TE_{06} output mode of a gyrotron into a gaussian-like beam. *International Journal of Infrared and Millimeter Waves*, 20(4):543 558, 1999.

[128] K. Ohkubo, S. Kubo, H. Idei, M. Sato, T. Shimozuma, and Y. Takita. Coupling of tilting gaussian beam with hybrid mode in the corrugated waveguide. *International Journal of Infrared and Millimeter Waves*, 18(1):23 41, 1997.

[129] J. W. Oosterbeek, A. Burger, E. Westerhof, M. R. De Baar, M. A. Van den Berg, W. A. Bongers, M. F. Graswinckel, B. A. Hennen, O. G. Kruijt, J. Thoen, R. Heidinger, S. Korsholm, F. Leipold, and S. Nielsen. A line-of-sight electron

cyclotron emission receiver for electron cyclotron resonance heating feedback control of tearing modes. *Review of Scientific Instruments*, 79(9):093503, 2008.

[130] T. J. Orzechowski, B. R. Anderson, W. M. Fawley, D. Prosnitz, E. T. Scharlemann, S. M. Yarema, A. M. Sessler, D. B. Hopkins, A. C. Paul, and J. S. Wurtele. High gain and high extraction efficiency from a free electron laser amplifier operating in the millimeter wave regime. *Nuclear Instruments and Methods in Physics Research Section A: Accelerators, Spectrometers, Detectors and Associated Equipment*, 250(1):144–149, 1986.

[131] A. W. Overhauser. Polarization of nuclei in metals. *Phys. Rev.*, 92:411–415, 1953.

[132] G. S. Park, S. Y. Park, R. H. Kyser, A. K. Ganguly, and C. M. Armstrong. Gain broadening in an inhomogeneous gyrotron traveling wave amplifier. In *1990 Electron Devices Meeting Technical Digest*, pages 703–705, 1990.

[133] A. Pavolotsky, D. Meledin, C. Risacher, M. Pantaleev, and V. Belitsky. Micromachining approach in fabricating of THz waveguide components. *Microelectronics Journal*, 36(7):683–686, 2005.

[134] D. E. Pershing, K. T. Nguyen, J. P. Calame, B. G. Danly, B. Levush, F. N. Wood, and M. Garven. A TE_{11} Ka-band gyro-TWT amplifier with high-average power compatible distributed loss. *Plasma Science, IEEE Transactions on*, 32(3):947–956, 2004.

[135] J. Petillo, K. Eppley, et al. The MICHELLE three-dimensional electron gun and collector modeling tool: Theory and design. *Plasma Science, IEEE Transactions on*, 30(3):1238–1264, 2002.

[136] J. J. Petillo, E. M. Nelson, J. F. DeFord, N. J. Dionne, and B. Levush. Recent developments to the MICHELLE 2-D/3-D electron gun and collector modeling code. *Electron Devices, IEEE Transactions on*, 52(5):742–748, 2005.

[137] O. A. Peverini, R. Tascone, G. Virone, A. Olivieri, and R. Orta. Orthomode transducer for millimeter-wave correlation receivers. *Microwave Theory and Techniques, IEEE Transactions on*, 54(5):2042–2049, 2006.

[138] B. Plaum, E. Holzhauer, and C. Lechte. Numerical calculation of reflection characteristics of grooved surfaces with a 2D FDTD algorithm. *Journal of Infrared, Millimeter and Terahertz Waves*, 32(4):482–495, 2011.

[139] A. V. Raisanen, D. Choudhury, R. J. Dengler, J. E. Oswald, and P. H. Siegel. A novel split-waveguide mount design for millimeter-and submillimeter-wave frequency multipliers and harmonic mixers. *Microwave and Guided Wave Letters, IEEE*, 3(10):369–371, 1993.

[140] M. Rosay, J. C. Lansing, K. C. Haddad, W. W. Bachovchin, J. Herzfeld, R. J. Temkin, and R. G. Griffin. High frequency dynamic nuclear polarization in MAS spectra of membrane and soluble proteins. *J. Am. Chem. Soc.*, 125:13626–27, 2003.

[141] M. Rosay, L. Tometich, S. Pawsey, R. Bader, R. Schauwecker, M. Blank, P. M. Borchard, S. R. Cauffman, K. L. Felch, R. T. Weber, R. J. Temkin, R. G. Griffin, and W. E. Maas. Solid-state dynamic nuclear polarization at 263 GHz: spectrometer design and experimental results. *Physical Chemistry Chemical Physics*, 12(22):5850–5860, 2010.

[142] M. Rosay, V. Weis, K. E. Kreischer, R. J. Temkin, and R. G. Griffin. Two-dimensional 13C-13C correlation spectroscopy with magic angle spinning and dynamic nuclear polarization. *Journal of the American Chemical Society*, 124(13):3214–3215, 2002.

[143] W. Rowan, M. Austin, J. Beno, R. Ellis, R. Feder, A. Ouroua, A. Patel, and P. Phillips. Electron cyclotron emission diagnostic for ITER. *Review of Scientific Instruments*, 81(10):10D935, 2010.

[144] J. Schneider. Stimulated emission of radiation by relativistic electrons in a magnetic field. *Physical Review Letters*, 2(12):504–505, 1959.

[145] J. Schur, S. Biber, F. Gumbmann, B. Mottet, O. Cojocari, L. P. Schmidt, and H. L. Hartnagel. Micromachined split-block Schottky-diode mixer for 600 GHz. In *Infrared and Millimeter Waves, 2004 and 12th International Conference on Terahertz Electronics, 2004. Conference Digest of the 2004 Joint 29th International Conference on*, pages 325–326. IEEE, 2004.

[146] M. A. Shapiro. Private communication. 2010.

[147] D. J. Singel, H. Seidel, R. D. Kendrick, and C. S. Yannoni. A spectrometer for EPR, DNP, and multinuclear high-resolution NMR. *Journal of Magnetic Resonance*, 81:145–161, 1989.

[148] J. R. Sirigiri. *A novel wideband gyrotron traveling wave amplifier.* PhD thesis, Massachusetts Institute of Technology, 2003.

[149] J. R. Sirigiri, K. E. Kreischer, J. Machuzak, I. Mastovsky, M. A. Shapiro, and R. J. Temkin. Photonic-band-gap resonator gyrotron. *Physical Review Letters*, 86(24):5628–5631, 2001.

[150] J. R. Sirigiri, M. A. Shapiro, and R. J. Temkin. High-power 140-GHz quasioptical gyrotron traveling-wave amplifier. *Physical Review Letters*, 90(25):258302, 2003.

[151] E. I. Smirnova, C. Chen, M. A. Shapiro, J. R. Sirigiri, and R. J. Temkin. Simulation of photonic band gaps in metal rod lattices for microwave applications. *Journal of Applied Physics*, 91:960, 2002.

[152] E. I. Smirnova, A. S. Kesar, I. Mastovsky, M. A. Shapiro, and R. J. Temkin. Demonstration of a 17-GHz, high-gradient accelerator with a photonic-band-gap structure. *Physical Review Letters*, 95(7):74801, 2005.

[153] C. H. Smith, A. Sklavonuos, and N. S. Barker. SU-8 micromachining of millimeter and submillimeter waveguide circuits. In *Microwave Symposium Digest, 2009. MTT'09. IEEE MTT-S International*, pages 961 964. IEEE, 2009.

[154] R. Temkin, A. Barnes, R. Griffin, S. Jawla, I. Mastovsky, E. Nanni, M. Shapiro, A. Torrezan, and P. Woskov. Recent progress at MIT on THz gyrotron oscillators for DNP/NMR. In *Infrared Millimeter and Terahertz Waves (IRMMW-THz), 36th International Conference on*, 2011.

[155] R. J. Temkin, A. B. Barnes, R. G. Griffin, S. Jawla, E. Nanni, and A. C. Torrezan. 460 and 527 GHz gyrotron systems for DNP / NMR. In *Third International Symposium on Dynamic Nuclear Polarization*, 2011.

[156] R. J. Temkin, K. Kreischer, S. M. Wolfe, D. R. Cohn, and B. Lax. High frequency gyrotrons and their application to tokamak plasma heating. *Journal of Magnetism and Magnetic Materials*, 11(1-3):368–371, 1979.

[157] R. J. Temkin, K. E. Kreischer, W. J. Mulligan, S. MacCabe, and H. R. Fetterman. A 100 kW, 140 GHz pulsed gyrotron. *International Journal of Infrared and Millimeter Waves*, 3(4):427–437, 1982.

[158] M. Thumm. Modes and mode conversion in microwave devices. *Generation and Application of High Power Microwaves*, pages 121–171, 1997.

[159] M. K. Thumm. *State-of-the-art of high power gyro-devices and free electron masers.* Kernforschungszentrum Karlsruhe, 1993.

[160] M. K. Thumm and W. Kasparek. Passive high-power microwave components. *Plasma Science, IEEE Transactions on*, 30(3):755–786, 2002.

[161] K. R. Thurber, W.-M. Yau, and R. Tycko. Low-temperature dynamic nuclear polarization at 9.4 T with a 30 mW microwave source. *Journal of Magnetic Resonance*, 204(2):303 313, 2010.

[162] A. C. Torrezan. *Frequency-tunable second-harmonic submillimeter-wave gyrotron oscillators.* PhD thesis, Massachusetts Institute of Technology, 2010.

[163] A. C. Torrezan, Han Seong-Tae, I. Mastovsky, M. A. Shapiro, J. R. Sirigiri, R. J. Temkin, A. B. Barnes, and R. G. Griffin. Continuous-wave operation of a frequency-tunable 460-GHz second-harmonic gyrotron for enhanced nuclear magnetic resonance. *Plasma Science, IEEE Transactions on*, 38(6):1150–1159, 2010.

[164] A. C. Torrezan, Han Seong-Tae, M. A. Shapiro, J. R. Sirigiri, and R. J. Temkin. CW operation of a tunable 330/460 GHz gyrotron for enhanced nuclear magnetic resonance. In *Infrared, Millimeter and Terahertz Waves, 2008. IRMMW-THz 2008. 33rd International Conference on*, pages 1–2, 2008.

[165] A. C. Torrezan, M. A. Shapiro, J. R. Sirigiri, R. J. Temkin, and R. G. Griffin. Operation of a continuously frequency-tunable second-harmonic CW 330-GHz gyrotron for dynamic nuclear polarization. *Electron Devices, IEEE Transactions on*, 58(8):2777 2783, 2011.

[166] R. Q. Twiss. Radiation transfer and the possibility of negative absorption in radio astronomy. *Australian Journal of Physics*, 11(4):564 579, 1958.

[167] M. Vahidpour and K. Sarabandi. Micromachined J-band rectangular waveguide filter. In *General Assembly and Scientific Symposium, 2011 XXXth URSI*, pages 1 4. IEEE, 2011.

[168] V. Vitzthum, M. A. Caporini, and G. Bodenhausen. Solid-state nitrogen-14 nuclear magnetic resonance enhanced by dynamic nuclear polarization using a gyrotron. *Journal of Magnetic Resonance*, 205(1):177 179, 2010.

[169] H. Wang, H. Li, Y. Luo, and R. Yan. Theoretical and experimental investigation of a Ka-band gyro-TWT with lossy interaction structure. *Journal of Infrared, Millimeter and Terahertz Waves*, 32(2):172–185, 2011.

[170] K. Wang and D. M. Mittleman. Metal wires for terahertz wave guiding. *Nature*, 432(7015):376 379, 2004.

[171] R. A. Wind, M. J. Duijvestijn, C. Vanderlugt, A. Manenschijn, and J. Vriend. Applications of dynamic nuclear-polarization in C-13 NMR in solids. *Progress in Nuclear Magnetic Resonance Spectroscopy*, 17:33 67, 1985.

[172] D. S. Wollan. Dynamic nuclear polarization with an inhomogeneously broadened ESR line. I Theory. *Phys. Rev. B*, 13:3671 3685, 1976.

[173] D. S. Wollan. Dynamic nuclear polarization with an inhomogeneously broadened ESR line. II. Experiment. *Physical Review B*, 13(9):3686, 1976.

[174] P. P. Woskov, V. S. Bajaj, M. K. Hornstein, R. J. Temkin, and R. G. Griffin. Corrugated waveguide and directional coupler for CW 250-GHz gyrotron DNP experiments. *Microwave Theory and Techniques, IEEE Transactions on*, 53(6):1863 1869, 2005.

[175] P. P. Woskov, M. K. Hornstein, and R. J. Temkin. Transmission lines for 250 and 460 GHz CW gyrotron DNP experiments. In *Infrared and Millimeter Waves and 13th International Conference on Terahertz Electronics, 2005. IRMMW-THz 2005. The Joint 30th International Conference on*, volume 2, pages 563 564 vol. 2, 2005.

[176] P. P. Woskov, E. A. Nanni, M. A. Shapiro, S. K. Jawla, J. S. Hummelt, R. J. Temkin, and A. B. Barnes. 330 GHz helically corrugated waveguide. In *Infrared, Millimeter and Terahertz Waves (IRMMW-THz), 2011 36th International Conference on*, pages 1–2. IEEE, 2011.

[177] V. K. Yulpatov. Nonlinear theory of the interaction between a periodic electron beam and an electromagnetic wave. *Radiophysics and Quantum Electronics*, 10(6):471 476, 1967.

[178] V. K. Yulpatov. Averaged equations for oscillations in the CRM-monotron. *3rd Winter School for Engineers, Saratov*, 4:144 178, 1974.

[179] V. E. Zapevalov, V. V. Dubrov, A. S. Fix, E. A. Kopelovich, A. N. Kuftin, O. V. Malygin, V. N. Manuilov, M. A. Moiseev, A. S. Sedov, N. P. Venediktov, and N. A. Zavolsky. Development of 260 GHz second harmonic CW gyrotron with high stability of output parameters for DNP spectroscopy. In *Infrared, Millimeter, and Terahertz Waves., 34th International Conference on*, pages 1 2, 1979.

[180] E. V. Zasypkin, I. G. Gachev, and I. I. Antakov. Experimental study of a W-band gyroklystron amplifier operated in the high-order TE_{021} cavity mode. *Radiophysics and Quantum Electronics*, 55(5):1 9, 2012.

[181] N. I. Zaytsev, T. B. Pankratova, M. I. Petelin, and V. A. Flyagin. Millimeter- and submillimeter-wave gyrotrons. *Radio Eng. Electron. Phys.*, 19(5):103 107, 1974.